

# Northumbria Research Link

Citation: Mustafa, Abba Imam (2022) Theoretical and experimental studies for improving the design of the solar field and organic Rankine cycle turbine in a small linear Fresnel reflector solar thermal power plant. Doctoral thesis, Northumbria University.

This version was downloaded from Northumbria Research Link:  
<https://nrl.northumbria.ac.uk/id/eprint/51555/>

Northumbria University has developed Northumbria Research Link (NRL) to enable users to access the University's research output. Copyright © and moral rights for items on NRL are retained by the individual author(s) and/or other copyright owners. Single copies of full items can be reproduced, displayed or performed, and given to third parties in any format or medium for personal research or study, educational, or not-for-profit purposes without prior permission or charge, provided the authors, title and full bibliographic details are given, as well as a hyperlink and/or URL to the original metadata page. The content must not be changed in any way. Full items must not be sold commercially in any format or medium without formal permission of the copyright holder. The full policy is available online: <http://nrl.northumbria.ac.uk/policies.html>

Theoretical and experimental studies for  
improving the design of the solar field and organic  
Rankine cycle turbine in a small linear Fresnel  
reflector solar thermal power plant

MUSTAFA ABBA IMAM

PhD

2022

Theoretical and experimental studies for  
improving the design of the solar field and organic  
Rankine cycle turbine in a small linear Fresnel  
reflector solar thermal power plant

MUSTAFA ABBA IMAM

A thesis submitted in partial fulfilment of the  
requirements of the University of Northumbria at  
Newcastle for the degree of Doctor of Philosophy

Department of Mechanical and Construction  
Engineering

January 2022

## Abstract

Providing sustainable, cost-effective and environmentally friendly energy for consumer societies and industrial economies has been a major concern for industrialized and developing countries. For that reason, there is a renewed interest in the generation of energy from various solar technologies. Among others, Concentrated Solar Power (CSP) technologies has the potential to meet such demands. However, most recent solar energy harnessing technologies require substantial energy to attain efficient power production with compact plant size and the least payback time. Linear Fresnel coupled with organic Rankine cycle solar thermal power plant may prove to be a promising choice due to its capacity to overcome techno-commercial constraints related with conventional reflector based CSP Technologies.

Theoretical and experimental studies for improving the design of a solar field and organic Rankine cycle turbine in a small Linear Fresnel Reflector solar thermal power plant is performed in this study. In the initial stage, the design and optimization of the 3D optical model of the LFR solar field is presented in an attempt to minimize the drift and variation in ray concentration and improve the optical performance. In the solar field optimization, key variables such as the mirror curvature, width, length, the distance between consecutive mirror centre lines and height were selected. Subsequently, a Monte Carlo Raytracing and thermal analysis were performed to investigate the impact of the optimized mirror elements on the optical performance of the solar field. A comparative analysis between two LFR configurations, Central LFR (CenLFR) and Compact LFR (ComLFR) is put forward by adopting a similar approach.

Furthermore, a small-scale organic Rankine cycle turbine used for low-temperature applications capable of generating electrical power was theoretically and experimentally investigated. A single-stage axial turbine expander deploying R365mfc, and the new environmentally friendly Novec649 organic working fluids were selected. Modelling of the turbine and comparative analysis of the two working fluids is performed adopting a simple CFD approach proposed. The effect of the range of inlet definition variables such as temperature, pressure, rotational speed and key thermodynamic properties of the fluids on the work output and isentropic efficiency as well as the influence of rotor tip clearance (rotor gap) on the turbine power were investigated and analysed. In the closing stage, the shading analysis of the solar field and environs is performed using different approaches. In this context, shading resulting mainly from structures such as buildings and vegetation is considered. The analysis



considers sun and shadow effects that can be easily and dynamically improved or even animated within the program to evaluate the timing and effect of obstructions and the resulting consequence on the optical performance of the solar field.

The numerical approaches were validated with optical and thermal experimental data gathered from a linear Fresnel plant erected in Almatret, Spain. Results show a good correlation between the numerical approach and experimental study. Findings from the solar field study show that optimising key mirror elements such as the curvature, width, length, receiver height from the mirror plane, and the distance between two consecutive mirror centrelines can significantly impact the LFR solar field optical performance. This leads to an improved concentration factor which can enhance the energy conversion efficiency of LFR plants and greatly minimize the cost of thermal storage, which results in a low Levelized cost of electricity (LCOE) and offers LFR the economic potential to compete with other CSP power plants. Next to that, results of the comparative analysis show minimized drift in ray concentration and the computed energy efficiency for separate mirror elements, and the overall solar field show improved optical performance for the central configuration. Despite blocking and shading effect minimized in the compact configuration, findings show lower optical efficiency, mainly due to the receiver being fixed and its distance away from the primary mirrors. In both solar field studies, it was observed that losses are greatly influenced by the solar field orientation.

As per the ORC turbine, it was observed that the inlet turbine temperature and pressure have the greatest effect on the power, work output and isentropic efficiency. The selection of an organic working fluid and its application in ORC turbine is a crucial aspect mainly due to the dependence of its categorization on the temperature of the heat source, defined by the fluid thermodynamic and thermophysical. As expected, the computed peak power output is generated by the “ideal” turbine expander design with zero clearance of blade tips. Exceeding the 200  $\mu\text{m}$  rotor gap results in a sharp detrimental effect on the turbine performance. Shading analysis was found to be a fundamental step in the phase of design, installation and operation of a solar field. Shading of any form can have a negative influence on the performance of an entire solar field. Such estimations are significant, especially when designing collectors for places where the available land strip does not align with a particular orientation, as in the case of the north-south configuration.

## Acknowledgement

First of all, I would like to thank the almighty God for giving me the strength and ability to understand, learn and complete this research work.

I am very grateful to my supervisor, Prof. Khamid Makahmov, whose expertise, understanding, generous guidance and support, made it possible to embark on this research that was of great interest to me. It was due to his dedication, friendly and overwhelming attitude of always being available on SOS that I was able to complete my research in a respectable manner. It was a pleasure working with him.

I am very grateful to my co-supervisor Dr Rahmati Muhammed, and the research team Dr Irina Makahmov, Dr Fadi Kawash, Dr Shine Win and Dr John Nkor, whose valuable support, a timely suggestion with kindness and interaction on a routine basis on my findings helped me shape my work and learn many valuable things. It is also my privilege to thank project partners of the Innova MICRO solar for their valuable contribution and support, especially in conducting the experiments.

I would also like to extend my sincere gratitude and warm appreciation to my parents and siblings for their unprecedented all-round support that led me to where I am today. I would also like to acknowledge my friends Faheem Malik, Shivam Salokhe, Nnamdi Maduka, whose guidance and interest in my research was very beneficial.

Finally, and most importantly, huge thanks to my sponsor, Petroleum Technology Development Fund (PTDF) and most precisely, the overseas scholarship team for the moral and financial support. I would like to convey my deep regards to Northumbria university for the opportunity to pursue this research work towards a PhD in an environment that provides first-class facilities and support.

## **Dedication**

Every challenging work requires self-efforts as well as guidance from those that are very close to us. This thesis is dedicated to my parents, whose unprecedented love, affection, support and prayers guided me to pursue my dreams and enable me to attain such success and honour, along with all respected teachers.

## Declaration

I declare that the work contained in this thesis has not been submitted for any other award and that it is all my own work. I also confirm that this work fully acknowledges opinions, ideas and contributions from the work of others.

Any ethical clearance for the research presented in this thesis has been approved.

I declare that the word count of this thesis is currently 88778 words.

Name: Mustafa Abba Imam

Signature:

Date: 08/01/2022

## Content

Abstract.....	I
Acknowledgement.....	III
Dedication.....	IV
Declaration.....	V
Content.....	VI
List of figures.....	IX
List of tables.....	XV
Nomenclature.....	XVI
Greek Symbols.....	XVI
Subscripts and superscript.....	XVII
Abbreviation.....	XVII
 <b>Chapter 1: Introduction.....</b>	 <b>1</b>
1.1 Problem statement.....	1
1.2 Background.....	6
1.2.1 Parabolic trough collector (PTC).....	7
1.2.2 Central receiver system (CRS).....	7
1.2.3 Parabolic dish collector (PDC).....	8
1.2.4 Linear Fresnel reflector (LFR).....	8
1.2.5 Optical and thermal modelling.....	10
1.2.6 Organic Rankine cycle turbine.....	11
1.2.7 Heat transfer and organic working fluids.....	12
1.2.8 Shading analysis.....	12
1.3 Research aim.....	12
1.4 Objectives.....	13
1.5 Outline of thesis.....	13
 <b>Chapter 2: Literature Review.....</b>	 <b>17</b>
2.1 Introduction.....	17
2.2 Concentrating solar power.....	17
2.2.1 History and context.....	18
2.2.2 Distribution of the solar resource for CSP.....	22
2.2.3 Current technologies for concentrating solar power.....	23
2.2.4 Linear Fresnel reflectors (LFR).....	24
2.2.4.1 LFR solar field configuration.....	25
2.2.4.2 LFR geometry and optical analysis.....	27
2.2.4.3 LFR receiver and secondary reflector configurations.....	40
2.2.4.4 LFR power plants.....	48
2.2.5 Parabolic trough collectors (PTC).....	50
2.2.5.1 PTC solar field configuration.....	51
2.2.5.2 PTC geometry and optical analysis.....	52
2.2.5.3 PTC receiver configurations.....	55
2.2.5.4 PTC power plants.....	57
2.2.6 Parabolic dish collectors (PDC).....	58
2.2.6.1 PDC solar field configuration.....	60
2.2.6.2 PDC geometry and optical analysis.....	61
2.2.6.3 PDC receiver configurations.....	65
2.2.6.4 PDC power plants.....	71
2.2.7 Central receiver system (CRS).....	73
2.2.7.1 CRS solar field configuration.....	75
2.2.7.2 CRS geometry and optical analysis.....	76

2.2.7.3	CRS receiver configurations.....	81
2.2.7.4	CRS power plants.....	86
2.2.8	Heat transfer fluids.....	91
2.2.8.1	Oil.....	93
2.2.8.2	Molten salts.....	95
2.2.8.3	Water/steam.....	97
2.2.8.4	Air/gases.....	98
2.2.8.5	Liquid metals.....	100
2.2.8.6	Organics.....	101
2.2.9	Power cycles for concentrating solar power.....	102
2.2.9.1	Organic Rankine cycle.....	102
2.2.9.2	Steam turbines.....	122
2.2.9.3	Stirling engines.....	125
2.2.9.4	Brayton cycles.....	125
2.2.10	Future growth, cost, and value of CSP.....	126
2.3	General discussion on concentrated solar power technologies.....	132
<b>Chapter 3: Linear Fresnel Reflector Solar Field.....</b>		<b>144</b>
3.1	Introduction.....	144
3.2	Innova Micro SOLAR Project.....	145
3.3	Numerical approach and optical modelling of the LFR.....	147
3.3.1	LightTools Illumination Design Software Applications.....	147
3.3.2	Solar field configuration.....	148
3.3.3	Modelling primary mirrors.....	150
3.3.4	The efficiency of LFR solar field.....	151
3.3.5	Optimization and Monte Carlo Ray Tracing (MCRT).....	152
3.4	Thermal modelling – receiver tube.....	156
3.4.1	Receiver tube.....	157
3.4.2	Mesh details and sensitivity analysis.....	158
3.4.3	Model governing equations.....	159
3.4.4	Material properties: heat transfer fluid (HTF).....	161
3.4.5	Boundary conditions.....	162
3.4.6	Solver setting.....	163
3.5	Analysis of results and discussion.....	163
3.5.1	Monte Carlo Ray Tracing – analysis of simulation results.....	166
3.5.2	Thermal performance.....	184
3.6	Summary and conclusion.....	186
<b>Chapter 4: Comparative Analysis of Linear Fresnel Reflector Configurations.....</b>		<b>188</b>
4.1	Introduction.....	188
4.2	Linear Fresnel Reflector Solar Field – Comparative Analysis .....	188
4.3	Numerical approach and optical modelling of the LFR.....	189
4.3.1	Solar field configuration.....	189
4.3.2	Modelling primary mirrors.....	191
4.3.3	Optimization and Monte Carlo Ray Tracing (MCRT).....	192
4.3.4	The efficiency of LFR solar field.....	194
4.4	Analysis of results and discussion.....	194
4.4.1	Monte Carlo Ray Tracing - analysis of simulation results.....	196
4.5	Summary and conclusion.....	205
<b>Chapter 5: Organic Rankine Cycle Turbine.....</b>		<b>207</b>
5.1	Introduction.....	207
5.2	The Organic Rankine cycle turbine.....	208

5.3	Organic working fluids selection.....	209
5.4	CFD methodology and numerical approach.....	210
5.4.1	Mesh details and sensitivity analysis.....	211
5.4.2	Model governing equations.....	212
5.4.3	Material properties: Organic fluid.....	214
5.4.4	Boundary conditions.....	214
5.4.5	Solver setting.....	215
5.5	Results and discussion.....	216
5.6	Summary and conclusion.....	222
<b>Chapter 6: Solar Field Shading Analysis.....</b>		<b>225</b>
6.1	Introduction.....	225
6.2	Sun path.....	226
6.3	Assessing the impact of shading.....	228
6.4	Summary and conclusion .....	231
<b>Chapter 7: General Discussion.....</b>		<b>233</b>
<b>Chapter 8: Conclusion and Recommendation for Future Work.....</b>		<b>243</b>
8.1	Conclusion.....	243
8.2	Recommendation for future work.....	249
<b>Reference.....</b>		<b>252</b>

## Table of figures

### Chapter 1

Figure 1.1	Parabolic troughs (line focus, mobile receiver).....	9
Figure 1.2	Solar towers (point focus, fixed receiver).....	10
Figure 1.3	Parabolic dishes (point focus, mobile receiver).....	10
Figure 1.4	Linear Fresnel reflectors (line focus, fixed receiver).....	11
Figure 1.5	Organic Rankine Cycle Turbine.....	11
Figure 1.6	Flow chart showing an outline of thesis.....	14

### Chapter 2

Figure 2.1	Solar resource for CSP technologies.....	22
Figure 2.2	Linear Fresnel reflector solar field.....	24
Figure 2.3	Central Linear Fresnel Reflector Configuration (a) and Compact Linear Fresnel Reflector Configuration (b).....	26
Figure 2.4	Linear Fresnel Solar Field North-South orientation (Left) and East-West Orientation (Right).....	27
Figure 2.5	Scheme of the three mirror profiles addressed: (a) flat-shape mirrors, (b) parabolic-shaped mirrors, and (c) cylindrical-shaped mirror.....	27
Figure 2.6	Scheme of the reflection in a cylindrical mirror.....	29
Figure 2.7	An image of the Fresdemo prototype with the main geometrical features.....	30
Figure 2.8	Concentration factor variation across the Fresdemo receiver for (a) flat mirrors, (b) parabolic mirrors, and (c) cylindrical mirrors along the day 21st June.....	31
Figure 2.9	Schematic description of ray tracing simulation: general LFC layout (right), beam spread at the primary mirror (lower left) and receiver consisting of secondary mirror and absorber (upper left).....	31
Figure 2.10	Concentrated solar irradiance maps on the receiver, for the three configurations, considered, on the 21st June at solar noon (12:00 solar hour).....	34
Figure 2.11	Images of SLFR solar system (a), and SLFR solar system with extended support (b)...	34
Figure 2.12	Curves of solar altitude angle, optical efficiency of SLFR concentrator before and after end losses adjustment.....	35
Figure 2.13	Photograph (Left) and Schematic representation (Right) of Solar field at Vallipuram, India based on LFR and secondary concentrators.....	36
Figure 2.14	Design parameters of the Linear Fresnel Reflector Solar Field.....	36
Figure 2.15	The photograph of the studied Fresnel solar field prototype (Left) and set up of the installation. (Right).....	38
Figure 2.16	Theoretical and measured power for the day 13/04/2015 and Daily theoretical and measured efficiency for the day 08/04/2015.....	39
Figure 2.17	Fresnel Solar Field deploying various receiver configurations .....	40
Figure 2.18	Sketch of Compact Linear Fresnel Reflector (CLFR).....	41
Figure 2.19	Compact LFR plant in Kimberlina, USA (Left) and Linear Fresnel collector prototype, Italy (Right).....	41
Figure 2.20	Fresdemo prototype at the Plataforma Solar de Almería (PSA) in Spain (Left) and Puerto Errado -1 (PE1) Fresnel solar field (right).....	42
Figure 2.21	Stainless steel absorber tube with spectrally selective coating.....	43
Figure 2.22	Common receiver configurations used in Linear Fresnel collectors.....	44
Figure 2.23	Receiver assembly used for the FRESDEMO project at PSA.....	44
Figure 2.24	Real-time flux distributions in MTCR on spring equinox when S1 and S2 are used.....	46
Figure 2.25	Real-time flux distributions in STRSC on spring equinox when S1 and S2 are used....	47
Figure 2.26	Areva Solar's compact linear Fresnel reflectors at the Kimberlina power station (up to 482°C) in California with multiple tube receiver with simple trapezoidal secondary reflector.....	48



Figure 2.27	Novatec's linear Fresnel collector solar fields at the PE1 (Nova1) and PE2 (SuperNova) power stations (up to 520°C).....	49
Figure 2.28	General view of the Parabolic Trough Collector.....	51
Figure 2.29	Path of parallel rays at a parabolic mirror (Left) and Geometrical parabolic trough parameters.....	52
Figure 2.30	Focal length as shape parameter (Left) and Relation between the focal length and the rim angle for a constant trough aperture width.....	53
Figure 2.31	Schematic of a typical parabolic trough receiver.....	55
Figure 2.32	Absorber tube integrated in a parabolic trough collector.....	56
Figure 2.33	Photo of the AndaSol" solar power plant, Marquesado del Zenete (Left) and Simplified flow diagram.....	58
Figure 2.34	Dish mounted PCM storage system for the Stirling power cycle.....	59
Figure 2.35	Geometrical concentration of parabolic dish.....	61
Figure 2.36	Geometrical dish parameters and representation of the rim angle in a cross-section of a paraboloid.....	62
Figure 2.37	Model of parabola dish in ray-tracing simulation.....	64
Figure 2.38	Schematic of a regenerative Brayton heat engine couple with a two-axis tracking parabolic dish collector.....	64
Figure 2.39	Schematical representation of an external receiver (left) and a cavity receiver (right)...	65
Figure 2.40	Direct illumination cavity receivers and their integration into Stirling engines.....	66
Figure 2.41	Indirect illumination receiver.....	67
Figure 2.42	schematic diagram of parabolic dish collector with cylindrical receiver apparatus (a) and photo of the studied dish with its receiver.....	68
Figure 2.43	The effect of HTF inlet temperature on HTF outlet temperature (different ambient air temperatures in range of 296 - 305 K, solar irradiation intensity in range of 600 -1050 W/m <sup>2</sup> , receiver aperture diameter and height of 0.2 and 0.4m respectively).....	68
Figure 2.44	The effect of solar irradiation intensity on HTF outlet temperature (HTF inlet temperature in range of 309-343 K and different ambient air temperatures in range of 296-305 K, receiver aperture diameter and height of 0.2 and 0.4m respectively).....	69
Figure 2.45	Enlarged view of different types of receivers.....	69
Figure 2.46	Temperature contours for various inclinations (a) semi-cavity receiver (b) cavity receiver (c) modified cavity receiver at 400 °C.....	70
Figure 2.47	Maricopa parabolic dish power plant (USA).....	72
Figure 2.48	The Shenandoah dish is shown in (a) schematic view and (b) as installed. (Kinoshita, 1983).....	72
Figure 2.49	Schematic of a central receiver system solar field.....	74
Figure 2.50	Central receiver concentrated solar power plant layout.....	75
Figure 2.51	The heliostats configuration completely surround central receiver tower (Left) and heliostats located north of the receiver tower, and the receiver.....	76
Figure 2.52	Heliostat geometry.....	77
Figure 2.53	The geometrical configuration of unit vectors associated with sun, tower, and mirror.....	79
Figure 2.54	(a) shows the relationship between the standard deviation of the Gaussian distribution of the radiation and the k value. (b) shows the aiming strategy in the case $H_{rec} < (2 \cdot rk)$ (c) shows the aiming strategy in the case $H_{rec} > (2 \cdot rk)$ .....	81
Figure 2.55	Diagrams of different central receiver configurations, with red denoting the absorbing surface.....	82
Figure 2.56	Two types of solar towers receivers, (a) external receiver and (b) cavity receive.....	83
Figure 2.57	Operation of the novel Variable Velocity Receiver vs a Traditional External Tubular Receiver.....	84
Figure 2.58	Central receiver volumetric receiver.....	85

Figure 2.59	The PS10 power plant description and layout.....	87
Figure 2.60	The PS10 power plant solar field.....	87
Figure 2.61	The SOLAR TRES power plant description and layout.....	89
Figure 2.62	Operating temperature range for various HTFs.....	92
Figure 2.63	Schematic of axial flow (left) and radial inflow (right) turbines.....	106
Figure 2.64	Meridional view (left) and architecture of turbine stage (right).....	107
Figure 2.65	Schematic of radial outflow turbine.....	109
Figure 2.66	Operation of the scroll expander.....	111
Figure 2.67	Schematic of a twin-screw expander.....	112
Figure 2.68	Operation of a rotary vane expander.....	114
Figure 2.69	Diagram of possible applications of ORC according to the energy source.....	117
Figure 2.70	Schematic diagram of an ORC connected with a small solar field and with energy storage.....	117
Figure 2.71	ORC with solar energy and coupled directly to an RO process.....	118
Figure 2.72	Cogeneration with ORC technology and biomass combustion.....	119
Figure 2.73	Typical plant with the geothermal generation with ORC.....	120
Figure 2.74	Combined cycle turbine/microturbine of gas – ORC.....	122
Figure 2.75	Indicative configuration for a large-scale steam turbine power plant.....	123
Figure 2.76	Status of concentrated solar power (CSP) plants worldwide.....	127
Figure 2.77	Growth of CSP production under four scenarios.....	129
Figure 2.78	Growth of CSP production by region.....	130
Figure 2.79	Production and consumption of CSP electricity by 2050.....	131
 <b>Chapter 3</b>		
Figure 3.1	Innova Micro SOLAR Project LFR solar filed layout.....	146
Figure 3.2	The 3D model of the solar field Innova Micro SOLAR Project LFR solar filed.....	147
Figure 3.3	Solar Field configurations for proposed study.....	148
Figure 3.4	Modelling layout and schematic representation of the Innova Micro Solar pilot plant..	149
Figure 3.5	schematic design showing the layout of reflectors (mirrors).....	151
Figure 3.6	Flow chart of the iterative algorithm.....	153
Figure 3.7	Sun Model and Solar Field. (a) Shows the Solar field with direction indicators.....	155
Figure 3.8	Monthly average irradiance data for Spain (July and December) and the USA (May and December).....	156
Figure 3.9	Stainless steel absorber tube with spectrally selective coating.....	157
Figure 3.10	View of the converged mesh (a) Medium mesh, (b) fine mesh, (c) refined mesh.....	158
Figure 3.11	Mesh details and sensitivity analysis.....	159
Figure 3.12	Schematic of the physical domain of receiver pipe.....	160
Figure 3.13	Temperature dependent fluid properties of thermonol 62: specific heat capacity and viscosity (Left) and Thermal conductivity and density (Right).....	162
Figure 3.14	The converged residuals momentum, energy, mass, turbulence and mass flow rate.....	163
Figure 3.15	Solar field before (right) and after optimization (left).....	164
Figure 3.16	Results from optimization of solar field: (a) left - is the tilt angle of mirrors at the reference point and (b) right - is the alterations in mirror curvatures.....	164
Figure 3.17	The result of merit function of the optimised solar field.....	166
Figure 3.18	Pictorial (symmetrical) representation of optimised mirror curvatures – M- mirrors 1- 9.....	166
Figure 3.19	Raytracing results - power concentrated on the receiver in July (left) and annual harnessed energy (right).....	167
Figure 3.20	Monthly average energy (Left) and annual energy (Right) concentrated on the receiver.....	167

Figure 3.21	The concentration density of irradiance impinging on the receiver at 9:00 am in July considering north-south (NS) and east-west (EW) orientations (a) Flat, (b) Uniform curvature, (c) Optimised mirrors.....	168
Figure 3.22	The concentration density of irradiance impinging on the receiver at 12:00 noon in July considering north-south (NS) and east-west (EW) orientations (a) Flat, (b) Uniform curvature, (c) Optimised mirrors.....	169
Figure 3.23	The concentration density of irradiance impinging on the receiver at 3:00 pm in July considering north-south (NS) and east-west (EW) orientations (a) Flat, (b) Uniform curvature, (c) Optimised mirrors.....	170
Figure 3.24	Solar field ray tracing at 9: 00 am: north-south (NS) – Left and east-west (EW) solar field – Right showing the effect oof end losses.....	171
Figure 3.25	The concentration of irradiance impinging on the receiver at 9:00 am in July considering north-south (NS) and east-west (EW) orientations (a) Flat, (b) Uniform curvature, (c) optimised mirrors.....	171
Figure 3.26	The concentration of irradiance impinging on the receiver at 12:00 noon in July considering north-south (NS) and east-west (EW) orientations (a) Flat, (b) uniform curvature, (c) Optimised mirrors.....	172
Figure 3.27	The concentration of irradiance impinging on the receiver at 3:00 pm in July considering north-south (NS) and east-west (EW) orientations (a) Flat, (b) Uniform curvature, (c) Optimised mirrors.....	173
Figure 3.28	The concentration density of irradiance impinging on the receiver at 9:00 am in December considering north-south (NS) and east-west (EW) orientations (a) Flat, (b) Uniform curvature, (c) Optimised mirrors.....	175
Figure 3.29	The concentration density of irradiance impinging on the receiver at 12:00 noon in December considering north-south (NS) and east-west (EW) orientations (a) Flat, (b) Uniform curvature, (c) Optimized mirrors.....	175
Figure 3.30	The concentration density of irradiance impinging on the receiver at 3:00 pm in December considering north-south (NS) and east-west (EW) orientations (a) Flat, (b) Uniform curvature, (c) Optimised mirrors.....	176
Figure 3.31	Solar field ray tracing at 9: 00 am: north-south (NS) – Left and east-west (EW) solar field – Right showing the effect of end losses.....	177
Figure 3.32	The concentration of irradiance impinging on the receiver at 9:00 am in December considering north-south (NS) and east-west (EW) orientations (a) Flat, (b) Uniform curvature, (c) Optimised mirrors.....	178
Figure 3.33	The concentration of irradiance impinging on the receiver at 12:00 noon in December considering north-south (NS) and east-west (EW) orientations (a) Flat, (b) Uniform curvature, (c) Optimized mirrors.....	178
Figure 3.34	The concentration of irradiance impinging on the receiver at 3:00 pm in December considering north-south (NS) and east-west (EW) orientations (a) Flat, (b) Uniform curvature, (c) Optimised mirrors .....	179
Figure 3.35	Power concentrated on receiver by different mirror profiles: flat mirrors, uniform mirror curvature and optimized mirrors for north-south (Left) and east-west (Right) in July.....	180
Figure 3.36	Energy efficiency of the different mirror profiles: flat mirrors, uniform mirror curvature and optimized mirrors for north-south (Left) and east-west (Right) in July...	181
Figure 3.37	Power concentrated on receiver by different mirror profiles: flat mirrors, uniform mirror curvature and optimized mirrors for north-south (Left) and east-west (Right) in December.....	181
Figure 3.38	Energy efficiency of the different mirror profiles: flat mirrors, uniform mirror curvature and optimized mirrors for north-south (Left) and east-west (Right) in December.....	182

Figure 3.39	Monthly average energy concentrated on the receiver (left) and annual energy harnessed by north-south and east-west solar field configurations (right).....	183
Figure 3.40	Solar fields showing ray concentration of various mirror shapes (a) – Flat mirrors, (b) – uniform curvature mirrors, (c) – optimized (different curvature) mirrors.....	184
Figure 3.41	Comparison between theoretical and experimental result for values of temperature inlet and outlet.....	185
Figure 3.42	Comparison between theoretical and experimental result for values thermal efficiency.....	185

## Chapter 4

Figure 4.1	Central LFR solar field configuration.....	189
Figure 4.2	Compact LFR solar field configuration.....	190
Figure 4.3	Modelling layout and schematic representation of the Innova Micro Solar pilot plant	191
Figure 4.4	Design and geometrical parameters of primary mirrors.....	192
Figure 4.5	Optimized central (a) and compact (b) LFR solar field configurations.....	195
Figure 4.6	Results from optimization of primary mirrors of the central LFR (a) tilt angle (b) curvature.....	195
Figure 4.7	Results from optimization primary mirrors of the compact LFR (a) tilt angle (b) curvature.....	196
Figure 4.8	The result of merit function of the optimised solar field.....	196
Figure 4.9	The concentration density of irradiance impinging on the receiver in June considering north-south orientations (a) Central LFR receiver (b) Compact LFR right receiver, (C) Compact LFR left receiver.....	198
Figure 4.10	The concentration factor of irradiance impinging on the receiver in June considering north-south orientations (a) Central LFR receiver (b) Compact LFR right receiver, (C) Compact LFR left receiver.....	200
Figure 4.11	The concentration density of irradiance impinging on the receiver in December considering north-south orientations (a) Central LFR receiver (b) Compact LFR right receiver, (C) Compact LFR left receiver.....	201
Figure 4.12	The concentration factor of irradiance impinging on the receiver in December considering north-south orientations (a) Central LFR receiver (b) Compact LFR right receiver, (C) Compact LFR left receiver.....	202
Figure 4.13	Solar field ray tracing showing the effect of end losses on the central and compact LFR configurations.....	203
Figure 4.14	Energy efficiency of primary mirrors of the two solar field configurations in May: Central LFR (right) and Compact LFR (left) .....	203
Figure 4.15	Energy efficiency of primary mirrors of the two solar field configurations in December: Central LFR (right) and Compact LFR (left) .....	204
Figure 4.16	Energy produced by Central and compact LFR configurations – average monthly energy (Left) and annual energy (Right).....	205

## Chapter 5

Figure 5.1	Organic Rankine cycle driven LFR plant.....	208
Figure 5.2	Organic Rankine Cycle (ORC) turbine.....	209
Figure 5.3	Computational meshes of the blade passage for stator and rotor blades.....	211
Figure 5.4	Generated meshes for the turbine Volute and Diffuser.....	212
Figure 5.5	The basic workflow for solver simulation.....	215
Figure 5.6	The converged residuals momentum, energy, mass, turbulence and mass flow rate.....	216
Figure 5.7	Fluid temperatures at turbine outlet (Left) and turbine power for various inlet temperatures and pressures (Right) .....	218
Figure 5.8	Temperature contours in the complete turbine (a) Novec649 (b) R365mfc.....	218

Figure 5.9	Contour of pressure characteristics on complete turbine (a) 0 $\mu\text{m}$ gap contour (b) 200 $\mu\text{m}$ gap contour .....	219
Figure 5.10	Effect of tip clearance (rotor gab) on turbine power output (Left), and comparison of the effect of tip clearance (rotor gab) on Novec649 and R365mfc (Right).....	220
Figure 5.11	Effect of tip clearance (rotor gab) on turbine blades (a) 0 $\mu\text{m}$ gab contour (b) 200 $\mu\text{m}$ contour (c) 0 $\mu\text{m}$ gab streamline (b) 200 $\mu\text{m}$ gab streamline.....	221
Figure 5.12	Isentropic efficiency for different inlet temperature pressure (Left) and Turbine work output for different inlet temperature pressure (Right).....	222
 <b>Chapter 6</b>		
Figure 6.1	Building Layout with east-west solar field orientation (a) and Building Layout with east-west solar field orientation (b).....	227
Figure 6.2	Sun-path during summer (July) season (a) and Sun-path during winter (December) season (b) .....	227
Figure 6.3	Pseudo-colour shading analysis (a) and Raytracing (b) in winter (December) season for east-west solar field orientation.....	228
Figure 6.4	Pseudo-colour shading analysis (a) and Raytracing (b) in winter (December) season for north-south solar field orientation.....	229
Figure 6.5	Total power (w/m <sup>2</sup> ) of solar field in December (a)- east-west orientation, (b) north-south orientation.....	229
Figure 6.6	Pseudo-colour shading analysis (a) and Raytracing (b) in summer (July) season for east-west solar field orientation.....	230
Figure 6.7	Pseudo-colour shading analysis (a) and Raytracing (b) in summer (July) season for north-south solar field orientation.....	230
Figure 6.8	Figure 6.8: Total power (w/m <sup>2</sup> ) of solar field in July (a) - east-west orientation, (b) north-south orientation.....	231

## Table of tables

### Chapter 2

Table 2.1	The four families of Concentrated Solar Power technology.....	23
Table 2.2	Optical and geometrical data of the selected configurations.....	32
Table 2.3	Useful energy efficiency for the three optimized configurations considered, on the 21st June at 17:00 solar hour.....	33
Table 2.4	Technical characteristics of Kimberlina (Left) and Puerto Errado 1 power plants (Right) .....	49
Table 2.5	Technical characteristics of Maricopa power plant.....	72
Table 2.6	Heliostat geometry design parameters.....	78
Table 2.7	The PS10 power plant design features.....	87
Table 2.8	The SOLAR TRES power plant design features.....	89
Table 2.9	Temperature range and thermophysical characteristics HTF based on mineral and synthetic oil.....	94
Table 2.10	List of various molten salts and their thermophysical characteristics.....	96
Table 2.11	List of Some Molten Salts and Their Thermophysical Properties.....	101
Table 2.12	Electricity from CSP plants a share of total electricity consumption.....	128

### Chapter 3

Table 3.1	Dimensional input data for the raytracing Monte Carlo software to optimize the design of the LFR.....	150
Table 3.2	Main parameters used in the raytracing- Monte Carlo numerical simulations.....	154
Table 3.3	Shows the results of the ray sensitivity analysis.....	155
Table 3.4	Features of therminol 62 heat transfer fluid.....	161
Table 3.5	Result of optimization showing curvature and corresponding radius for 5 iteration steps: R-radius, C-curvature.....	165

### Chapter 4

Table 4.1	Geometric parameters of the proposed LFR solar field.....	191
-----------	---	-----

### Chapter 5

Table 5.1	The key features of the turbine and dimensions.....	209
Table 5.2	Thermo-physical properties of organic fluids.....	210
Table 5.3	A detailed grid independence mesh study.....	211
Table 5.4	Input parameters for the experimental and numerical simulation for investigation of the ORC turbines.....	216
Table 5.5	boundary conditions employed in numerical simulation for investigation of the ORC turbines.....	217

## Nomenclature

$A_{primary\ mirrors}$	area of the primary mirrors, $m^2$
$C$	curvature, $m$
$C_p$	specific Heat Capacity, $J/Kg\ K$
$DNI$	direct Normal Irradiance, $W/m^2$
$E$	energy ( $W/m^2$ )
$f_n$	focal length of $n_{th}$ mirror, $m$
$h$	height of absorber from mirror array, $m$
$h_{conv}$	coefficient of convective losses ( $W/m^2.K$ )
$h_{rad}$	coefficient of radiative losses ( $W/m^2.K$ )
$Hits_{avg}$	hits average, -
$M$	mass flow rate, $kg/s$
$MF_{group}$	merit function value, -
$N_{Items}$	number of different parameters for each ray used in merit function, -
$N_{Rays}$	the total number of rays traced
$N_{ReceiverRays}$	the number of rays that hit the receiver
$p_{primary\ mirror}$	primary mirror reflectivity, -
$Q$	heat flux, $W$
$Q_{conv}$	convection losses ( $W/m^2$ )
$Q_n$	distance from central point, $m$
$Q_{rad}$	radiation losses ( $W/m^2$ )
$r$	radius, $m$
$r_{nc}$	radius of curvature
$R_{sphere}$	spear relativity, -
$S_a$	Absorber surface ( $m^2$ )
$S_m$	Surface of mirrors ( $m^2$ )
$S_n$	distance between two consecutive mirror centre lines, $m$
$T$	temperature, $K$
$T_{ij}$	the target for the $j^{th}$ parameter of the $i^{th}$ ray -
$U$	Overall heat loss coefficient ( $W/m^2.K$ )
$V_{ij}$	the value of the $j^{th}$ parameter of the $i^{th}$ ray, -
$W$	width of mirror, $m$
$w_{ij}$	the weight of the $j^{th}$ parameter of the $i^{th}$ ray, -
$w_{loss}$	the weight of the efficiency penalty term, -

## Greek symbols

$\delta_n$	tilt angle of $n_{th}$ mirror, $^\circ$
$\eta$	efficiency, -
$\epsilon$	Emissivity
$\sigma$	Stefane-Boltzmann constant, $5.67 \times 10^{-8} W/m^2K^{-4}$

## Subscripts and superscripts

<i>ie</i>	incident on receiver
<i>e</i>	energy
<i>th</i>	thermal efficiency
<i>opt</i>	optical
<i>n</i>	distance from central point
<i>s</i>	solar
<i>u</i>	useful
<i>fm</i>	mean fluid
<i>in</i>	inlet
<i>out</i>	outlet

## Abbreviations

<b>ASE</b>	Archimede Solar Energy
<b>CC</b>	Combined Cycle
<b>CED</b>	Cumulative Energy Demand
<b>CFD</b>	Computational Flid Dynamics
<b>CLFR</b>	Compact Linear Fresnel Reflectors
<b>CPC</b>	Compound Parabolic Concentrators
<b>CPV</b>	Concentrating Photovoltaics
<b>CSF</b>	Concentrating Solar Fuels
<b>CSP</b>	Concentrated Solar Power
<b>CTR</b>	Central Tower Receiver
<b>DHW</b>	Domestic Hot Water
<b>DNI</b>	Direct Normal Irradiance
<b>DSG</b>	Direct Steam Generation
<b>EW</b>	East-West
<b>FPC</b>	Flat Plate Collector
<b>GW</b>	Gigawatt
<b>GWe</b>	Gigawatt Electric
<b>GWP</b>	Global Warming Potential
<b>HTF</b>	Heat Transfer Fluid
<b>HVAC</b>	Heat, Ventilation, Air Conditioning and Cooling
<b>IPH</b>	Industrial Process Heat
<b>ISCCS</b>	Integrated Solar Combined Cycle
<b>kWe</b>	Kilowatt Electric
<b>LCOE</b>	Levelized Cost of Energy
<b>LFR</b>	Linear Fresnel Reflectors
<b>MCRT</b>	Monte Carlo Ray Tracing
<b>MW</b>	Megawatt
<b>MWe</b>	Megawatt Electric
<b>MWt</b>	Megawatt Thermal
<b>NREL</b>	National Renewable Energy Laboratory
<b>NS</b>	North-South
<b>ODP</b>	Ozone Depletion Potential
<b>ORC</b>	Organic Rankine Cycle



<b>OWF</b>	Organic Working Fluid
<b>PDC</b>	Parabolic Dish Collector
<b>PSA</b>	Plataforma Solar De Almeria
<b>PTC</b>	Parabolic Trough Collector
<b>RIT</b>	Radial Inflow Turbine
<b>ROT</b>	Radial Outflow Turbine
<b>SEGS</b>	Solar Electric Generating Systems
<b>TDC</b>	Top Dead Centre
<b>TES</b>	Thermal Energy Storage
<b>TETR</b>	Traditional External Tubular Receiver
<b>TIT</b>	Turbine Inlet Temperature
<b>VAC</b>	Vapor Absorption Chiller
<b>VVR</b>	Variable Velocity Receiver

## Chapter 1 : Introduction

### 1.1. Problem statement

It is universally acknowledged that two of the major global challenges are energy security and environmental sustainability [1]. There are growing concerns over sustainability criteria, land-use change, global warming climate change mitigation, and greenhouse gas emission reduction. The search for sustainable, cost-effective and environmentally friendly energy sources for consumer societies and industrial economies has been a subject that requires urgent attention [2]. Besides, the uncertainty in the prices of fossil fuels and increasing demand for energy, which was first experienced in the early 70s, prompted the search for alternative energy from sustainable sources [3]. As a result, substantial efforts are being made by both developing and industrialised countries to effect a gradual transition from conventional fossil fuel-based energy sources to renewable, sustainable and environmentally friendly energy sources. This led to immense scientific research and technological development in various ways of energy generation by deploying renewable energy technologies.

Renewable energy provides an encouraging cluster of technologies that are replenished at the same rate as they are being “used” for both near future and long-term planning. They can be obtained directly from the sun (thermal, photochemical, and photoelectric energy), indirectly from the sun (wind, hydropower, and photosynthetic energy contained in biomass energy), or from other natural movements and processes in the environment (such as geothermal and tidal energy). Wind, solar, biomass, and geothermal technologies are becoming more cost-effective in a growing number of markets, and they are making significant progress towards broader commercialisation. Each renewable energy technology is at a different research, growth, and commercialisation stage, with varying current and future projected costs, current industrial base, resource availability, and potential greenhouse gas emissions.

Most renewable energy systems are modular, permitting for load growth versatility. Renewable energy technologies are now accessible in a variety of markets, ranging from particular niche markets to integrated energy production. Renewable energy systems, as compared to competing traditional technologies such as natural gas combined cycle power plants, are relatively capital intensive for centralised energy generation. After initial investments, however, the economics of renewable energy systems benefit in relation to traditional technologies because operational and maintenance costs are lower than those encountered while using conventional fuels.

Over the last five years, the renewable energy markets – power, heating, and transportation – have increased exponentially [4]. The deployment of both existing and newer technologies, such as hydro, biomass and solar energy, has increased rapidly, resulting in increased confidence in the technologies, lower costs, and creating new opportunities. Global electricity production from renewable energy sources was likely to grow 2.7 times between 2010 and 2035. The use of modern renewables to generate heat will almost double, from 337 Mtoe in 2010 to 604 Mtoe in 2035 [4]. Global investments in renewable energy technologies continue to grow, with clear signals to build a clean energy future now being seen by global energy suppliers (and consumers).

Among the various renewable energy resources, energy from the sun is the essential natural energy resource because it dictates all environmental processes acting on the surface of the earth. The sun offers the earth with an immense amount of energy. It presents a captivating solution to all societies to meet their needs for clean, abundant sources of energy in the future [5]. The basis of solar energy is the nuclear interactions at the core of the sun, where the energy emanates from the conversion of hydrogen into helium. Sunlight is readily available, secure from geopolitical conflict and can be harnessed with the least adverse effect on the environment and global climate system from pollution emission [6].

Solar radiation, at its origin, the sun is a high-temperature, high-exergy energy source capable of producing an irradiance estimated to be  $63 \text{ MW/m}^2$ . Moreover, the Sun-Earth geometry dramatically limits the solar energy impinging on the earth's surface to about  $1 \text{ kW/m}^2$  [7]. It is estimated that more energy from the sunlight strikes the earth than all the other energy consumed on the planet in a year [8]. The potential of solar energy to generate electricity and heat to be supplied to our modern economies in a variety of productive activities has been widely proven but not yet broadly adopted around the globe due to relatively cheap fossil fuels.

Solar energy can be harnessed directly, as in the case of Photovoltaic and thermal energy systems. The Photovoltaic Systems constitute solar cells in which the photovoltaic effect directly transfers photon energy into electrical energy [9]. Solar thermal energy systems such as Evacuated Tubes, Flat Plate Collector, and Concentrating Solar Power convert energy from sunlight to generate heat and electricity based on the application of heat engines. Different from the PV systems, which can use diffuse flux, solar thermal systems are not able to use radiation diffused by clouds, dust, or other elements. Instead, these technologies are restricted to using only direct normal solar radiation.

Production of electricity and heat generation from solar energy is currently one of the key research areas in the field of renewable energy. For electricity generation through solar radiation, the power plants could deploy the technology of solar concentration. Concentrating Solar Power (CSP) technology has been a fairly efficient means of generating energy to meet thermal and electrical needs. By deploying large-area concentrating mirrors, CSP technologies focus sunlight on a focal point known as the receiver with a small aperture. Inside this receiver is a working fluid that is heated to high temperatures of hundreds of degrees to either be directly used in a thermodynamic power cycle or to heat another working fluid to a high temperature through a heat exchanger for use in the thermodynamic cycle to generate electrical power.

Concentrating solar power (CSP) technologies now constitute feasible commercial possibilities for large-scale power plants as well as for smaller electricity and heat-generating plants. CSP has an inherent capacity to store thermal energy for short periods of time for later conversion to electricity. When integrated with thermal storage capacity, stored thermal energy in the molten salt or the HTF can be used to generate electricity with CSP plants, even in hazy weather conditions or after sundown [1]. CSP plants can also be equipped with backup heating using combustible fuels [10, 11]. With these factors, CSP is set to take its place as an essential part of the world's energy mix.

Presently, four possible concentrated solar power technologies vary according to configuration, ranging from linear Fresnel reflectors (LFR), parabolic trough collector (PTC), parabolic dish collector (PDC) and the central receiver system (CRS) [12]. The dish engine is a point focusing CSP technology that drives a compact Stirling or Brayton engine to produce electrical power and is more suitable for modular power generation, mostly on a scale of 1-30 kW. The other three (3) combine with utility-scale power such as steam cycles or organic Rankine cycle turbines to produce electricity and can be improved with large-scale thermal storage to increase the supply of power [13].

The Linear Fresnel reflectors (LFRs) CSP systems consist of an array of flat or slightly modified mirrors that concentrate solar radiation onto a fixed receiver tube mounted at a certain height above the mirror array. The receiver remains fixed, ideal for line focussing consisting of either a single or multiple-tube receiver. The fluid passing through the receiver tube at a high pressure absorbs heat from the incident solar radiation from the solar field. The Heat transfer fluid temperature rises until it reaches saturation temperature [3]. The simplicity in plant design

and maintenance, compact plant size, lower operation and investment cost are key advantages of LFR over other CSP technologies [6].

However, LFRs systems are regarded as a low-efficiency technology, which is mainly due to very little previous research where the actually achievable concentration is analysed [3]. Compared to other CSP technologies and the PTC in particular, Linear Fresnel reflectors are considered to be able to achieve very low average optical/thermal efficiency due to the combination of a fixed receiver and the one-axis tracking mirror panels in a horizontal plane resulting in greater cosine losses than troughs. However, cost competitiveness, compact plant size, multistage heating and use of modified mirrors resulting in considerable efficiencies and high concentration ratios being the key advantages over other CSP systems have rekindled a renewed interest in linear Fresnel reflectors CSP Technologies [14].

The previous literature review shows great research interest for determining sustainable designs of LFR with high performance. Experimental and numerical studies have been performed in the past, taking into account the entire LFR solar field or focusing attention on individual components like primary reflectors, receiver tubes cavity and secondary reflectors. In contrast, most studies on LFR deployed uniform geometrical features to analyse the optical performance of the collectors and the solar field in general. Very few studies dealing with the LFR solar field focusing on modelling and optimisation of key system component parts and geometrical elements such as mirror profile, height, width or distance between consecutive mirror centre lines have been performed.

Furthermore, a range of solar to electric energy conversion systems can be deployed to different concentrator types. Consequently, the vast majority of CSP systems currently in operation have been applied to steam generation for deployment in steam turbine energy [4]. However, for low-temperature applications, the so-called organic Rankine cycle (ORC) is preferred. The ORC employs a lower boiling point organic fluid, which makes it compatible and suitable for low-temperature applications. For smaller systems (in the form of a few kWe), ORC systems may achieve higher efficiencies than steam turbines. A few small Linear Fresnel CSP systems have been fitted with ORC systems [15].

In addition, selecting a suitable fluid and its application as heat transfer fluid (HTF) in a receiver tube and an organic working fluid (OWF) in ORC is imperative [16]. Depending on the application, the source and the amount of heat to be deployed, the fluid must demonstrate excellent thermodynamic properties at the lowest possible temperatures and pressures and also

meet some criteria, such as being economical, non-toxic, non-flammable, environmentally friendly and tolerating a high use of the available energy from the heat source [17].

In the present work, the theoretical and experimental studies for improving the design of the solar field and organic Rankine cycle turbine in a small Linear Fresnel Reflector solar thermal power plant was performed. The modelling and optimisation of a 3D optical model for an LFR solar field are presented. By deploying the key solar field parameters as variables, the geometry of the solar field is modified by a simple optimisation approach proposed. The modelling and optimisation employed are to simulate the optical and thermal performance of the systems. Employing Monte Carlo Raytracing Technique, the performance of the key component parts of the optimised solar field such as the primary mirrors is compared with flat and uniform mirror curvatures. The goal is to minimise the drift in ray concentration and analyse the impact on the computed optical efficiency for separate mirror elements and the overall solar field for the mirror's configurations.

A steady-state numerical simulation to analyse the thermal performance is carried out, taking into account the main features and optimum operating condition of the receiver tube for various concentrated heat fluxes (in  $\text{W/m}^2$ ). From this model, the fluid outlet temperatures and thermal efficiencies are computed for a range of values of the definition variables (inlet temperature, fluid speed, thermal flux onto the absorber, etc.). The thermal analysis is performed using Therminol 62 thermal oil as the heat transfer fluid.

Furthermore, a small-scale organic Rankine cycle used for a low-temperature application, capable of generating electrical power (integrated with the LFR solar field), is theoretically and experimentally investigated. A single-stage axial ORC turbine is modelled and investigated using two different new environmentally friendly working fluids. The effect of the range of inlet definition variables such as temperature, pressure and rotational speed on the work output and isentropic efficiency as well as the influence of rotor tip clearance (rotor gap) on the turbine power were investigated and analysed.

Regarding the choice of working fluid for the ORC, the R365mfc and the new environmentally friendly Novec649 were the two selected as the working fluids for the investigation. Depending on the source, the chosen heat level and the intended application, these fluids must exhibit optimum thermodynamic properties at lower temperatures and pressures. They must meet multiple criteria, such as being economical, non-toxic, non-flammable, environmentally

friendly, as well as handling a high energy availability of the heat source. Thus, the influence of R365mfc and Novec649 on the system performance is compared.

In addition, a shading analysis of the solar field and surrounding area is performed using different approaches proposed. In this context, shading resulting mainly from structures such as buildings and vegetation is considered. The analysis considers sun and shadow effects that can be easily and dynamically improved or even animated within the program to evaluate the timing and effect of obstructions the resulting consequence on the optical performance of the solar field.

Subsequently, the results and analyses of the theoretical study and experimental investigation of separate components parts of the plant were carried out. This includes the calibration of mathematical models using experimental data and their improvement. Next to that, a critical evaluation and discussion of the facts and information obtained from various investigations performed were presented.

## **1.2. Background**

In recent years, the quest for a sustainable and cost-effective energy source for consumer societies and industrial applications has been a major drive for renewable energy technologies. Although many advancements are being made for harnessing energy from several renewable sources, sustainability, reliability, and storage techniques still have to be put in place to maximise energy utilisation. Energy from the sun is the most plentiful energy source and is readily available for applications such as thermal power generation, industrial process heat and agricultural processing.

To generate electricity and heat from solar energy, solar power plants use concentrating technologies. The fact that this results in an enhanced efficiency justify its ability to fulfil electrical and thermal energy demands. Concentrating solar power technologies deploy an array of reflectors (mirrors and heliostats) that concentrate solar radiation onto a receiver (line or point focus) placed at a certain height above the reflectors. The solar field can generate high temperatures to operate thermodynamic cycles using Heat Transfer Fluids.

Concentrating Solar Power (CSP) may play a major role in the future energy mix, particularly in regions with a substantial annual global direct irradiation, where it appears to be a more cost-effective technology compared to other electricity generation technologies such as photovoltaics [18]. CSP plants' versatility improves energy security. Unlike solar photovoltaic

(PV) technologies, they have the ability to store heat energy for short periods of time and convert it to electricity later. This is achieved by integrating thermal storage in CSP plants that will continue to generate electricity even when the sun is obscured by clouds or after sunset [11]. In addition, CSP plants very low levels of greenhouse gas emissions make them a crucial technology in the fight against climate change and Greenhouse gas emission reduction.

According to the receiver configuration, concentrating type, solar field orientation and tracking mechanism, CSP technologies can be grouped into four. These mainly include Parabolic trough Collectors, Linear Fresnel Reflectors, Parabolic dish collectors, and the central receiver system, all of which are well advanced and mature technologies.

### 1.2.1. Parabolic trough collector (PTC)

These types of collectors are usually aligned in north-south orientation using a single-axis tracking mechanism to track the sun in the southeast direction to get the required output level. The design of such a collector constitutes inside reflector surface, which concentrates the solar beam radiation on a linear absorber placed at the focal line to absorb the energy [7]. Figure 1.1 illustrates a simple PTC plant configuration.

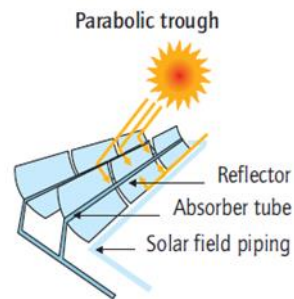


**Figure 1.1:** Parabolic troughs (line focus, mobile receiver)

### 1.2.2. Central receiver system (CRS)

The central receiver concentrated solar power technology constitutes the deployment of small reflectors (hundreds to thousands), also known as the Heliostats. The set of heliostats is designed to track the sun in both azimuth and elevation, thereby concentrating the solar radiation onto a central receiver, normally positioned at the top of a tower [19]. Since very high temperature is generated, Direct Steam Generation or molten salts are used as a heat-absorbing medium. A central tower power plant design is shown in Figure 1.2 below.



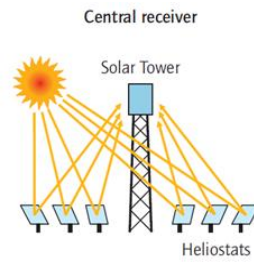


**Figure 1.2:** Solar towers (point focus, fixed receiver)

### 1.2.3. Parabolic dish collector (PDC)

A parabolic dish is a point focusing solar concentrator (see Figure 1.3 below) integrated with a full point dual-axis solar tracker. Concentrated solar radiation is collected on a single focal point comprising of the assembly of a turbine or Stirling engine; hence no additional heat transfer fluid or heat exchanger is required. Compact size, low compatibility with thermal storage and hybridisation are key features for its competitiveness with other CSP technologies [20].

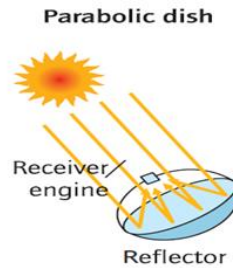


**Figure 1.3:** Parabolic dish-engine systems (point focus, mobile receiver)

### 1.2.4. Linear Fresnel reflector (LFR)

Linear Fresnel reflectors are a modified form of a parabolic trough. By maintaining the same aperture, the parabolic trough is split into extended rows of mirrors, which are either flat or designed to have some curvature that concentrates the beam radiation similar to that of the trough. Ideally, the concentrated beam radiation is focused on a receiver tube containing the Heat Transfer Fluid. The high operating temperature, multistage heating, and capacity for a direct steam generation are the key features, which supports its wide spectrum deployment [13].

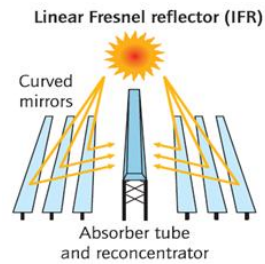


**Figure 1.4:** Linear Fresnel reflectors (line focus, fixed receiver)

As shown in Figure 1.4, linear Fresnel collectors utilise an array of low-profile, flat or nearly flat primary reflectors and a fixed receiver assembly consisting of one or more linear receiver tubes and an optional secondary reflector [21]. The primary reflectors track the sun in the daytime while the receiver assembly remains fixed. Due to the fact that the wind torque load is roughly proportional to the square of the mirror height, the low-profile reflector architecture allows increasing concentration ratio without increasing wind loads, which is otherwise the case for parabolic troughs and large-sized heliostat mirrors for central-receiver systems [13].

Early research work focussed on the parabolic dish and trough collector types. Later advancement saw the development of a central tower type collector development, which successfully operated between the early 80s and late 90s. Development on linear Fresnel reflector came at a later stage, and since then, no meaningful progress was made until in the mid-80s. LFRs offer many advantages compared to the other CSP technologies [2].

LFR offer considerable advantages compared to the PTC. Rotating joints at the end of each collector line of the conventional parabolic trough are not used in LFR. They do not necessarily have metal–glass welds at the ends of each receiver tube module to maintain a vacuum within the outermost tube. In addition, mirrors of PTC are notably curved, which is more expensive to manufacture and require heavy structures in order to hold nearly 6 m of aperture [22]. Besides the simplicity in plant design, lower maintenance and operation costs, their compact plant size makes them more suitable for integrated solar power plants.

Compared to the central tower technology, in which thousands of heliostats are designed separately with a three-dimensional tracking system, Linear Fresnel mirrors can share the same drive mechanism, as all of them rotate around their separate axis [23]. Such a single-axis tracking system is more cost-effective and much simpler than that of central towers plants. A series of research projects have been performed on Stirling engine- parabolic dish collectors due to the expected higher efficiency conversion ratio. Their integration as all-in-one and flexibility turned out to be on the downside instead of advantage, as economies of scale cost

reductions are limited, and photovoltaic technology has been a major competitor in the same area that has greatly lessened its cost [3].

Therefore, the quest to overcome techno-commercial constraints associated with conventional reflector based CSP technologies is open to Linear Fresnel collectors. Thus, as a result, there is a renewed interest in linear Fresnel reflectors from promoters of CSP technologies. However, Linear Fresnel Reflectors are regarded as a low-efficiency technology, which is mainly due to very little previous research conducted to analyse the performance of the field. Compared to other CSP technologies and the PTC in particular, Linear Fresnel Reflectors are said to achieve very low average optical/thermal efficiency due to the combination of a fixed receiver and the one-axis tracking mirror panels in a horizontal plane resulting in greater cosine losses and thermal power variation, concentrated on to a receiver and its flux map over a given time of the day.

#### **1.2.5. Optical and thermal modelling**

Numerous experimental and numerical studies [24, 25] have been performed in the past, taking into account the LFR solar field as a whole or by focusing attention on individual components like primary reflectors, receiver tubes cavity etc., while most studies on LFR deployed flat mirrors to analyse the optical performance of the collectors and solar field in general, very few studies dealing with reflectors focusing on optimisation of mirror profiles are performed. In this study, a different approach is proposed. First, by performing a system optimisation, the profile of flat mirrors is being modified to minimise drift in ray concentration and improve optical efficiency. Using mirror width, height, tracking system type, the distance between two consecutive mirror centre lines as optimisation variables, the flat collectors are optimised to assign curvatures, each different from the other.

Subsequently, through system simulation, a Monte Carlo Ray Tracing Technique is deployed to carry out a detailed analysis of the optical performances of different mirror profiles (flat, uniform curvature and optimised mirrors). By deploying the same approach proposed, the optical efficiency of the so-called Compact Linear Fresnel Reflector (ComLFR) was analysed. In addition, a comparative analysis was conducted between the Central and Compact Linear Fresnel configuration.

A steady-state numerical simulation to analyse the thermal performance of the solar plant is carried out, taking into account the main features and optimum operating condition of the receiver tube for various concentrated heat fluxes (in  $\text{W/m}^2$ ). From this model, the fluid outlet

temperatures and thermal efficiencies are computed for a range of values of the definition variables (inlet temperature, fluid speed, thermal flux onto the absorber). The thermal analysis is performed using Therminol 62 thermal oil as the heat transfer fluid.

The challenges associated with Linear Fresnel Reflectors can be overcome with the proposed good optical design approach; this includes the optimisation of key geometrical elements of the solar field such as mirror profile, their width, height, the distance between two consecutive mirror centre lines and their orientation. This results in reducing the maximum lateral drift and uncertainty of reflected rays' direction, increased by the long distance between the mirrors and the fixed receiver and minimising the concentration ratio variation along the day, as well as improving the overall optical and thermal efficiency of the solar field.

#### 1.2.6. Organic Rankine cycle turbine

A small-scale axial-outflow ORC turbine with a power output of a few kW is capable of transforming the energy from a low-temperature heat source into useful power employing an appropriate organic working fluid. Until recently, very little attention has been accorded to these systems due to the low thermal efficiency of the Rankine cycles which are operated at low temperatures. Such systems, however, present a simple structure at low cost and can integrate existing technologies such as linear Fresnel reflector plants.

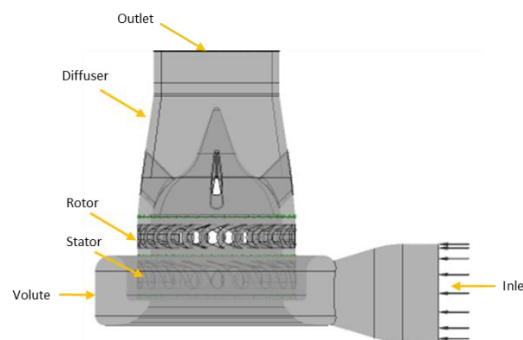


**Figure 1.5:** Organic Rankine Cycle Turbine

Generally, the turbine inlet temperature (TIT), the turbine pressure ratio and the mass flow rate in the turbine inlet are among the essential factors in the turbine system [26]. TIT is increased in the conventional turbine systems to enhance the turbine output. When low-grade heat sources are deployed, however, this is not the case. In addition, Rankine cycles operating at low temperatures have low thermal efficiency. These are significant challenges to overcome. Therefore, the organic substance deployed as a working fluid must demonstrate low latent heat and high density. To increase the turbine inlet mass flow rate, such properties are preferable.

A numerical simulation of an ORC was conducted in order to evaluate its optimum operating conditions. The organic substances selected for this purpose must demonstrate appropriate thermodynamic properties. Therefore, we have chosen the R365mfc and Novec649 as the working fluids in this investigation.

#### **1.2.7. Heat transfer and organic working fluids**

The selection of suitable fluids and their application as heat transfer fluids (HTF) in a receiver tube and an organic working fluid (OWF) in ORC are very crucial aspects mainly due to the dependence of their categorization on the temperature of the heat source, defined by the fluid thermodynamic and/or thermophysical properties for instance temperature and critical pressure, chemical stability and density [15]. Also, these fluids should meet multiple criteria, such as being economical, non-toxic, non-flammable, environmentally friendly, as well as a capacity to handle a high use of the energy availability of the heat source [15].

The thermal analysis is performed using Therminol 62 as the heat transfer fluid, which has suitable thermo-physical properties. As for the Organic working fluid, the R365FMC and the new environmentally friendly NOVEC649 were deployed. A comparative analysis of these working fluids was conducted based on the influence on the output pressure, temperature, density, mass flow rate and overall power output of the ORC turbine.

#### **1.2.8. Shading analysis**

Shading effect on linear Fresnel solar field can result in factors that contribute to energy losses and thus affect net energy collection by the heat transfer fluid in the absorber, electricity generation and cost of electricity. In this analysis, shading resulting mainly from structures such as buildings and vegetation is considered. The analysis considers sun and shadow effects that can be easily and dynamically improved or even animated within the program to evaluate the timing and effect of obstructions the resulting consequence on the optical performance of the solar field. The analysis was performed using computer software tools, namely, shadow-analyses, sketch-up and LightTools.

### **1.3. Research aim**

The proposed research aims at theoretical and experimental studies for improving the design of the solar field and organic Rankine cycle turbine in a small Linear Fresnel Reflector concentrating solar thermal power plant. It encompasses modelling the whole system, using all

results of experimental investigations on the performance of separate components and the whole plant.

#### 1.4. Objectives

The following are objectives of this research:

- i. Literature review on the state-of-the-art concentrating solar thermal power plants based on various thermal prime movers: this will focus on key areas such as the designs, components, configurations, modelling and experiments.
- ii. Critical evaluation and discussion on the facts and information obtained from various resources.
- iii. Analysis of provided experimental data on the performance of separate components.
- iv. Optimization of the components and configuration of the plant.
- v. The development of power plant components and whole plant mathematical models based on results obtained.
- vi. Conclusions and recommendations on the optimized plant.

#### 1.5. Outline of thesis

This thesis is structured as follows (see Figure 1.6);

**Chapter 1:** This chapter provides an introduction to this thesis and presents the essential background on the focus, relevance and how the current project was inspired. The scope, aim and objectives, as well as the overview of the thesis structure, were also outlined.

**Chapter 2:** This Chapter contains a literature review on the state-of-the-art in thermal solar power plants based on various thermal prime movers: this focuses on key areas such as the designs, components, configurations, modelling and experiments. Critical evaluation and discussion on the facts and information obtained from various resources are presented.

**Chapter 3:** The development of the power plant's solar field components, mathematical models and theoretical simulations of these components using LightTools and ANSYS R20 CFD tool are described. This Chapter is split into several sections,

- i. The modelling and optimisation of a 3D optical model for an LFR solar field are performed using LightTools optical modelling software. Deploying the solar field elements such as mirror width, height, incident angle, tracking system type, the distance between two consecutive mirror centre lines as variables, the solar field geometry is

modified by a simple optimisation approach proposed. The modelling and optimisation employed is to simulate the optical and thermal performance of the systems.

- ii. A Monte Carlo Ray Tracing Technique is deployed through system simulation to carry out a detailed analysis of the optical performances of different mirror profiles (flat, uniform, and optimised mirror curvatures). Whilst the raytracing is being performed, the concentration factor, which is defined as The ratio of the aperture area of reflecting mirrors and the area of the collector receiving the concentrated solar radiation [6] in the form of irradiance, radiant intensity and ray density for average monthly and yearly sun data of the various mirror shapes is investigated.
- iii. A steady-state analysis of thermal performance (flow model, heat transfer and heating of the Heat Transfer Fluid) is carried out, taking into account the main features and optimum operating condition of the receiver tube for various concentrated heat fluxes (in  $\text{W/m}^2$ ). From this model, the fluid outlet temperatures and thermal efficiencies are computed for a range of values of the definition variables (inlet temperature, fluid speed, thermal flux onto the absorber, etc.). The thermal analysis is performed using therminol 62 as the heat transfer fluid.

**Chapter 4:** Deploying a similar approach presented in chapter 3, a comparative analysis between two linear Fresnel configurations, central and compact LFR solar field is performed.

**Chapter 5:** A 3D geometry of a single-stage axial ORC turbine expander (stator/rotor and complete) is modelled and investigated employing the ANSYSR20-CFD using two separate environmentally friendly working fluids (NOVEC649 and R365FMC). The effect of the range of inlet variables such as the temperature, pressure and rotational speed on the work output and isentropic efficiency as well as the influence of rotor tip clearance (rotor gap) on the turbine power were investigated and analysed.

**Chapter 6:** Shading analysis of the solar field and surrounding area is performed using different proposed approaches. In this context, shading resulting mainly from structures such as buildings and vegetation is considered. The analysis considers sun and shadow effects that can be easily and dynamically improved or even animated within the program to evaluate the timing and effect of obstructions and the resulting consequence on the optical performance of the solar field. The analysis was performed using computer software tools, namely, shadow-analyses, sketch-up and LightTools from Synopsys.

*Chapter 7:* General discussion: A critical evaluation and discussion on the facts and information obtained from various investigations performed were presented in this Chapter.

*Chapter 8:* Conclusions and recommendations. In this Chapter, an overall summary of current research work, the main findings and outcome on the optimised plant are discussed, and the conclusions are drawn.



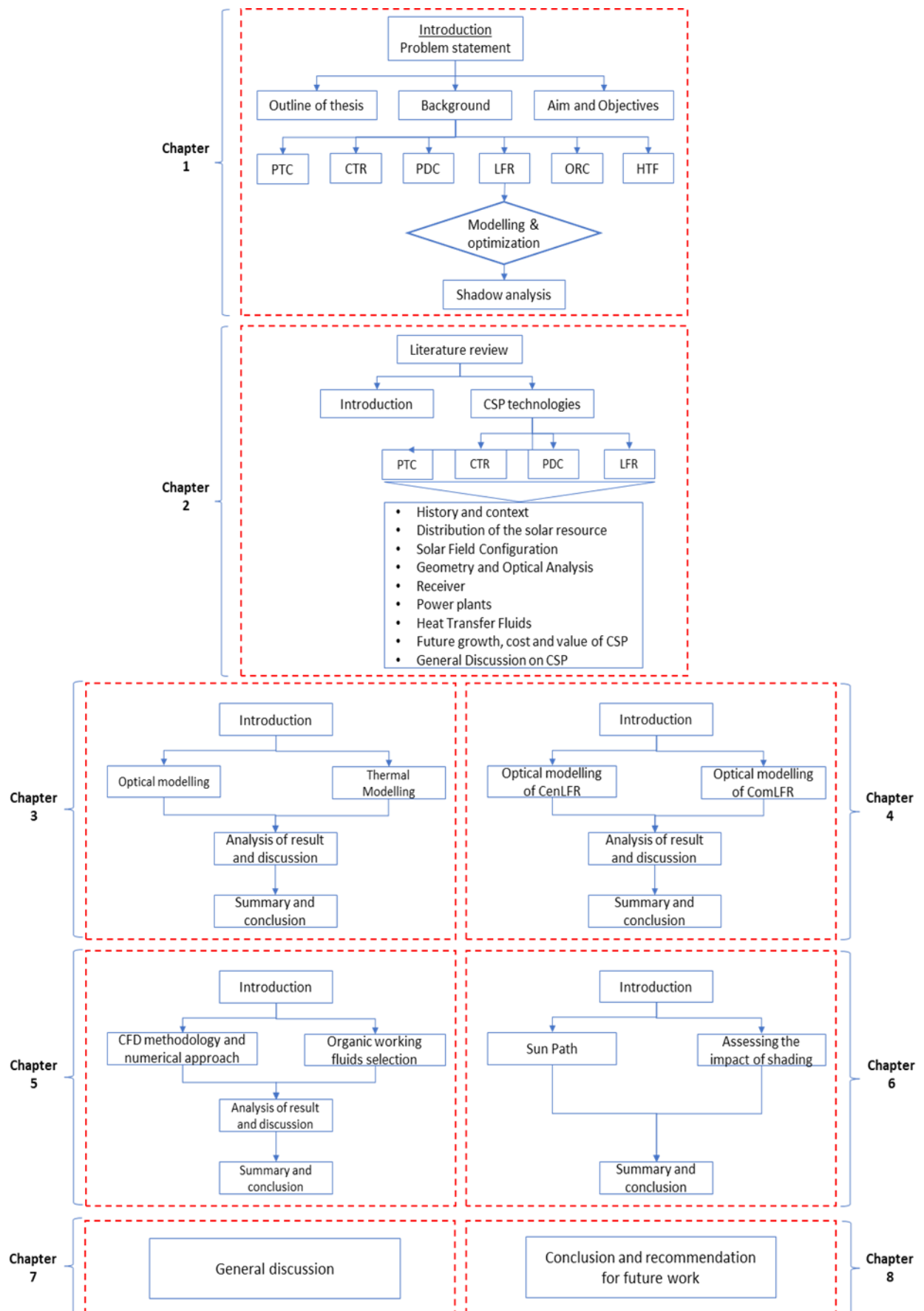


**Figure 1.6:** Flow chart showing the outline of the thesis

## **Chapter 2 : Literature review**

### **2.1. Introduction**

This Chapter constitutes a review on the state-of-the-art in thermal solar power plants technologies with specific emphases given to concentrating technologies, based on various thermal prime movers; this will focus on key areas such as the designs, key component parts, configurations, modelling and experiments. Moreover, the prospects of thermal solar plants technologies in the context of utility-scale power plants, their performance, and technical challenges are presented. Next to that, a critical evaluation and discussion on the facts and information obtained from various resources are put forward.

Solar thermal power plants deploying optical concentration technologies are promising candidates for generating energy to provide for both thermal and electrical demand while delivering a significant portion of the clean and renewable energy needed in the future. Over the recent years, several industrialised economies and developing regions, notably North America (USA, Mexico), Europe (Spain, Italy), Asia (India, China) and North Africa (Egypt, Morocco), have been focussing on generating energy from concentrating solar power systems to generate heat and electrical energy.

A range of solar thermal systems has been deployed for application in solar thermal power plants, mainly concentrated photovoltaics, Fresnel lenses, parabolic trough type, central tower receiver type, parabolic dishes, and Linear Fresnel reflectors. Most of these thermal solar technologies have recorded commercial successes, while others are still in the pilot and demonstration phase. Despite the notable development achieved over the recent years in their deployment, considerable efforts still need to be accorded to research in this field, focusing on storage, optical design, heat transfer and working fluids and turbine design.

### **2.2. Concentrating solar power (CSP)**

Concentrating Solar Power (CSP) generates energy from clean solar resources with very low levels of greenhouse gas emissions. As a result, it has a strong capability of being a crucial technology in the fight against climate change. In addition, CSP plants' versatility improves energy security. CSP, unlike solar photovoltaic (PV) technologies, has the ability to store heat energy for short periods of time and convert it to electricity later. CSP plants, when combined with thermal storage power, will continue to generate electricity even when the sun is obscured

by clouds or after sunset. CSP plants can also be fitted with combustible fuel backup control IEA [11].

These factors allow CSP to provide dependable electricity that can be dispatched to the grid whenever needed, including after sunset to meet late evening peak demand or round the clock to provide base-load demand. CSP is a promising technology for all regions that need clean, versatile, and reliable power because of these characteristics. CSP can also be viewed as an enabling technology for integrating greater quantities of intermittent renewable resources such as solar PV or wind power into grids because of these characteristics [11].

Although large, on-grid power plants can generate the majority of CSP electricity, these technologies also have a lot of potential for specialised applications like process heat for industry, co-generation of heating, cooling, power, and water desalination. CSP also has the ability to be used in developing-world applications, including household cooking and small-scale manufacturing. The use of CSP technologies to create concentrating solar fuels (CSF), such as hydrogen and other energy carriers, is a vital field for further research and development. By combining hydrogen with natural gas in pipelines and distribution grids and generating cleaner liquid fuels, solar-generated hydrogen will help decarbonize the transportation and other end-use sectors.

### **2.2.1. History and context**

Global investments in renewable energy technology are continuing to grow, with clear signals to build a clean energy future now being seen by global energy suppliers (and consumers). In recent years, the global wind industry has recorded the largest increase in renewable generation, growing by 275 TWh, or around 17%, from 2020. Solar PV electricity generation was expected to rise by 145 TWh or almost 18% and to approach 1000 TWh in 2021. Overall, renewables usage improved by 3% in 2020, mainly due to an increase in electricity generation from solar PV and wind of 330 TWh. Production from solar PV and wind was set to grow by 17% in 2021, up from 16% in 2020 [4, 11, 27].

CSP technology witnessed its first mainstream commercial development between 1984 and 1995, after which further commercial deployment was not realised until 2005, although in that regime, substantial research, development, and demonstrations were achieved. Subsequently, commercial CSP deployment has begun and gained significant momentum. Total installed capacity is comparatively smaller than the solar PV, given that the commercialization of the technology is a decade or so behind [4].

The notion of concentrating solar power has been a subject of interest throughout history. For instance, the idea of mirrored panels concentrating solar flux was described by Archimedes around 200 BC. The optical characteristics of a parabolic trough collector were described by a Greek mathematician Diocles in the second century BC, and the Italian Comte de Buffon illustrated the development of heliostats design in 1746. Moreover, in 1878, a dish/steam engine system was demonstrated at a universal exhibition in Paris by Augustin Mouchot.

A more contemporary historical landmark was a parabolic trough driven pumping plant by Frank Schuman built in Egypt in 1913. Experimental and demonstrational plants were developed all through the twentieth century. Real meaningful development of CSP as an industry was realised in the 1980s in California [4]. Favourable policy frameworks by the government to promote the deployment of CSP led to the installation of nine separate parabolic trough collector based ‘Solar Electric Generating Systems (SEGS)’. These plants configurations were based on steam turbines and employed oil as the preferred heat transfer fluid inside the trough receivers.

Furthermore, the framework also included the installation of the Plataforma Solar de Almeri´a targeted at multiple CSP technologies, which began with Central tower [3]; the achievement of the solar to electricity conversion efficiency record by means of Vanguard Dish Stirling module in 1984 [28, 29] and the erection of Solar Electric Generating System (SEGS) during the 1980s with an aggregate installed capacity of 354 MW. Development on Linear Fresnel Reflector came at a later stage, and since then, no meaningful progress was made in the mid-80s, when oil prices reached minimum values.

These plants, with approximately 2,000,000 m<sup>2</sup> of collector aperture area, remain operational under utility ownership after more than 20 years and have proven that the technology is commercially viable. At the early stage of construction, the tenth plant suffered from the lower oil price regime, and amendments in government policy resulted in a loss of investment and subsequent departure of the company leading the project (LUZ). However, CSP technology has advanced from an installed capacity of just 354 MW during the 1984 – 1995 period to annual average growth of almost 31% between 2020 and 2030, corresponding to an average of 6.7 GW of capacity additions annually, and the capital cost has considerably reduced [4, 30].

The lead role in the development of renewable energy technologies was realised around that time by countries in north-western Europe, with Denmark and Germany at the forefront. The emphasis was to promote wind energy, given its huge potential compared to solar resources in

those countries. Though wind turbines in recent years have been of the order of 3-5 MW per unit, they were in few hundreds of kilowatts at that regime. Furthermore, despite the capital cost being similar or higher than the CSP, the smaller modules present a much easier investment path [4].

The discovery of Linear Fresnel technology goes back several decades. The first notable linear Fresnel reflector concentrator prototype was unveiled by Giovanni Francia, 1964 in Italy. Subsequently, due to its flexibility and design concept, the technology gained more influence, and a number of linear Fresnel collectors have been designed and tested [13]. The first LFR commercial power plant in the world, the "NOVA-1", was built in Almeria, Spain, by the German company Novatec Bissol, with a capacity of 1.4 MW. The plant has provided electrical power to the local network since March 2009 [6].

Photovoltaic systems backed by government initiatives have shifted from small off-grid remote, and high-cost space/satellite applications to residential applications and have recently seen large multi-MW capacities installed. The global quest to promote the penetration of renewable energy systems has emerged promising, and total market demand for electricity using renewable energy technologies continues to increase exponentially, despite the deployment of renewables such as solar and wind contributing to only a few per cent of the global electricity demand [4].

Despite the vast number of concentrating central tower programmes, only a handful was installed in recent regimes. Meaningful developments, classified as small demonstration systems with outputs ranging from 0.5 to 10 MW, and the majority of them operated during the 1980s [31-33]. Liquid sodium, saturated or superheated steam, nitrate-based molten salts, and air have all been used as thermal fluids in the receiver. The most notable projects of central tower systems are the European projects situated in Spain at the premises of the Plataforma Solar de Almeri'a [34] and in the USA, the 10-MW Solar One and Solar Two plants [35, 36]. However, new plants are projected to be installed in the near future.

The continuing challenges for CSP in the past and more recently is the reliance on the economies of scale afforded by large steam turbines, resulting in a large degree of risk capital per project for relatively new technology. Moreover, necessary investment in this field is expected to increase given the rapid growth in the size of the renewable energy projects [4].

Growing concerns over global warming and climate change have emerged to dominate the political agenda across energy supply. There has been a renewed interest in the development

of CSP plants since 2005, supported partly by the recognition that it is a technology that could rapidly offset substantial greenhouse gas emissions and offer the important benefit of distributable solar power by deploying integrated thermal storage. Spain has been at the forefront in promoting the growth of CSP power plants through specific and targeted feed-in tariff initiatives that have demonstrated the technology. In 2014, approximately 2,400 MW was approved for operation, with half already operational. In the USA, the region of the south sunbelt has been identified as a suitable location for CSP through tax credit and loan guarantees, with around 1.8 GW expected to be in operation. Significantly, the majority of new installations nowadays integrate thermal storage, typically within the operational range of 6 hours [37].

Other countries with declared CSP projects or currently under control include the Middle East (Egypt, Israel) and North Africa (Morocco, Algeria), Greece, Portugal, Italy, Cyprus, Australia, Malta, China, India and South Africa. India took a major initiative in 2015 by setting up the Jawaharlal Nehru National Solar Mission, with a target of 20 GWe of combined CSP and PV capacity to be installed by 2022. As of 2015, China set a target to attain 1 GW of CSP. This activity has combined to provide a rate of growth from 2005 to 2012 of around 40%. This growth rate is similar to that which was witnessed by wind energy during its first regime of modern commercial deployment, which commenced around 1990 and faster than that for PV when the first commercial deployment started to accelerate around 1992. Despite the industry being in its nascent stages and vulnerable to sudden policy amendments in key countries, continued robust growth in the global installed capacity is projected [4].

As a consequence of the 15 years lack of meaningful progress in the deployment of CSP plants, the capacity of installed PV grew to be around ten times greater than the CSP, and as a result, PV witnessed a considerable reduction in cost over the recent years, whereas CSP remains in an early stage of cost reduction path. In 2012, PV maintained a lower cost to CSP for non-dispatchable electricity generation under most applications. From an energy storage point of view, CSP emerged as an attractive candidate due to the potential benefits of built-in thermal energy storage and dispatchability, in addition to other non-electrical applications such as fuels [4, 38].

While the issue of climate change mitigation and greenhouse gas emission reduction has dominated future energy agenda, the infinite nature of fossil fuels and the fact that their demand is now far greater, the supply from conventional sources is well recognized, and in spite of the large levels of variations, the overall trend is towards price increase. This could prove to be a

driver for technology change, increasing demand for solar electricity and encouraging the development of such energy sources [4].

### 2.2.2. Distribution of the solar resource for CSP

The composition of the atmosphere and the weather are the key factors that influence the amount of direct sunlight available from one location to another. DNI is generally found in arid and semi-arid areas with consistently clear skies, which are typically located between 15° and 40° north or south latitude. In summer, the atmosphere is normally too cloudy and humid closer to the equator, and the weather is usually too cloudy at higher latitudes. At higher altitudes, where sunlight absorption and scattering are much smaller, DNI is also significantly stronger [11].

North Africa, southern Africa, the Middle East, north-western India, the southwestern United States, Mexico, Peru, Chile, the western part of China, and Australia are thus the most favourable areas for CSP resources. The extreme south of Europe and Turkey, as well as other southern US locations, Central Asian countries, locations in Brazil and Argentina, and other parts of China, may be suitable.

Satellite data has been used in recent attempts to map the DNI resource around the world (Figure 2.1). Current solar resource maps agree on the most favourable DNI values but not on the less favourable ones. There are significant differences, especially in the suitability of north-eastern China, where the most important consumption centres are located [11]. However, accurate measurements can only be obtained by ground-based monitoring; thus, satellite results must be scaled with ground measurements to achieve adequate precision.

Several studies have examined the capacity of key regions (notably the United States and North Africa), paying particular attention to land availability. Without storage, CSP plants need approximately 2 hectares per MWe, depending on the DNI and technology.

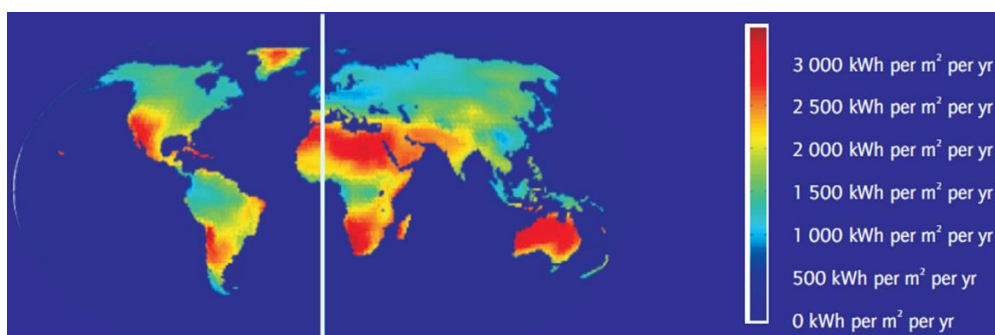


**Figure 2.1:** Solar resource for CSP technologies (DNI in kWh/m<sup>2</sup>/y) [11]

Despite the fact that the Earth's "sunbelts" are relatively narrow, CSP has enormous technological potential. The capacity in the southwestern US states for CSP applications, if fully developed, will meet the electricity needs of the entire US many times over. The Middle East and North Africa's potential will cover about 100 times the combined consumption of the Middle East, North Africa, and the European Union. In short, CSP will be largely capable of meeting global demand for no-carbon or low-carbon energy and fuels. However, one significant problem is that electricity demand is not always located near the best CSP resources.

### 2.2.3. Current technologies for concentrating solar power

Concentrating solar power systems intercept the direct flux component of solar radiation. Different from the flat-plate photovoltaic (PV) systems, which can use diffuse flux, CSP systems are not able to use diffused radiation by clouds, dust or other elements. This makes them perform best in areas with a high percentage of clear sky days, in places that are not occupied by strong dust or smog. Currently, there are four major CSP technology families that can be classified based on how the sun's rays are focused and the receiver configuration (Table 2.1) [2, 11].

These technologies (linear Fresnel, central parabolic trough, central receiver tower and parabolic dish) constitute certain advantages and, in some cases, specific market segments. Over the recent years, project and technology developers have shown interest in pursuing all types of CSP technologies. Hence, significant effort is invested in research on how to improve the technical and economic challenges faced by CSP systems such as optical design, energy storage and cost reduction. In addition to these models that are commercially deployed [7].

**Table 2.1:** The four families of Concentrated Solar Power technology

Receiver type \ Focus type		Line focus	Point focus
		Collectors track the sun along a single axis and focus irradiance on a linear receiver. This makes tracking the sun simpler.	Collectors track the sun along two axes and focus irradiance at a single point receiver. This allows for higher temperatures.
Fixed	Fixed receivers are stationary devices that remain independent of the plant's focusing device. This eases the transport of collected heat to the power block.	Linear Fresnel Reflectors	Towers (CRS)
Mobile	Mobile receivers move together with the focusing device. In both line focus and point focus designs, mobile receivers collect more energy.	Parabolic Troughs	Parabolic Dishes



#### 2.2.4. Linear Fresnel reflectors

Linear Fresnel reflectors are modified forms of a parabolic trough; thus, its architecture may vary for each separate mirror dimension and the overall arrangement [2]. By maintaining the same aperture, the parabolic trough is split into extended rows of primary mirrors, which are either flat or designed to have some curvature that concentrates the solar radiation onto a focal line comprising of one or more linear receiver tubes containing the Heat Transfer Fluid and an optional secondary reflector [23]. The primary reflectors follow the sun in the daytime whilst the receiver assembly remains fixed [39], as presented in Figure 2.2 below.

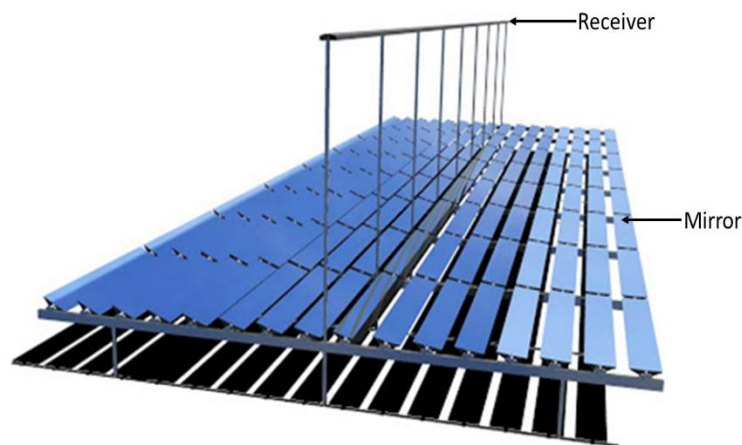


**Figure 2.2:** Linear Fresnel reflector solar field

Unlike the parabolic trough collector, in which the receivers always stay in focus and move with the reflective surfaces [3], Fresnel receivers are fixed whilst the mirrors rotate along their separate axis to track and focus sun rays onto the receiver [39]. This static nature of the receiver assembly provides considerable design flexibility, accessibility to low and easy maintenance [3]. Conversely, with the receiver being fixed, the mirrors do not focus exactly on the receiver focal point when the sun is out of its reference position. To minimise this lateral drift when the receiver is not in the mirror focus, it is recommended to rotate the mirror around an axis that belongs to the reflective surface [40].

Regarding the reflector design perspectives, Fresnel mirrors aperture is relatively narrow; there is no need to adopt a parabolic form. A cylindrical shape may be used instead [40], which is simpler to manufacture and thus results in lower prices. In addition, the curvature of the mirror being so small, the total reflective surface used results in compact plant size. On the other hand, trough mirrors are notably curved, which is more expensive to manufacture and necessitate heavy structures in order to hold almost 6m in length of aperture [22].

Compared to the central tower technology, in which between hundred and thousands of heliostats are designed separately with a three-dimensional tracking system[2], Linear Fresnel mirrors can share the same drive system, as all of them in a row rotate around their separate axis at the same speed. Such a single-axis tracking system is more cost-effective and much simpler in operation and maintenance than central towers plants [41]. In addition, linear Fresnel compact plant size means they require less land area compared to the Central Tower Systems in which a considerable land size is required to set up a solar field comprises hundreds of heliostats.

The parabolic dish is a point focusing solar concentrator integrated with a full point dual-axis solar tracker. Concentrated solar radiation is collected on a single focal point comprising a heater of a turbine or Stirling engine assembly; hence, no external Heat Transfer Fluid is needed. Compact size, low compatibility with thermal storage, and the possibility for hybridization are essential features for its competitiveness with other CSP technologies. However, according to Abbas, Muñoz-Antón [42], their integration as all-in-one and flexibility turned out to be on the downside instead of an advantage, as economies of scale cost reductions are limited and the photovoltaic technology has been a competitor for the same area that has greatly reduced its cost.

However, Fresnel features also imply some challenges. Unlike the parabolic trough collector, in which the receiver always stays in focus and moves with the reflective surface, linear Fresnel receivers are fixed. When the sun is out of its reference position, the mirrors do not focus exactly on the receiver centrelines, which leads to total thermal power variation, concentrated on to a receiver and its flux map over a given time. This issue results in low average concentration factors and reduces the optical efficiency of the solar field [3].

The aforementioned challenges, faced with linear Fresnel reflector systems (mainly lower optical efficiency and storage capacity), are currently under extensive study. Several research and developments in this field recorded in recent years have proposed various approaches and design configurations for the various concentrating solar fields taking into account key features such as selection of the mirror's separation, their shape, width and their orientation, as well as the receiver and secondary reflector designs.

#### **2.2.4.1. Linear Fresnel reflectors solar field configuration**

LFR solar field may vary according to the receiver architecture, which can be either single tube, multitube (evacuated or non-evacuated – vertical, horizontal, or triangular [25, 41, 43,

44] and with or without secondary reflector), mirror array design (flat, cylindrical or parabolic), choice of working fluid and the orientation. Generally, from an orientation point of view, two LFR solar field configurations are commonly used, the central and compact configuration. For the central linear Fresnel Reflector configuration, the receiver is mounted in the centre of the mirror array. Mirrors are configured to track the sun while concentrating on the central receiver placed above the plane of the primary mirror as shown in Figure 2.3(a).

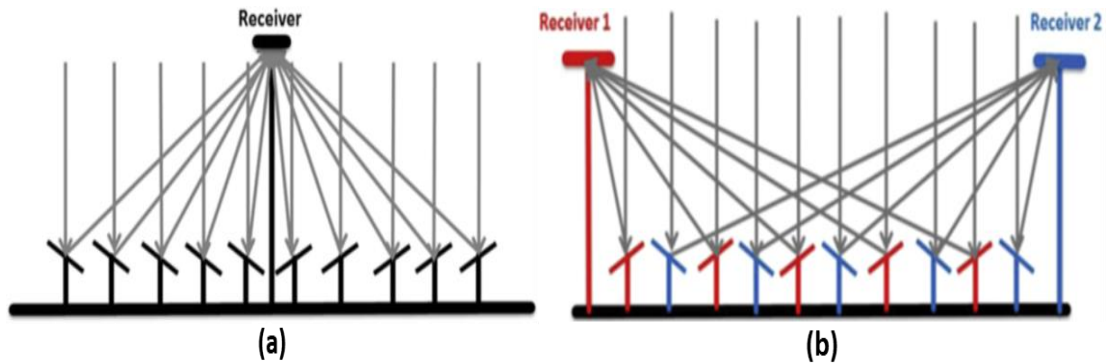


**Figure 2.3:** Central Linear Fresnel Reflector Configuration (a) and Compact Linear Fresnel Reflector Configuration (b) [45]

Generally, for a large size solar field, several units of parallel mirrors are required. The compact linear Fresnel collector (CLFC), in these cases, seems like a very attractive choice [46, 47]. Its architecture, as seen in Figure 2.3 (b) constitutes installing one linear absorber at either side of the mirror array so that consecutive mirrors focus on different receivers. This configuration offers some benefits by minimizing losses due to shading and blocking, especially for mirrors positioned far from the absorber, which turn to be almost perpendicular. Hence, a greater filling factor may be realized for a given field width without increasing these optical losses [45].

Linear Fresnel solar field orientation can be aligned in a north-south direction configured for east-west tracking and in an east-west direction. The north-south orientation is commonly deployed in industry, as it results in a higher annual energy collection. Whereas for horizontal fields, east-west field orientation leads to a more uniform energy production throughout the year. Figure 2.4 shows the two main linear Fresnel solar field orientation.

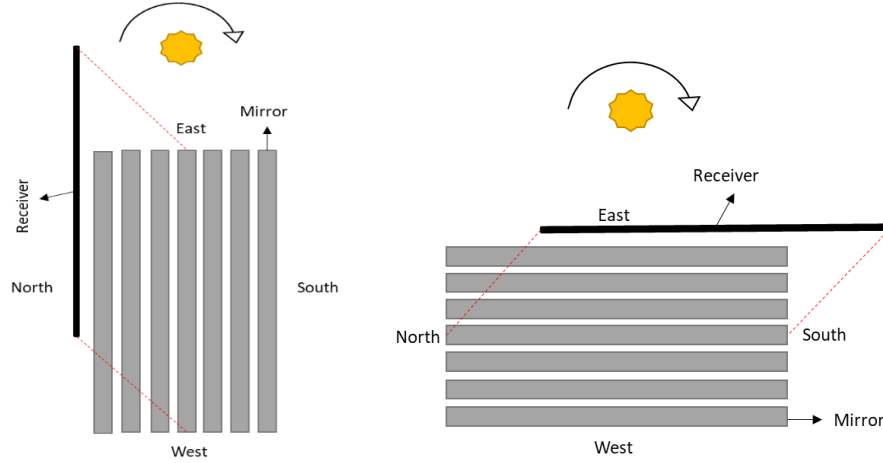


**Figure 2.4:** Linear Fresnel Solar Field North-South orientation (Left) and East-West Orientation (Right)

The previous literature review indicates that there is great research interest in establishing sustainable designs of LFR with high performance. While most studies focused on receiver and secondary reflector designs, very little attention has been given to the primary reflector component. The primary mirrors form an integral part of the linear Fresnel solar field, and any development that can lead to improved performance of the primary mirrors can greatly influence the deployment of LFR technologies in the near future.

#### 2.2.4.2. LFR geometry and optical analysis

LFR is deployed as an optical concentrator, which means that the mirror facets that constitute the primary reflector focus the sun rays onto the receiver. Generally, concentration takes place at the aperture of the primary reflector. The collector's concentration rate is calculated by the form of the mirrors that make up the reflector. The transversal profile of the mirrors determines its geometrical shape; the shapes discussed in this work are the commonly deployed notably, flat, parabolic, and cylindrical (Figure 2.5).

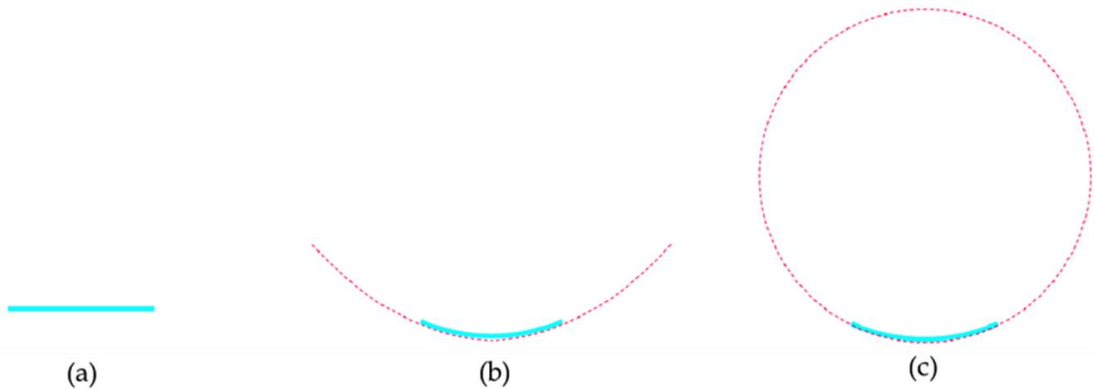


**Figure 2.5:** Scheme of the three mirror profiles addressed: (a) flat-shape mirrors, (b) parabolic-shaped mirrors, and (c) cylindrical-shaped mirror [48]

**Flat-shaped mirrors:** The simplest setup is flat-shaped mirrors (Figure 2.5a); the transversal mirror profile is a straight line in this case. The width of the image reflected by a flat-shaped mirror is almost identical to the mirror's real width from an optical standpoint. Flat-shaped mirrors have the drawback of not being able to concentrate radiation by themselves because the field of reflection is the same as the area of the reflected image. When the mirrored image of a group of mirrors is oriented to the same location, concentration occurs. Another drawback to using flat-shaped mirrors is that the mirrors' width must be almost equal to the receiver's width; hence, if wider mirrors width were deployed, this may result in variation and drift in ray concentration on the receiver (overflow effect). As a consequence, the width of flat-shaped mirrors and receivers must be compatible.

**Parabolic mirrors:** optical concentration technologies can realise a precise concentration by deploying a Parabolic geometry (Figure 2.5b). By definition, the rays concentrating perpendicularly to the aperture are mirrored into the focal point of the parabola. This condition is accomplished in solar collectors with parabolic reflectors when the reflectors monitor the sun's movement throughout the day. PTCs and LFRs have used parabolic mirrors since the beginning of their operations based on this geometrical theory [7, 48].

Achieving a parabolic profile in the transversal section of the mirror, particularly in the LFR technology, is a difficult task to accomplish compared to other options from a construction standpoint. One option is to have the mirror made specifically to desired specifications. This option, however, is ruled out because it restricts supplier availability and raises costs. A mechanically assembled straight mirror into a preformed pattern with the desired parabolic profile is an alternative option. The mirrors must be as thin as possible to achieve this assemblage and adopt the desired shape. This pattern may be a solid plate or a series of “ribs” profiles. Both choices necessitate that the material is pre-formed into the desired shape. As a result, the primary reflector's optical behaviour is optimised. However, as opposed to other geometries, the cost of manufacturing the pattern is higher [48].

**Cylindrical mirrors:** Cylindrical mirrors (Figure 2.5c) are not as accurate geometrically as parabolic mirrors, but they are simpler and less expensive to make constructively. The rays are focused in this geometry when the distance between the mirror and the receiver is substantially greater than the mirror's diameter [25, 48].

A cylindrical mirror, which is a part of a diameter, and a ray,  $r$ , impinging perpendicularly on the mirror's aperture in a point  $P$  are shown in Figure 2.6. The ray is redirected to  $f$  after being

mirrored. According to specular reflection laws [49], the angles produced by the reflected ray and the incidence angle,  $\theta$ , which are angles referring to the normal vector of the mirror, are identical. The point  $f$  is located at a distance  $B$  from the circumference's centre  $O$ . The radius of the circumference that contains the cylindrical mirror is the distance between the points  $O$  and  $M$ .

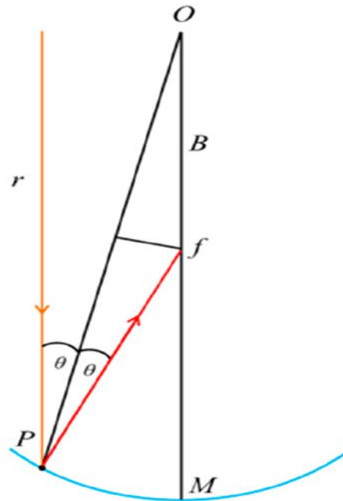


**Figure 2.6:** Scheme of the reflection in a cylindrical mirror

An isosceles triangle is formed by the points  $P$ ,  $f$ , and  $O$ , which have equal angles in both directions. Two right triangles can be made from this triangle. The relation between the angle of incidence/reflection  $\theta$ , the radius  $R$  of the circumference that contains the mirror, the distance  $B$  is given by:

$$B = R / (2 \cdot \cos \theta) \quad (2.1)$$

As previously stated, the mirror's width must be smaller than the distance to the receiver to achieve ray concentration in cylindrical geometry. The former produces a small  $\theta$  angle value, while the latter produces  $\cos \theta \approx 1$ . As a result, the rays strike the centre of the circumference radius,  $B = R/2$ . This is where the LFR's receiver is mounted.

As a result, the mirror takes the shape of a circumference section with a radius two times that of the focal distance or the distance between the mirror and the receiver. Each mirror has a single focal distance to the receiver from an optical standpoint, resulting in a different radius of curvature for each mirror. The cost of producing different preformed patterns for each radius of curvature would increase the LFR's cost.

Most experimental and numerical studies [24, 25, 50] performed in the past on investigating the performance of LFR solar field considered independent variables such as the number of

mirrors, their height, width, the distance between consecutive mirror centre lines and the receiver height. On the receiver and secondary reflector point of view, variables such as height, thickness and length are considered for the former, whereas for the latter, key elements such as the shape of the reflector surface, which could be a parabola or an involute depending on the use of receiver shapes, are considered.

The performance of three (3) mirrors, flat, parabolic and cylindrical reflective shapes, was investigated by [3] adopting the Fresdemo configuration, an LFR solar field mounted in the Plataforma Solar de Almeria by Solarmundo. The solar field constotutes 25 mirrors 60 cm wide, with a distance of 85 cm between two consecutive mirror centrelines, and a 50 cm wide receiver placed 8 m above the central mirror (see Figure. 2.7). The analysis was done through a ray-tracing model in Matlab, with four independent variables that define the solar field: the filling factor, the quantity of mirrors, their width and the receiver height; the first three variables define the array of mirrors, whilst the last one defines the focusing point.

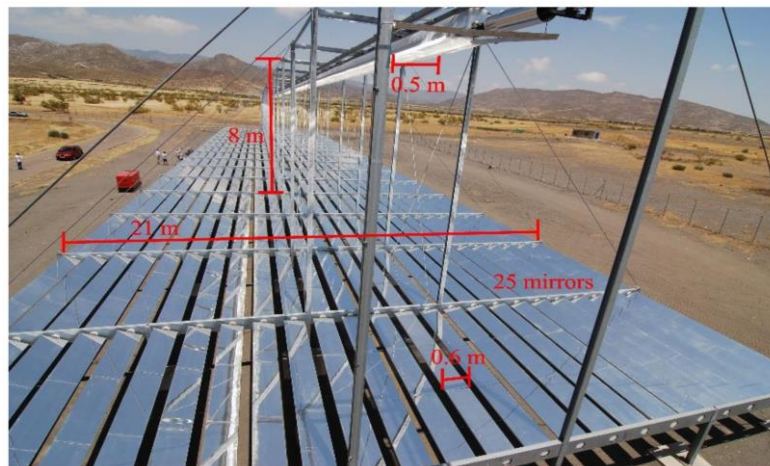


**Figure 2.7:** An image of the Fresdemo prototype with the main geometrical features [3].

Findings from the investigation show that when flat mirrors were used with the defined configuration, the radiation intensity would be as shown in Figures 2.8. It may be observed that the peak concentration factor is very low, around 18 suns; in addition, after the general shape, one may deduce that the sides of the receiver lose an important part of the radiation. This implies the mirrors being flat, they do not imply an extra concentration, and they are wider than the receiver itself.



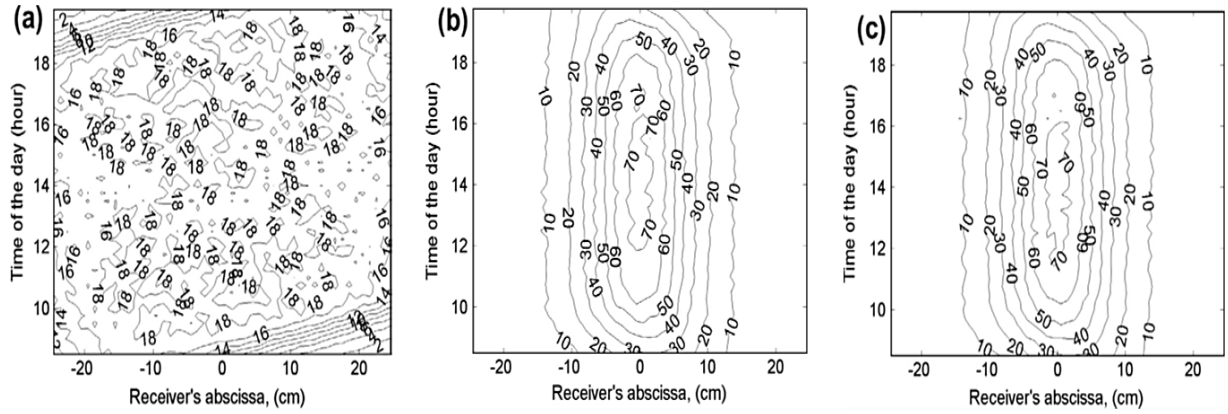


**Figure 2.8:** Concentration factor variation across the Fresdemo receiver for (a) flat mirrors (b) parabolic mirrors and (c) cylindrical mirrors along the day 21st June, [3]

The first conclusion that can be drawn from comparing Figures 2.8b and 2.8c is that the concentration characteristics of parabolic and cylindrical forms are identical when the same reference is used. Even though the maximum concentration factor is marginally higher for the former, with a wider concentration line of 70 suns, the global variance is negligible. This can be shocking at first glance, but it is not when we consider that the mirrors' aperture is extremely small: between 1 and 2 degrees. Based on these observations, it appears that the designer should prefer cylindrical shapes, which are easier to create than parabolic mirrors.

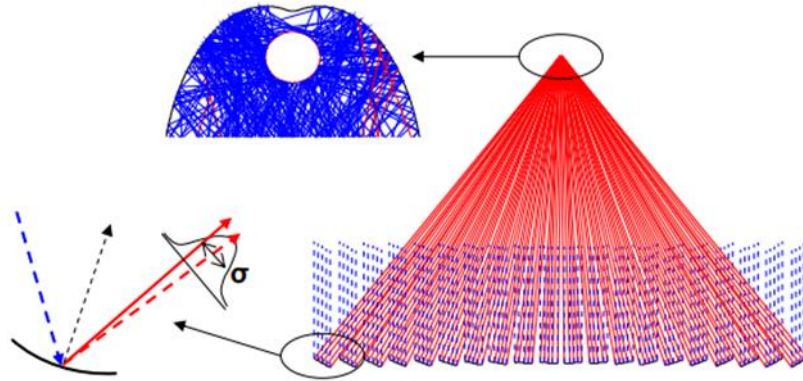


**Figure 2.9:** Schematic description of ray tracing simulation: general LFC layout (right), beam spread at the primary mirror (lower left) and receiver consisting of secondary mirror and absorber (upper left) [51]

The optimization of the geometry of primary reflectors of a solar field based on linear Fresnel was performed by Barale, Heimsath [51] as a part of the FREESUN project being built in Sicily. The simulation included many of the most important loss mechanisms, such as the cosine effect, shading, blocking, end losses, and material optical features (reflectance, transmittance, and absorptance). Variations from the ideal specular reflection (Fresnel reflection at interfaces) were also modelled due to the lack of perfect precision of certain



collector components, such as the tracking device, mirror morphology, and receiver alignment, among others (Figure 2.9). The divergence from a perfect reflection (dashed red), i.e., the actual direction of reflection influenced by errors (solid red), was viewed as a statistical event with a Gaussian distribution, whose standard deviation was calculated using experimental data on real components.

$$\sigma = \sqrt{\sigma_{tracking}^2 + \sigma_{shape}^2 + \sigma_{receiver}^2 + \sigma_{other}^2} \quad (2.2)$$

The study revealed that the contribution of errors to the optical performance of the primary mirrors is greatly influenced by the distance between the collectors and the receiver. Hence the greater the distance, the more reduction in the optical performance and the adoption of uniform curvature mirror (use of the same curvature for all mirrors) result in a lower concentration ratio [3].

Comparative analysis between central and compact linear Fresnel reflectors was performed in [45]. For an appropriate comparative study, it is essential for the authors to define a criterion for the comparison. In that context, a new variable is defined, the useful energy efficiency (*Eq. 2.3, 2.4*), which only accounts for the radiation that impinges on the receiver with intensities above a reference value. Flux intensity across the receiver surface depends largely on the mirror profiles. The investigation was conducted assuming hourly data of a typical year with reference to a configuration similar to that of the FRESDEMO.

**Table 2.2:** Optical and geometrical data of the selected configurations. [45]

Optical and geometrical parameters	Central LFR	Compact LFR - complete	Compact LFR - complete
Number of primary mirrors	24-36-48	24-36-48	24-36-48
Total solar field width (m)	50	50	50
Total primary mirrors length (m)	100	100	100
Primary mirrors width (m)	1	1	1
Primary mirrors height (m)	2	2	2
Receiver height (m)	12.5-25-37.5	12.5-25-37.5	12.5-25-37.5
Receiver width (m)	1	1	1
Receiver length (m)	100	100	100
Mirror axis orientation	N – S	N – S	N – S
Mirror reflectivity	0.93	0.93	0.93

$$\eta_{energy}(\%) = \frac{E_{incident\ on\ receiver}}{DNI \cdot A_{primary\ mirrors}} 100 \quad (2.3)$$

$$\eta_{optical}(\%) = p_{primary\ mirror} \cdot \frac{E_{incident\ on\ receiver}}{DNI \cdot A_{primary\ mirrors}} 100 \quad (2.4)$$

Two different concepts of Compact LFR were considered: Compact LFC-complete, where all mirrors alternate their tilt aiming to one or another receiver; and Compact LFC-hybrid, where only the farthest mirrors from both receivers, i.e., those positioned in the centre of the field, alternate their tilt focussing to one or another receiver. Table 2.2 presents optical and geometrical parameters selected for the study. The simulations have been performed for 100 000 rays, and the times chosen for the simulation are June 21<sup>st</sup> at 12:00 solar time (Figure 2.10) and the same day at 17:00 solar time. Table 2.3 summarizes the useful energy efficiencies for each of the proposed configurations and for each point.

**Table 2.3:** Useful energy efficiency for the three optimized configurations considered, on the 21st June at 17:00 solar hour [45]

Useful energy efficiency			
	Central LFC	Compact LFR - hybrid	Compact LFR - complete
21st June at 12:00 solar hour	74.23	64.82	50.56
21st June at 17:00 solar hour	51.01	29.82	24.62

The results in Figure 2.10 were obtained when the sun was close to the zenith. It is observed that concentrated solar irradiance is higher for the Compact LFR - hybrid configuration compared to the central LFC configuration. This is largely due to the filling factor of the optimal central LFC configuration (36 mirrors in a field of 50 m wide), which is lower than the optimal Compact LFR - hybrid configuration (48 mirrors in a field of 50 m wide). In fact, the central LFC configuration's useful energy efficiency (Table 2.3) is higher in contrast to the Compact LFR - hybrid configuration because efficiency considers the total primary mirrors area generating that concentrated irradiance. The Compact LFC-complete configuration is the one with lower concentrated irradiance and lower useful energy efficiency because the average distances from the mirrors to the receiver are greater than in the other two cases, and the dispersion of the rays is greater.

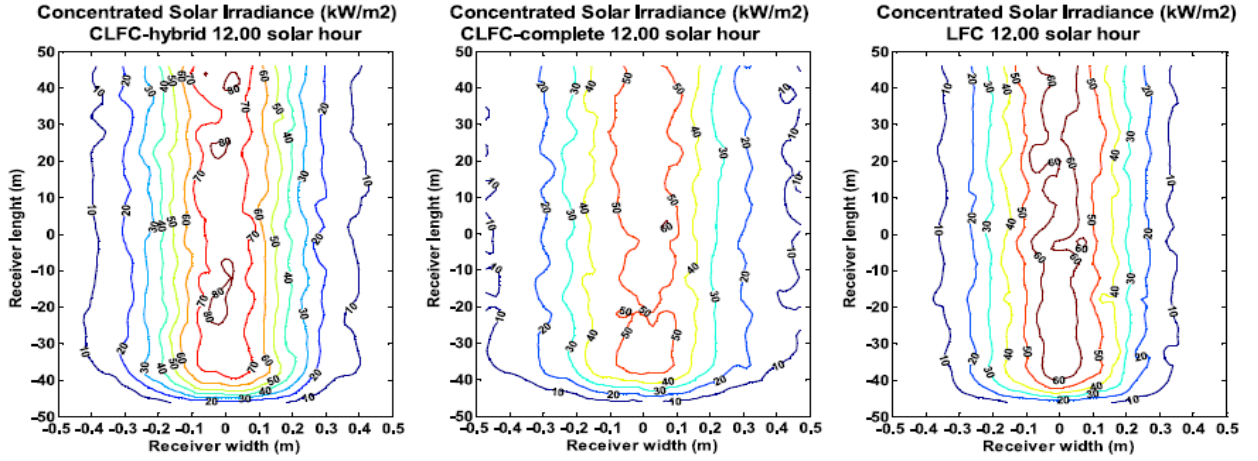


**Figure 2.10:** Concentrated solar irradiance maps on the receiver, for the three configurations considered, on the 21st June at solar noon (12:00 solar hour) [45]

We can conclude from the analysis that compact linear Fresnel compared to a central configuration reduce losses due to blocking and shading. However, this minimization is not sufficient to overcome other negative effects of the compact Fresnel collectors, as the greater variation of the rays reaching the receiver, initiated by the fact that mirrors must be located farther from the receiver, generates lower efficiencies.

A scalable linear Fresnel reflector (SLFR) solar system was proposed by He, Wang [52]. The optical solar field, which comprises an array of linear plat mirrors close to each other, is designed to minimize the inter-row shading and blocking. Scalable mechanical mirror support, which can integrate different mirrors, is designed to generate different temperatures. The mechanical structure can be adjusted to minimize the end losses. Lastly, the thermal efficiency of the SLFR with two-stage mirrors is examined.

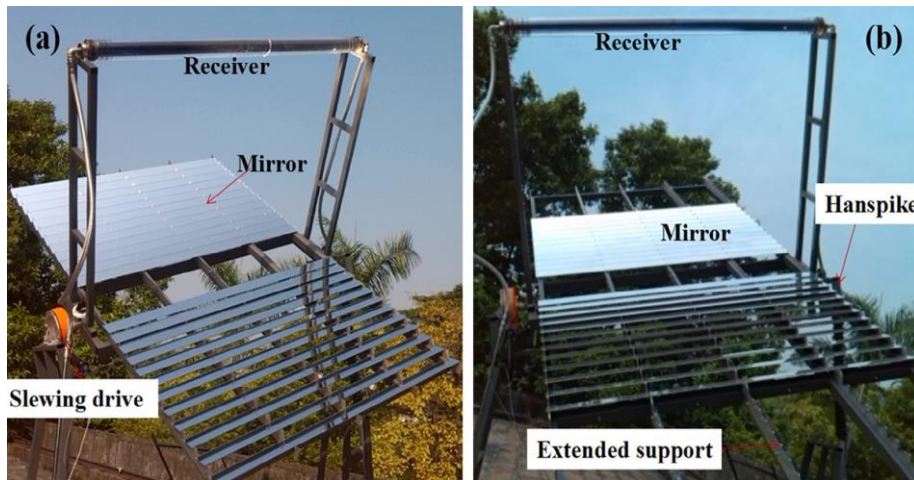


**Figure 2.11:** Images of SLFR solar system (a), and SLFR solar system with extended support (b) [52]

The SLFR solar field is depicted in Figure. 2.11 above. The SLFR is oriented to the East-West direction and configured for North-South tracking of the sun. In the mirror field of SLFR, the central point of each mirror maintains the same straight line. The tilt of each mirror is varied so that the impinging sunlight is directed to the focus point after a single reflection. The flat mirrors follow the sun as a whole, so the inter-row shading and blocking do not need to be considered when the sun is at indirect incidence.

Each mirror can be characterized by location ( $Q_n$ ) of the  $n_{th}$  mirror ( $n$ ), tilt angle ( $\delta_n$ ), the width of the mirror ( $D$ ) and the distance of adjacent mirrors ( $S_n$ ). Using the expressions (Eq. 2.5 – 2.9), these parameters were obtained by deploying a simple geometrical optics approach.

$$\tan 2\delta_n = Q_n/f_n \quad (2.5)$$

$$S_n = D/2 [(\sin\delta_n + \sin\delta_{n-1})\tan 2\delta_n + \cos\delta_n + \cos\delta_{n-1}] \quad (2.6)$$

$$Q_n = Q_{n-1} + S_n \quad (2.7)$$

$$\text{Here, } n \geq 1 \quad (2.8)$$

$$r_{nc} = 2 \frac{f_n}{\cos \delta_n} \quad (2.9)$$

After adjustment, as shown in Figure 2.12. below, the peak thermal efficiency of 64% is obtained, and the mean thermal efficiency is higher than before the adjustment. The results indicate that the inclination design reduced the end losses effectively, and the SLFR can obtain excellent thermal performance after adjustment.

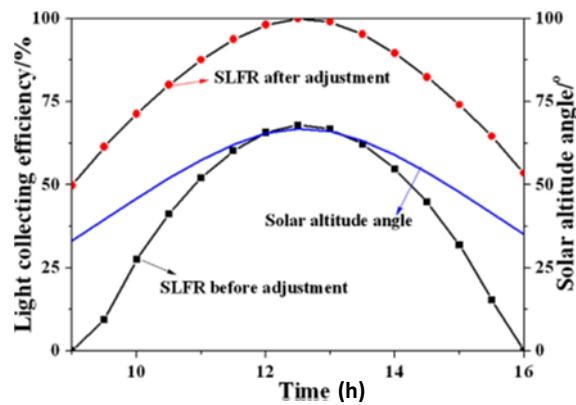


**Figure 2.12:** Curves of solar altitude angle, the optical efficiency of SLFR concentrator before and after end losses adjustment. [52]

A pilot-scale solar Linear Fresnel Reflector of 154 m<sup>2</sup> is modelled and optically examined with two different secondary reflector profiles by Balaji, Reddy [53]. The design features deployed for optical modelling were adopted from the LFR system installed at the pilot plant (Figure 2.13) in Vallipuram (12.65°CN, 79.74°CE), Tamil Nadu, India, with the parabolic secondary reflector. The LFR system comprises a storage-integrated solar collector field of about 125 kWth with flexible steam output (50 bar pressure and 350–400 °C temperature).

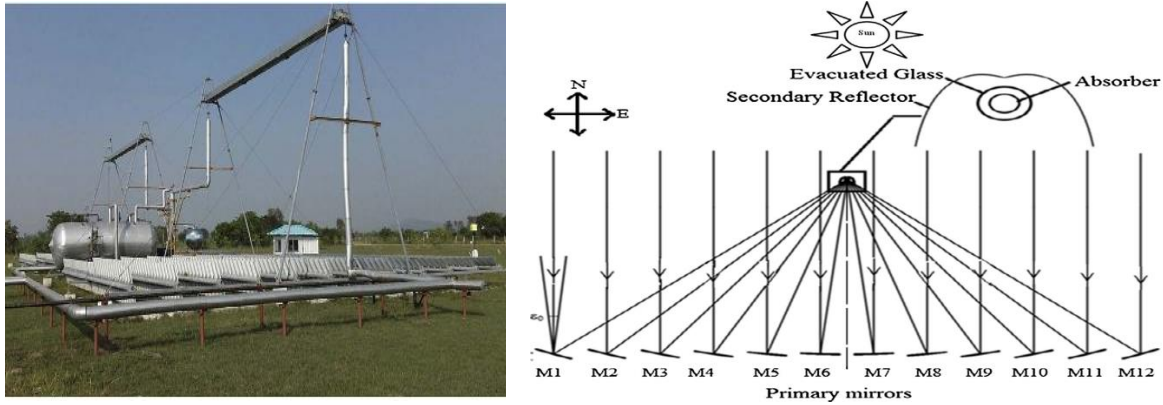


**Figure 2.13:** Photograph (Left) and Schematic representation (Right) of Solar field at Vallipuram, India based on LFR and secondary concentrators [53]

The study considers twelve main Fresnel reflectors with a width of 1.07m, a length of 12m, and an effective reflector area of about 154m<sup>2</sup>. The reflectors' focal point is eight metres above the ground. The absorber has a diameter of 70mm and is enclosed in a 125mm diameter evacuated protective glass. Because the primary reflectors are all the same width, the curvature and tilt of each must be adjusted so that rays incident on the absorber at the focal point 'h' after reflection from all the primary reflectors. The main reflectors can have a large radius of curvature and can have linear, parabolic, or circular profiles. The reflectors may all have the same focal length ( $f$ ) or a different radius of curvature.

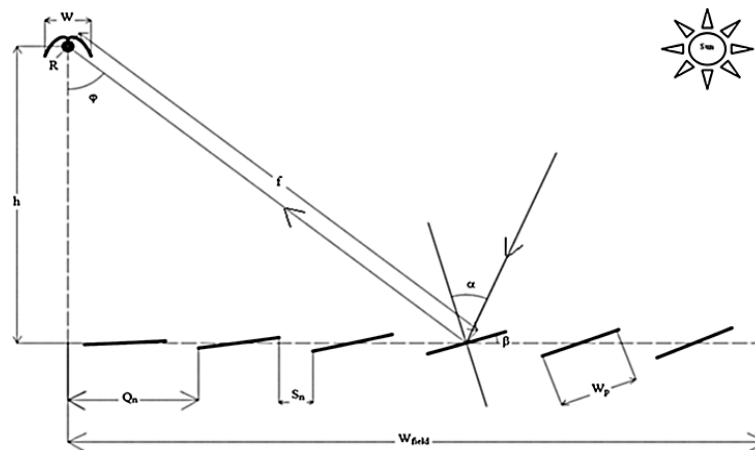


**Figure 2.14:** Design parameters of the Linear Fresnel Reflector Solar Field [53]

As shown in Figure 2.14, the  $n_{th}$  mirror in the LFR array is defined by three parameters: locations ( $Q_n$ ), tilt ( $\beta_n$ ), and shift ( $S_n$ ). The tilt angle ( $\beta_n$ ) is the angle formed by the  $n_{th}$  primary mirror with the horizontal plane, and it is calculated using Eq. 2.10 [4].

$$\beta_n = \frac{1}{2} \tan^{-1} \left[ \frac{Q_n + (W/2) \cos \beta_{n-1}}{f + (W/2) \sin \beta_{n-1}} \right] \quad (2.10)$$

The gap between adjacent mirrors shifts ( $S_n$ ) is used to improve the LFR system's performance by minimising the shade produced by adjacent mirrors, especially at higher incidence angles. The Shift ( $S_n$ ) is computed using the formula Eq. 2.11 [4]:

$$S_n = W \sin \beta_{n-1} \tan (2\beta_n + \varepsilon_0) \quad (2.11)$$

The  $n_{th}$  mirror's location ( $Q_n$ ) is calculated [4] from the centre of the mirror field using (Eq. 2.12).

$$Q_n = Q_{n-1} + W \cos \beta_{n-1} + S_n \quad (2.12)$$

Starting with the initial guess of  $\beta_n = 0$ ,  $S_0 = 0$ ,  $Q_0 = W / 2$ ,  $Q_n = W / 2$ , and  $n = 1, 2, \dots, m$ , where ' $m$ ' represents the total number of mirror elements, Eq. 2.10 – 2.11 are solved iteratively to obtain the values of  $Q_n$ ,  $\beta_n$ , and  $S_n$ . The focal length ( $f_n$ ) and tilt angle ( $\beta_n$ ) of the individual mirrors determine the curvature radius of the primary mirrors [12]. The radius of curvature of circular/parabolic primary mirror is calculated using Eq. 2.13- 2.15. The optical angle ( $\varphi_n$ ) is defined as the angle formed by the optical axis and the line connecting the focus and the primary mirror.

$$\varphi_n = \tan^{-1} \frac{Q_n}{h} \quad (2.13)$$

The  $n_{th}$  main mirror's focal length ( $f_n$ ) is computed as

$$f_n = \sqrt{h^2 + Q_n^2} \quad (2.14)$$

As a result, the primary reflector's circular radius of curvature is given by;

$$r_{nc} = 2 \frac{f_n}{\cos \delta_n} \quad (2.15)$$

Findings from the study reveal that at fixed equivalent acceptance angle, aperture width, and tilt of the main mirrors, the LFR system with Parabolic (PB) secondary reflector has higher optical efficiency of 62.3% with secondary efficiency of 83.3%. In contrast, the LFR system with involute (IN) secondary has an optical efficiency of 59.5% and a secondary efficiency of

78.33%. The efficiency of the PB-LFR and IN-LFR systems with various acceptance angles is investigated. The PB & IN secondary with equivalent acceptance angles of 45 degrees have a more uniform flux distribution around the absorber and are more effective than those with other acceptance angles. With a PB secondary reflector, a more uniform distribution flux on the absorber will extend the life of the selective coating material and the absorber tube.

Beltagy, Semmar [54] have carried out the theoretical and experimental analysis of a Fresnel type solar concentrator. In the study, the theoretical model was used to easily determine various essential parameters design of the set-up compared to measured data. For a 250kW installed capacity of thermal prototype, the results show a daily thermal efficiency of over 40% realised. The photograph of the studied Fresnel solar field prototype and installation set-up is depicted in Figure 2.15.

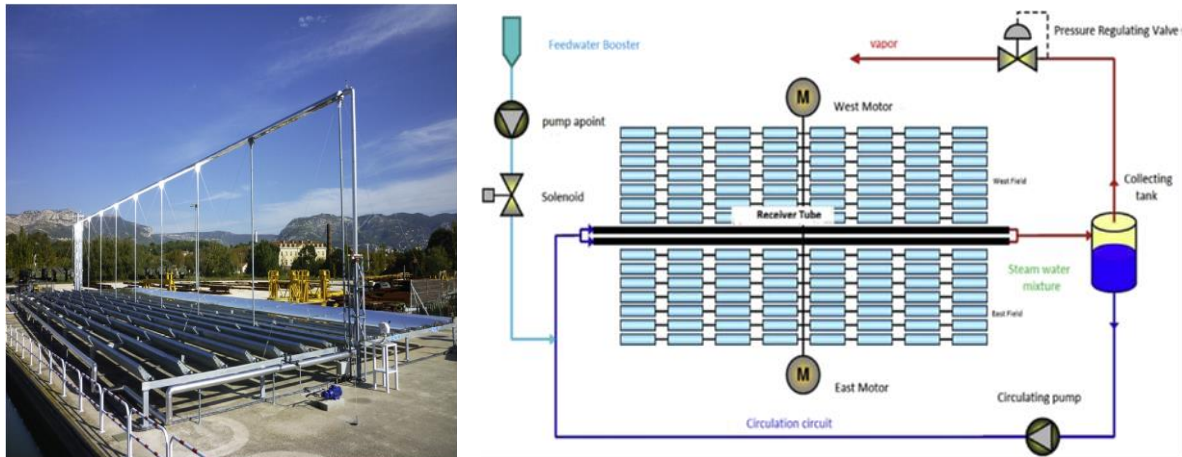


**Figure 2.15:** The photograph of the studied Fresnel solar field prototype (Left) and set up of the installation. (Right) [54]

The tests are performed in the solar division of the CNIM in Seyne on the sea, France. The model is working on a fully automatic operational basis. The system control records different parameters, which permit measuring of the energy performances. In order to validate the recorded performances, the measured and the theoretical performance parameters were continuously checked. The expected performances are calculated by means of a theoretical calculation that takes into account the various phenomena involved. The comparison between the projected results allows to validate the running of the prototype and help make various improvements to enhance the performance.

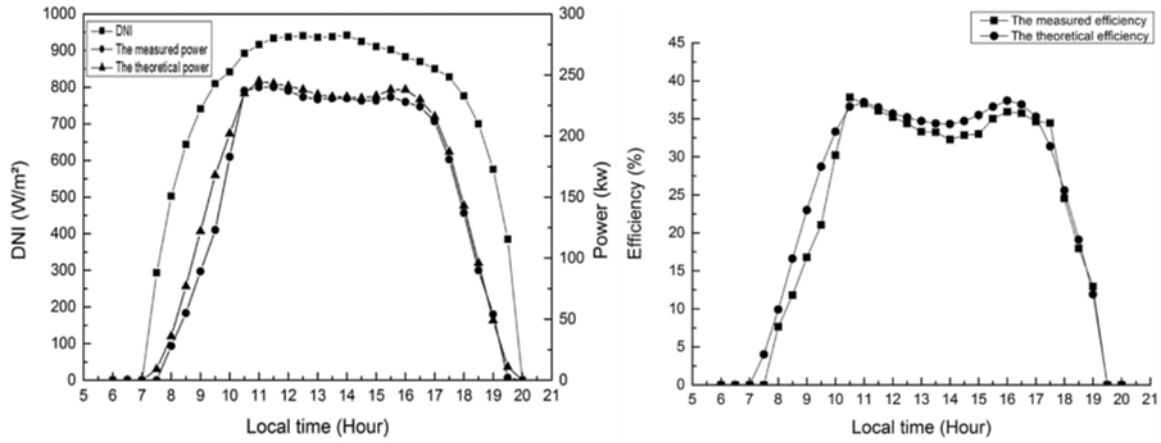


**Figure 2.16:** Theoretical and measured power for the day 13/04/2015 and Daily theoretical and measured efficiency for the day 08/04/2015. [54]

The power (irradiance) as a function of time changes considerably from 50 to 250 MW for one day (see Figure 2.16). The daily efficiency indicates significant variation during the day and fluctuates from 10 to 43%. Apart from the early morning and late afternoon, theoretical results are in good agreement with experimental measurements. The peak power value achieved 250kW with a daily efficiency of 40%. Thus, it can be concluded that the theoretical model used explains well the physical phenomena of the test bench and validate experimental results.

Boito and Grena [14] analysed results obtained from the optical optimization of a linear Fresnel collector. The variables deployed in the optimization are the mirror widths, positions and focal lengths; the mirrors can be of varying size and focal length, and they can be non-uniformly spaced. The optimal target function was the plant cost divided by the collected solar radiation in a year. Four different mirror configurations were optimized (uniformly spaced identical mirrors; nonuniformly spaced identical mirrors; mirrors of the same width with uniform spacing and variable focal lengths; and finally, a full optimization), with a discussion of the resulting gain on the target function (i.e. the reduction of the ratio between the plant cost and the collected radiation).

The results reveal that the use of suitable optimization strategies can lead to a projected gain of about 12% with respect to the initial configuration (all mirrors identical and adjacent). A complete optimization leads to a gain of 4.5% over a simple uniform optimization. This gain is largely due to the likelihood of controlling the focal lengths (the optimization of focal lengths leads to a 2.8% gain over the uniform case). In comparison, only a minor improvement (less than 0.4%) is obtained with non-uniformly spaced identical mirrors.



#### 2.2.4.3. LFR receiver and secondary reflector configurations

The concept of LFR receiver and secondary reflector has been extensively analysed in the past. Advancements are being made to improve receiver assembly design to enhance the optical efficiency of collectors. Different views on the number of receivers per mirrors array, location, and orientation have been presented [43, 55, 56]. Instead of using single receiver tubes, most recent technologies adopt many multi-tube receivers (thinner tubes) to increase the receiver surface, thus leading to an increased collector intercept factor. Figure 2.17 shows LFR different receiver designs and orientations.

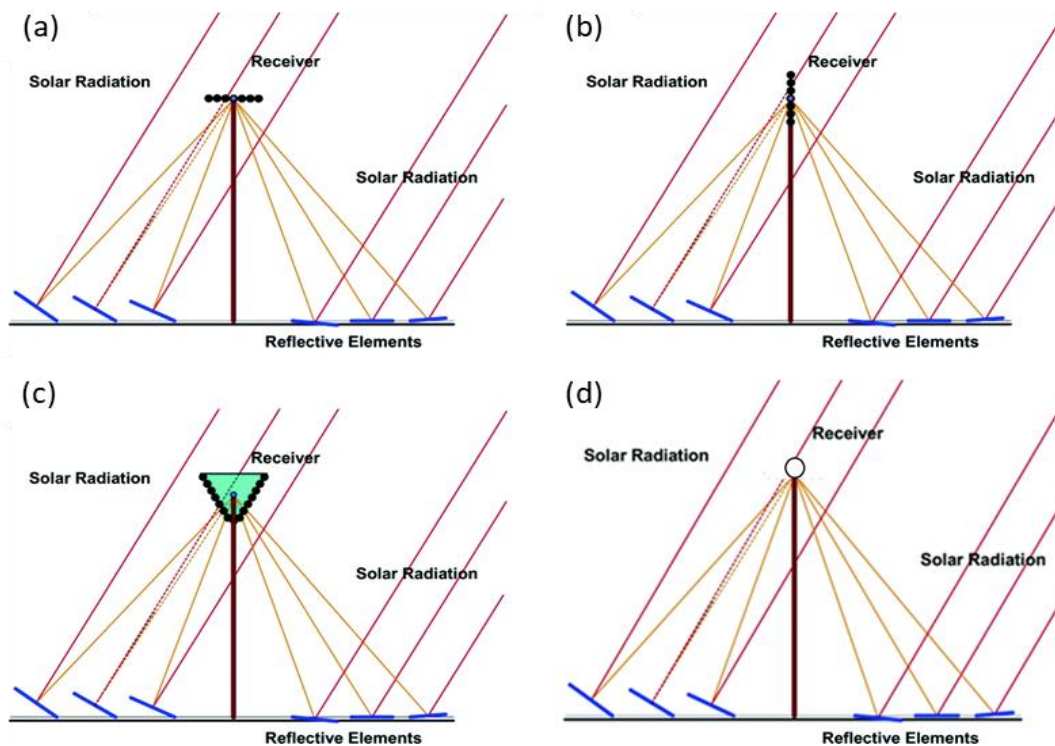


**Figure 2.17:** Fresnel Solar Field deploying various receiver configurations (a) central LFR with multitube horizontal, (b) multitube vertical, (c) multitube triangular and (d) single horizontal receiver, reprinted from reference [43, 56, 57]

**Multi-Tube Receiver:** Early LFR research and prototypes adopted the multi-tube receiver concept. However, recent discoveries in the so-called Compact Linear Fresnel have rekindled renewed interest in such receiver design. One of such receiver designs is the trapezoidal cavity receiver. Being one of the most conventional designs, it comprises a parallel set of tubes in series arranged horizontally in the cavity. Hence the design does not require a secondary receiver. A Compact Linear Fresnel configuration deploying Multi-Tube Receiver is shown in Figure 2.18.

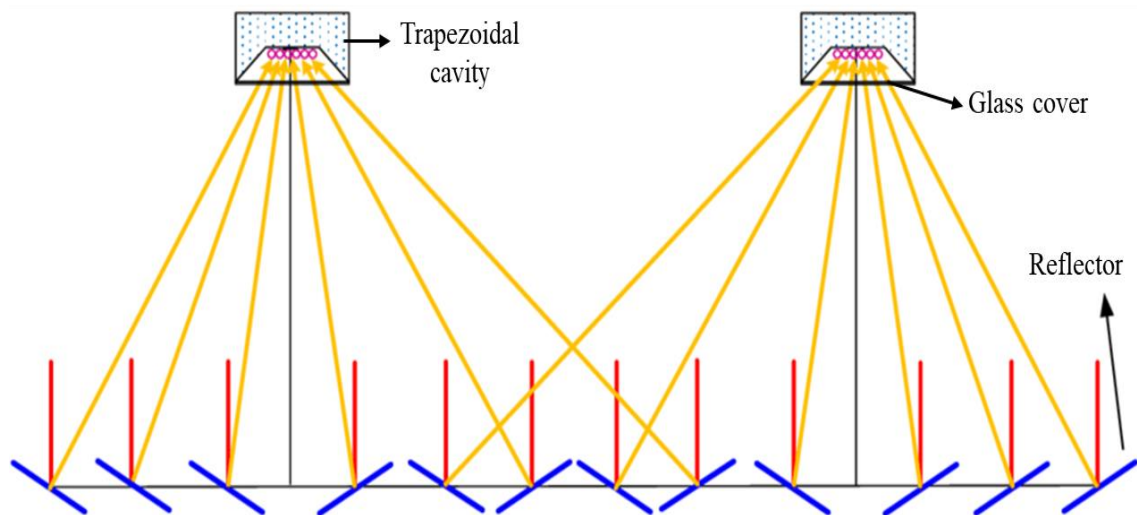


**Figure 2.18:** Sketch of Compact Linear Fresnel Reflector (CLFR) [58]

Re-radiation losses can be greatly minimized by protecting the selective coating by incorporating a glass cover at the opening of the cavity. As an added advantage, the glass cover is responsible for some greenhouse effect that benefits receiver performance and convection losses as a result of the vacuum existing inside it. Nonetheless, generating a vacuum in a great cavity of not elementary geometry comes with some technical impediments, which has drawn the attention of research towards a selective property that can resist ambient pressure. Presently, these coatings have not attained the commercial operation stage.

The CLFR plant in Kimbarlina (Figure 2.19 left) consists of a multi-tube receiver and without a secondary reflector, while the LFR power plants such as Puerto Errado 2 in Spain, a prototype in Sicily (Figure 2.19 right), Italy and Dhursar in India are configured with single-receiver tubes and secondary reflectors deployed. Despite several studies that analyse the thermal behaviour of the receiver with selective property, the tubes are usually not covered by selective paint [45].



**Figure 2.19:** Compact LFR plant in Kimbarlina, USA (Left) and Linear Fresnel collector prototype, Italy (Right) reprinted from [59]

**Single Tube Receiver:** Primarily, only one tube is deployed in a single-tube receiver design with a diameter range usually between 7.5 cm and 18 cm. In such a configuration, the receiver is housed by a cavity provided with a secondary reflector in the shape of a double parabola and a glass cover located at the bottom of the cavity. State-of-the-art designs are considering the alternative of the tube coated with a selective property and protected from the environment by concentric glass cover to reduce losses due to convection and re-radiation and, thus, increase the temperature of the working fluid [45].

Furthermore, the use of single-tube receiver configuration without a selective property has attracted a lot of interest; notably, the Puerto Errado 1 (Figure 2.20 right) and two plants in Murcia, Spain, [60, 61] and prototype in Belgium, developed by the Solarmundo company [62], use the single-tube technology without secondary reflector and selective property [45]. The Fresdemo prototype erected at the Plataforma Solar de Almería (PSA) in Spain [63] use the single-tube technology with a secondary reflector (Figure 2.20 left) [45]. The use of a large size single absorber tube may also help enhance the optical efficiency, avoiding additional maintenance work required for the secondary reflector [64, 65]. Linear Fresnel solar field configuration without secondary reflectors currently occupies a valuable position in industrial applications and attracts more attention [21].

A commercial evacuated tube specifically designed for CSP solar plants working at medium/high-temperature levels is shown in Figure 2.21. This design meets the fundamental requirements of supporting the deployment of diathermic oil and realizing high efficiency at such temperature levels. A spectrally selective coating is deposited on the steel tube in the selected evacuated absorber tube technology. This is a multilayer thin-film structure with an inferior metal layer reflecting infrared radiation and a superior antireflective ceramic content.

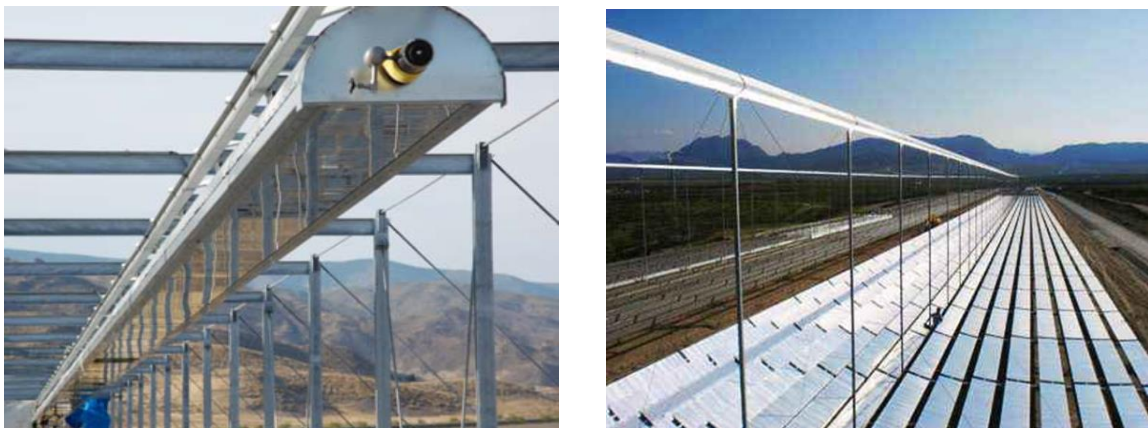


**Figure 2.20:** Fresdemo prototype at the Plataforma Solar de Almería (PSA) in Spain (Left) and Puerto Errado -1 (PE1) Fresnel solar field (right) [66, 67]

At the solar receiver's operating temperature (up to 400 °C), a graded ceramic-metallic content ensures a high absorptance in the solar wavelength range and low emittance conduct. To limit reflection losses, the exterior glass has an AR coating on both sides.

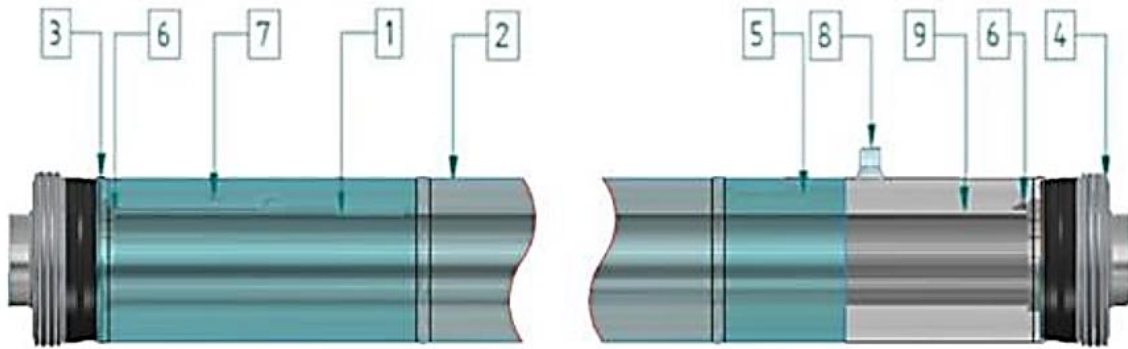


**Figure 2.21:** 1. Stainless steel absorber tube with spectrally selective coating; 2. Glass jacket with Anti Reflective (AR) coating; 3. Glass to metal seals; 4. Thermal expansion compensators; 5. Vacuum annulus; 6. Not Evaporable Getter (NEG) pills; 7. Barium getter; 8. Pump nipple; 9. Serial number.

A secondary reflector is often employed when a single receiver tube is used to reduce manufacturing and hardware cost and increase the collector optical performance. Designing an optimum secondary reflector can be a very complicated process, and the choice of deployment may also depend on the rest of the collector and receiver design. Different simplification assumptions adopted in the optical analysis may result in different designs and vary in shapes. Some examples of secondary reflector designs are shown in Figure 2.22.

The cavity receivers of an LFC constitutes an absorber tube and a secondary reflector. To minimize loss due to heat, the absorber is generally either shielded with a glass tube (Figure 2.22a) or the bottom of the cavity is enclosed with a glass plate (Figure 2.22b). Another approach is to apply a non-evacuated glass tube around an absorber pipe with an air-stable coating. Since the redirected rays by the secondary reflector are not loss-less, an element of the short wavelength radiation is absorbed by the secondary reflector, increasing its temperature. At the same time, the absorber is being heated at the expense of radiation and convection heat losses to the surroundings [67].



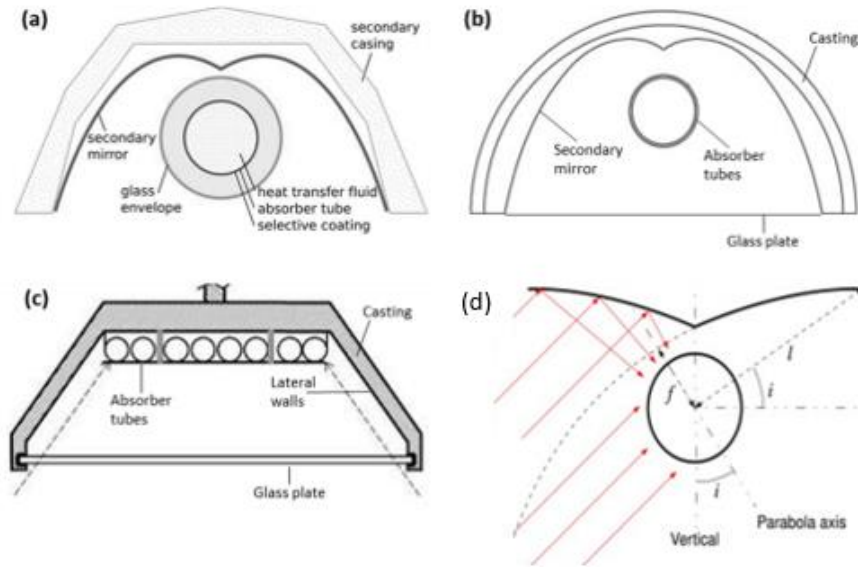


**Figure 2.22:** Common receiver configurations used in Linear Fresnel collectors. (a) Secondary absorber tube glass plate on the bottom. (b), Secondary concentrator with absorber tube and glass plate. (c), Row of tubes inside a cavity. (d) A flatter secondary reflector design[68, 69].

Traditional secondary reflector designs are likely to follow or emerge from the shapes of compound parabolic concentrators (CPC) [70-72]. In such designs, the reflector surface could be a parabola [73] or an involute [74], depending on the use of receiver shapes [75]. In the case of linear Fresnel design, one or multiple circular absorber tubes are used in general. Moreover, in the case of FRESDEMO (Figure 2.23 left) [76] and NOVATEC (Figure 2.23 right) [77], the secondary reflector adopted a shape similar to an involute used in the CPC using a tube as its receiver. Some recent study shows that a flatter-shaped secondary reflector surface may perform better [68], as is illustrated in Figure 2.23 (right). The fact that a secondary reflector may not be required because of its added manufacturing complexity and additional maintenance requirement, particularly when a large-sized, evacuated receiver tube is used, is a matter that is subject to contention [64].

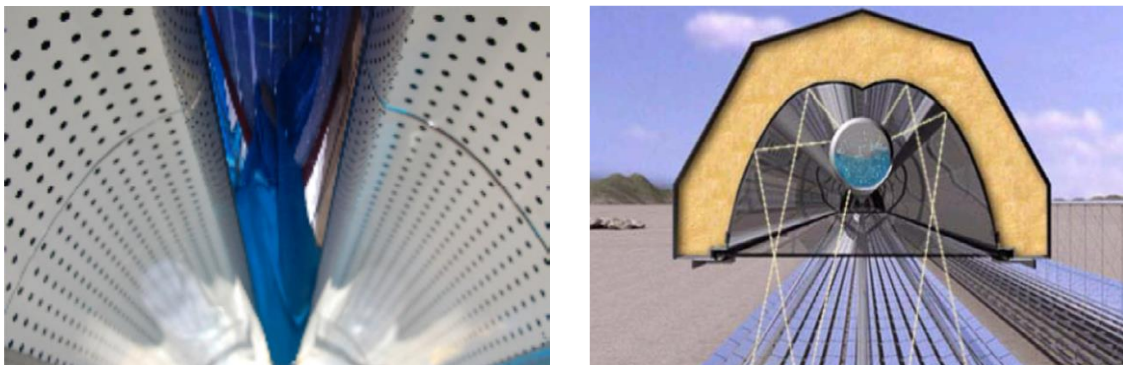


**Figure 2.23:** Receiver assembly used for the FRESDEMO project at PSA. Secondary concentrator is equipped with photogrammetric measurement foil (Left) [63] and Nova-1 receiver assembly by Novatec Solar, reprinted from reference (Right) [77]

Optical and thermal analysis of a linear Fresnel reflector was performed by Bellos, Tzivanidis [78]. The collector's thermal analysis was carried out using three separate working fluids: thermal oil, molten salt, and liquid sodium. The receiver and glass have outer diameters of 70 mm and 115 mm, respectively, which are common for these technologies. The analysis was carried out for various working fluid temperature ranges: the Syltherm was tested from 350 K to 650 K, the molten salt from 550 K to 850 K, and the liquid sodium from 400 K to 900 K. SolidWorks Flow Modelling is used for both optical and thermal analysis.

Initially, Eq. (2.16) [79] is used to measure the collector's net aperture ( $A_a$ ). By assuming that the reflectors are horizontal, this parameter accounts for the area of the reflectors. The maximum possible collection area is taken into account in this description.

$$A_a = N_{rf} \cdot W_0 \cdot L \quad (2.16)$$

The solar direct beam irradiation  $Q_s$  available was calculated as follows:

$$Q_s = A_a \cdot G_b \quad (2.17)$$

The energy balance in the fluid volume was used to measure the usable heat production ( $Q_u$ ).

$$Q_u = M \cdot C_p \cdot (T_{out} - T_{in}) \quad (2.18)$$

The linear Fresnel reflector's thermal efficiency ( $\eta_{th}$ ) is defined as the ratio of usable heat to available solar energy:

$$\eta_{th} = Q_u / Q_s \quad (2.19)$$

Eq. (2.20) is used to calculate the flow's heat transfer coefficient ( $h$ ):

$$h = \frac{Q_u}{(\pi \cdot D_{ri} \cdot L)(T_r - T_{fm})} \quad (2.20)$$

The mean fluid temperature ( $T_{fm}$ ) is estimated as:

$$T_{fm} = \left( \frac{T_{in} + T_{out}}{2} \right) \quad (2.21)$$

According to the final results, the collector's exergy efficiency is optimised at 700 K, and it is 30.20% with liquid sodium and 30.05% with molten salt. According to performance criteria, liquid sodium was found to be the best choice, followed by molten salt and thermal oil. The liquid sodium's superior efficiency is due to its high heat transfer coefficient. Furthermore, for molten salt action, the pumping work is maximised.

Receiver failure and fluctuating operation of the linear Fresnel Reflector (LFR) are challenges that result from non-uniform solar flux concentration. Qiu, Li [66] proposed an aiming strategy optimization approach to minimise these effects by combining a multi-objective Genetic Algorithm (GA) with Monte Carlo raytracing to homogenise the flux distribution. The GA optimization strategy (S2) is compared with the traditional one-line aiming strategy (S1). Based on the approach, the flux distributions in a Multi-Tube Cavity Receiver (MTCR) and the Single-Tube Receiver with a Secondary Collector (STRSC) are optimized at a standard condition.

Real-time flux distributions in MTCR on spring equinox when S1 and S2 are used is depicted in Figure 2.24, while the distributions in STRSC is shown in Figure 2.25. The study shows that under a real-time condition, S2 denotes that fluxes in the two receivers can be effectively homogenised over the entire time span with a modest efficiency loss of 0.2–3.8% points compared to conventional one-line aiming strategies (S1). As S2 replaces S1, the MTCR flux non-uniformity indexes are significantly reduced from 0.77–1.09 to 0.02–0.06, and the STRSC flux non-uniformity indexes are steeply reduced from 0.59–0.70 to 0.29–0.37. The current approach is found to be efficient and sufficient for homogenising fluxes in LFR receivers.

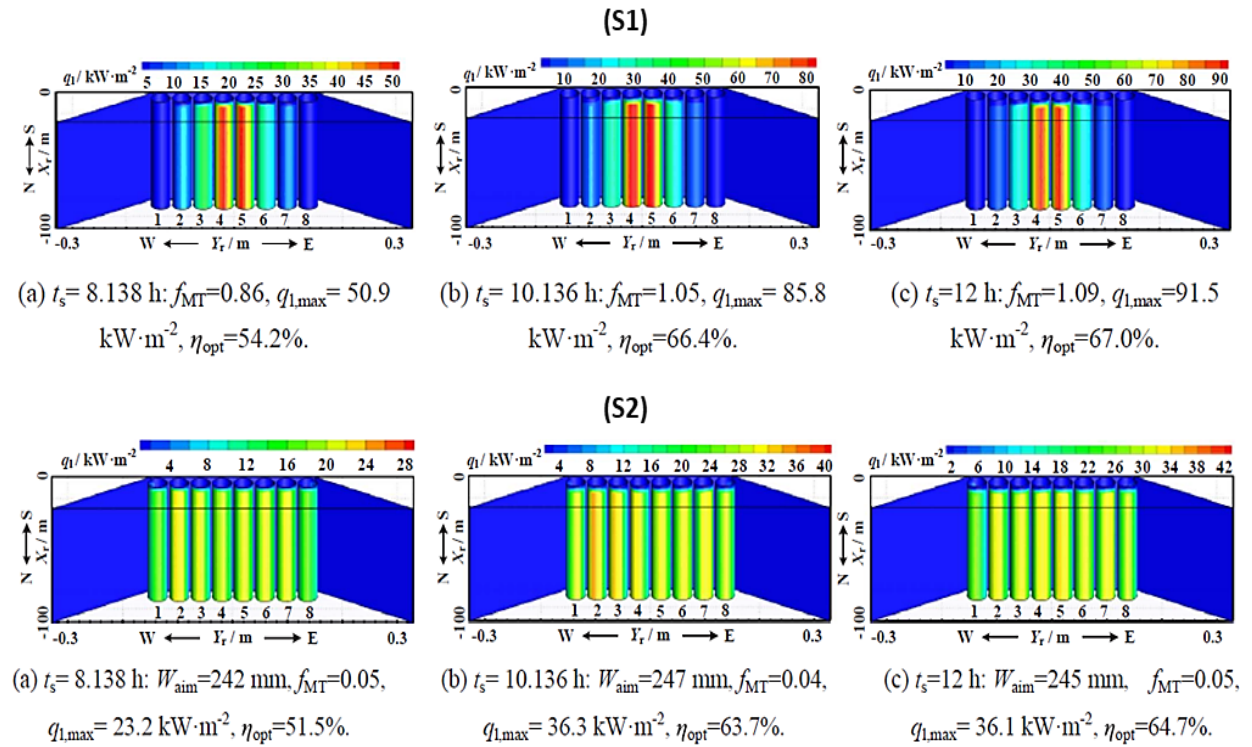


**Figure 2.24:** Real-time flux distributions in MTCR on spring equinox when S1 and S2 are used. [66]

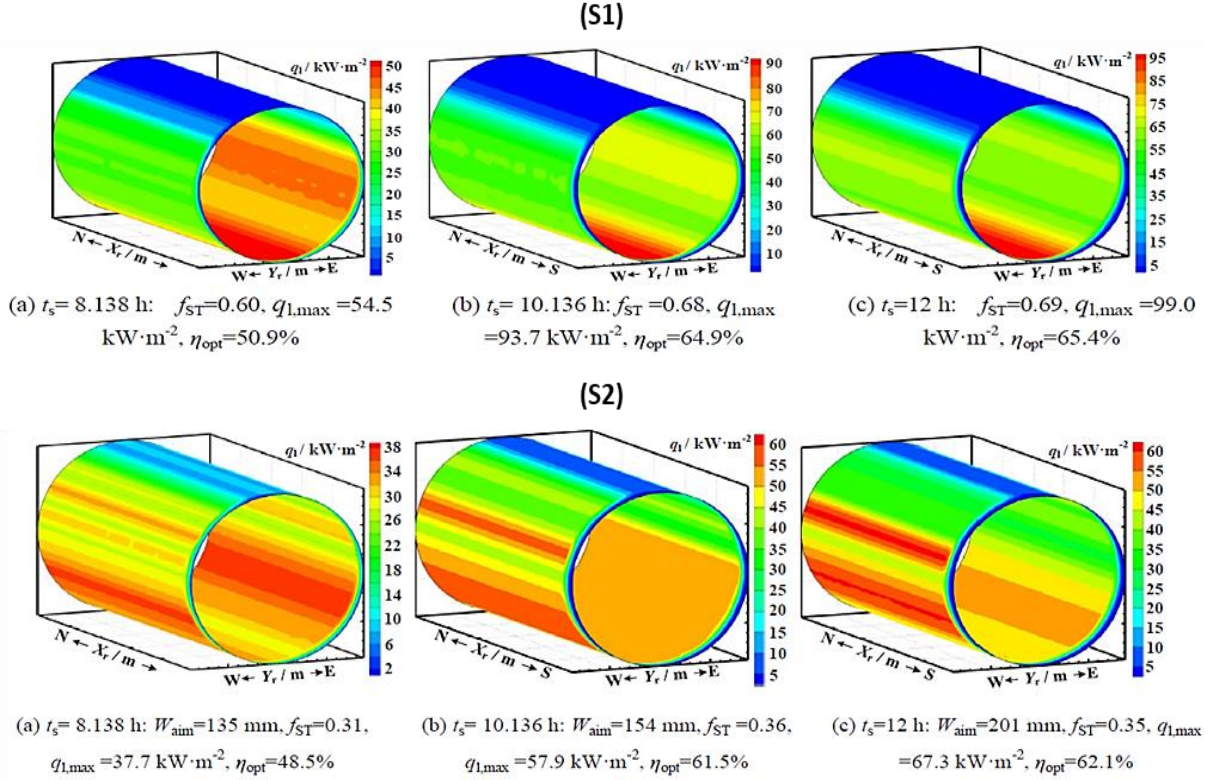


**Figure 2.25:** Real-time flux distributions in STRSC on spring equinox when S1 and S2 are used [66]

Abbas, Valdés [80] have investigated the concentration process for LFR optimizing different optical designs, circular-cylindrical and parabolic-cylindrical mirrors with different reference positions. In the study, an optical design process was suggested to minimize lateral drifts in the concentration factor variation of LFR. By deploying analytical and raytracing methods, authors in [81, 82] analysed the Concentration characteristics of LFR with flat vertical, flat horizontal and tubular receivers. The analytical approach resulted in a uniform distribution at the centre position while the ray-tracing method produced peak illumination at the centre combined with a decrease of illumination away from the centre.

The study presented a broad theory of LFR optics, including a demonstration of how to evaluate the distortion of the reflected rays as mirrors rotate for tracking the sun. This demonstration was also useful in determining the width of the mirror in order to reduce the lateral drift of the reflected rays to a value that corresponded to the receiver's width. It's worth noting that each mirror's rotation axis must be aligned with its reflecting surface, a requirement that must be met by the mechanical nature of the mirror supporting structure. The study thus, developed an optical design process based on this principle to minimise the variance of the concentration factor during the day.



The optimization of secondary reflectors has been broadly studied by Canavarro, Chaves [83], [84] and Zhu [85]. Their findings proposed an elliptical secondary reflector as a low-cost option to attain high concentration ratios. Prasad, Reddy [79] performed an optical investigation by testing various cavities with the aim of achieving a relatively uniform heat flux distribution on the absorber tube boundary. Balaji, Reddy [53] compared parabolic and involute geometry for the secondary reflector shape and confirmed that the former is more beneficial than the latter. In order to maintain uniform flux distribution across the length of the tube absorber, Grena and Tarquini [68] examined the deployment of two parabolic wings as a secondary reflector. Lin, Sumathy [50] proposed a V-shaped cavity receiver that can attain an optimal temperature of 120 °C while the stagnation temperature is close to 260 °C.

#### 2.2.4.4. LFR power plants

**Kimberlina (USA):** Kimberlina, located in California, is the first Compact Linear Fresnel Reflectors (CLFR) project in North America, with a capacity of 5 MW built by Areva Solar (previously Ausra) [13]. The technical characteristics of the Kimberlina power plant are mentioned in Table 2.4. One group of Fresnel reflectors in this power plant is made up of 13 flat, narrow Fresnel reflectors. This CLFR technology deploys a receiver assembly that includes multiple large-diameter receiver tubes (Figure 2.26) [86].



**Figure 2.26:** Areva Solar’s compact linear Fresnel reflectors at the Kimberlina power station (up to 482°C) in California with multiple tube receiver with simple trapezoidal secondary reflector [86]

Each reflector is capable of tracking and focusing sunlight onto the receiver mounted above the reflectors. Irradiation from the sun that is concentrated passes heat to water, allowing it to evaporate. This power station was observed to generate steam at temperatures up to 482°C [44] through a direct-steam generation system that was used to produce electricity. Areva Solar has commenced the development of large-scale plant construction projects worldwide [13].

**Table 2.4:** Technical characteristics of Kimberlina (Left) and Puerto Errado 1 power plants (Right) [A14]

Name	Kimberlina Solar thermal power plant	Name	Puerto Errado 1 Thermosolar Power plant
Location	Bakersfield/CA	Location	Calasparra, Spain
Lat/long location	35°34'0.0"N, 119°11'39.1"W	Lat/long location	38°16'42.28"N, 1°36'1.01"W
Capacity	5 MW	Capacity	1.4 MW
Land area	12 acres	Land area	7 ha
No of line	3	No of line	2
Line length	385 m	Line length	806 m
Mirrors width in line	2 m	Mirrors width in line	16 m
No of mirrors across line	10	Collector manufacture	Novatec Solar Espana S.L (Nova-1)
Collector manufacture	Ausra	Heat Transfer fluid type	Water
Receiver type	Non-Evacuated	Solar field inlet temperature	140°C
Receiver length	385 m	Solar field outlet temperature	270°C
Heat Transfer fluid type	Water	Power cycle pressure	55 bar
Power cycle pressure	40 bar		

**Puerto Errado 1 and Puerto Errado 2:** The 1.4 MW Puerto Errado 1 and 30 MW Puerto Errado 2 power plants are located in Calasparra, Spain. Table 2.5 (right) presents the technical requirements for the Puerto Errado 1. Since April 2009, this CSP plant has been operational [86]. There are also two rows of Fresnel reflectors, each of which is 806 m long, and the technique for generating steam is that direct sun irradiation is directed toward the linear receiver, which is positioned at the height of 7.40 m above the ground.



**Figure 2.27:** Novatec's linear Fresnel collector solar fields at the PE1 (Nova1) and PE2 (SuperNova) power stations (up to 520°C) [86]

The plant consists of a direct steam generation system without large-scale thermal storage embedded. The most recent designed SuperNova collector loop uses vacuum receiver tubes with a secondary reflector and has generated steam at temperatures up to 520 °C. The reliability of the receiver tubes and optical performance determines whether the Novatec collectors can achieve even higher temperatures [13].

Furthermore, A coal-based thermal power plant was combined with a CSP plant in Lake Liddell, New South Wales, Australia, using Fresnel reflectors. As a result, an offset of 4000

tonnes of CO<sub>2</sub> from the use of coal to generate electricity is achieved annually [86]. SkyFuel's DOE-funded linear Fresnel development has made efforts to develop high-temperature molten salt linear Fresnel collectors with baseload storage via their ReflecTech reflective film technology. The linear Fresnel design can generate temperatures up to 500 °C using molten salt as the heat transfer fluid for the solar field and storage systems. In addition, the technology was designed to use large-diameter receiver tubes. However, this turned out to be a major concern given the unavailability of such tubes.

#### **2.2.5. Parabolic trough collectors**

PTCs concentrate direct solar beams onto a focal line on the reflector axis. A fluid carrying receiver tube absorbs the solar energy impinging on the surface of the tube and raises its enthalpy installed in this focal line. The receiver constitutes a black metal (absorber) tube, concealed in a glass tube, placed along the focal line of the receiver to minimize heat losses [7]. It is sufficient to use a single-axis tracking of the sun, thus producing long collector modules. Large collector fields supply the thermal energy, which is used to drive a steam turbine, which, on its part, integrates an electric generator.

The applications of PTCs can be viewed from two categories. The most significant and primary application of such a system is its deployment in concentrating solar power (CSP). Presently, there are various commercial plants for such applications that have been tested under real operating conditions. PTCs can effectively generate heat at temperatures between 50 and 400 °C. The technology is among the most mature solar technology to produce heat at temperatures up to 400 °C for solar thermal electricity generation or process heat applications [87]. Nevertheless, the use of an oil-based heat transfer process restricts operating temperatures today to 400 °C, resulting in only modest steam qualities [88].

The other form of PTCs application requires between 100 and 250 °C operating temperatures. A typical application of such temperature range can be found in industrial process heat (IPH) low-temperature heat demand with high consumption rates (space heating, domestic hot water (DHW), and swimming pool heating) and heat application for refrigeration and cooling [7]. Most of the facilities are located in the United States and Spain, although some have recently been built in other countries. There are also some projects and facilities for other applications such as detoxification, desalination and Pumping irrigation water [7].

### 2.2.5.1. PTC solar field configuration

A parabolic trough collector (PTC) comprises a parabolic collector plate, a receiver assembly comprising an absorber (working fluid chamber), and a concentric transparent cover. The absorber is fixed permanently at the focus of the parabolic collector. The concentric transparent cover is used to minimize losses of the absorber tube, and hence a vacuum pressure is maintained [5]. A rigid frame supports the parabolic concentrator, and the solar tracking device is fixed on the rigid frame for single-axis tracking of the sun by the parabolic concentrator. Figure 2.28 shows the schematic diagram of PTC.

Collector field apertures are usually within the range of 6 m, with about 100 to 150 m in length and concentration factors are between 20 and 30. Such a system can generate up to 300 to 400 °C [5]. PTCs concentrating solar power systems are best coupled with steam power systems, both direct and indirection generating systems. A well-known example of such design is the SEGS plants in the United States. Also, quite a number of such plants are presently under development or construction worldwide [5].

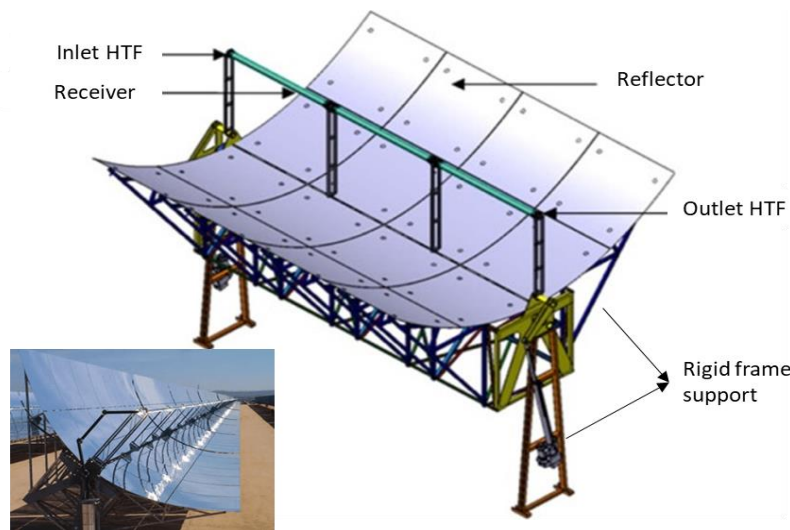


**Figure 2.28:** General view of the Parabolic Trough Collector [89].

PTC solar field orientation can either be in a north-south direction, configured for east-west tracking of the sun [90] or vice versa. Large collector fields supply the thermal energy, which is used to drive a steam turbine, which, on its part, integrates an electric generator. Compared to the east-west, the total annual energy collected by a north-south parabolic trough solar field is slightly higher. However, such an amount of energy is attainable during the summer period, and much less is recorded in winter. The east-west field orientation offers more energy in the winter than a north-south field and less in summer, providing a more constant annual output.

Therefore, the preference of orientation relies on the intended application and whether more energy is required during summer or during winter. PTCs can only concentrate direct solar direction, referred to as beam radiation or Direct Normal Irradiance (DNI) [7]. This is the portion of sun rays in the atmosphere that reaches the Earth's surface as a parallel beam and is not strayed by fumes, dust, or clouds.

### 2.2.5.2. PTC Geometry and Optical Analysis

The collector, the parabolic trough, is a trough with a cross-section that resembles a segment of a parabola (Eq 2.22). It is a symmetrical segment of a parabola around its vertex, to be precise. They have a focal line that is made up of the focal points of parabolic cross-sections. Radiation entering in a plane parallel to the optical plane is mirrored in a way that allows it to pass through the focal line [20], see Figure 2.29.

$$y = \frac{1}{4f}x^2 \quad (2.22)$$

where  $f$  is the focal length, i.e. the distance between the vertex of the parabola and the focal point

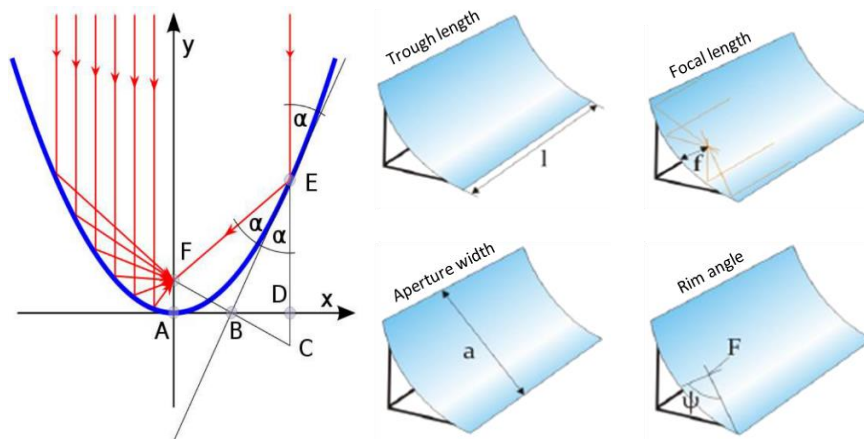


**Figure 2.29:** Path of parallel rays at a parabolic mirror (Left) and Geometrical parabolic trough parameters [20]

The parabola, the segment of the parabola hidden by the mirrors, and the length of the trough must all be calculated in order to geometrically define a parabolic trough. Trough length, focal length, aperture width (the distance between one rim and the other), and rim angle (the angle between the optical axis and the line between the focal point and the mirror rim) are the four parameters most widely used to describe the shape and scale of a parabolic trough (Figure 2.30).



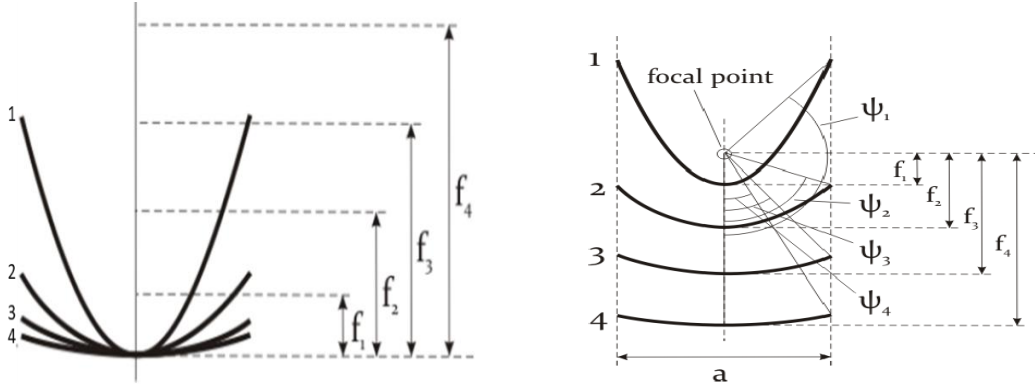


**Figure 2.30:** Focal length as shape parameter (Left) and Relation between the focal length and the rim angle for a constant trough aperture width (Right) [20]

The focal length of a parabola, or the distance between the focal point and the vertex, is a parameter that fully defines the parabola (in the stated mathematical expression of a parabola,  $y = \frac{1}{4f}x^2$ , the focal length  $f$  is the lone parameter).

The rim angle is an important parameter such that it determines the shape of the cross-section of the parabolic trough. This implies that the cross-section of a parabolic trough with the same rim angle are geometrically similar. To fully analyse the cross-section of a parabolic trough, i.e. size and shape, two of the three parameters, focal length, aperture width, and the rim angle, are sufficient. This implies that two of the parameters are sufficient to obtain the third one. Angle  $\psi$  can be expressed as a function of the aperture width to the focal length.

$$\tan \psi = \frac{\frac{a}{f}}{2 - \frac{1}{8}\left(\frac{a}{f}\right)^2} \quad (2.23)$$

Next to that, another important parameter to measure is the surface area, i.e. the aperture area and area of the trough collector. At a given DNI and suns potion, these parameters determine the radiation capture. The aperture area  $A_{ap}$  is calculated as the product of the aperture width  $a$  and the collector length:

$$A_{ap} = a \cdot l \quad (2.24)$$

The surface area of a parabolic trough can be crucial in deciding the trough's material requirements. The following formula is used to measure the area:

$$A = \left( \frac{a}{2} \sqrt{1 + \frac{a^2}{16f^2}} + 2f \cdot \ln \left( \frac{a}{4f} + \sqrt{1 + \frac{a^2}{16f^2}} \right) \right) \cdot l \quad (2.25)$$

Mohammad, Al-Kayiem [91] consider a conventional power plant with trough collectors in order to provide mathematical modelling for evaluating the thermal efficiency of a parabolic trough power plant. The following equations (Eq. 2.26 – 2.28) are used to measure the amount of energy gained in the trough collector [86]:

$$Q_{gain} = m_{cl}(h_7 - h_6)\eta I A_p \quad (2.26)$$

$$\eta = \eta_o U_L \left( \frac{\Delta T}{l} \right) \quad (2.27)$$

$$\Delta T = T_m - T_a \quad (2.28)$$

where  $m_{cl}$  denotes the mass flow rate of the working fluid moving through the trough collector,  $I$  denotes Direct Normal Irradiance,  $A_p$  denotes the collector's aperture field,  $T_m$  denotes the average temperature between the collector's inlet and outlet ( $T_m = (T_6 + T_{a7})/2$ ),  $T_a$  denotes the ambient temperature, and  $U_L$  denotes the loss coefficient [86].

The sum of solar energy fed into the trough system, the work of the steam turbine, the total work of the cycle, and the total performance of the new power plant are determined as follows [86]:

$$Q_{solar} = m_{cl}(h_7 - h_6) + m(h_1 - h_9) \quad (2.29)$$

$$W_{st} = \dot{m}(h_1 - h_2) \quad (2.30)$$

$$W_{cycle} = W_{st} - \Sigma W_{pumps} \quad (2.31)$$

$$\eta_{tot} = \left( \frac{W_{cycle}}{Q_{solar}} \right) \quad (2.32)$$

Several researchers have studied the design performance of PTC with particular emphasis given to its parabolic concentrators and structures. Geyer, Lüpfert [92] built two high-performance PTC (Eurotrough 100 and Eurotrough 150) with an optical concentration ratio of 82:1 and an operating temperature of over 500 °C. They also implemented a wind channel and used Finite Element Analysis (FEA) to evaluate the collector's geometrical structure, and finding from the study shows up to 20% higher efficiency of an additional thermal annual output. A study in [5] on the reflector plates of PTC revealed that the main challenge associated with PT is the collector self-weight.

The solar tracking system is one of the key components used to enhance the efficiency of PTC. The solar tracking device enables the PTC to track the movement of the sun all through the day

for the concentration of solar radiation. Jebasingh and Herbert [5] analysed the thermal efficiency of a dual-axis sun tracking PTC system and confirmed a 48% improvement in thermal efficiency compared to a PTC configured with a fixed or single-axis tracking system

### 2.2.5.3. PTC receiver configuration

Receivers for parabolic trough power plants are responsible for converting the radiation impinging on them into heat and conveying it to HTF that flows to the power block. High radiation absorption and low heat losses are critical. The heat expansion of the receiver due to temperature changes between the operating and non-operating states is a constructive challenge. It is also worth noting that the receivers in a parabolic trough power plant are movable components that necessitate versatile pipe connections.

Several geometrical and physical specifications must be met by the receiver. The reflected radiation must strike the absorber surface, posing geometric challenges. The radiation, if possible, must be fully transformed to heat, and the optical and thermal losses at the receiver components' surfaces must be kept to a minimum. To achieve this, special coatings and thermal insulation measures are used.

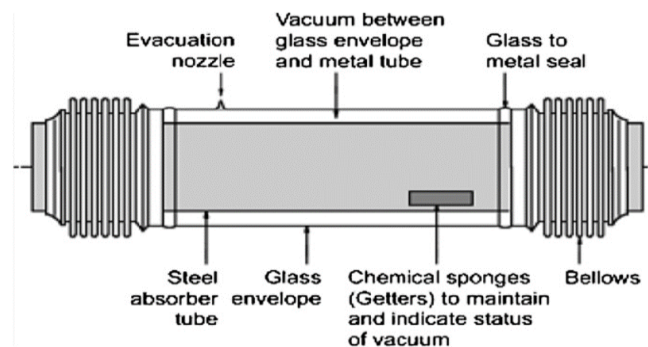


**Figure 2.31:** Schematic of a typical parabolic trough receiver [93]

The main components of the PTC receiver are the absorber tube and the glass envelope. The receiver, also known as the heat collector part (HCE), shown in Figure 2.31, is enclosed in a glass envelope, with air or vacuum between them to minimise convective heat losses and allow for thermal expansion. A selective material with high solar irradiation absorbance and low thermal remittance is coated on the metal tube. The glass-metal seal is important for minimising heat loss due to convection and radiation [94].

The receiver must be designed in such a way that it achieves high radiation absorption and low thermal losses. Low radiative, convective, and conductive losses are all examples of low thermal losses. In order to achieve this, its absorptance must be high in the visible light range,



and its emissivity must be low in the infrared range. The absorber tubes' selective coatings are made of cermet, a substance of metallic nanoparticles embedded in a ceramic matrix.

The absorber tube must have an adequate diameter to allow a high intercept factor. The intercept factor is the proportion of total reflected radiation to that which hits the absorber surface. However, in order to keep thermal losses low, the absorber diameter should not be too large. A larger diameter absorber tube has a larger surface area per metre and hence loses more heat than a smaller diameter absorber tube. For solar radiation, the glass tubes, which are made of borosilicate glass, should have a transmittance of at least 0.96. The glass sheath has a special anti-reflective coating that ensures low reflectivity. According to ARCHIMEDE, this coating increases transmittance by 0.04 per cent (from 0.92 without coating to the mentioned 0.96 with coating) [20].

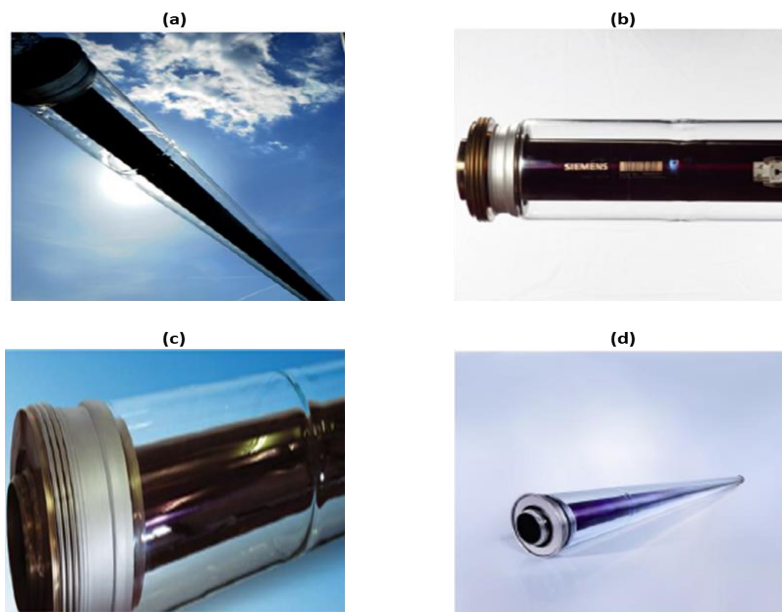


**Figure 2.32:** Absorber tube integrated in a parabolic trough collector (a), Siemens UVAC 2010 (b), Archimede HEMS08 (c), Schott PTR 70 (d) [20]

The German Schott AG, the Italian ARCHIMEDE Solar Energy (ASE), and the German Siemens AG, which acquired the Israeli company Solel Solar Systems, which had developed a receiver, are the frontrunners in the development of parabolic trough power plant receivers [20]. Thermo oil is used as a heat transfer fluid in Schott and Siemens receivers. As a result, the receivers are made to work at a temperature of 400 °C. The first direct steam generation plants also used Siemens receivers. ARCHIMEDE, on the other hand, devised a heat transfer fluid receiver for molten salt. It is planned to operate at a maximum temperature of 580 °C [95].

The optical efficiency improvement can only be achieved taking into account the reflection, transmission and absorption properties of the receiver. Several optimization studies have been performed with the aim of improving the heat transfer rate of absorber tubes adopting key variables such as length, height, diameter and heat transfer fluid, and flux and intensity of incident radiation. A one-dimensional heat transfer analysis on parabolic trough solar receiver was conducted in [96] outcome of the study shows that a 48% reduction of heat loss was recorded, which greatly improved performances of the system [5].

Heat transfer performance on the absorber tube of PTC has been studied considering synthetic thermal oil as working fluid and applying unilateral longitudinal vortex, which shows minimized thermal losses of 2.23–13.62% [97]. Kalogirou [90] discussed the performance analysis by considering parameters such as optical efficiency, concentration ratio and concentrated flux density for the absorber. The study shows that absorber tubes designed using metal pipe and better coating across the absorber enhance solar absorption ability and low emittance coefficient. This eventually results in minimised thermal losses and improved thermal efficiency.

#### **2.2.5.4. PTC power plants**

According to the findings, there are 20 operating parabolic power plants in the world, 11 of which are in Spain, 2 in Iran, 5 in the United States, and one in Italy and Morocco. A total of 27 parabolic trough power plants have been built around the world. Some key plants installed in Spain include 150 MW in Solnova, 100 MW in Andasol Solar Power Station, and the 50 MW in Ibersol Ciudad Real. Similarly, in the USA, the 354 MW by the Solar Energy Generating Systems, Martin Next Generation Solar Center, with a capacity of 75 MW, Nevada Solar One, with a capacity of 64 MW, are the main PTC plants. In addition, there is one active plant in Morocco with a 20 MW capacity. The capacity of the plant in Italy is equal to 5 MW [5].

**Andasol:** The “AndaSol” solar power plant is located in the Marquesado del Zenete, a large valley in Andalusia, Spain, and uses a parabolic trough collector and a molten-salt thermal storage device to generate electricity from solar. The 50 MW AndaSol project will be able to meet the demand for electricity after sunset, thanks to its thermal storage system. The solar resources in the Marquesado del Zenete will only allow for around 2,000 annual equivalent full-load hours without thermal storage. However, improvement in the annual equivalent full-load hours to 3,589 can be realised with the thermal storage system. This is the key to lowering

production costs because it allows the power block to work better and the service and maintenance workers to be more productive. Picture of the plant and design are shown in Figure 2.33.

The Andasol project has one of the strongest direct solar radiation opportunities in Spain due to its altitude of 900-1,100 m. The collectors are made up of 90 kilometres of absorption pipes and curved mirrors in each power station unit. Each plant has 312 collector rows and can produce 50 MW. There are 28 mirrors and three absorption pipes in a collector. The construction of Andasol 1 commenced in July 2006, and the plant became operational in March 2009. The plant is developed and promoted by the Spanish ACS Cobra Group as the lead and the German Solar Millennium Group, the minority shareholder.

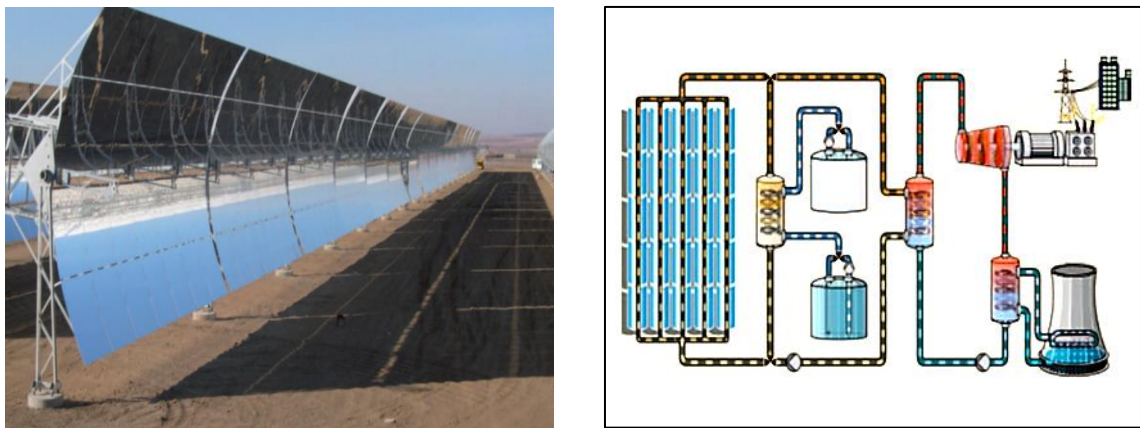


**Figure 2.33:** Photo of the Andasol” solar power plant, Marquesado del Zenete (Left) and Simplified flow diagram (Right) [95]

The plant's trough-shaped mirrors focus the radiations onto a pipe in the collector's centre. The radiations heat the fluid in the pipe, which then generates steam in the power block through a heat exchanger. As in traditional power plants, the steam generated is used to drive the turbine. Turbines power the generators that generate electricity. Direct steam processing and molten salt heating in absorber tubes improve performance and lower power production costs. The collectors' orientation is carried out automatically via the control room of the power station [95].

#### 2.2.6. Parabolic dish collectors (PDC)

A Parabolic Dish Collector is a point-focus CSP system (Figure 2.34). The sun's rays are focused at a focal point propped above the dish's centre while the dish and receiver both track the sun in azimuth and elevation. At the focal point of most dishes, there is an independent engine/generator (such as a Stirling system or a micro-turbine) [9]. The dish structure must

fully track the sun to focus the beam into the thermal receiver. A heat transfer fluid and cooling water are not required with this design [98].

The highest solar-to-electric conversion efficiency of any CSP system is achieved by parabolic dishes. Parabolic dishes compete with PV modules, especially concentrating photovoltaics (CPV), as well as other CSP technologies, due to a number of factors, including their small size, the possibility of hybridization [99]. The exception is very large dishes that have been proven compliant with thermal storage and fuel backup. Dishes, according to proponents, would be able to cope with larger solar thermal systems due to mass production [99].

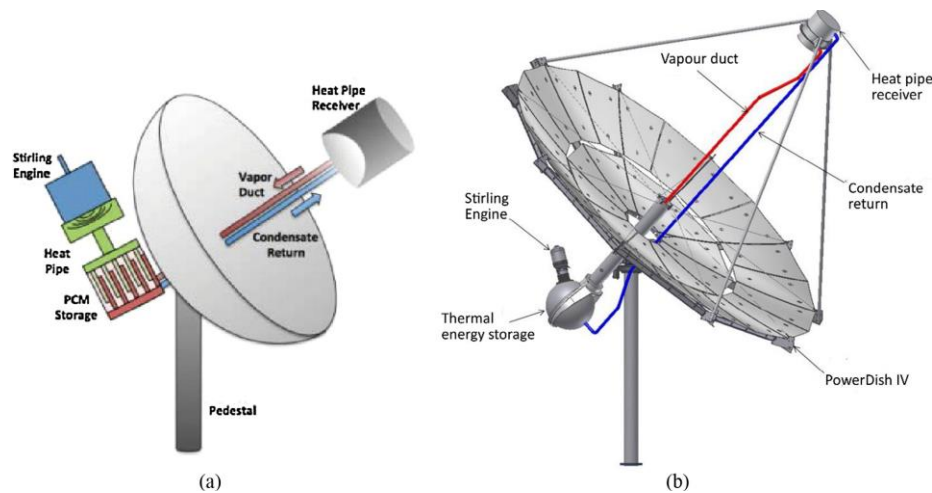


**Figure 2.34:** Dish mounted PCM storage system for the Stirling power cycle (a) Sandia and (b) Infinia [100, 101]

Since parabolic dishes are limited in size (typically tens of kW or less) and generate electricity independently, a large-scale plant will need hundreds or thousands of them to be co-located. Other CSP designs, on the other hand, may have capacities ranging from 1 MW to hundreds of megawatts. The optimal size of troughs, LFRs, and towers, which range from 100 MW to 250 MW, is determined by the power block's performance.

Parabolic dishes have several important advantages, including emerging as the most efficient of all collector systems since they always point to the sun and generate high temperatures. They are highly efficient at thermal-energy absorption and power conversion systems, achieving a concentration ratio in the range of 600–2000 and having modular collector and receiver units that can either function independently or integrated with a larger system of dishes. Also, open water circuit is not needed for the operation of dish/engine systems. This is a significant advantage over systems based on the Rankine cycle, particularly if they have wet cooling systems [102].

Thermal storage solutions generally are not available for PDC. Some other CSP systems have a significant benefit over PV in that they can incorporate thermal storage. Hybridization, on the other hand, is a viable option for delivering power on demand. In addition, PDCs are still in their pilot and demonstration stages, and electricity generation costs (€/kWh) and investment costs (€/kW) are higher than the large-scale central receiver or parabolic trough power plants. Compared to the PV systems, the PDC, like any other CSP system, has moveable parts and uses only direct normal radiation [102].

#### **2.2.6.1. PDC solar field configuration**

A parabolic collector, receiver, heat engine (Stirling engine, micro gas turbine), and generator are the main components of a solar dish/engine system. Solar dish systems are power conversion units that use direct radiation to generate electricity, much like any other CSP system. The paraboloid collector and a heat engine (Stirling engine or micro gas turbine) attached directly to a receiver in the paraboloid mirror's focal point are their distinguishing features.

Parabolic-dish systems that produce electricity using a central power converter collect the absorbed sunlight from individual receivers and channel it through a heat-transfer fluid to the power-conversion systems. The thermal receivers are heat pipes in which the boiling and condensing of an intermediate fluid are deployed to transfer the heat to the engine. The heat engine system takes the heat from the thermal receiver and uses it to generate electricity. The requirement to circulate heat transfer fluid throughout the collector field creates design challenges such as pumping requirements, piping layout, and thermal losses [103].

The most important application of this type of concentrator is for parabolic dish-engine systems. A parabolic dish-engine system constitutes electric generators placed at the focal point of each dish to generate energy in the form of electricity rather than as heated fluid. The power conversion component incorporates the thermal receiver and the heat engine. The thermal receiver absorbs the impinging beam of solar energy, transforms it to heat, and transfers the heat to the heat engine. Hydrogen or helium are the most preferred heat transfer medium generally employed as the working fluid for an engine.

This distributed parabolic dish system does not have thermal storage capabilities but can be designed to run on fossil fuel during periods without sunshine. The Stirling engine is the most preferred type of heat engine employed in dish-engine systems. Concentrating photovoltaics

and microturbines [104] are alternative power conversion unit technologies that are proposed for future applications.

### 2.2.6.2. PDC geometry and optical analysis

Parabolic dish systems, like the trough collectors, adopt the geometric properties of parabola, but as a three-dimensional paraboloid, as shown in Figure 2.35. The parabolic dish is a point focusing system; hence, impinging solar radiation is concentrated to a common focal point of the receiver, which can generate heat to an operating temperature of over 1000 °C, similar to the central receiver tower.

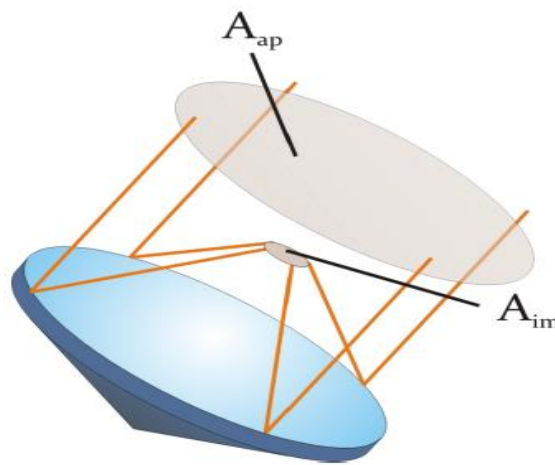


**Figure 2.35:** Geometrical concentration of parabolic dish [102]

The concentration ratio, like any other concentrating device, is one of the collector's most important parameters. It determines the Stirling engine's potential operating temperatures. The concentration ratio  $C$  is defined as the ratio of the radiant flux density in the focal spot or the Sun image,  $G_{im}$ , to the direct irradiance on the collector's aperture,  $G_{b,ap}$ .  $C$  is the ratio of the radiant flux density at the focal spot to the direct normal irradiance since the direct irradiance at the collector aperture is just the direct normal irradiance: [102].

$$C = \frac{G_{im}}{G_{b,ap}} = \frac{G_{im}}{DNI} \quad (2.33)$$

The geometrical concentration ratio can be used to calculate a mean concentration ratio, which is a useful approximation. The  $C_G$  is the ratio of the (projected) collector aperture area  $A_{ap}$  to the focal spot area, i.e. the area of the Sun image  $A_{im}$  or the receiver aperture area (assuming the receiver aperture is the same size as the Sun image):

$$C_G = \frac{A_{ap}}{A_{im}} \quad (2.34)$$



A solar dish, as previously said, is shaped like a paraboloid or a near approximation of one. The geometrical figure of a paraboloid has infinite dimensions, but a paraboloid mirror only covers a part of it. The aperture area, the aperture diameter, or the rim angle, which is the angle between the optical axis and the line between the focal point and the mirror rim, can be used to define the dimension of the section the paraboloid mirror covers. The rim angle is sufficient to determine the collector shape completely.

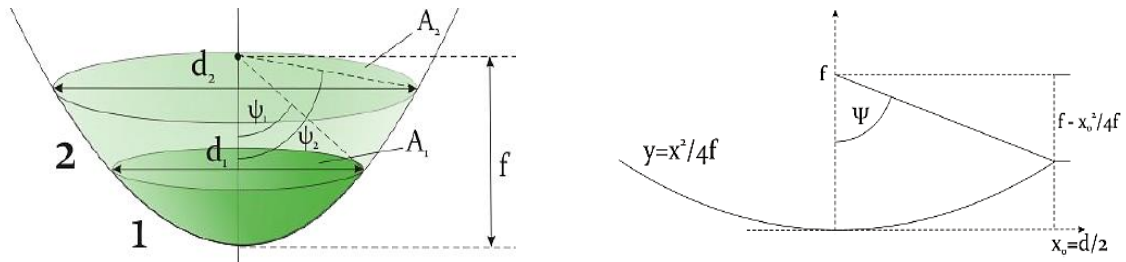


**Figure 2.36:** Geometrical dish parameters and representation of the rim angle in a cross-section of a paraboloid [102]

The ratio of the aperture diameter to the focal length is proportional to the rim angle (or to the ratio of the focal length to the aperture diameter). The algebraic representation of the parabola in Figure 2.36 is  $y = \frac{x^2}{4f}$ , so the following relationship can be used:

$$\tan \psi = \frac{x_0}{f - \frac{x_0^2}{4f}} \quad (2.35)$$

Eq. (2.35) can be translated into (2.36) by considering that  $2x = d$  with  $d$  being the collector's aperture diameter.

$$\tan \psi = \frac{\frac{d}{f}}{2 - \frac{1}{8} \left( \frac{d}{f} \right)^2} \quad (2.36)$$

That denotes the relationship between the rim angle and the aperture diameter/focal length ratio. To express the  $d$ - $f$  ratio as a function of the rim angle, Eq. (2.36) is transformed as follows:

$$\frac{d}{f} = \frac{4}{\tan \psi} + \sqrt{\frac{16}{\tan^2 \psi}} = 16 \quad (2.37)$$

In an energy review of a solar parabolic dish power plant in [86], the model was focused on calculating the thermal losses from solar energy input. Conduction, convection, and radiation are three heat transfer processes that can waste thermal energy. Since the absorber tube's

thickness is so small and has such a high thermal conductivity, conduction heat transfer is neglected. As a result, the usable heat at a solar dish collector's absorber tube is measured as follows.

$$\dot{Q}_{useful} = \dot{Q}_{solar} - \dot{Q}_{loss,externalconv} - \dot{Q}_{loss,internalconv} - \dot{Q}_{loss,rad} \quad (2.38)$$

An energy balance for the flowing working fluid in the solar dish collector can be written as follows to determine the amount of useful acquired heat:

$$Q_{useful} = \dot{m}C_p(T_{out} - T_{in}) \quad (2.39)$$

The following is a formula for calculating the amount of loss caused by external and internal convection:

$$Q_{gain} = h_{outer}A_{outer}(T_{surr} - T_{fluid}) \quad (2.40)$$

$$Q_{gain} = h_{inner}A_{outer}(T_{surface} - T_{fluid}) \quad (2.41)$$

The quantity of wasted thermal energy through radiation loss is attained as follows:

$$Q_{loss,radiation} = \varepsilon\sigma A_{outer}(T_{surface}^4 - T_{surr}^4) \quad (2.42)$$

After subtracting losses from useful obtained thermal energy, the total thermal efficiency of a solar dish power plant is determined as follows [86]

$$\eta_{th} = \frac{Q_{useful}}{Q_{solar}} \quad (2.43)$$

A study of solar parabolic dish collector geometry and flux distribution at focal region was performed by Sup, Zainudin [105]. The rim angle is a critical factor in determining the imaging and non-imaging diameters of flux radiation. Deploying a ray-tracing simulation and 2D computer-aided method, the imaging and non-imaging geometry was simulated. The diameter was calculated by tabulating the flux distribution on a coordinated graph. The imaging diameters vary from 17 to 286 millimetres, while the non-imaging diameters range from 23 to 345 millimetres. The imaging and non-imaging diameters due to the reflex rim angle are 37 mm and 53 mm, respectively. The model of the parabola dish in ray-tracing simulation is depicted in Figure 3.37 below.



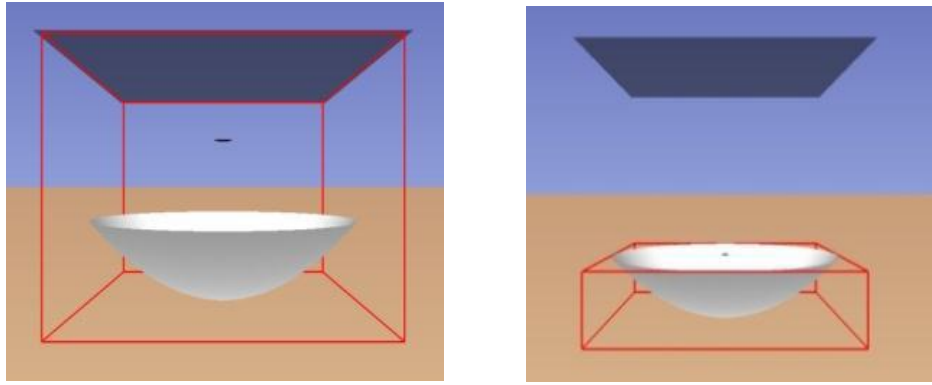


**Figure 2.37:** Model of parabola dish in ray-tracing simulation. (Left) 10 meter diameter; (Right) 20 meter diameter [105]

Findings show that larger imaging and non-imaging diameters result from an acute rim angle. It demonstrates that the optimal parabolic dish parameter is critical for achieving high focus point strength. The solar parabolic dish's optical efficiency and concentration ratio are both affected by the focal region location. For accurate reading and heat collection, choosing the right focus point is critical. Since optical losses from solar radiation reflection are taken into account, the rim angle gives the true value of concentrated radiation.

Malali, Chaturvedi [106] studied the thermodynamics of a regenerative Brayton heat engine cycle with a parabolic-dish solar collector in great detail (Figure 2.38). The thermal efficiency of the coupled device for power generation applications is investigated. The non-dimensional parameters that control the coupled system's optimal output are defined. The performance of the coupled device is measured using three parameters: the Brayton cycle pressure ratio, the parabolic dish collector concentration ratio, and the Brayton cycle maximum temperature ratio. The efficiency of the coupled system is then optimised in relation to the aforementioned parameters by using a MATLAB programme to solve the resultant system of three coupled non-linear algebraic equations.

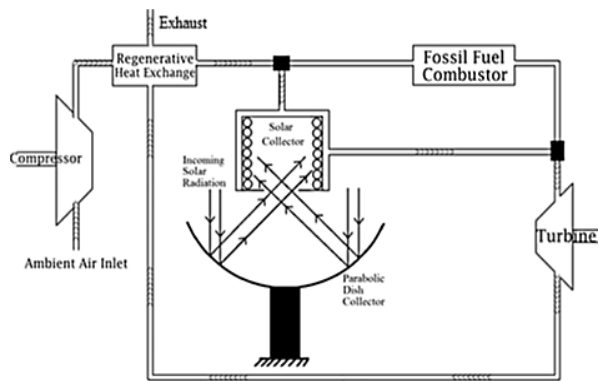


**Figure 2.38:** Schematic of a regenerative Brayton heat engine couple with a two-axis tracking parabolic dish collector [106]

Variations in heat exchanger efficiency, total concentrator error, rim angle, and non-dimensional radiation flux parameters affect the coupled system's optimal performance. The effect of these variables on engine size is also discussed. Lower values of total concentrator error and higher values of heat exchanger efficiency result in higher optimal efficiency of the coupled device, according to the report. It is also observed that when a solar thermal power generation system employs the regenerative Brayton cycle, the optimum efficiency point shifts to lower engine pressure ratio values.

### 2.2.6.3. PDC receiver configuration

The interface between the concentrator and the heat engine in a solar dish system is the receiver. It serves two purposes: first, it absorbs and transforms a significant portion of the radiation reflected by the collector. Second, it passes heat to the heat engine's working gas. High absorption rates and good heat transfer characteristics are thus important specifications for the receiver. Different receivers are needed for Stirling engines and micro gas turbines. The most effective micro gas turbine receivers employ "volumetric absorption," which involves concentrated solar radiation passing through a fused silica quartz window and being absorbed by a porous matrix. Wide heat transfer areas in a small space are provided by honeycombs and reticulated open-cell ceramic foam structures.

Generally, external receivers and cavity receivers are the two types of receiver geometries that can be used for parabolic dish collectors (Figure 2.39). External receivers are generally spherical in shape and absorb radiation from all directions. The radiation passes through an aperture in cavity receivers and faces in only one direction to the vertex of the collector.

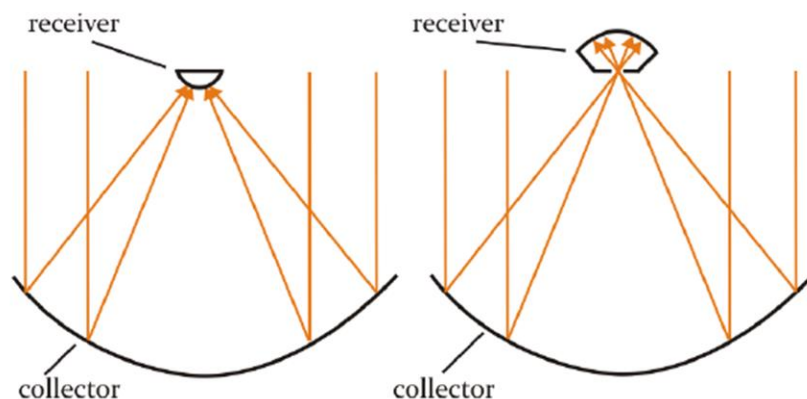


**Figure 2.39:** Schematic representation of an external receiver (left) and a cavity receiver (right) [102]

Collectors with a wide rim angle might be interested in the external receiver. However, at the high operating temperatures of dish systems, heat losses, especially radiative heat losses, at

unprotected external receivers are very high. On the other hand, in a cavity receiver, a large portion of the released radiation stays within the cavity and is absorbed again, resulting in a lower overall radiative heat loss. The cavity's effective absorptance is greater than the inner surface's absorptance. Because of the concave form of the absorber surface, this is possible. Furthermore, convective heat loss at cavity receivers is lower than at unprotected external receivers. Only cavity receivers have been used in dish/Stirling systems to date due to these advantageous properties of cavity receivers. External receivers, on the other hand, have been used in lower-temperature parabolic dish applications.

**Direct Illumination Receivers:** The concentrated radiation heats the Stirling engine's working gas directly in a bundle of thin pipes at direct illumination receivers. In comparison to indirect illumination receivers, it is the simplest type of receiver. Direct illumination receivers are used in the majority of completed systems [107]. An illumination receiver integration in a Stirling engine is shown in Figure 2.40 below.

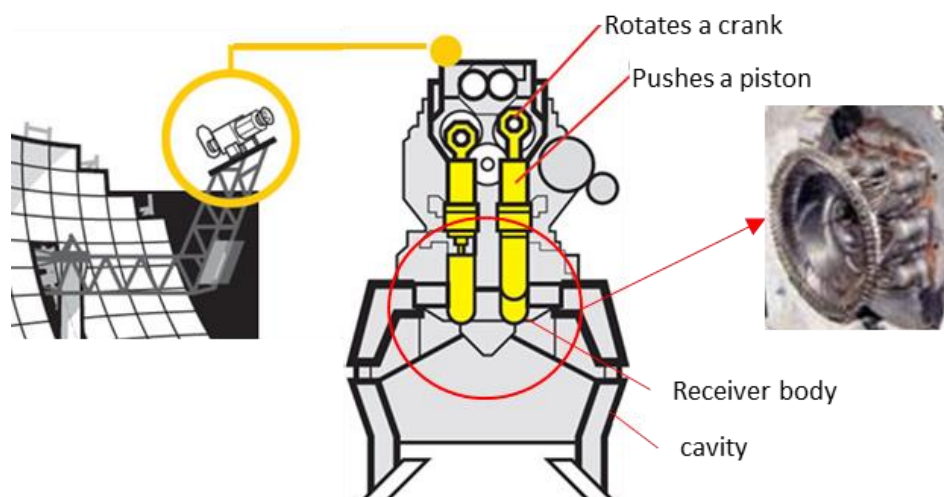


**Figure 2.40:** Direct illumination cavity receivers and their integration into Stirling engines [107, 108]

Other forms of direct illumination receivers consist of tubes that are linked to the engine's working room. The tubes are generally made of a nickel alloy that is heat and corrosion-resistant. The temperature of the receiver is regulated by thermocouples attached to the backside. The illuminated tube sectors reach a maximum temperature of about 900°C. The receiver is positioned about 15 cm behind the concentrator's focal point, reducing the radiation flux. The cavity in front of the receiver tubes is formed by a water-cooled aluminium cylinder. The receiver is thermally isolated on the backside by a ceramics body and a stainless steel shell [109].

**Indirect Illumination Receivers:** The working gas in an indirect illumination receiver (Figure 2.41) is heated indirectly by an intermediate heat transfer fluid. The absorber heats the solvent, which causes it to evaporate. It condenses at the heater tubes that hold the Stirling engine's working gas, releases the condensation heat to the working gas, and then flows back to the absorber through gravity. This type of receiver is also known as a reflux receiver due to the evaporation-condensation cycle. A liquid metal, such as sodium, is usually deployed as the working fluid.

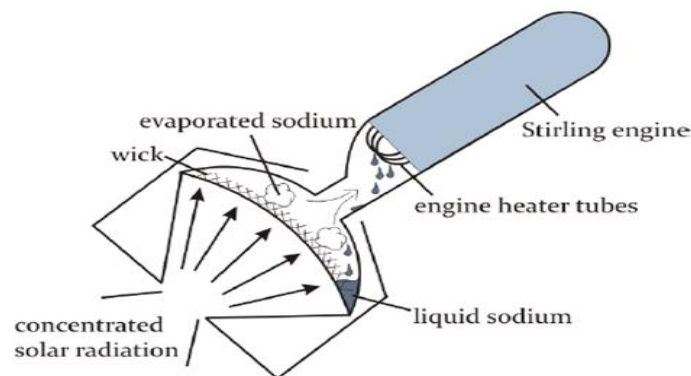


**Figure 2.41:** Indirect illumination receiver [102]

When opposed to direct illumination receivers, indirect illumination receivers have a few advantages. They have the benefit of operating at constant temperatures, while directly illuminated heater tubes can experience significant temperature gradients from front to back and along the tube length, reducing efficiency and limiting life [110]. It also makes nonuniformities in concentrator flux profiles easier to tolerate and equilibrate.

Furthermore, indirect illumination receivers allow for higher heat transfer rates in general. Higher engine performance is possible because of this, as well as smaller variations between receiver peak temperature and engine working gas temperature [110]. The use of an intermediate heat-transfer fluid often decouples the receiver's configuration from the engine's. This allows for the development of more powerful receivers while also optimising the Stirling engine design. Finally, in a hybrid solar/fossil-fuel receiver, adding a gas burner is simpler than in a direct illumination receiver [107].

Karimi, Gheinani [111] developed and proposed a detailed mathematical model for a cylindrical cavity receiver mounted at the focal point of a parabolic dish collector (PDC) device in a study. The model's key approach is focused on the receiver's non-isothermal internal walls. The model was tested using experimental data, and the statistical parameters indicate that the model and experimental data are in good agreement. On the thermal efficiency of the device,

the effect of some operational parameters such as HTF mass flow rate and global solar irradiation strength, as well as some geometrical parameters of the solar receiver such as receiver aperture diameter and length, were investigated. The schematic diagram of parabolic dish collector with cylindrical receiver apparatus is shown in Figure 2.42.

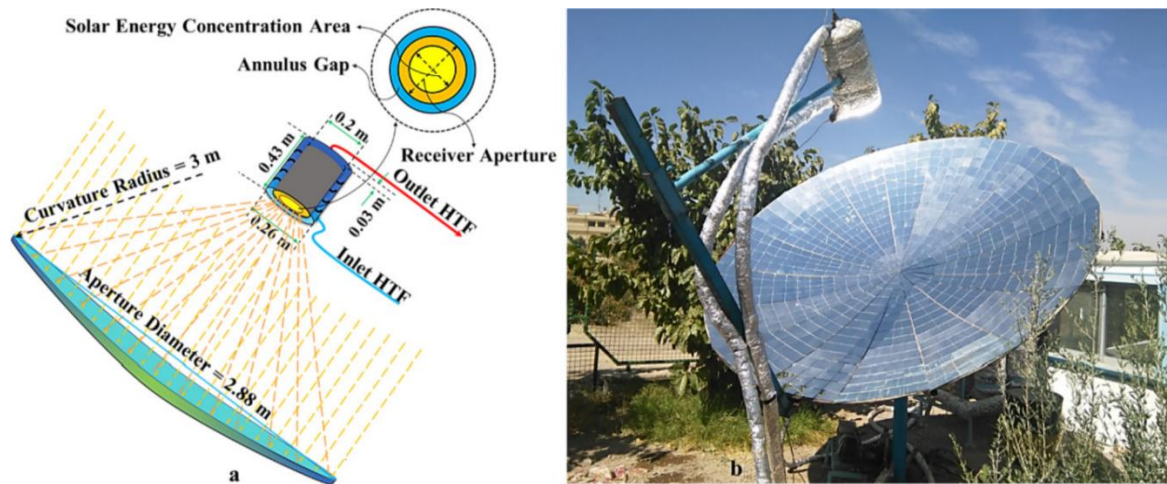


**Figure 2.42:** schematic diagram of parabolic dish collector with cylindrical receiver apparatus (a) and photo of the studied dish with its receiver [111]

The effect of HTF inlet temperature on HTF outlet temperature shows that at constant HTF mass flow speeds, increasing the HTF inlet temperature causes the HTF outlet temperature to rise linearly. The effect of solar irradiation intensity on HTF outlet temperature and receiver thermal efficiency shows that the HTF outlet temperature increases linearly throughout the day, but the receiver thermal efficiency remains constant. The results of analysing the range of 0.01-0.11 kg/s of HTF through the receiver at constant other parameters are shown in Figures 2.43 and 2.44, respectively.

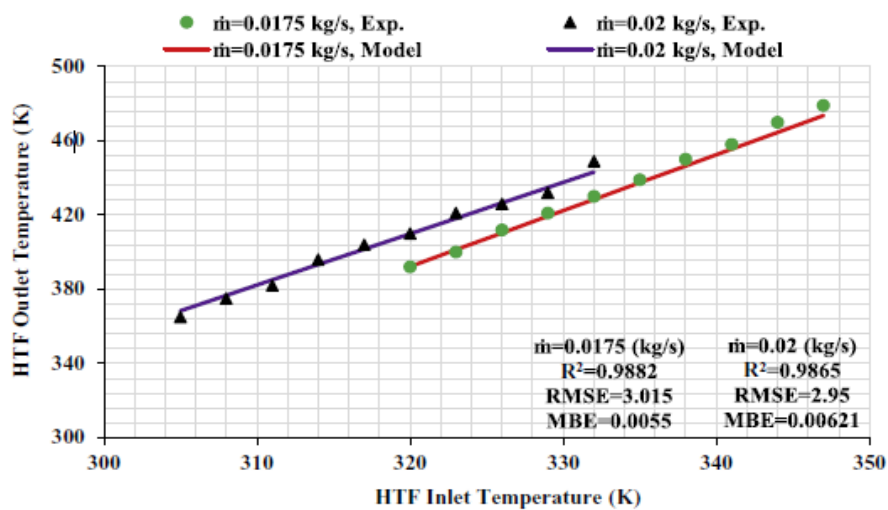


**Figure 2.43:** The effect of HTF inlet temperature on HTF outlet temperature (different ambient air temperatures in range of 296 - 305 K, solar irradiation intensity in range of 600 -1050 W/m<sup>2</sup>, receiver aperture diameter and height of 0.2 and 0.4 m respectively) [111].

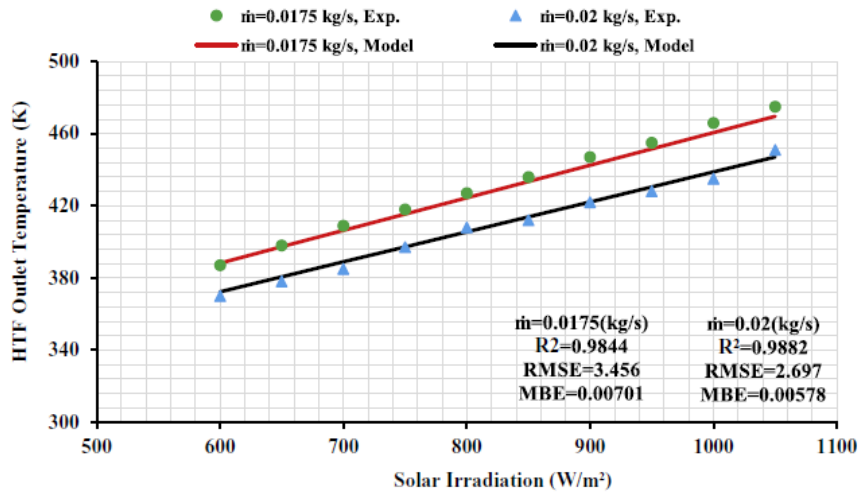


**Figure 2.44:** The effect of solar irradiation intensity on HTF outlet temperature (HTF inlet temperature in range of 309-343 K and different ambient air temperatures in range of 296-305 K, receiver aperture diameter and height of 0.2 and 0.4 m respectively) [111]

Furthermore, the receiver length increases the HTF and thermal efficiency of the receiver dramatically for a range of 0.05 to 0.4 m, but the differences are minor. It can be explained that for a given range of receiver length and constant solar irradiation intensity and HTF mass flow rate, the contact area and solar energy adsorbing surface increase, and as a result, the HTF outlet temperature and receiver thermal efficiency increase. After that, the receiver's ability to gain solar energy reaches its maximum value, and no further improvements were noticed.

A numerical investigation is performed by Kumar and Reddy [112] to examine the natural convective heat loss from three forms of receivers for a fuzzy focal solar dish concentrator, namely cavity receiver, semi-cavity receiver and modified cavity receiver (Figure 2.45).

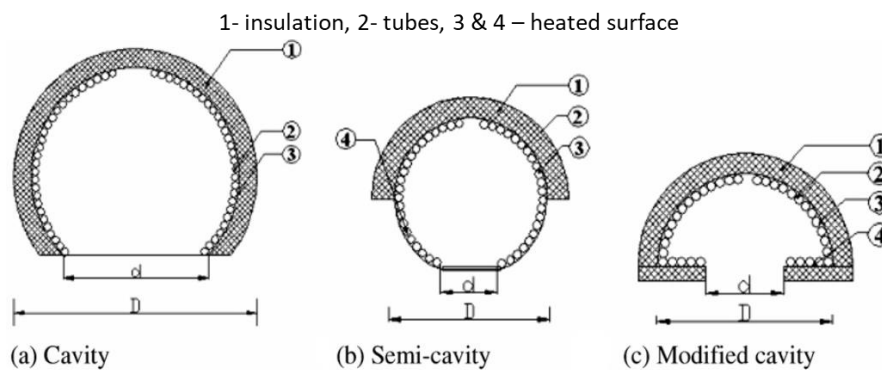


**Figure 2.45:** Enlarged view of different types of receivers. [112]

The natural convection heat loss from the receivers is estimated by varying the inclination from 0 (cavity aperture facing sideways) to 90 (cavity aperture facing down) degrees since the positioning and geometry of the receiver greatly influence the natural convection heat loss. A comparative study is conducted to predict the natural convection heat loss from the cavity,



semi-cavity and modified cavity receivers. Temperature contours for various inclinations from results obtained are depicted in Figure 2.46.

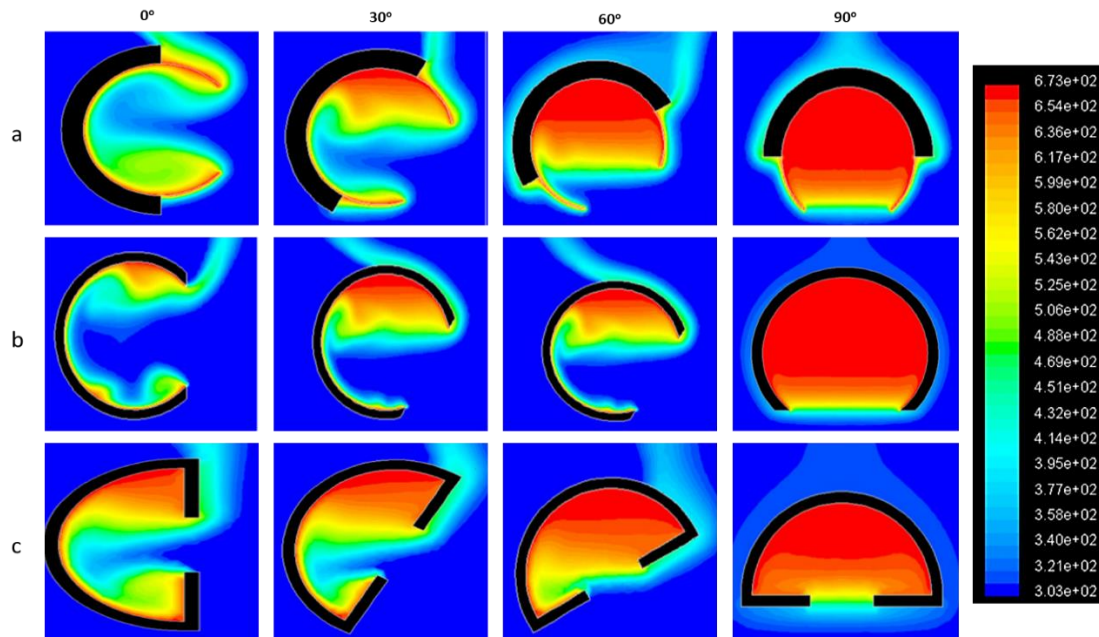


**Figure 2.46:** Temperature contours for various inclinations (a) semi-cavity receiver (b) cavity receiver (c) modified cavity receiver at 400 °C [112]

In all three examples, convection heat loss is substantial at 0 degrees and reduces monotonically as the angle increases up to 90 degrees. The modified cavity receiver's convection heat losses at 0- and 90-degrees inclination are 26.03 percent and 25.42 percent of the cavity receiver's convection heat loss, respectively. For the modified cavity receiver, the effect of area ratio ( $A_w/A_1$ ) on convective heat loss is explored, and an optimum  $A_w/A_1$  of 8 is discovered for minimum natural convection heat loss. The modified cavity receiver is the preferred receiver for a fuzzy focal solar dish collector system, and natural convection at 90 degrees was considered in the current model for accurate total heat determination.

Cherif, Ghomrassi [113] conducted a parametric analysis of a parabolic dish receiver system in order to determine the best configuration for achieving optimal system efficiency. For four receiver tubes and two receiver inlet/outlet configurations: position 1 and position 2, a series of numerical simulations were run. The receiver's inlet/outlet configuration effect is influenced by the receiver's geometric properties, according to the thermal analysis. Position 2 yields the highest thermal efficiency value for the "medium" height cylindrical receiver ( $H = 0.075$  m,  $H = 0.048$  m), while position 1 ensures the highest thermal efficiency value for the "elevated" height cylindrical receiver ( $H = 1.2$  m,  $H = 0.468$  m). Thus, from position 1 to 2, the thermal efficiency increases by 62.6 per cent for the configuration with  $H = 0.075$  m. Furthermore, for

a configuration with  $H = 1.2$  m, moving the location from 1 to 2 reduces thermal efficiency by 53%.

The heat transfer in a square, rectangular open cavity by natural convection has been investigated in several studies. Clausen [114] proposed an analytical model for a large cubical receiver that allowed for the calculation of convective losses from cavity receivers and demonstrated that the energy transmitted by the air through the aperture is primarily due to buoyancy and the wind effect. An analytical model for predicting the optical output of a solar dish concentrator with a cavity receiver was proposed in [115]. The results showed that the receiver radius to focal length ratio ( $r/f$ ) is related to the net heat efficiency and solar to net heat efficiency of the system and that the solar to net heat efficiency is optimum for a certain value of ( $r/f$ ).

A solar dish collector with a modified cavity receiver was investigated by Reddy, Veershetty [116]. They used a computational model to determine how wind characteristics, receiver configuration, and receiver orientation affected receiver heat loss. They suggested a Nusselt number correlation as a function of wind effects to estimate the receiver's combined convection heat losses. Harris and Lenz [117] studied the thermal activity of a solar receiver with a variety of geometric shapes both experimentally and theoretically (cubical, cylindrical, conical and hemispherical). They came to the conclusion that cavity geometry has a minor impact on overall machine performance.

#### **2.2.6.4. PDC power plants**

**Maricopa Solar (USA):** Maricopa solar has a capacity of 1.5 MW located near Peoria, Arizona. It consists of 60 solar dishes, each with a Stirling engine and a 25 kW electrical energy power generator. Moreover, hydrogen is used as a working fluid in this power plant and a four-cylinder Stirling engine and mirrors with silver-plated glass and solar reflectance of 94% [118]. Maricopa Solar's specifications are mentioned in Table 2.5. In addition, sunlight heats hydrogen to 750 °C, and the Stirling engine is cooled by air. Maricopa Solar [118] has demonstrated the generation probabilities of electrical energy and industrial output of electricity. The Maricopa parabolic dish power plant is shown in Figure 2.47.



**Table 2.5:** Technical characteristics of Maricopa power plant [86]

Name	Maricopa Solar
Location	Peoria, AZ
Lat/long location	33°33'31,0"North, 112°13'7,0"West
Capacity	1.5 MW
Land area	15 acres
No of dishes	60
Dish description	Each SunCatcher produces 25 kW of Power
Dish manufacture	Stirling Energy system (SES) (Sun Catcher TM)



**Figure 2.47:** Maricopa parabolic dish power plant (USA) [102]

**Shenandoah project:** The Solar Total Energy Project (STEP) in Shenandoah, Georgia, was a large-scale industrial solar cogeneration project that operated from 1982 to 1991 at a garment factory. General Electric Corporation built and Solar Kinetics, Inc. manufactured the 7 m diameter dish used at Shenandoah. The reflector consisted of 21 die-stamped aluminium gores (or "petal" shaped segments), which were bolted to sheet metal ribs and held together by a steel hub. Prior to shaping the gores, a 3 m acrylic aluminised film was applied to the flat sheet blanks (protected by an opaque film).

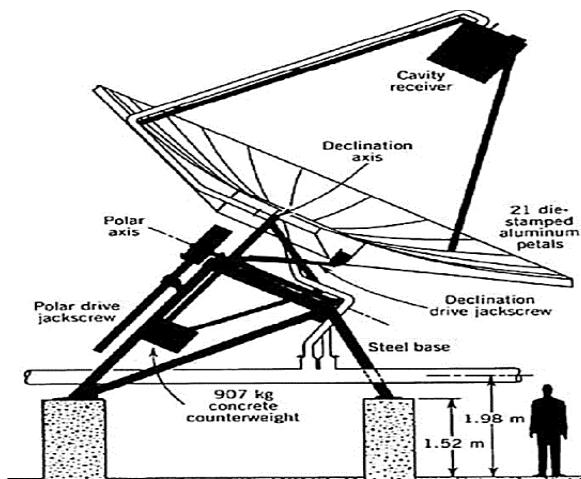


**Figure 2.48:** The Shenandoah dish shown in (a) schematic view and (b) as installed. (Kinoshita, 1983) [119, 120]

The tracking device was supported on a steel tripod frame fixed on concrete piers, with polar and declination axes of rotation. A revolving concrete yoke counter-weighted the reflector frame around the polar axis. The solar field consisted of 114, 7-meter-diameter dishes that generated heat in receivers using a synthetic oil heat transfer fluid in a cavity coil style receiver (Figure 2.48). The Shenandoah receiver was a cavity-type receiver with a heat exchanger made

of stainless steel coils. The oil was heated to 399 degrees Celsius and used to produce steam for a Rankine steam turbine generator, with low-pressure process steam extracted for pressing clothes and powering an absorption chiller. The plant included a thermocline oil tank for continuous operation during short-term solar transients, as well as buffer energy storage.

***The HYPHIRE hybrid solar/fossil fuel power plant:*** The HYPHIRE project was the first to apply the idea of a hybrid solar/fossil fuel power plant to solar dish/Stirling engine technology. A plant like this provides the benefits of continuous efficient operation, even for applications that are not connected to the grid, which could be especially beneficial to small remote communities. The hybrid system also has environmental advantages: when biogas is used, there are no carbon dioxide emissions (CO<sub>2</sub>). The system is intended for commercialization in the Sunbelt area for decentralised power production.

The fluid used in the Stirling engine in the HYPHIRE project's dish/Stirling system is helium, the cold source is ambient air, and the hot source is solar radiation. Any power combination from gas and solar input up to 45 kW (thermal) is transferred without temperature drop using a heat pipe receiver. This second-generation hybrid heat pipe receiver was extensively designed and tested in the lab and in the field. During the test process, the control system was adjusted and improved, resulting in a smooth and efficient operation.

Over a 360-hour cycle, the device was successfully operated in all modes, including solar-only, combustion-only, and solar-and-combustion parallel mode. During cloudy times, the device worked flawlessly. The cost of the first 100 systems was estimated to be € 7,000 per kW, dropping to € 1,600 per kW for a sequence of 10,000 systems per year. Nitrogen oxide (NO<sub>x</sub>) emissions were found to be just below 0.5g/kg fuel, while methane equivalent hydrocarbon emissions were found to be between 0.1 and 1g/kg fuel. One of the last tasks was to reduce carbon monoxide emissions, which were about 5-10g/kg of gasoline. In addition, HYPHIRE looked into the demand for hybridised dish/Stirling units as well as solar radiation sites in Morocco [111].

### **2.2.7. Central receiver systems**

A central receiver tower configuration constitutes an array of heliostats, usually a large mirror field that tracks the movement of the sun in both azimuth and elevation, thereby focussing solar radiation onto a common focal point (receiver) placed at the central top of the tower, as depicted in Figure 2.49. This allows complex high efficient energy transformation at a single large

receiver point [2]. Because very high temperature is generated, Direct Steam Generation or molten salts are used as heat-absorbing medium [11].

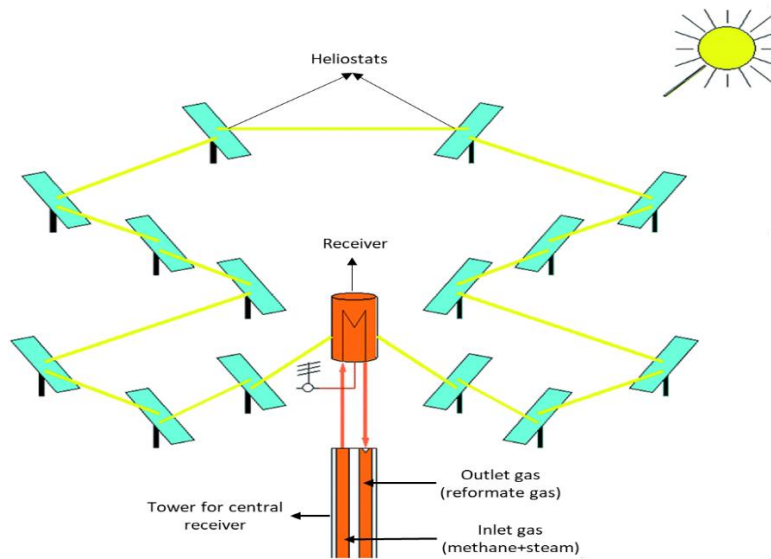


**Figure 2.49:** Schematic of a central receiver system solar field [121]

Since Central Receiver Systems enable several intermediate steps between the integration in a traditional Rankine cycle and the higher exergy cycles using gas turbines at temperatures above  $1300^{\circ}\text{C}$ , they have a significant potential for mid-term cost reduction of electricity generated. This leads to higher efficiencies and greater throughputs. Another option is to deploy Brayton cycle turbines, which need higher temperatures than those employed in the Rankine cycle [122]. Plant sizes of 10 to 200MW are chosen due to economy-of-scale constraints, despite advanced integration schemes claiming economic sense for smaller units as well [122].

In the early 1990s, a combined US/German study found the potential for molten salt and air-cooled facilities [123] and this first generation of commercial plants was intensively studied. Since then, several penetration strategies have been proposed, and many more are likely to be developed in the future, because solar towers have the advantage of allowing for a very open integration design that can be based on dispatching scenarios, annual capacity factors, and hybridization schemes. Molten salt technology, open or closed-loop volumetric air technologies, and saturated steam technology are three of the most promising power tower technologies that are expected to lead to commercial plants [122].

Central receivers have several benefits, such as harnessing solar energy optically and transferring it to a common focal point (receiver), reducing thermal-energy transport requirements. Central receivers can typically achieve concentration ratios of 300 – 1500 and are highly efficient in collecting energy and converting it to electricity. Next to that, they are quite

large (generally more than 10 MW) and thus gain from economies of scale [9], and they can easily store thermal energy.

#### 2.2.7.1. CRS solar field configuration

The central-receiver heliostats have apertures ranging between 50 to 150 m<sup>2</sup> (Figure 2.50). The heliostats concentrate impinging solar radiation onto the receiver, which absorbs the concentrated solar radiation, transferring its energy to a heat transfer fluid. The heat-transport system, consisting mainly of valves, pumps, and pipes, conveys the transfer fluid in a closed-loop between the receiver, storage, and power-conversion units [9]. A thermal-storage system normally stores the absorbed energy as sensible heat for the extension of the heat supply to the power-conversion system.

The storage system also decouples the collection of solar energy from its conversion to electricity. The power-conversion system comprises a turbine generator, steam generator, and support equipment, which transforms the thermal energy into electricity and supplies it to the utility grid [103]. After energy collection by the solar system, the conversion of thermal energy to electricity has many similarities with the conventional fossil-fuel-based thermal power plants [31].

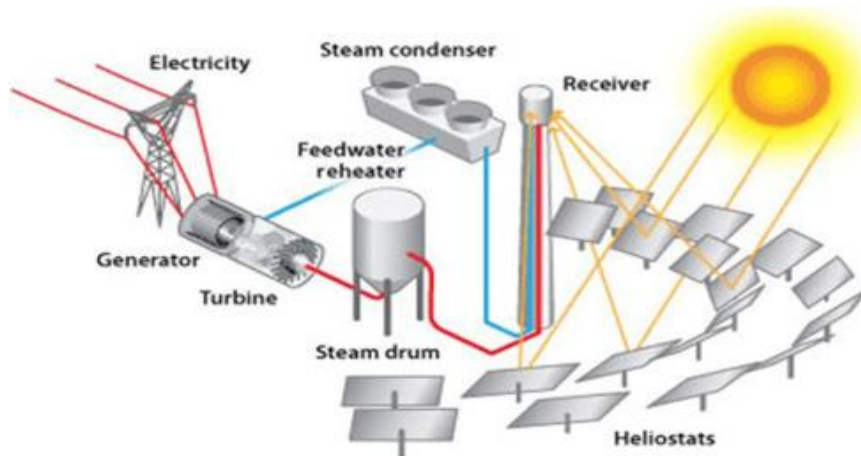


**Figure 2.50:** Central receiver concentrated solar power plant layout [124]

Generally, the collector and receiver systems can be deployed using three separate configurations. As shown in Figure 2.51 (left), the heliostats in the first configuration completely surround the central receiver tower, which is cylindrical and has an exterior heat transfer surface. In the second (Figure 2.51 - right), the heliostats are stationed north of the receiver tower (in the northern hemisphere), and the receiver constitutes an enclosed heat-

transfer surface. In the third, the heliostats are positioned north of the receiver tower, and the receiver, a vertical plane, comprises a north-facing heat-transfer surface [90].

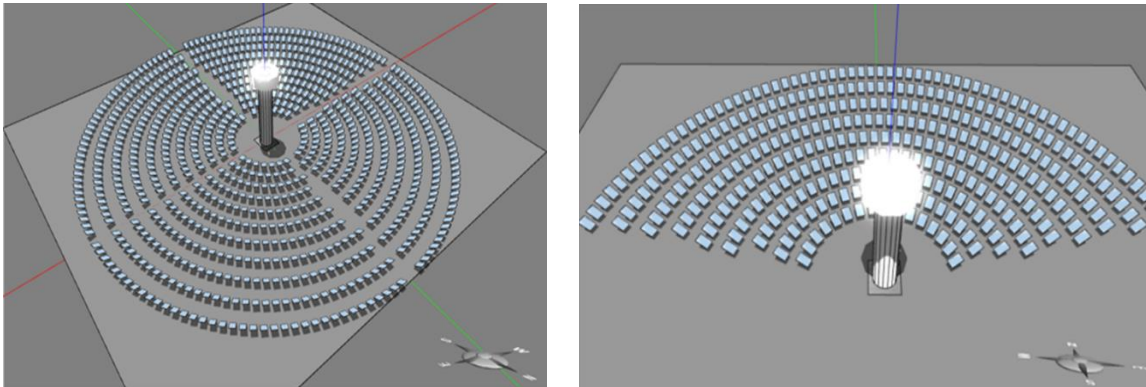


**Figure 2.51:** The heliostats configuration completely surround receiver central tower (Left) and heliostats located north of the receiver tower, and the receiver (Right)

The average solar flux between 200 and 1000 kW/m<sup>2</sup> is concentrated on the receiver. A relatively high temperature of more than 1500 °C is achievable with such high flux and combines thermal energy into more efficient cycles. Central receiver systems can easily be coupled with fossil-fuelled plants for hybrid operation in a wide range of options and have the capability to operate more than half the hours of each year at nominal power using thermal energy storage [9].

Moreover, it is the choice of the heat-transfer fluid, medium power conversion cycle, and thermal storage that defines a central-receiver system. The heat-transfer fluid may either be water/steam, liquid sodium, or molten nitrate salt (sodium nitrate/potassium nitrate), while the thermal-storage medium could be oil blended with crushed rock, molten nitrate salt, or liquid sodium. All depend on steam-Rankine power-conversion systems, although a more advanced system has been suggested that would use air as the heat-transfer fluid, ceramic bricks for thermal storage, and either a steam-Rankine or open-cycle Brayton power conversion system [90].

#### 2.2.7.2. CRS geometry and optical analysis

When one heliostat's mirror area is greater than the receiver area, the heliostat mirror assembly must be shaped in such a way that the radiation is concentrated. Spilled energy refers to the flux that spreads beyond the aperture. Curving the mirror, on the other hand, is optional. According to recent studies [125], the completely flat mirror panel would have provided the best economy from a machine perspective for an ATS-heliostat with a surface area of 147 m<sup>2</sup>. The modification of the curvature necessitates some additional work.



The focal length is the primary determinant of reflector curvature, but other considerations, such as the position of a particular heliostat in the field can also be considered. The variables that must be considered vary depending on the canting system used. Canting and focussing are usually distinguished in solar systems. Focusing mirrors usually refer to bent (or shaped in some other way) glass to achieve a specific curvature. It is much easier to bend glass as a cylinder than as a sphere due to the Poisson's ratio, and therefore it is easier to bend glass in just one direction [126].

The reflective surface of a heliostat with glass mirrors is usually divided into several flat (or curved) mirror facets. Heliostat canting is the process of arranging these facets into a specific shape (or pattern). The mirror facets may be arranged to resemble a paraboloid of revolution or a spherical mirror, for example. These are not the only choices, however. Over the years, a plethora of methods for arranging the mirror facets have been suggested, and new methods are still being created.

The geometry of a single heliostat is represented in Figure 2.52, which describes the active, reflective region that is used to reflect the beam radiation to the receiver.  $W_{helio}$  denotes the heliostat's width,  $H_{helio}$  denotes its height, and  $D_{helio}$  denotes the heliostat's footprint diameter.  $H_{gap}$  and  $W_{gap}$  are the lengths of the gaps between the panels in the horizontal and vertical dimensions, respectively. In the horizontal and vertical dimensions,  $N_{panel,h}$  and  $N_{panel,v}$  reflect the number of panels, respectively. All of these variables are crucial when measuring the heliostat's active, reflective field [127].

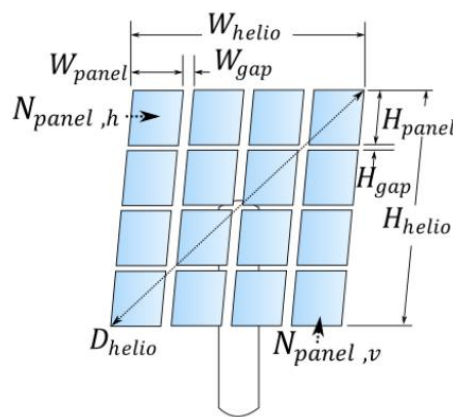


**Figure 2.52:** Heliostat geometry [127]

The three heliostats in the big, medium and small categories were chosen for their economic viability, practicality, and suitability for use in utility-scale power tower plants. It is believed

that the heliostats are rectangular in shape. Table 2.6 presents the main design geometrical parameters required to determine the optical efficiency of the three heliostat fields [128].

**Table 2.6:** Heliostat geometry design parameters [94]

Heliostat geometry design parameter	Large heliostat	Medium heliostat	Small heliostat
Heliostat total area (m <sup>2</sup> )	115.56	43.33	16.69
Heliostat height (m)	9.00	6.42	3.21
Heliostat width (m)	12.84	6.75	5.20
Heliostat footprint diameter (m)	15.68	9.32	6.11
Number of facets in the horizontal direction (-)	4	3	2
Number of facets in the vertical direction (-)	4	2	1
Individual facet dimensions (m)	3.21 × 2.25	3.21 × 2.25	3.21 × 2.60
Reflective surface ratio (-)	0.9583	0.9700	0.9200
Heliostat mirror reflective area (m <sup>2</sup> )	111.40	42.03	15.36

Optical losses in a heliostat can result from a variety of factors, including tracking, canting, sun shape, swaying motions in a tower, wind loads and gravitational bending due to structural, alignment, mirror surface uniformity and azimuth axis tilt errors [129]. A “single circular normal distribution of the energy flux” [130] can be used to characterise the reflected picture on the receiver at any point in time:

$$F(x, y) = \frac{1}{2\pi\sigma_{tot}^2} \exp\left(\frac{-(x^2+y^2)}{2\sigma_{tot}^2}\right) \quad (2.44)$$

By integrating the flux distribution along the receiver aperture axis, the image intercept/spillage losses can be determined [131] as;

$$\eta_i = \frac{1}{2\pi\sigma_{tot}^2} \int_x \int_y \exp\left(\frac{-(x^2+y^2)}{2\sigma_{tot}^2}\right) dy dx \quad (2.45)$$

The value  $\sigma_{tot}$ , which stands for total effective beam dispersion error, is given by the convolution of the following Gaussian distribution functions: astigmatic effects  $\sigma_{ast}$ , sun form  $\sigma_{sun}$ , tracking errors  $\sigma_{track}$  beam quality  $\sigma_{bq}$  and is expressed as a standard deviation [127]. These variables are statistically independent of the effective beam dispersion error, so they are combined as follows [132].

$$\sigma_{tot}^2 = \sum \sigma^2 = \sigma_{sun}^2 + \sigma_{bq}^2 + \sigma_{track}^2 \quad (2.46)$$

In a study by Bhattacharjee and Bhattacharjee [133], the performance of an inclined heliostat solar field in relation to solar geometrical factors was examined. The investigation's criticality is assessed in terms of field optical performance, intercept efficiency and flux distribution on

the receiver. According to Boudaoud, Khellaf [134], the optical efficiency of the solar field is defined as the ratio of the net power obtained by the receiver ( $Q_{rec}$ ) to the total solar energy incident on the heliostat solar field. Cosine performance, shading and blocking efficiency, intercept efficiency, reflection, and atmospheric attenuation efficiency are all factors in the overall field optical efficiency [135].

$$\eta_{opt} = \frac{Q_{rec}}{I_d \times A_h \times N_h} \quad (2.47)$$

$$\eta_{opt} = \eta_{cos} \times \eta_{sb} \times \eta_{int} \times \eta_{atten} \times p \quad (2.48)$$

The position of the mirror in relation to the sun can be used to determine its orientation. Figure 2.53 shows how the mirror orientation can be expressed in terms of solar geometrical angles and the mirror positional angle [136].

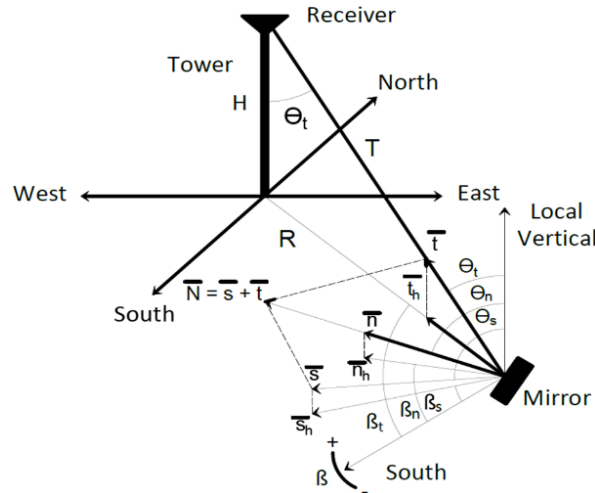


**Figure 2.53:** The geometrical configuration of unit vectors associated with sun, tower, and mirror [136].

The time profile of the mirror tilt angle is given by the Eq (2.49), where  $\theta_n$  is the mirror tilt angle.

$$\tan \theta_n = \frac{[\sin^2 \theta_s + \sin^2 \theta_t + 2 \sin \theta_s \sin \theta_t \cos (\beta_t - \beta_s)]^{1/2}}{(\cos \theta_s + \cos \theta_t)} \quad (2.49)$$

The time profile of the mirror azimuth angle is given by the equation here  $\beta_n$  is the mirror azimuth angle.

$$\tan \beta_n = \frac{\sin \theta_s \sin \beta_t + \cos \delta \sin \tau}{\sin \theta_t \sin \beta_t + \sin \lambda \cos \delta - \cos \lambda \sin \delta} \quad (2.50)$$

According to Ahmadi, Ghazvini [86], the Concentration Ratio (CR) is equal to the ratio of the area of the receiver to the total area of concentrating heliostats, as shown in Eq. (2.51)



$$CR = \frac{\text{Area of Receiver}(m^2)}{\text{Total Area of Heliostat}(m^2)} \quad (2.51)$$

In [137], a model is demonstrated for evaluating the thermal efficiency of a cavity receiver in a central tower. It is assumed that a uniform distribution is formed on the cavity receiver's absorber tube during the modelling process. Radiation thermal losses must be measured in order to calculate the central tower receiver's thermal efficiency. Since the temperature is high and radiation loss is so prevalent, other potential thermal losses are ignored. As a result, the central tower receiver's thermal efficiency is calculated as follows;

$$P_{in,solar} = ICA_R \quad (2.52)$$

$$P_{loss,radiation} = A_R \varepsilon \sigma T_R^4 \quad (2.53)$$

$$\eta_{th} = \frac{P_{in} - P_{loss,radiation}}{P_{in}} = 1 - \frac{\sigma T_R^4}{IC} \quad (2.53)$$

The Stefan-Boltzmann constant is equal to one in the equations above. The maximum achievable temperature in the central tower receiver, according to the above equation, is;

$$T_{R, max} = \left(\frac{IC}{\sigma}\right)^{0.25} \quad (2.54)$$

Servert, González [138] have proposed a model of aiming strategy that is parameterized to allow for user-defined strategies. According to the line that connects the receiver and each heliostat site, the  $H_{aiming}$  coordinate of the aiming point for each heliostat is set. The  $Z_{aiming}$  coordinate, on the other hand, is determined by a “vertical aiming factor,” which is defined as  $k$  in [139]. For each individual heliostat, this parameter takes into account the standard deviation of the Gaussian distribution of solar radiation on the receiver surface.

The parameter  $k$  is defined as a multiplier of the Gaussian distribution's standard deviation, as shown in Eq. (2.55). As depicted in Figure 2.54c, heliostat aiming points are adjusted alternately in the same row (one heliostat aiming to the higher zone, the next heliostat aiming to the lower zone) in the case  $H_{rec} > (2 \cdot r_k)$ .

$$r_k = (\sigma_{e,SLR} / \cos \alpha_t) \quad (2.55)$$

$$H_{rec} \leq (2 \cdot r_k), \quad Z_{aiming} = \text{Receiver centre hieght} \quad (2.56)$$

$$H_{rec} \geq (2 \cdot r_k), \quad Z_{aiming} = \text{Receiver centre hieght} \pm \frac{1}{2} \cdot (H_{rec} \mp 2 \cdot r_k) \quad (2.57)$$

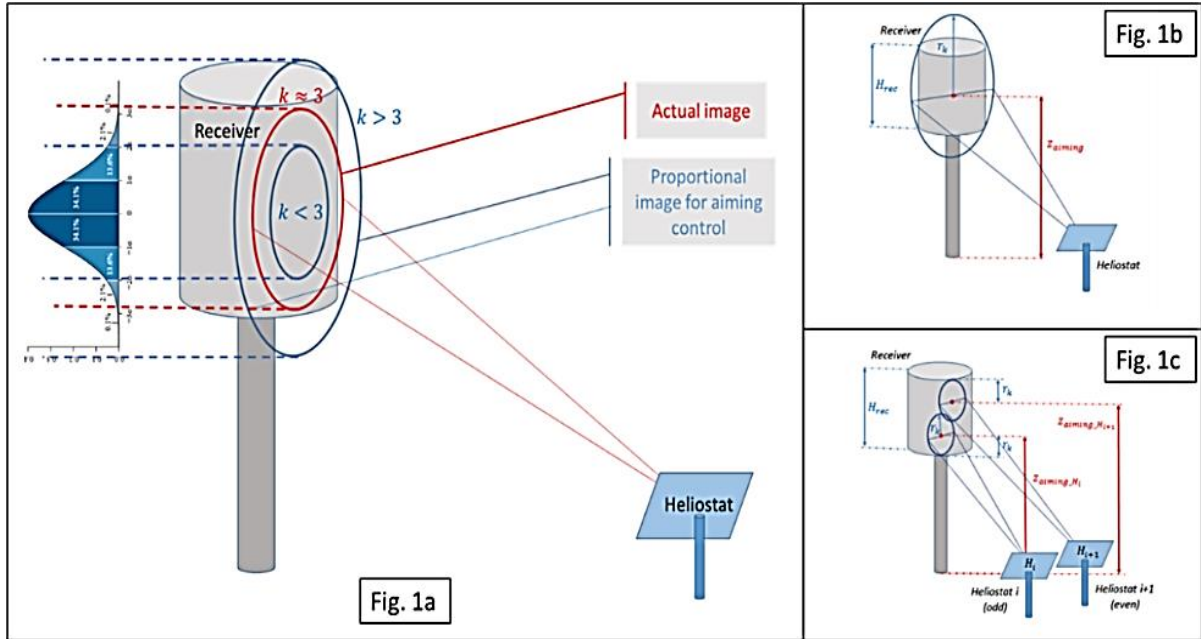


**Figure 2.54:** (a) shows the relationship between the standard deviation of the Gaussian distribution of the radiation and the  $k$  value. (b) shows the aiming strategy in the case  $H_{rec} < (2 \cdot r_k)$  (c) shows the aiming strategy in the case  $H_{rec} > (2 \cdot r_k)$  [138]

The reasoning behind this aiming strategy is straightforward: heliostats with larger scattered radiation aim at the receiver's core, while heliostats with smaller scattered radiation can have their aiming points identified in different zones of the receiver. The aim of this strategy is to reduce spillage losses while achieving uniform radiation on the receiver surface. Multiple strategies can be tested using the same algorithm by changing just one parameter, while alternative strategies will necessitate the development of different algorithms, which might not be as versatile [138].

### 2.2.7.3. CRS receiver configuration

The technology deployed in Central receiver systems constitutes a point-focus heliostat field. The heliostat fields have large concentration ratios of around 1000; hence, absorptance is the most significant factor in central receiver performance [140]. External receivers and cavity receivers are the two leading designs for the central receiver system, as shown in Figure 2.55 [141]. The absorbing surface of an external receiver is on the receiver's outer surface, which is normally cylindrical, and the heliostat field, in this case, willfully surround the central receiver.

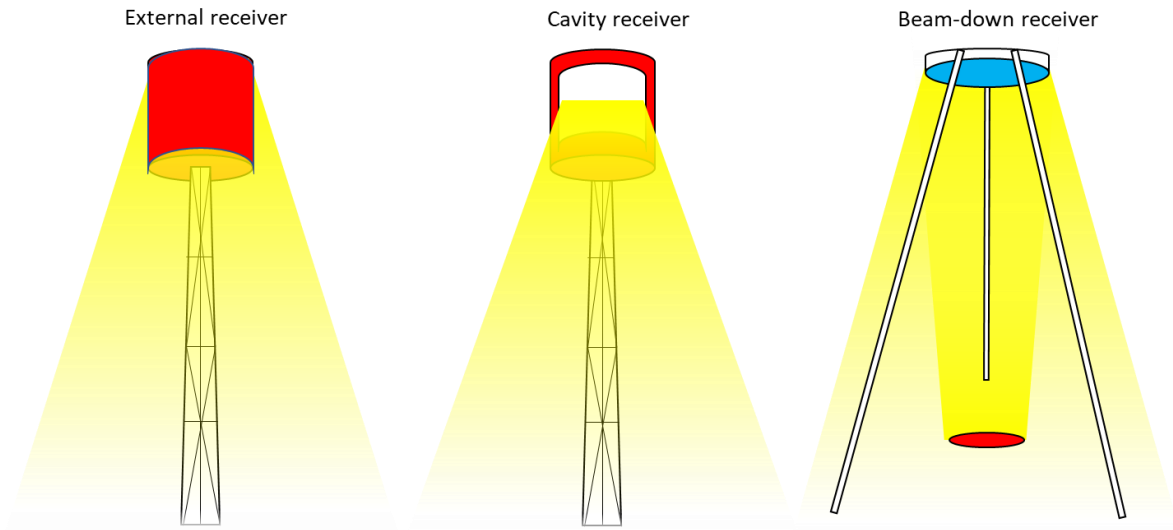


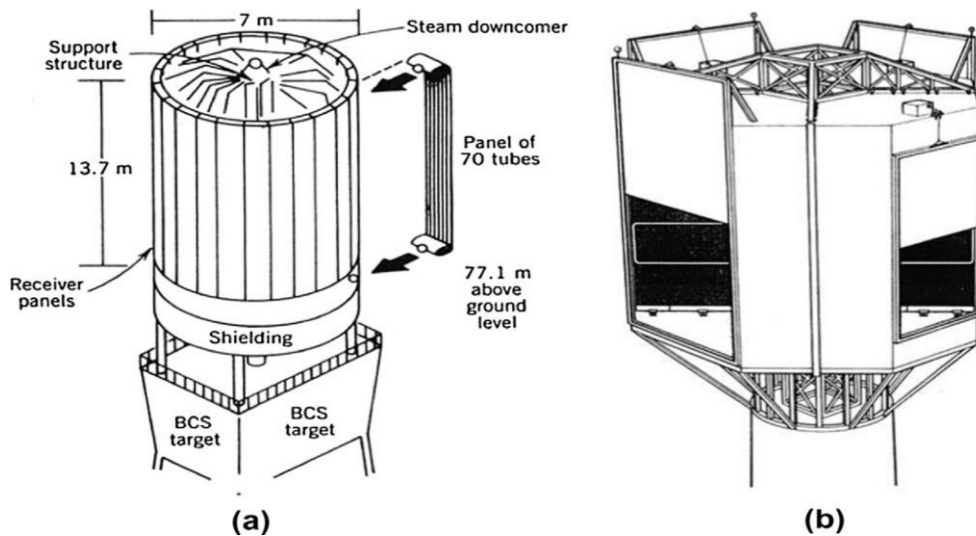
**Figure 2.55:** Diagrams of different central receiver configurations, with red denoting the absorbing surface. In an external receiver (left), sunlight from all around the receiver can be absorbed. In a cavity receiver (centre), sunlight can only be absorbed from the side of the receiver that the cavity is facing. In a beam-down receiver (right), the receiver is on the ground, and the sunlight is reflected down to it from a secondary reflecting optic [141]

In a cavity receiver, sunlight is concentrated on an aperture heading to an internal cavity where the sunlight is absorbed. The heliostat field is only on the side of the receiver that the aperture faces in this configuration (e.g., in the northern hemisphere, the aperture would face north, and the heliostat field would only remain on the north side of the receiver). The "beam-down" concept is a less mature central receiver design, so named because the raised receiver is substituted by a reflecting optic that focuses sunlight from the heliostats to a ground receiver (see Figure 2.55) [142].

It is also possible to stop the elevated receiver by mounting the heliostat field on a hill [143]. Although a beam-down test plant is in operation at the Masdar Institute in the United Arab Emirates [144], it is unclear whether the benefits (mainly the capacity to locate the heavy receiver on the ground) outweigh the disadvantages (e.g., additional reflective losses are introduced as a result of the additional optics, and a secondary concentrator is needed at the receiver to realize comparable concentration ratios). Any modifications to the absorbers for external or cavity receivers may theoretically be extended to beam-down receivers as well.

The external receiver deployed at the Solar One (Barstow, California, USA) is mounted at the top of the central tower, as shown in Figure 2.56; it consists of 70 panels (receiver diameter: 7 m), six of which are for preheating water and eighteen for generating steam. The height to diameter ratio of external receivers is usually 1:1 to 2:1. Water/steam, molten salts (MS),

synthetic oils and liquid sodium are the most preferred heat transfer fluids, with molten salts and liquid sodium having a much higher heat removal capacity than steam and synthetic oils [145, 146].



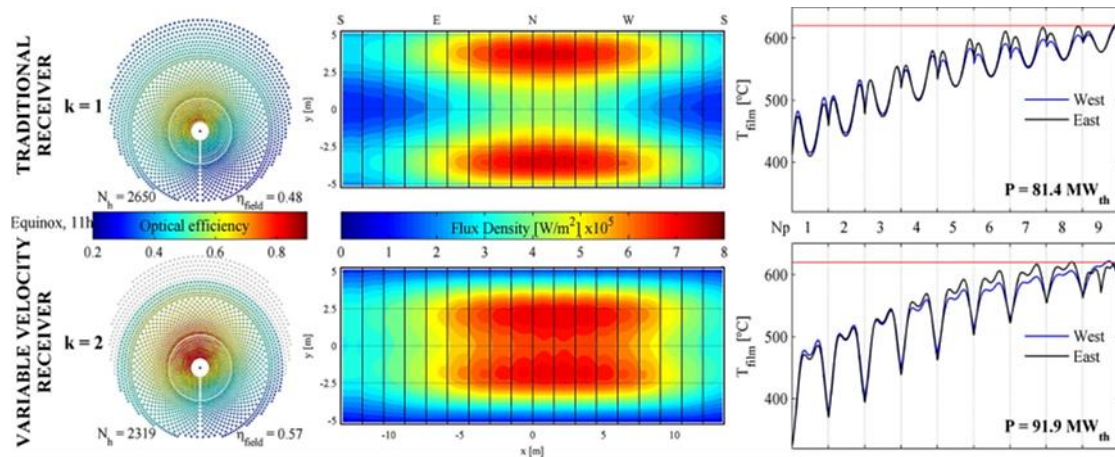
**Figure 2.56:** Two types of solar towers receivers [60]: (a) external receiver and (b) cavity receive [146].

Figure 2.56b shows an example of a cavity receiver configuration. The flux from the heliostat field is concentrated onto the cavity's absorbing surfaces through an aperture (about one third to one half of the internal absorbing surface area [145]. The aperture size is kept as small as possible to minimise convection and radiation losses while still allowing enough solar flux to reach the receiver.

In addition to the state-of-the-art technologies of molten salt and water/steam, open volumetric air receivers, pressurised air receivers, liquid metals, and solid particles are all technologies in various stages of development [147]. Ho and Iverson [141] discuss liquid receivers, gas receivers, and solid particle receivers. Deploying sCO<sub>2</sub> closed-loop Brayton cycles and direct heating of the CO<sub>2</sub> in tubular receiver designs, external or cavity, for high fluid pressures of about 20 MPa and temperatures of about 700 °C, higher thermal-to-electric efficiencies of 50% and higher can be achieved.

Hoffschmidt [148] proposed higher temperature MS, higher steam parameters, smaller heat exchanger, smaller storage, and less sensitive receiver temperature operation as techniques aimed at improving MS systems. Furthermore, reduced thermal losses, cavity arrangement, face down can design, standard vacuum absorber for first temperature stage, and selective coatings for higher solar radiation absorption are all ways to increase receiver efficiency [148].

The enhancement of the solar flux captured by the receiver to maximise the peak flux is considered in [149]. They propose the Variable Velocity Receiver (VVR), Figure 2.57, which consists of a Traditional External Tubular Receiver (TETR) with valves that allow each panel to be divided into two separate panels. This increases the heat transfer fluid's velocity in particular areas of the receiver, preventing tube overheating. The new design also allows for better targeting techniques, resulting in increased solar field optical performance and a potential reduction in the number of heliostats.



**Figure 2.57:** Operation of the novel Variable Velocity Receiver vs. a Traditional External Tubular Receiver. proposed in [149]

A VVR needs a solar field that is 12.5% smaller than that needed by a conventional TETR. In addition, the VVR offers benefits for winter service by allowing the panels to be split in half, raising the number of passes and the velocity of the heat transfer fluid.

Important stresses are caused by high temperatures, thermal shocks, and a temperature gradient on the receiver walls caused by a high, non-homogeneous, and variable flux. The receiver's life span is shortened as a result of these stresses. An open-loop method is proposed in [150] for controlling the flux density distribution delivered on a CRS flat plate receiver. Various aiming point distributions on the receiver's aperture are considered. The method yields promising results for heliostat power, with the potential to extend the component's life significantly.

The effect of wind and return air on a volumetric receiver was numerically analysed in [151]. The receiver is depicted in Figure 2.58. The volumetric receiver is made of a porous material that absorbs solar radiation at various depths throughout its thickness. Solar absorption has a greater effective area than thermal radiation losses. Air is drawn through the absorbent pores by a fan, and the heat is captured by the convective flow. The absorber thermal radiation loss is minimised due to the volumetric effect [152].

Feckler, et al. [153] examined volumetric air receivers. This component is made up of a high-temperature resistant cellular material that absorbs radiation and passes the heat to an air flow that is fed from both the outside and the inside. It's referred to as volumetric because the radiation will pass through the open, permeable cells of the material and into the receiver's "volume." In contrast to a closed tubular receiver, a greater amount of heat transfer surface facilitates solid to gaseous heat transfer in this way. In a traditional steam turbine setup, the heated air is guided to the steam generator. A cellular metal honeycomb structure was also deployed. It is made up of winded pairs of corrugated and flat metal foils. To improve local turbulence and radial flow, many variants of the pure linear honeycomb structure have been added.

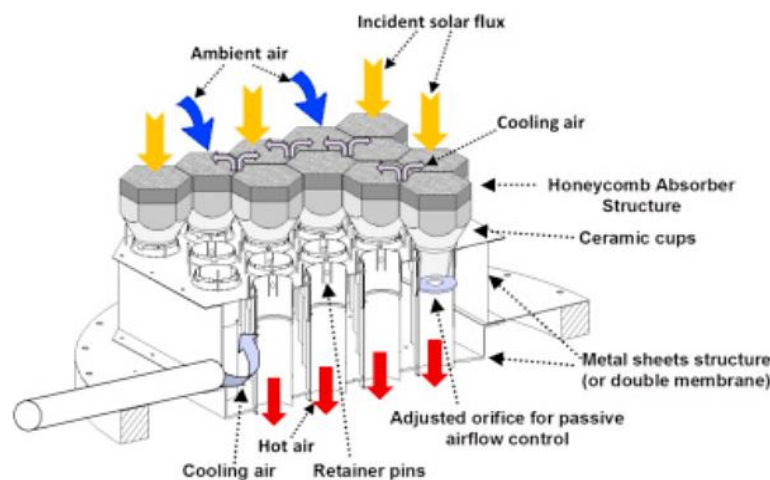


**Figure 2.58:** Central receiver volumetric receiver reprinted from [154]

Pyromark 2500, black silicone-based paint with high-temperature stability, is the most common absorber coating for external receivers [155]. It has a high solar absorptance of about 0.95 and a high emittance ( $>0.85$ ) at high operating temperatures. While the high emittance suggests space for improvement in efficiency, the importance of reliability makes it a competitive choice due to the high temperatures, large heat fluxes, and a large number of thermal cycles encountered by central receivers. Lower emittance spectrally selective coatings for central receivers have been tested, but their efficiency did not improve significantly above Pyromark 2500.

While there are coatings that would improve performance, such as cermet absorbers, the main challenge for compatibility with central receivers is high-temperature stability in the air. Transmission losses become more severe with higher concentrations, so vacuum or inert gas enclosures are undesirable. Metallic photonic crystals are one possible solution. If spectral

selectivity can be achieved for a surface that is robust at high temperatures in the air, there is room for performance improvement.

As compared to the same coating used for a conventional external receiver, an alternative approach to enhancing receiver efficiency is by receiver design (e.g., novel geometries), which can increase effective absorptance and minimise losses [156]. A directionally selective absorber (or a reflective cavity intended to provide directionally selective performance) applied to a central receiver in another approach could lower the necessary solar concentration ratio for efficient high-temperature activity, resulting in a smaller heliostat field and significantly lower concentrator cost [37].

Because of the cavity geometry, light entering through the aperture is much more likely to be absorbed at a point on the broad interior cavity surface than to be reflected out of the aperture. The absorptance of cavity receivers is naturally strong. As a result, better absorber surfaces than Pyromark paint are not needed. Falling particle receivers, in which small particles absorb sunlight in a cavity and transmit heat to the air (or other working fluid) as they pass through, are one field of research [157]. Since the particles have a much higher surface area to volume ratio, there is less thermal resistance between the absorbing surface and the air [158, 159].

While some of these central tower receiver technologies may be easily implemented in future installations, those more sophisticated and innovative receiver designs certainly require further studies.

#### **2.2.7.4. CTR power plants**

***PS10 - An 11 MW Solar Thermal Power Plant:*** TSA Consortium (Technology Program Solar Air Receiver) operational results, which were successfully run by DLR and CIEMAT for nearly 400 hours between April and December 1993, and for shorter periods in 1994 and 1999, demonstrating that a receiver outlet temperature of 700 °C was crucial in convincing the Spanish company Abengoa to promote the first commercial demonstration plant with this technology. PS10 was established in 1999 with the aim of constructing and connecting a 10 MW plant in Seville to the grid (Spain) [31].

The PS10 plant, whose civil work began in June 2004, concentrates the sun's rays onto the top of a 115-meter-high tower using mobile mirrors that are regulated to face the sun. The solar receiver atop the tower creates saturated steam, which is then circulated to a traditional steam turbine, which generates electricity. The plant is expected to produce 23 GWh of electricity per



year. Figure 2.59 and Table 2.7 provide a diagram as well as the key design and performance characteristics [95].

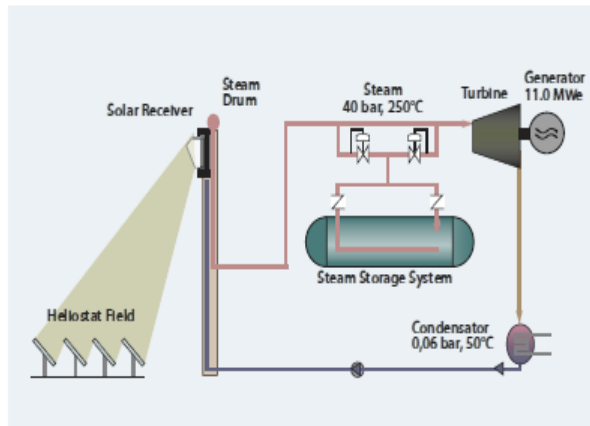


**Table 2.7:** The PS10 power plant design features [95]

Location	Sanlúcar M., Spain
Nominal electrical power	11.02 MW
Tower height	100.5 m
Receiver technology	Saturated steam
Receiver geometry	Cavity 180o, 4 panels 5.40 m x 12.00 m
Heliostats	624 @ 120 m <sup>2</sup>
Thermal storage technology	Water/steam
Thermal storage capacity	20 MWh, 50 min @ 50% rate
Steam cycle	40 bar 250oC, 2 Pressures
Electric generation	6.3 kV, 50 Hz -> 66 kV, 50 Hz
Ground area	55 ha
Annual electricity production	23.0 GWh

**Figure 2.59:** The PS10 power plant description and layout [95]

A massive solar field of 624 heliostats is featured on the PS10 (Figure 2.60). Each heliostat is a 120 m<sup>2</sup> curved reflective surface mirror that moves around. The receiver on the tower is designed to generate saturated steam at 40 bar-250 °C from thermal energy produced by concentrated solar radiation flux and is based on a cavity principle to minimise radiation and convection losses. Steam is pumped into the engine, where it expands to generate mechanical work and electricity [95].



**Figure 2.60:** The PS10 power plant solar field [95]

To ensure wet inner walls in the tubes, the receiver is essentially a forced circulation radiant boiler with a low ratio of steam at the panels' output. It was built with special steel alloys to



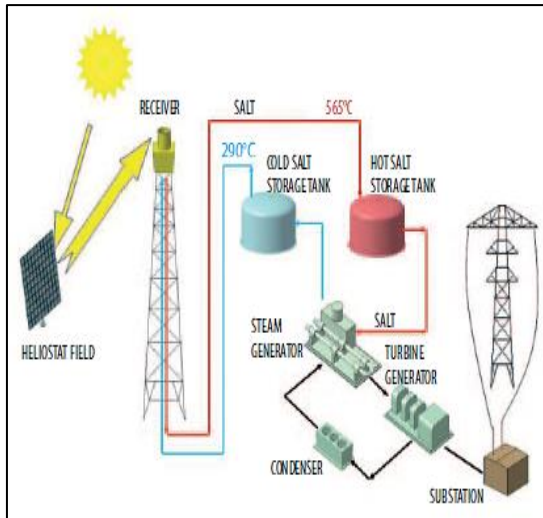
withstand large heat fluxes and possible high temperatures. It is made up of four vertical panels measuring 5.40 m wide by 12 m high, each with a heat exchange surface of 260 m<sup>2</sup>. These panels are grouped into a 7-meter-radius semi-cylinder.

The plant has a saturated water thermal storage facility with a thermal capacity of 20 MWh for cloudy times (at 50% load). The system is made up of four tanks that are run in a specific order depending on their charge status. Part of the steam provided by the receiver is used to load the thermal storage system during the full load operation of the plant. When energy is required to cover a transient time, energy from saturated water is recovered at a pressure of 20 bar, allowing the turbine to operate at 50% partial load.

***SOLAR TRES - 15 MW solar tower with molten salts storage:*** The SOLAR TRES project's main goal is to demonstrate the technological and economic feasibility of molten salt solar thermal power technologies for delivering clean, cost-competitive bulk electricity [31]. The project aims to secure a prominent position for European industry and research institutions in the production and commercialization of these promising technologies, with a total cost of € 15.3 million, including a €5 million EU contribution. The SOLAR TRES demonstration facility (Figure 2.61 and Table 2.8), a 15 MW solar tower with molten salts storage, has been located in Ecija, Spain, near Seville.

The objectives of SOLAR TRES are as follows:

- Installation costs total of 2.500 euros / kW (electrical).
- Taking advantage of previous lessons, improving efficiency, increasing availability and reducing operating costs by approaching electrical costs by 0,04/kWh.
- The achievement of sustainable production of renewable energy sources without any negative environmental impact contributes to a 57 kton/year reduction in greenhouse gas emissions and supports EU renewable energy commitments.
- Promoting liberalisation, competitiveness and reliability of the electricity market.
- Contributing towards social goals by supporting the development of a deprived area, reducing regional inequality and implementing cohesion policy by creating significant employment.

**Table 2.8:** The SOLAR TRES power plant design features [95]

Location	Ecija, Spain
Receiver thermal power	120 MW
Turbine electrical power	17 MW
Tower height	120 m
Heliostats	2,480
Surface of heliostats	285,200 m <sup>2</sup>
Ground area covered by heliostats	142.31 ha
Storage size	15 hr
Natural gas boiler thermal capacity	16 MW
Annual electricity production (min.)	96,400 MWh
CO <sub>2</sub> mitigation (best available technology)	23,000 ton/year
CO <sub>2</sub> mitigation (coal power plant)	85,000 ton/year

**Figure 2.61:** The SOLAR TRES power plant description and layout [95]

The project SOLAR TRES benefits from various advances in the technology of molten salts, which includes:

- The use of a large area heliostat in the collector sector significantly reduces plant costs, especially as less driving mechanism is necessary on a single mirror field.
- The receptor has been designed to minimise thermal stress and resist inter-granular stress corrosion creases with a 120 MW (thermal) high thermal efficiency cylindrical receiver system capable of working at high flow and low heat loss. A highly efficient, reliable and cost-effective integrated header and nozzle design is to be used to achieve high heat efficiency.
- An enhanced physical plant design with a molten-salt flow loop that decreases the number of valves removes “dead legs” and allows safe drainage to prevent freezing of salt.
- A better thermal storage system (15 hours, 647 MWh, 6,250 t of a salt) deploying insulated tank immersion heaters – an efficient and risk-free, high-temperature liquid nitrate salt storage system with high-temperature liquid salt at 565 °C in stationary storage drops only 1-2°C/day. Cold salt is stored at 240 °C, which provides a considerable margin for the design.
- This innovative design places components in the receptor tower structure above the salt storage tanks at a height that allows the salt-molten system to drain back to the tanks, providing a passive fail-safe design with forced recirculating the steam drum deploying

a 43 MW steam generator. This simplified design increases installation accessibility and decreases operation and maintenance costs.

- A higher-pressure reheating turbine – more efficient (38% average a year) – can start and stop daily and responds well to the changing changes, guaranteeing 30 years' lifetime with good efficiency.
- Enhanced heliostat and high-temperature nitrate salt process instrumentation and control systems
- A better electric heat tracing system to protect salt circuit freezing, storage tanks, valves, pumps.

*Solgate: From REFOS to the new Generation of CRS Plants.* Using solar energy in the gas turbine of a Combined Cycle system (CC) has a number of benefits over other solar hybrid power plant concepts. Solar preheating of compressor discharge air until it reaches the gas turbine's combustor is a promising way to incorporate solar.

Since the solar energy absorbed in the heated air is directly converted with the high efficiency of the CC plant, solar air preheating provides enhanced performance. As compared to solar steam generation, this results in a smaller heliostat field size and thus a lower total investment cost for the solar portion. Solar air preheating has a significant cost-cutting potential for solar thermal power. This principle may also be extended to a broad range of power levels (from 1 to 100 MWe). Instead of CC, highly efficient recuperated gas turbine cycles can be used at lower power levels. The solar share can be varied depending on the receiver outlet temperature, and it may be considerably higher than in other hybrid concepts (e.g., integrated solar combined cycle system with parabolic troughs).

Molten salt receivers (up to 560 °C) [160] or pressurised volumetric receivers [161, 162] can be used for solar pre-heating of the air. Several receiver modules are mounted on the tower of a solar tower plant due to the small size of the quartz window. A pressurised receiver unit and a secondary concentrator are located in front of each module. The secondary concentrator, which has a hexagonal entry aperture (located in the heliostat field's focal plane), refocuses solar radiation into the aperture of the pressure tank, which is sealed by a domed quartz window to retain pressure. After passing through the window, the radiation is absorbed in the volumetric absorber, which then transfers the heat to the air stream passing through it through forced convection.

The REFOS project was started in 1996 to show that the necessary receiver technology was technically feasible [162]. The REFOS project's goal is to design, instal, and test modular pressurised volumetric receivers under operating conditions that are indicative of gas turbine coupling. The emphasis is on solar air preheating testing, as well as basic materials science. With an absorbed thermal power (design conditions) of 1 MWt (design efficiency: 80%), a maximum air outlet temperature of 800°C, and a pressure of 15 bar, a cluster of three-receiver modules will be tested.

The project is headed by DLR, which is being carried out in collaboration with CIEMAT in Spain and G1H in Germany. The REFOS test system is located in the Plataforma Solar de Almera (PSACESA-1)'s solar tower test facility. The design conditions were demonstrated in 1999 with a single module operating at 800 °C air outlet temperatures at 15 bar and 400 kWt power levels. The scale-up to 1MWt is currently being planned by adding two new modules to the test system.

#### **2.2.8. Heat transfer fluids**

In solar thermal systems, sunlight is concentrated on a receiver, where it is absorbed and ultimately transformed into thermal energy. The thermal energies are usually supplied via convection to Heat Transfer Fluids (HTF), which can also be carried out in less traditional ways (e.g., radiation, conduction). The multi-functional HTF needs to gather, transport, and exchange heat gained from solar radiation and is therefore an essential part of a CSP system [37].

HTF is one of the key components for CSP systems overall performance and efficiency. Since a significant amount of HTF is needed to operate a CSP plant while maximising its performance, it is necessary that HTF costs are minimised. In order to generate electricity, the hot HTF can also be stored in an insulating tank if no sun is available, in addition to heat transfer from the receiver to the steam generator [163].

The desired characteristics of an HTF include a high boiling point and thermal stability, high-temperature vapour pressure (<1 atm), a low melting point, low viscosity, low metal alloy corrosion, high thermal conductivity, high thermal capacity for energy storage and low cost [164, 165]. The freezing point of the HTF is another important element regarding its temperature stability. The daytime nature of the sun forces the HTF to operate between the maximum operating temperature of the CSP plant and night-time. Therefore, the HTF might

freeze in or below night-time and safety measures should be integrated into the system so that the HTF does not freeze in the plumbing, which can cause damage and speedy wear [37].

The toxicity, environmental danger, stability, material compatibility (e.g. metals, the effect of impurities and cost) are also factors not to be ignored in practical applications. Another important issue that needs to be examined experimentally is the long-term durability of different HTFs [166]. Moreover, recent studies have examined the optical transmission of several HTFs with the purpose of using these as beam splitting filters for direct absorption[167]. The HTFs are categorized into six main groups based on material types; (1) molten salts, (2) water/steam; (3) air and other gases, (4) thermal oils, (5) organics, and (6) fluid metals [168, 169]. Working temperatures of various HTFs are indicated in Figure 2.62.

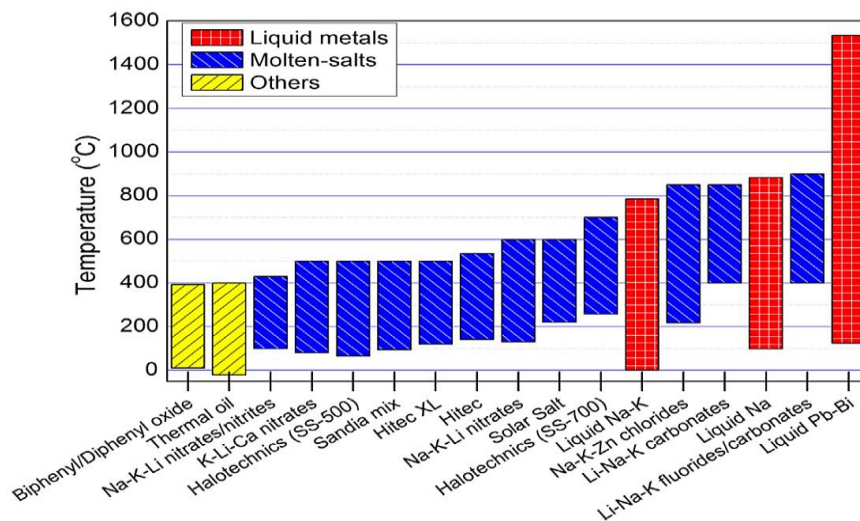


**Figure 2.62:** Operating temperature range for various HTFs [163].

Given the functionality of the HTF, their performance is determined by a wide range of constraints, both practical and fundamental. Because of their stability over a relatively large temperature range, synthetic and mineral oils are the HTF choice for most solar thermal plants. Molten salts, on the other hand, promise higher efficiencies as high operating temperatures have attracted a lot of interest. These efficiency gains are, however, combined with the challenges of melting the salts and higher pumping costs [37].

The capacity for thermal energy storage for night power production is an important concern for CSP designs. Spain pioneered the technology for thermal energy storage and thermal energy storage of the CSP systems with molten salts after the launch at the end of 2008 in Spain of the trough plant 'Andasold-1' [170]. Currently, nearly half of the CSP plants in Spain have thermal energy storage capacities; molten salts are being used in almost all thermal storage systems. In

addition, these molten-salt materials not only withstand high temperatures and are suitable for thermal energy storage but are also relatively cheaper than other HTF types.

Container and tube alloy corrosion is a major issue for CSP systems. In a corrosive system that attacks metal containers, HTFs act as the electrolyte [13]. High operating temperatures are required in order to improve CSP system efficiency, and molten salt is the most attractive HTF candidate for high temperatures up to 800 °C. However, in CSPs operated with molten salts, the problem of corrosion is greater compared to other HTFs due primarily the high operating temperature [163].

#### 2.2.8.1. Oil

Oils are the most frequent types of HTFs in CSP applications. Mineral oil, silicone oil, and synthetic oils have all been studied and used as HTFs. Mineral oils usually include an oil distillate blend of higher alkanes. On the other hand, synthetic oils are produced artificially from petroleum components chemically modified. They have almost identical thermal conductivities of about 0.1 W/(m K), and their costs are the costs are 0.3, 3 and 5 \$ per kg for mineral, synthetic and silicone oils, respectively [171]. Synthetic oil has both higher and lower thermal conductivity, which enhances its appeal than mineral oils (e.g. Caloria HT 34) [37]. In addition, in the first solar power generator station (SEGS1), mineral oils could be quite flammable and were responsible for an accident in 1999. Synthetic oils, by comparison, are less inflammable and preferred to mineral oil [37].

For solar-thermal applications, the oils are important HTFs, offering a combination of the best possible high temperature and low freezing point. Table 2.9 shows the temperature range and thermophysical characteristics of certain commercially available heat transfer fluids based on mineral and synthetic oil. These HTFs are liquid under environmental conditions and need no external temperature control to ensure their viscosity is relatively low. In parabolic solar plants, synthetic oils (e.g. Therminol® VP- 1, Solutia) are used but limited by a relatively low operating temperature of around 393 °C [37].

In principle, HTF performance improves with increasing temperature (due to a decrease in liquid viscosity and consequently the required pump capacity), but solar engineers usually face stabilisation problems that ultimately set the operating temperature and the maximum exergetic efficiency achieved. Some recent studies suggest that thermal fluid based on biphenyl and diphenyl oxides like Therminol VP-1 and Dowtherm-A gradually decomposes at close to 400

°C temperatures. This gradual heat breakup results in the formation of hydrogen gas which penetrates the vacuum cabinet through steel pipes and increases the heat loss [37].

**Table 2.9:** Temperature range and thermophysical characteristics HTF based on mineral and synthetic oil.

Fluid Name and Manufacturer	Chemistry	Temperature Range	Density (Kg/M3)	Specific H. (Kj/Kg·K)	Viscosity (Mpa·S)	Thermal C. (W/M·K)
<b>Mineral Oils</b>						
Therminol XP, Solutia	white mineral oil: petroleum	–20 to 315 °C	875	1.85	22.7	0.124
Heat transfer oil S2, Shell	hydrocarbons	max. 320 °C	863	10	25	0.134
Xceltherm 445FP, Radco	naphthenic oil	max. 288 °C	862	36	36	0.132
Duratherm 600, Duratherm	paraffinic hydrocarbons	max. 315 °C	844	1.97	65.86	0.142
<b>Synthetic Oils</b>						
Therminol VP-1, Solutia Dowtherm A, Dow/IMCD	biphenyl and diphenyl oxide 73% diphenyl oxide, 27% biphenyl blend	12 to 400 °C 15 to 400 °C	1060 1064	1.57 1.56	3.57 5	0.136 0.140
Royco 782, Anderol Inc.	60–70% polyphaloeffins, 30–40% esters	–40 to 205 °C	829	1.96	18	0.167
Syltherm XLT, Dow/IMCD	dimethyl polysiloxane	–40 to 400 °C	814	1.86	0.8	0.102
Duartherm S, Duratherm PSF-20cST	silicone-based	–50 to 343 °C	957	1.69	49.24	0.13
Silicone HTF, Clearco	polydimethylsiloxane	–50 to 220 °C	950	1.6	20	0.142
Duratherm G, Duratherm	polyalkylene glycol	–40 to 260 °C	914	1.97	82.08	0.164

In 2013, Ouagued, Khellaf [172] used seven different thermal oils as HTFs to investigate the efficiency of PTC in Algerian climatic conditions. Marlotherm SH, Syltherm 800, Therminol D12, Santotherm 59, Santotherm LT, Syltherm XLT, and Marlotherm X were the oils used. They discovered that these oils are thermally stable up to 300–400 degrees Celsius. The cost of these thermal oils in PTC applications was also investigated; in general, the costs were found to be relatively high, with the highest cost being 129US \$/kW h/day for Santotherm LT. Among the seven oils tested, Syltherm 800 had the highest thermal ability [163].

A recent study [173] looked at the experimental performance of medium-temperature solar thermal collectors using Dow-corning 550 silicon oil as the HTF. In contrast to pressurised water, Dow-corning 550 silicon oil had better heat collection characteristics and a lower saturation rate. This silicon oil has a steady thermal conductivity over a wide temperature spectrum; it is less corrosive and flammable. The main disadvantage of this silicon oil HTF is



that it needs a higher pumping rate due to its low specific heat power, making the process more expensive [173].

#### **2.2.8.2. Molten salts**

Molten salts can function at much higher temperatures than oil as one promising class of HTFs. Lower vapour pressure of the melting salts than synthetic oils can enable the higher operating temperature. Although due to receptacle material limitations, the highest molten salt operating temperature ( $>1000\text{ }^{\circ}\text{C}$ ) cannot yet be met, the current operating temperature (up to  $550\text{ }^{\circ}\text{C}$ ) results in greater exergetic effectiveness and lower cumulative energy demand (CED). Their operating temperature is reduced. In addition, molten salts may be used for thermal storage directly, which increases electricity generation hours and also reduces LCOE [174].

At high temperatures, molten salts have properties identical to water, such as similar viscosity and low vapour pressure [168]. HTFs based on molten salt are widely used in modern CSP systems, with the first molten-salt power tower systems installed in 1984. The THEMIS tower (2.5 MWe) in France and the Molten-salt Electric Experiment (1 MWe) in the United States were both ground-breaking systems [175]. Another significant benefit of using molten salts in power tower systems is their ability to store thermal energy [163].

By 1996, the US had developed a 10 MW power system called Solar Two, which was the first to deploy molten salt as both the HTF and the energy storage medium. Solar Two was also the first central receiver system to achieve thermal energy storage with molten salt, and it had a three-hour energy storage capacity. The plant's three-year service aided the commercialization of molten-salt power tower technology significantly. Gemasolar, the second solar tower system, was built in Spain in 2008. Gemasolar has a 17 MWe capacity and 15 hours of thermal energy storage for off-peak use. This was the first commercially successful central receiver facility, and it used molten salt as both the HTF and the energy storage medium [175].

Molten salts have far greater volumetric thermal and viscosity capacity (at their respective operating temperature) than oil-based HTFs from the thermophysical standpoint. Table 2.10 provides a representative list of various molten salts and their thermophysical characteristics [176]. The majority of today's salts are dependent on nitrates/nitrites, which are found in a variety of HTFs. However, the processing of nitrate salt is limited around the world. Although their own thermal properties restrict the salts' high-temperature stability, the stability of piping and container materials must also be considered when it comes to the temperature range under which the salts are treated[163].



**Table 2.10:** List of various molten salts and their thermophysical characteristics[163, 176]

Fluid	Chemistry	Temperature range	Density (kg/m <sup>3</sup> )	Specific H. (kJ/kg·K)	Viscosity (mPa·s)	Thermal C. (W/m·K)
<b>Nitrates</b>						
Hitec	NaNO <sub>3</sub> –NaNO <sub>2</sub> –KNO <sub>3</sub>	142 to 535 °C	886	1.85	22.7	0.124
Solar Salt	NaNO <sub>3</sub> –KNO <sub>3</sub>	220 to 600 °C	375	10	25	0.134
<b>Chlorides</b>						
K-Mg chlorides	KCl–MgCl <sub>2</sub>	435 to 800 °C	1060	1.57	3.57	0.136
Halotechnics SS-700	–	257 to 700 °C	2310	0.79	4	0.35–0.4
<b>Fluorides and Carbonate</b>						
FLiNaK	LiF–NaF–KF	454 to>900 °C	2020	1.88	2.9	0.92
Li-Na-K fluorides	LiF–Na <sub>2</sub> CO <sub>3</sub> –K <sub>2</sub> CO <sub>3</sub>	~400 to 920 °C	2100	1.9	–	1.18
Li-Na-K carbonates	Li <sub>2</sub> CO <sub>3</sub> –Na <sub>2</sub> CO <sub>3</sub> –K <sub>2</sub> CO <sub>3</sub>	~400 to 850 °C	2143	1.45	4.3	1.25

While salt-based HTFs are very promising, further research and development can still be significantly improved. The issue of solidification of molten salts when at sundown is one of the most important areas of research. Hitec Solar Salt, for example, has a freezing point above 140°C that gives an important consideration to anti-freezing strategies because of its diurnal nature. The practicality of using molten salts in parabolic solar dry collectors has also been studied and has also identified salt solidification as one of the biggest problems of this technology [177].

Ultimately, the consolidation of salt increases costs by freeze prevention mechanisms. These problems have traditionally been resolved by the continuous circulation of fluid over the day (added pumping costs), by auxiliary heats (fuel costs added) or electric heaters along the pipeline (electricity cost added) [178]. Researchers, therefore, consider it of great importance that the freezing point of these HTFs should be reduced without compromise to their thermal fluid performance [163].

Bradshaw and Siegel [179] investigated the chemical stability of molten salts and identified key mechanisms for degradation. The nitrite production process in the HTF is done in the presence of oxygen and depends on the partial pressure in the area. The nitrate reaction was identified as the characteristic degradation process irrespective of other existing components. Nitrates also react in the air to carbonates and oxides with carbon dioxide and moisture to degrade the characteristics of the salt mix. Molten fluoride salts may release harmful acids such as HF with exposure to the atmosphere and increase metal corrosion rates considerably.

Consequently, it is important to carefully monitor the operating environment of some molten salts.

Another problem to tackle is the corrosion of metal alloys by molten salts. Although several common nitrate-based salts, like Hitec, demonstrated an insignificant corrosion of seamless stainless steel, other copper and nickel-based alloys reported 1-10  $\mu\text{m}$  annually at 570 °C of corrosion. For halogen-based salts, the rates of corrosion can be  $>100 \mu\text{m}$  a year [180]. For use with chloride and fluoride salts, pipes and containers made in Inconel and Hastelloys have been recommended. Further experimental studies are needed to establish the material compatibility of molten salts in the presence of air and impurities at different temperatures.

### 2.2.8.3. Water/steam

The HTF transports the heat to the power cycle in a traditional solar thermal power plant, most frequently a water-steam cycle like a steam-Rankine plant. The idea of direct steam generation was tested by engineers to prevent high costs in connections with HTF or the large heat exchanger equipment that combined the HTF with the power cycle (Direct steam generation). Such systems have been researched and developed since the 1980s when alternatives to oil-based technologies were investigated [181].

Water collects heat directly, and it is transformed into overheated steam that is fed to the power cycle directly. The high-temperature water-vapour mixture ( $>400 \text{ }^{\circ}\text{C}$ ) has an increase in heat capacity compared to other gases, thus improving the receiver efficiency and power cycle [163]. On the other hand, the thermal energy obtained at the receiver is brought to the steam generator by the non-water dependent HTF and then transferred to the working fluid (usually water/steam) if the HTF is not water/steam. After that, the working fluid transports the energy to the turbine, which generates electricity. The use of water/steam as both HTF and a working fluid simplifies the system and improves performance, thus lowering electricity production costs [182].

The feasibility of DSG at the Direct Solar Steam plant at the Plataforma Solar de Almeria (PSA) in 1997-98 was initially demonstrated under real conditions [183]. The success of DISS and other studies has resulted in the development of pre-commercial DSG systems in Andalusia, Spain (11 MW PS10 and 20 MW PS20 plants, including the 5 MW INDITEP plant, as well as commercial power generation plants) [184, 185]. The results of these projects point to an 8 - 14% decrease in the use of synthetic oils as HTF for LCOE in comparison to SEGS-like plants [186].

Although the engineering problems arise because of the two-phase flow, several of them must be addressed despite promises of direct steam generation. These include the higher operating cost resulting from the high pressure necessary to pump the two-phase mixture [187]. The non-uniform transmission of heat from the pipes leads to large distribution in temperatures that can damage the pipes. The temperature and pressure at the outlet at a system level are another major concern. Current work on collector loop and power cycle design, temperature control and pressure control and collector piping cost savings are therefore central to research work [180].

In the most recent and largest CSP project, the Ivanpah solar power facility, which was launched in February 2014, water/steam is used as both HTF and working fluid. There are currently seven commercial CSP plants in operation around the world, all of which use water/steam as a single fluid. The first four plants (Puerto Errado 1, Puerto Errado 2, PS10 solar power tower, and PS20 solar power tower) are in Spain, while the remaining three are in California (Kimberlina solar thermal energy plant, Bakersfield, Sierra sun tower, Lancaster and Ivanpah solar power facility, Ivanpah dry lake) [37].

All of these plants were constructed between 2007–2014. Since these CSP plants are mainly located in deserts where vast land areas and high direct solar radiation intensity are available, the main problem with the water/steam HTF is a water shortage in desert regions [188]. At different temperatures and pressures, the viscosity of water/steam was recorded as  $2.0\text{E-}5$ ,  $2.9\text{E-}5$ , and  $3.7\text{E-}5$  Pas for steam at 300, 500, and  $700^\circ\text{C}$ , respectively, all measured at 40 atm. The thermal conductivity of water/steam is well-known, with values of 0.051, 0.069, and 0.096 W/(mK) for steam at the temperatures and pressures described above [37]. In the literature, high-temperature steam corrosion has been observed in a variety of alloys [180].

#### 2.2.8.4. Air/Gases

In large CSP plants, air is a relatively rare HTF. Only one system was built, a pre-commercial 1.5 MWe plant, which started operation in 2009 in Jülich (Solar tower of Jülich). A large temperature range can be reached with HTF air [164, 189]. In the solar tower of Juelich, the air is heated to around  $700^\circ\text{C}$  [146] at atmospheric pressure, and then hot air is deployed to generate steam. It is a research facility and model project in Southern Europe and North Africa, as well as for future power stations. The main advantage of this technology is its economic efficiency and high efficiency, as the atmospheric air is abundant and free of cost [190].

Furthermore, because air is very low in dynamic viscosity (about  $3\text{E-}5$  Pas at  $500^\circ\text{C}$ ) [189] in comparison with other fluid HTFs, such as moulded salts (app  $200\text{E-}5$  Pas for 'solar salt' at 500

°C) and fluid metals, air has good flow characteristics within the pipelines on the CSP system. Although the thermal conduciveness of the air is low compared with that of molten salts or metals [189], an additional advantage in efficient heat transfer is the improved flow property of the air. In Europe and Israel, air HTF is primarily investigated and tested, while the focus in the United States is on molten-salt HTF technology [191].

The complexities of handling heat transfer fluids can be reduced with gases such as chemical stability, material compatibility problems, screening and safety. Moreover, they can work at higher receiver temperatures, leading to greater efficiency in energy conversion and reduced operational costs. One promising prospect is direct expansion with the same fluid both in the receiver and in the turbine, thus reducing complexity and eliminating the need for a heat exchanger. Notwithstanding, the poor thermal capacity of the gases, which can be overcome with high pressures and high mass flow rates, is one of the biggest drawbacks.

Since its critical point (31 °C) is close to air temperature, CO<sub>2</sub> has been extensively studied as an HTF. The close proximity of the critical point results in significant cycle efficiency improvement, as a sharp increase in heat capacity of fluid is observed [192]. Several studies have examined the improvement of the performance of solar thermal systems (parabolic trough and Fresnel) with the use of close-critical CO<sub>2</sub> cycles, multi-stage enlargement/compression and regeneration and receptor design optimisation [192-194].

One of the disadvantages of using CO<sub>2</sub> is, however, that the cycle is to be shut, i.e., the liquid must be recirculated from the condenser into the turbine and back to the collector. Thicker pipes and leak prevention measures are required. However, the promise made by combining directly with the supercritical CO<sub>2</sub> cycle, high efficiency, and compact size has made CO<sub>2</sub> an attractive HTF [195, 196].

Unlike CO<sub>2</sub>, the use of air as HTF is simpler because of the operating pressure that can be close to the environment. There were no significant differences between air and CO<sub>2</sub> as HTF in terms of receiver performance [193]. However, the use of air offers other advantages, such as compatibility with thermal bunker storage and no fluid cost. For these reasons, air is usually used in central systems because the large area of a cavity receiver offsets the low heat transfer capacity of gas-based HTFs. [197, 198]. Research with other gas-phase HTFs, such as N<sub>2</sub>, have exhibited performance similar to synthetic oils; however, commercial development is unlikely due to the high capital cost [199].

A range of low carbon steel (containing 0,03–0,12%) high-temperature oxidation features in air was investigated [200–202], and high-temperature oxidation was found to be consistent with parabolic law, and impurity elements in commercial steels have different effects on oxidation. Materials like silicon, aluminium and chromium generally improve the resistivity of oxidation in the form of protective layers. In contrast, more noble metals like nickel, tin, and copper have a mild effect on steel oxidation [200, 202, 203]. Higher carbon steel content is good for reducing oxidation rate when the temperature is above 700 °C [202].

Other gases, such as helium and supercritical CO<sub>2</sub> (s-CO<sub>2</sub>), have been investigated for use as HTFs in CSP systems in addition to air. Helium was commonly used as a working substance in high-temperature nuclear reactors and was also relatively inexpensive due to its production from natural gas [204]. Massidda and Varone [205] studied heat transfer, pipe stresses, and pressure drops for Helium-based HTFs in solar absorber tubes in a recent numerical analysis-based investigation. Helium, like air, can be used at extremely high temperatures [204], allowing for higher performance. However, the low density and heat transfer between the fluid and the internal surfaces of the pipelines are major drawbacks. As a result, high pressures and fluid velocities are needed [205].

According to Ma and Turchi [206] of the NREL (National Renewable Energy Laboratory, Colorado, USA), s-CO<sub>2</sub> has the ability to function at extremely high temperatures and can be deployed as both an HTF and a working fluid for the power block [206]. In comparison to steam Rankine and helium cycles, s-CO<sub>2</sub> can achieve higher efficiencies at lower temperatures, resulting in better CSP efficiency. Because of the high pressures used, s-CO<sub>2</sub> is not suitable for PTC, which uses a large number of pipelines, but it is suitable for power towers.

#### **2.2.8.5. Liquid metals**

Since the 1940s, liquid metals have been used in nuclear power plants [164], and they are now being investigated for use as HTFs and thermal energy storage media in solar thermal systems. Despite the fact that liquid metals have yet to be used in commercial CSP applications, they have a number of promising characteristics, including a broad operating temperature range, low viscosity, and effective heat transfer. Liquid sodium, for example, has a temperature range of 98–883°C [164, 207].

Liquid metals have superior heat transport characteristics with high operating temperatures. Low steam pressure, high thermal conductivity and relatively low viscosity of liquid metals make these attractive choices. As a result, liquid metal figure of merit are approximately a

magnitude order higher than molten salts and several orders more than pressurised air, which enables operation at higher heat flux densities. Furthermore, efficiency is enhanced by operation at 700-1000 °C fluid outlet temperatures, compared to the current <650 °C [208].

The performance of liquid metals as an HTF is analysed by Pacio et al. [164, 209], and three promising candidates were compared: liquid sodium, Lead-Bismuth Eutectic (LBE) and molten tin (Table 2.11). The most positive characteristics of liquid sodium include the highest thermal capacity, the lowest density and point of melting. It also has relatively low costs and is compatible with common building materials such as steel. Liquid sodium and, to a lesser extent, LBE for operation in the nuclear sector have been investigated.

**Table 2.11:** List of Some Ionic Liquids and Liquid Metals Their Thermophysical Properties

Fluid	Substance	Temperature range in °C	Density (kg/m <sup>3</sup> )	Specific heat (kJ/kg·K)	Viscosity (mPa·s)	Thermal c. (W/m·K)
<b>Ionic Liquids</b>						
[emim][BF <sub>4</sub> ]	1-methyl-3-ethylimidazolium tetrafluoroborate	14 to 446 °C	1253	1.28	36	0.2
[bmim][BF <sub>4</sub> ]	1-methyl-3-butylimidazolium tetrafluoroborate	-87 to 424 °C	1175	1.66	120	0.19
[dmpil]Im	1,2-dimethyl-3-propylimidazolium bis(trifluorosulfonyl) imide	11 to 457 °C	1421	1.2	90	0.13
<b>Liquid Metals</b>						
sodium	Na	98 to 883 °C	808	1.25	0.21	46.0
lead-bismuth eutectic alloy	44.5–55.5 wt% Pb–Bi	125 - 1533 °C	9660	0.15	1.08	12.8
molten tin	Sn	232 - 2687 °C	6330	0.24	1.01	33.8

Alkaline metals, such as sodium, both in air and water, have high reactivity and are therefore potentially unsafe. LBE is relatively safer, as, in the presence of air and water, it oxidises slowly, but at high temperatures, it corrodes steels far faster than sodium. Studies of LBE's material compatibility with alternative structural materials like tungsten, molybdenum and aluminium-coated stones have proved promising and are currently being studied [210]. Molten tin has good thermophysical properties, but it needs to address its high melting point and incompatibility with steel at operating temperatures.

#### 2.2.8.6. Organics

In CSP frameworks, organic materials are often used as HTFs. For example, in commercial CSP systems, the biphenyl/diphenyl oxide pair (also known as Therminol VP-1) is commonly

deployed, especially in thermal plants in Spain. Biphenyl/Diphenyl oxide ( $C_{12}H_{10}O$ ) [163] is a eutectic blend of two very stable organic compounds, biphenyl ( $C_{12}H_{10}$ ) and diphenyl oxide ( $C_{12}H_{10}O$ ). A recent analysis [146] provides a list of plants that use biphenyl/diphenyl oxide. The first solar thermal plant using this organic material as the HTF, known as 'Alvarado 1,' was completed in 2009 in Badajoz, Spain. Biphenyl/Diphenyl oxide is currently used in eight solar thermal plants around the world, all of which are located in Spain.

This Biphenyl/Diphenyl oxide has a very narrow operating temperature range of 12–393 °C [146]. Therminol fluid and Dowtherm fluid are two commercially available biphenyl/diphenyl oxide HTFs. In the solar energy generation system in Mojave Desert, CA, Therminol fluid was used, and Dowtherm fluid was used in Nevada Solar One in Boulder City, NV. The Dowtherm fluid has a viscosity of 0.00059 Pas and a thermal conductivity of 0.01 W/(m K) at 300 °C [163].

Cabaleiro, Pastoriza-Gallego [211] studied the thermo-physical properties of this organic mixture, Biphenyl and Diphenyl oxide, as well as the eutectic compound, in a recent analysis (Therminol VP-1). Depending on the ratio of biphenyl and diphenyl oxide, the density values vary from 0.9971 to 1.0902 g/cm<sup>3</sup>. It was also discovered that the density increased as the diphenyl ether concentration increased. At the operating temperature range and 1 atm pressure, the average thermal conductivity of these mixtures was found to be 0.13 W/(mK). Therminol VP-1's heat capacity could be increased by 5.45 by adding 1 wt% SiO<sub>2</sub> nano-particles.

### **2.2.9. Power cycles for concentrating solar power**

A range of various solar to electric energy conversion systems can be deployed to the different concentrator types.

#### **2.2.9.1. Organic Rankine cycle**

Thermal energy conversion technologies are major subjects that have drawn much attention in recent years. The Organic Rankine Cycle (ORC) is widely regarded as a promising technology to produce low thermal electricity. As an attractive candidate for low-temperature application, ORC can make greater and/or more extensive use of its energy source to meet electricity demands and other applications such as the desalination of seawater and increasing the energy efficiency in the industrial sector [15].

Moreover, the use of residual heat rejected by the industry, which makes up more than half or more of the heat generated in the industry's installations, also need to be harnessed. However, as conventional steam power cycles struggle to improve the recovery of low-grade heat, it is

imperative to seek alternative means that can present a better performance of low-grade heat recovery. Organic Rankine Cycles are such enabling technology that can play a significant role in this regard. Its low-temperature application makes them a suitable choice for electricity generation, among others [15].

Several power plants were installed in the MW range worldwide over the previous decade. Despite its potential for the market, however, the penetration of ORC power stations within the kW range for several reasons did not reach a high level of maturity. The specific price remains too high for an attractive payback period, and that small ORCs are usually for SMEs (small and medium enterprises) who are generally less aware of the potential savings which this technology might generate. When it comes to small-scale plants, further design problems still arise, which limit broad technology availability [212].

With a total installed capacity of 4.95 MW [213], the ORC's market capacity in the 1-100 kW range is small. The high specific cost of technology is currently not competitive with other existing technologies despite the large market potential for small-scale ORC (e.g., wind, solar, etc.). In order to maximise the power generation of such power plants, efficiencies of the ORC components should be improved while maintaining the lowest possible cost. For the future development of ORC for decentralised power production, a compromise between these two parameters is essential [212].

An organic Rankine cycle turbine is fundamentally similar to a steam Rankine cycle; however, it employs a lower boiling point organic fluid, which makes it compatible and suitable for low-temperature applications. For smaller systems, in the form of a few kWe (1-100) ORC systems may achieve higher efficiencies than steam turbines. However, compared to water/steam systems, capital and operational maintenance (O&M) costs are higher per built MWe. ORC has been employed in various forms of low-temperature heat sources, including solar energy, geothermal energy, biomass energy and waste heat energy [214].

In general, ORC power systems include four main components - evaporator, condenser, pump and expander. The evaporator and condenser are main heat exchangers, which should be properly designed to operate under certain conditions with specified fluids. The present state of the art can be seen as sufficient for the technological requirements to ensure that heat exchangers are available as condensers and evaporators. The pumps were also well developed and can be purchased from the stand to meet the ORC system requirements [215].



The expander can, however, be regarded as the most advanced technical element of the ORC system. Expanders are the machines that harness the energy of high-pressure vapour expansion, which results in low pressure while passing through their inlet to the outlet port and then convert fluid energy into mechanical energy (rotational or reciprocating), often transformed into electric power through direct or indirect connections to a generator. In the general case of the organic Rankine cycle, the thermodynamic efficiency of the heat sources and thermal sinks is low due to limited temperature differences. The overall cycle performance is therefore highly sensitive to expansion machine efficiency [216]. Hence, the choice of an appropriate expander for a specific ORC application is therefore very important if further reductions in efficiency and commercial viability are to be avoided. Different expansion machines can be used depending on working fluid, application conditions (temperature, pressure, mass flow rate), and power levels [215].

#### **a. Primary classification of expanders**

The expansion machines are generally classified according to the nature of their operations. They are generally categorized as turbo-machines or volumetric-type machines. Dynamic pressure or high-speed fluid momentum are converted into mechanical energy when passed through a number of blades. The exiting fluid usually has low pressure and experiences a total enthalpy drop during the passage through the machines. Turbomachines are deployed in medium-to-large scale applications more commonly and are known for their higher efficiencies at the expense of a more complex technology [212]. Volumetric machines are cheaper, but performance is also lower, and often, these are preferred options for smaller power output (<50 kWe) [215].

Machines of a volumetric type are also called positive displacement machines. They work on a moving mechanical component for extracting power based on the principle of the force application. The pressurised liquid enters a chamber and increases the volume of the chamber by using a compressed fluid to apply the net force. The low-pressure fluid is released out of the expander when the chamber reaches its maximised expansion volume. Valves are often used to control the inlet and outlet flow of fluid and synchronise with the expanding chamber in volumetric machines. The volumetric expanders are suitable for small power outputs, often derived from compressors that have been reversely modified to heat, ventilation, air conditioning and cooling (HVAC). There are challenges and benefits associated with both turbomachines and volumetric expanders along with various types available for each main category [215].

The most common Turbo-expanders in the literature are radial inflow, radial outflow, and axial turbines [17, 217, 218]. Turbo-expanders are convenient in their high-power production range as opposed to volumetric machines, while they are inefficient in low electricity production. This is mainly due to high rotation speeds that lead to the failure of the bearing.

### **1. Turbo-expanders**

In the turbo-expander operation, a fluid with high pressure is sent into the turbine inlet from the evaporation outlet. The high static pressure of the fluid passing through nozzles is converted into a high flow velocity. The high-velocity fluid transfers its momentum to an assembly of rotating blades. The rotating blades are connected to a shaft coupled to the generator in order to transform mechanical energy into electric power [215].

Turbines used in ORC application generally differ from air, steam and other gas expansion machines because the enthalpy decrease is considerably higher than that used in the steam cycles. In ORCs, therefore, fewer turbine stages are needed, resulting in cheaper and light turbines. The dense vapour properties, however, largely vary from the ideal gas performance and the speed of sound is far less than that of lighter gases and steam, which influence the design of the nozzle [219]. In dense molecular fluids the low speed of sound often results in turbines operating in supersonic and transonic modes. As a result, a highly dissipative shockwave is common in such machines, which in off-design operation complicates the design and particularly at the expense of performance [220].

There are two major categories of turbo expanders: axial turbines and radial turbines, as shown in Figure 2.63 (adapted from [221]). In relation to the shaft, the main difference between the two categories is the flow of the working fluid. The flow of the working fluid in axial turbines is parallel to the shaft, whereas it is radial to the shaft at the inlet, which is converted into axial at the turbine outlet in radial turbines.

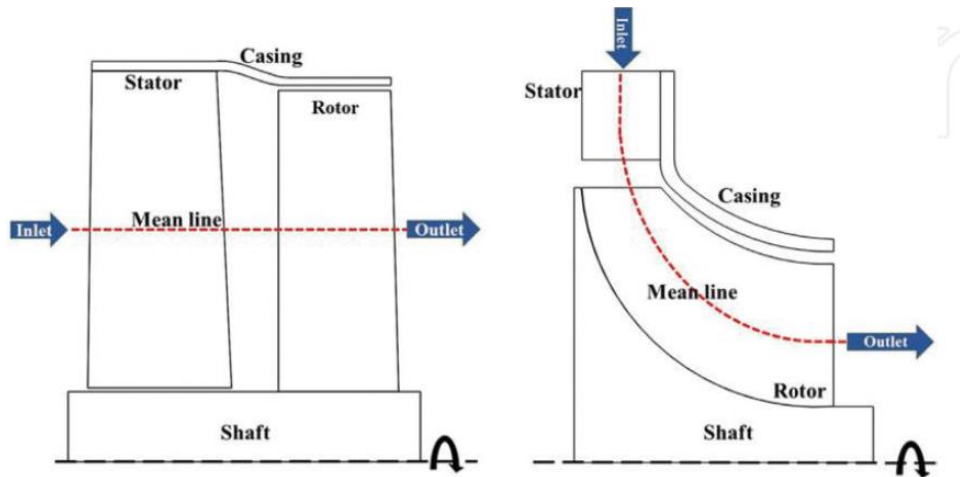


**Figure 2.63:** Schematic of axial flow (left) and radial inflow (right) turbines [221]

The selection of the appropriate turbine (axial or radial) is based primarily on the required operating conditions and resultant enthalpy drop. The axial turbine blades become very small at low mass flow rates, which leads to a significant efficiency drop due to the difficulty of maintaining a small tip clearance between the blades and the shroud. Therefore, in large-scale applications, axial turbines are always preferred where the mass flow rate is high, and the pressure rate is low. Radial turbines, in contrast, are used for low mass flow rate and high-pressure ratios applications such as turbochargers and ORC systems.

The radial turbines are less sensitive to the blade profile than the axial turbines at small flow rates. Thus, resulting in increased efficiency. In addition, high-density fluids are used in ORC applications which require a more robust turbine due to increased blade loading. In this case, the radial turbines are preferable because their blades are rigidly coupled to the hub. Radial turbines can handle a single-stage expansion ratio of 9:1 because of the radius reduction from rotor inlet to outlet, whereas axial turbines require a minimum of two stages. Therefore, if the system size is considered, radial turbines will also be preferable [215].

However, axial turbines generally provide improved performance under off-design conditions. In large-scale applications, such as large gas turbines, axial turbines have better efficiency than radial turbines due to the elimination of the flow turning in the meridional plane. Moreover, the disc is protected in the axial turbine at high temperatures because only the blades are exposed to heat. In radial turbines, the blades and the disc are both exposed to heat since expansion occurs at the inducer and at the impeller exducer. It should be mentioned, however, that ORC turbines normally operate at low temperatures where the high-temperature concerns are substantially lower than other applications [215].

**Radial Inflow:** The meridional view and overall turbine stage architecture of a radial inflow turbine (RIT), sometimes also called the inward flow radial (IFR 90), is presented in Figure 2.64. The high-pressure fluids, as can be seen, enter the inlet of the casing (volute), with its initial flow direction mainly radial that, at the rotor inlet stage, converts to the tangential direction and contains both radial and tangential components. The flow loses its tangential component while passing through the rotor. At rotor output, the outflow must have a minimum swirl flow.

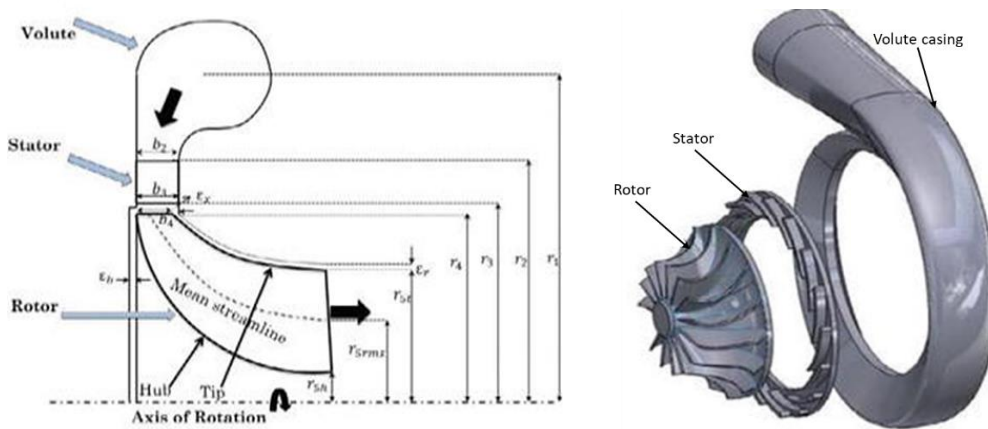


**Figure 2.64:** Meridional view (left) and architecture of turbine stage (right) [215]

The geometric parameters stated in Figure 2.64 are determined from the design process. They are defined as follows:  $r_1$  as volute inlet radius,  $r_2$  as stator inlet radius,  $r_3$  as stator exit radius,  $r_4$  as rotor inlet radius,  $r_{5t}$  as rotor exit tip radius,  $r_{5h}$  as rotor exit hub radius,  $b_2$  as nozzle inlet diameter,  $b_3$  as nozzle exit diameter,  $D_4$  as rotor inlet tip diameter and  $\xi$  as clearance.

The advantages of using radial turbines specifically for small-scale units over axial machines are listed below:

- Radial inflow machines are often produced as single-piece cast or forged machines, whereas axial machines often require separate production of blade and rotor.
- Single-piece rotors are more robust, stiff, and have improved rotor-dynamic stability, resulting in reduced overall cost.
- RITs can present improved off-design performance when variable geometry nozzles are deployed.
- Downsizing the axial machines for small ORC applications necessitates very small and numerous blades, which increase the wetted area, friction losses and blocking effect of the blades. The running clearance required between the rotor tip and casing becomes

an important fraction of the blade height, which means higher proportionate losses due to leakage.

- RITs aid larger pressure ratios in a single stage (up to 10 is common for RIT, but the axial might need three stages).

In Order to improve the system's performance, Kang [217] built and tested an ORC employing R245fa as the working fluid based on a two-stage radial-inflow turbine. The results showed power, turbine isentropic and cycle efficiencies of around 39 kW, 58.4% and 9.8%, respectively, with an evaporation temperature of 116 °C. By deploying variable temperature and mass flow rate, an off-design analysis of ORC system performance for a geothermal application using a radial-inflow turbine was carried out by Hu, Zheng [222]. With R245fa as the preferred working fluid, turbine efficiency, power output and ORC system efficiency 82.3%, 66.9 kW and 5.5% were realised at the design point and mass flow rate of 5.85 kg/s. A 1D analysis and 3D simulation of a radial-inflow turbine were conducted in [223] using different operating conditions, including off-design conditions deploying R143a as a working fluid. The system attained maximum efficiency and power outputs were 87.6% and 421.5 kW, respectively.

**Radial Outflow:** In a radial outflow turbine (ROT), the direction of the flow differs from that of a radial inflow machine. The flow enters the ROT through the centre, near the rotation axis, axially and then passes through the rotor and the station blades in the radial direction. The schemes of radial outflow turbines, which are also known as centrifugal turbines, are shown in Figure 2.65 (adapted from [224]).

In organic fluids, the low speed of sound necessitates supersonic or at least transonic flows that cause shock formation and interaction losses. The wide volumetric expansion of organic fluids demands wider areas to minimize losses at the exit of turbines. The ROTs can be inherent in the area as the flow moves in the radial path, thus avoiding supersonic flows and decreasing losses by the use of high-efficiency turbines.

The ROTs enable multi-stator-rotor ring arrangements to be implemented in a radial direction that maintains low rim speeds, leading to low mechanical stresses, reduced rotary losses and simple generator and grid connections. In addition, complete inlet stages can be modified. The ease of assembly over many stages makes it possible to reduce tightened tolerances and losses [215].

The ROTs main drawback is attributed to their lower performance than RITs as a wide area is in fluid contact during the flow. Moreover, the first phase often has inadequate flow passage areas for heavy/large molecular working fluid because of the inherent radius-to-surface square root proportions, which limit turbine applications for high-temperature applications. Compared to micro-/mini-ORC applications, ROTs are more appropriate for small-scale applications.

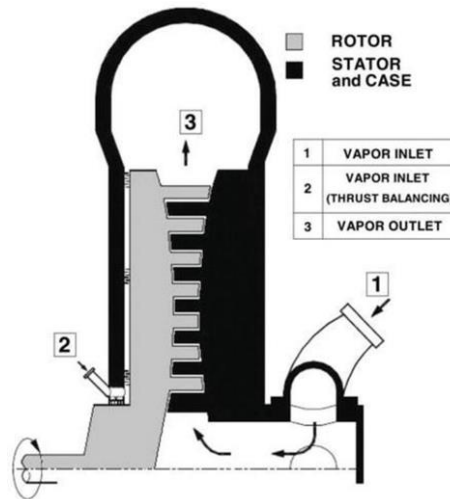


**Figure 2.65:** Schematic of radial outflow turbine [224]

An experimental investigation on a kW-scale ROT was performed by Pei, Li [225], using R123 as the preferred working fluid. The investigation was carried out using a radial-flow turbine with a maximum temperature change of 70 °C between the hot and cold sides; cycle and isentropic efficiencies were 6.5% and 65%. Using R245 as a working fluid and a low-temperature heat source, a radial-flow ORC turbine was experimentally investigated by Kang [226]. The maximum turbine efficiency of 78.7% was realised, in addition to the power output and cycle thermal efficiency 32.7 kW and 5.22%, respectively.

**Axial turbines:** The axial turbines are distinguished by the primary working fluid flow in the axial direction and parallel to the axis of rotation. For larger flow rates, axial machines are more suited, which means that their speed is higher. These machines are frequently suited in the ORC technology to medium to large power outputs in single or multi-stage settings ranging from 1 to 5. In nominal operations, isentropic efficiencies range from 80 to 90% [219] for axial machinery. The most commonly used turbocharged machines for power generation are axial machines, with approximately 70% of the power generated as the preferred large expander units.

One of the limitations of axial machines is that the axial channel experiences span-wise extensions with a negative effect on performance, taking into account the broad-scale expansion ratios. In addition, at the stator exit and at the converging-diverging nozzle arrangement, highly supersonic conditions are found that may not be conducive to good off-design performance. Axial machines have few limitations but are also popular in nuclear power applications with megawatt power output in ORC applications. They are adapted to large scale applications in power plant applications with steam or Brayton cycles [215].

Axial machines are adaptable, and the reasons for their flexibility include the following:

- Pressure can be as high as 300 bar (supercritical cycle) or too low (few hundredths of a bar, last stages of the steam cycle).
- The overall pressure ratio could be as high as several thousand or as low as 1.0002 in wind turbines.
- The diameters could be ranging from a few centimetres to 100 m in wind turbine applications.

The influence of mass flow rate and evaporation pressure on ORC performance was experimentally investigated by Pu, Yue [17] using a small-scale ORC system based on a single-stage axial turbine. The highest power output from the ORC system was 1979 W and 1027 W for R245fa and HFE7100, respectively. Al Jubori, Al-Dadah [227] proposed a new methodology integrating an ORC based on a small-scale axial turbine with R123 as the working fluid for a turbine of 70 mm mean diameter. Findings from the study show maximum isentropic efficiency and power output 82% and 5.66 kW, generating cycle efficiency of 9.5%.

Da Lio, Manente [228], [229] suggested and performed a preliminary mean-line design for an axial turbine stage with different maps of isentropic efficiency for various working fluids. The design and optimization of a partial-admission axial turbine used in an ORC system were performed by Martins, Braga [230]. R245fa was employed as the working fluid with the Redlich–Kwong–Soave equation of state as a real gas model for heat recovery below 140 °C. Maximum efficiency of about 81% was attained with a convergent nozzle.

## **II. Volumetric expanders**

The four main categories of Volumetric expanders can be classified into scroll, screw, piston, and rotary vane. Contrary to the turbo-chargers, in volumetric expansions, the fluid movement is cyclic. The fixed volume expansion ratio is an inherent feature of this type of expander. They operate by trapping the fluid with a fixed volume and moving it to the machine discharge,



causing mechanical work due to the pressure reduction. They are therefore also referred to as displacement expanders [215].

Some volumetric expanders, unlike turbines, may have valves at the inlet and outlet ports. The compressed fluid is fed into a chamber, the inlet valves are closed, the expansion process begins, and the outlet valve is opened to release the low-pressure fluid at the end of the expansion. These may be useful for controlling the timing and flow via an expander, but at the expense of significant losses. Piston-type expanders often have valves and scroll machines may also have these valves; however, screw, scroll, and vane type-expanders generally run without valves.

Another unique feature of volumetric expanders is the need for lubrication. Since they work on the concept of changing volumetric power, some parts must move in contact with other surfaces in order to increase the volume available for expansion. The friction created by the contact movement increases the wear, tear, and heat generated by the surfaces. Lubricant oil is frequently circulated, especially in the scroll- and screw-type expanders, to reduce friction, seal clearances, and minimise leakage losses [215].

**Scroll Expanders:** As shown in Figure 2.66, scroll expanders are made up of two spirals: an orbiting scroll and a fixed scroll. Within close tolerances, the orbiting scroll moves in tandem with the fixed scroll. Inside the chamber, the working fluid flows inwards from the centre and outwards between the orbiting and moving scrolls. They are popular because they can be made from a scroll compressor, lowering the machine's cost. The scroll expander may be restricted or compliant. A lubrication system is required in the first case to minimise friction between the contacting sidewalls. Due to the existence of a linking mechanism between the rotating and fixed scrolls, lubrication is not necessary for the latter. Furthermore, there are no exhaust valves needed, resulting in a reduction in noise [215].

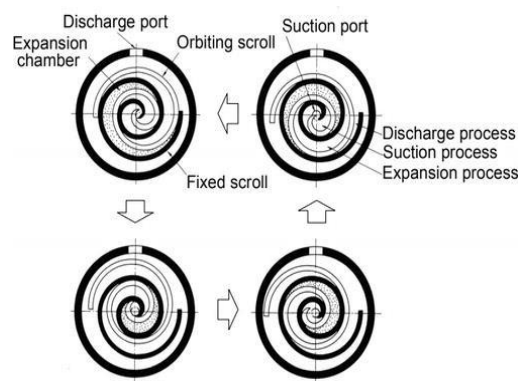


**Figure 2.66:** Operation of the scroll expander [231]



Due to their slow speed, scroll expanders are typically used in low-power applications (less than 10 kWe). Furthermore, they are favoured in small-scale applications due to their low part count, which reduces noise, improves reliability, and reduces cost. Scroll expanders have a volumetric ratio of 1.5 to 5, and a maximum power output of 12 kW has been recorded [232]. Scroll expanders can also have a high efficiency of up to 80%, depending on the operating conditions.

Eyerer, Wieland [233] replaced R245fa as the working fluid with the low-global-warming-potential fluid R1233zd in an analytical and experimental study of ORC for low temperature applications using a scroll expander. The investigation was conducted for various rotational speeds, mass flow rates and condensing temperatures. The results indicated that R1233zd surpassed R245fa by 6.92% in terms of cycle efficiency. Chang, Hung [234] experimentally investigated a low-temperature organic Rankine cycle for heat source temperatures below 100 °C, using a scroll expander and R245fa as the working fluid. The findings from the study showed expander efficiency, power output and cycle thermal efficiency of 73.1%, 2.3 kW and 9.44%, respectively.

**Screw Expanders:** Screw expanders are made up of two helical rotors with precise profiles that capture the required amount of working fluid. A schematic of a twin-screw expander is shown in Figure 2.67 (adapted from [235]).

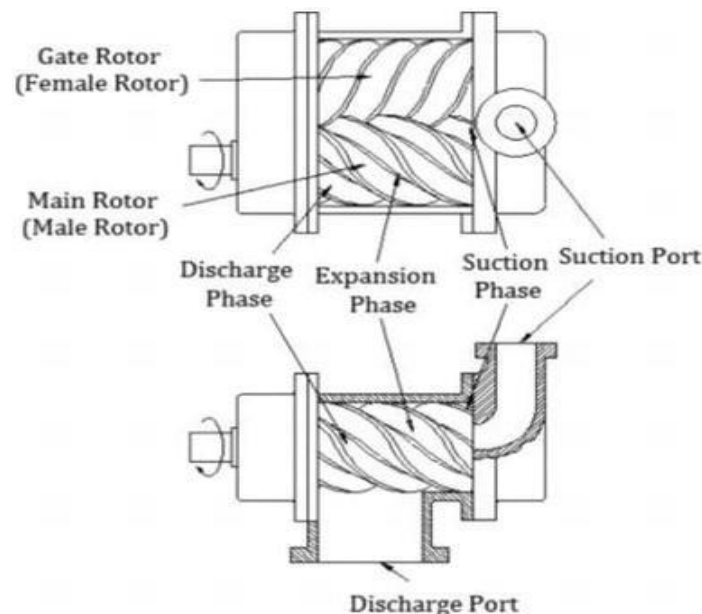


**Figure 2.67:** Schematic of a twin screw expander [235]

Volume profiles that start at one end of the rotor and terminate at the other end are generated by the synchronised movement of intermeshing rotors. In the meshed chamber, the working

fluid expands. Screw expanders can be used in systems of up to 1 MW of power output. Since the rotors are in direct contact, screw expanders require lubrication. If a fluid with a lubrication specification is used, however, lubrication may be avoided. Screw expanders, like scroll expanders, can work with wet working fluids because of their large mass fractions.

Since the rotor clearance is less than 50  $\mu\text{m}$ , leakage losses are minimal, minimising friction losses. Screw machines produce medium levels of noise and have high operating costs. The volumetric ratio can be anywhere between 2 and 8. The output power of an expander can range from 1.5 kW to 1 MW. It has been recorded that isentropic efficiencies can reach 70% [232]. They may run at higher RPMs than scroll machines, and if the machine runs at more than 5000 RPM, which is typical for screw machines, a gearbox might be needed. In ORC applications, screw machines are suitable for power applications ranging from 5 to 50 kW.

Clemente, Micheli [236] assessed the performance of various expanders, including radial turbine, axial turbine, screw and positive displacement expanders for heat recovery using a bottoming cycle design from the exhaust gases of a 100-kW gas turbine. The peak power attained was 26 kW with 8% cycle efficiency. Ziviani, Gusev [237] performed a numerical and experimental study of a single-screw expander for an ORC application with a heat source temperature of 125 °C. Two different working fluids (R245fa and SES36) were deployed. The results revealed that R245fa produced a 10% higher power output than SES36.

**Piston Expanders:** When the piston reaches the top dead centre (TDC), the working fluid enters the piston expander, and the inlet valve is closed. As the piston is moved by internal friction, the fluid expands, and the energy is transferred to the central crankshaft through the connecting rod. As the piston returns to TDC, the exit valve is opened at the bottom dead centre, and expanded working fluid begins to flow out of the chamber [215]

A single-piston or multiple piston-cylinder configurations may be used in piston expanders. The designs are not limited to piston-connecting rod and crank-based systems. Linear piston expanders, in which a single-piston oscillates in a cylinder and operates in two volume chambers at opposite ends, are gaining popularity. The axial arrangement, rolling pistons, and swash plates are some of the common types of piston expanders, in addition to the above.

As compared to corresponding turbomachines, piston expanders are considered to have lower isentropic efficiencies. The maximum efficiency registered is 76%, with the average being about 50% [232]. Piston expanders have pressure ratios of 6–14, which are relatively high. Volumetric expanders of this type are preferred in small- and micro-scale applications due to

their low power outputs. In general, the expander's output is estimated to be about 2 kW, but one study reported 18.6 kW with steam as the working fluid [232].

Piston expanders are capable of operating in two-phase working fluids. They are, however, heavy and prone to noise and vibration. Lubrication is needed in piston expanders, as it is in some volumetric expanders. However, it is difficult to enforce because the oil must be combined with the working fluid, lowering the cycle's performance. Weight balancing, torque impulse, heavyweight, precise valve control, and a large number of parts are the key drawbacks of piston expanders [221], but they have mature manufacturing technology.

**Rotary vane expanders:** The Wankel principle is used to control rotary vane expanders. A vane expander is depicted in Figure 2.68 (adapted from [232]). The working fluid reaches the expander at the spot having a small clearance. A rotor with moveable vanes is connected to a rotor that is asymmetrically oriented near the casing. The rotor rotates, allowing the vanes to travel outwards while trapping working fluid; as the rotation angle increases, the volume bound by successive vanes expands, causing the working fluid to expand.

Their power output is reported to range from a few watts to 2.2 kilowatts. Because of their modest rotational speeds, some volumetric expanders can be directly connected to the generator. Because of their simple design and low production costs, as well as increased torque and volumetric efficiency, they are typically favoured to minimise system costs. They're also commercially available and mechanically simple. They also have a low acoustic impact, as well as a basic and dependable structure. Due to leakages and increased friction losses, however, they have poorer isentropic efficiency than other volumetric expanders. Furthermore, to reduce wear and improve sealing, the machine must be greased. [215].

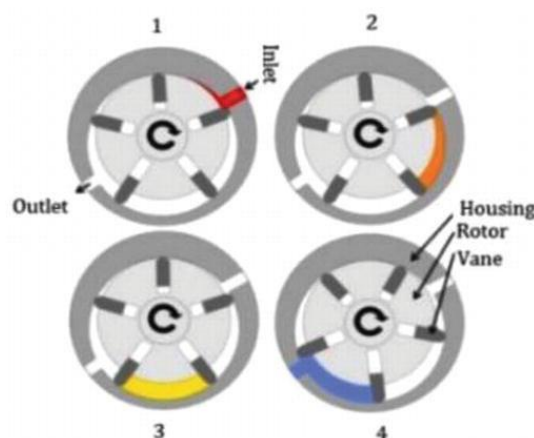


**Figure 2.68:** Operation of a rotary vane expander [232]

### b. Selection of the working fluid

The selection of a suitable working fluid is imperative to the performance of the organic Rankine Cycle. Depending on the application, the source, and the amount of heat to be deployed, the fluid must demonstrate excellent thermodynamic properties at the lowest possible temperatures and pressures and also meet some criteria, such as being economical, non-toxic, non-flammable, environmentally friendly and tolerating a high use of the available energy from the heat source. This limits the list to just a few fluids if all aspects that can restrict their use are considered, such as [238]:

- **Environmental:** As a result of growing concerns over sustainability criteria, mainly Global Warming and Climate Change, the Montreal and Kyoto protocols have produced guidelines on the Ozone-depleting Potential (ODP) and Greenhouse Warming Potential (GWP) of some fluids. The guidelines restrict the use of some fluids that are capable of causing destruction to the ozone layer and emission of gases resulting in the greenhouse gas effect.
- **Safety:** to avert any adverse effect resulting from leaks at the plant or during handling, the fluid must be non-toxic and non-flammable. In addition, the fluid should be non-corrosive to avoid higher costs of maintenance and/or damage to facility equipment. Thus, to ascertain the fluid's degree of danger, the ASHRAE security classification is used as an indicator.
- **Stability:** The temperature of the heat source can be limited by the chemical stability of the fluid deployed mainly due to breakages that could happen when exposed to certain temperatures, generating substances that could alter the manner in which the cycle works. In addition, it may result in toxic and irritating compounds that could cause health problems from leakages.
- **Pressure:** The complexity of the plant and equipment cost are usually higher when fluids requiring higher pressures are used due to the necessity to maintain high process efficiency.
- **Availability and low cost:** A fluid that is not readily available and/or high cost can present some challenges for its use in ORC plants for obvious reasons, in view of the financial feasibility of projects.
- **Latent heat and molecular weight:** A fluid can absorb more energy from the heat source in the evaporator when it has a greater molecular weight and latent heat. Thus, the consumption of the pump and size of the plant can be smaller as a result of the decrease in the flow rate required.

- **Low freezing point:** The freezing point of the fluid must be lower than the lowest temperature of the cycle.

Organic Rankine Cycle compatibility with low-temperature use makes the cycle's overall efficiency highly sensitive to inefficiencies in heat transfer, which relies largely on the fluid thermodynamic properties and its operating conditions. As a result, several types of research have been carried out to find a suitable fluid for such systems and meet all safety standards and environmental criteria [238].

An approach to evaluate the thermodynamic properties of working fluids under similar working conditions was carried out by Rayegan and Tao [239]. The effect of using alternative dry fluids on the efficiency of the ORC was analysed by Aljundi [240], and findings were compared with other refrigerants. Recently, research work [241] centred on evaluating multicomponent mixtures of working fluids with the aim to better match the heat and cold sources.

From a thermodynamic, environmental, physical properties (density, specific heat and latent heat), stability, compatibility, cost and safety point of view and their impact on the conversion of low temperature heats into electricity; the study of 35 working fluids was conducted by Chen, Goswami [242]. The results show that these properties play a significant role in the cycle performance.

Pu, et al. [17] investigated an ORC system comprising a single-stage axial turbine expander with an integrated turbine-generator. In their study, R245fa and HFE7100 were preferred as working fluids. R245fa was chosen as a working fluid for its appropriate evaporation pressure, overpressure on the condenser and comparatively high thermal efficiency. HFE7100 was also selected as the working fluid to be compared with R245fa. Deploying R-227ea as a working fluid, Borsukiewicz-Gozdur [243] experimentally investigated an ORC power plant and obtained an electrical efficiency of around 4.88%. Lee, Kuo [244] investigated the dynamic performance of a 50 kW ORC system considering the operating conditions of the condenser.

### **c. Applications of the ORC technology**

The versatility and modular aspects of the ORC and its suitability for low and medium temperature applications allow the repowering of plants in operation through the re-coupling process, mainly the use of residual thermal energy to produce electricity. Depending on the source, the energy from generated heat by deploying primary energy sources such as solar, biomass combustion or geothermal or from power cycle technologies and various heat recovery

sources such as waste heat processes can be used for electricity generation (Figure 2.69). In addition, heat extraction can be achieved, depending on the temperature of the heat source and the heat sink for heating, drying or even cooling using absorption chillers through the process of condensation [15].

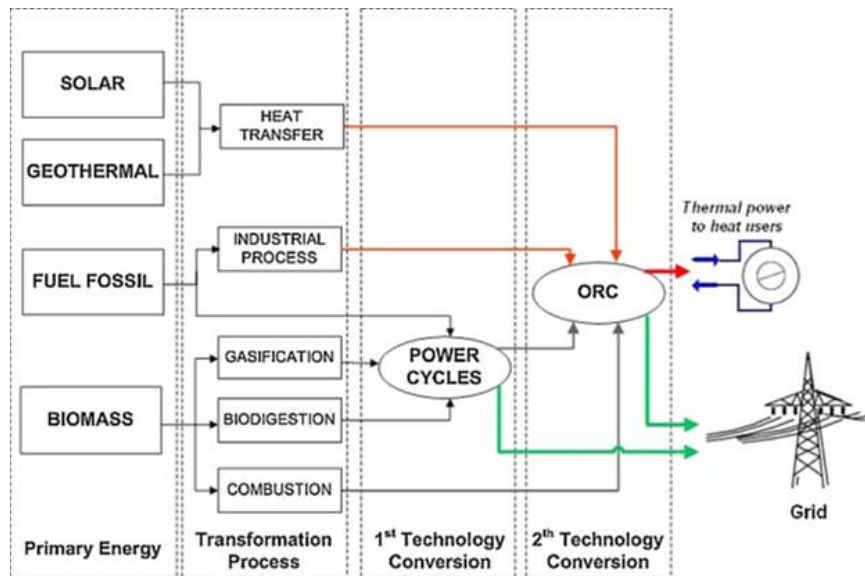


**Figure 2.69:** Diagram of possible applications of ORC according to the energy source [15]

**Solar Power Applications -Thermoelectric Plants:** Concentrating solar power technologies such as the parabolic dish use Stirling engines for small power generation. The parabolic trough collectors (PTC) and central tower can generate power on a large scale. Through an indirect means, solar radiation is concentrated on a receiver using primary reflectors. The receiver contains a fluid that can be heated directly or through the heat transfer fluid to run a steam cycle. The former is an emerging technology due to the challenges of the two-phase flow in terms of strength and materials cost, while the latter requires less pressure in the solar field but increases the heat losses in the transfer to the steam cycle, see Figure 2.70 [15].

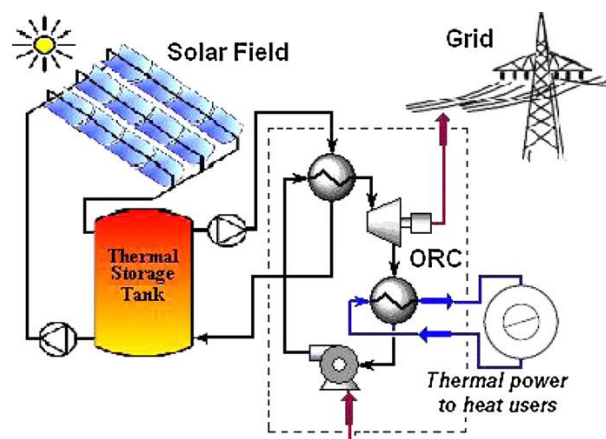


**Figure 2.70:** Schematic diagram of an ORC connected with a small solar field and with energy storage [15]



However, these are steam cycles that need high pressures, high temperatures and thus require a high installed capacity of around 30–80 MWe to be cost-effective. This has renewed interest in solar-driven ORC installations, which use solar radiation to directly heat the organic working fluid or the heat transfer fluid. This way, heat can be stored during the day for use at night. A 50 MW solar steam power plant requires around 2 km<sup>2</sup> land area compared to the ORC, which covers 0.01 km<sup>2</sup> to produce 1MW [245].

However, since one of the major challenges to implementing such small-scale plants is the capitation system [246], developments in other concentrator technologies such as the Linear Fresnel Reflectors are being considered. The Linear Fresnel Reflectors technology offers lower investment and maintenance costs, in addition to its compact plant size and simplicity in plant design, which makes this type of small power plant viable.

**Water desalination:** Apart from the generation of electricity, ORCs can be used for water desalination. The ORC can be coupled directly to run a pump of a process such as reverse osmosis (RO), as is presented schematically in Figure 2.71. Thus, the freshwater supply can be achieved autonomously in dry areas, where it is scarce, using only sunlight as the energy source, something that is abundant in these same locations. [15].

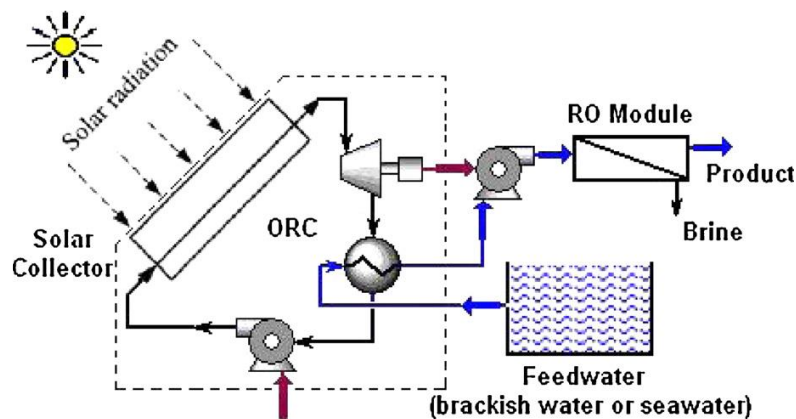


**Figure 2.71:** ORC with solar energy and coupled directly to an RO process [15]

Various studies have analysed different desalination processes, including the comparison of ORC-RO with other solar collector types whose economic performance varies 4.3 to 9.5 €/m<sup>3</sup> for seawater and 2 to 3.3 €/m<sup>3</sup> for brackish water, with the highest for Flat Plate Collectors (FPC) and lowest values for PTC. At the same time, the specific cost for RO photovoltaic brackish water ranges from 3.8 to 4.3 €/m<sup>3</sup> and 12.8 to 14.8 €/m<sup>3</sup> for seawater. Similarly, in [247], different types and trademarks of solar collectors are compared for a low-temperature ORC coupled to an RO process heating the working fluid (R245fa) directly.

**Biomass applications – combustion:** Biomass is recommended to be used on-site in combined heat and power facilities due to increased transportation costs resulting from its low density and the demand for heating/cooling and electricity generation. Power generation from biomass can be achieved after pyrolysis or gasification (e.g., gas engines, integrated gasification combined cycle) or external combustion (e.g., Stirling engines, organic Rankine, steam cycles). Higher conversion efficiencies can be achieved through external combustion at the expense of severe and problematic gas cleaning [248]. In contrast, external combustion is faced with the challenges of limited conversion efficiencies of around 30–35% at maximum.

There were 97 recognised facilities with a biomass-driven ORC system in 2008, using a boiler as the heat source. In terms of quantity, this accounts for nearly 45% use of ORC globally and 5.8% of the market in terms of power. The total capacity installed of these sites is 88 MWe [249]. In recent years, however, there have been renewed interest in this technology, and more than 140 medium-scale facilities for the generation of electricity using ORC technology through biomass combustion (e.g., Austria 1000 kWe, Arta Terme Italy 500 kWe, Bregenz, Allendorf Eder Germany 200 kWe) [250] have been installed. In addition, the residual heat of the condensation is used for residential purposes mainly, heating and domestic hot water, as well as for drying and/or cooling in industrial processes, as shown in Figure 2.72.

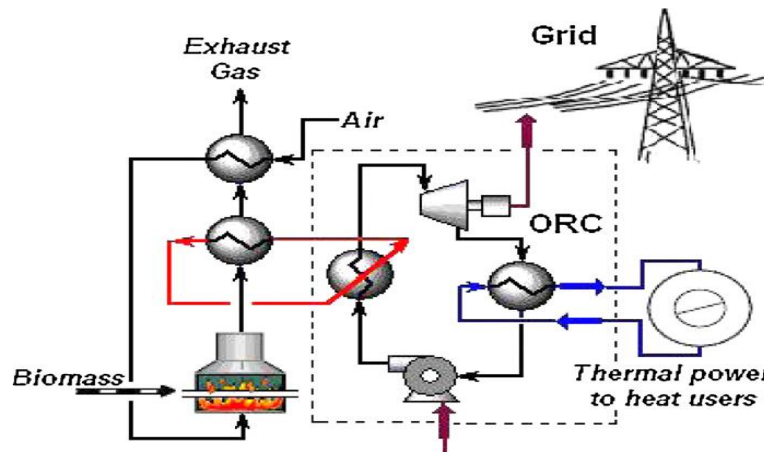


**Figure 2.72:** Cogeneration with ORC technology and biomass combustion

The challenges resulting from the requirement of high temperatures and high pressures for optimal performance has limited the application of this technology for conventional steam power cycles. In addition, this increases the costs of maintenance and staff; thus, such installations will need more than 5MWe to be economically viable [15].

ORC systems alternatively offer the option of co-generating on a small scale, in addition to other benefits such as low maintenance and staffing costs [251], reliability and high efficiency,



no high pressure, automatic and continuous working. All this puts the relatively low electrical efficiency of these systems on a secondary level.

**Geothermal energy applications:** One thing the world is not short of is the immense amount of geothermal heat and thus represents one of the most valuable sources of renewable energy. However, the possibility of harnessing this energy potential is subject to a few limited locations due to economic and technological reasons [252, 253]. Regarding geothermal energy resources with temperatures above 200°C and generating steam or a steam/brine mixture, the recommended approach of operation is to pass the steam directly into turbines in an open cycle with or without reinjection of fluid [254]. However, the use of direct steam is not feasible for sources with lower temperatures; hence, an alternative is to generate electrical energy using an ORC technology, as shown below (Figure 273). In such a concept, the heat transfer fluid of the ORC power plant absorbs heat from the geothermal fluid, thus achieving a benefit from the advantages of these plants.

In spite of the benefits that this type of facility offers, no more than 32% of installed geothermal plants in the world generate 372 MWe by ORC technology [255]. However, this figure only accounts for 3.8% of the total generated with this type of energy source. An example of a geothermal plant using an ORC of 210 kW and water at 98 °C as an energy source is in Neustadt–Glewe in Germany [256].

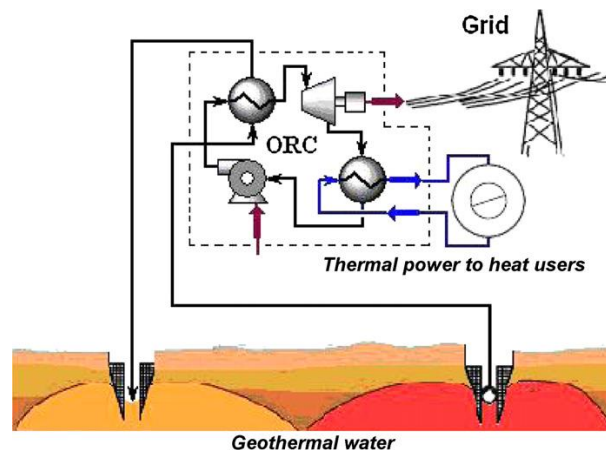


**Figure 273:** Typical plant with the geothermal generation with ORC. [15]

The feasibility of such type of plant may require more research to resolve the variability. For example, in a study by Desideri and Bidini [253], the findings from the study show that the optimization of regenerative Rankine cycle with a closed kind heat exchanger offers a promising choice for the exploitation of low temperature liquid-dominated geothermal sources. Whereas in Saleh, Koglbauer [257], the analysis of 31 working fluids performed indicated that

the fluids that had a lower critical temperature achieved the best results when the maximum temperature of the process was 100 °C. The comparison and analysis of plants in operation deploying low-temperature geothermal fluids and ORC's have been presented in various studies [258], where it is proven that the two plants can run with very high exergetic efficiency.

Other approaches for energy generation using low-temperature geothermal resources couples the ORC to a VAC (vapour absorption chiller). This achieves a lower condensation temperature and consequently enhances the generation potential. Thus, the whole system can be made viable [259].

**Combined cycle applications:** ORC can also recover the waste heat from other power cycles due to its wide range of operating temperatures. Such power cycle mainly includes internal combustion engines, gas turbines or attached cooling cycles. The coalescing of these processes results in combined cycles or “mini-cycles”, where the latter, given their small/medium power, is not feasible with conventional technologies. This boosts the interest in the deployment of ORCs for this type of application [15].

Recently, technological advances in the development of high-efficiency gas turbines have been recorded. One of the features of such systems is the relatively low temperature of the exhaust gases. In a study by Chacartegui, Sánchez [260], a precise analysis was conducted, where a conventional Rankine cycle coupled with a combined cycle high-efficiency gas turbine is compared with an ORC of a new combined-cycle high-efficiency gas turbine.

Depending on the working fluid, the overall efficiency of the new combination improves by 3% with regards to the first combination. Moreover, it is worthy to note that similar efficiencies (approximately 60%) were realised in both cases, with the second option requiring low inlet temperature, in addition to NO<sub>x</sub> reduction, construction and maintenance cost. Also, the study [260] shows how these new combined cycles are economically gaining attention when the cost of the ORC and the gas turbine is less than 2000 €/kW and 3500 €/kW, respectively.

A feasibility study to analyse the potential of combining micro-ORC with gas microturbines was presented in Invernizzi, Iora [261]. The study shows that for a 100kWe microturbine, it is feasible to achieve an additional 45kW of electricity employing residual heat by deploying a micro-ORC and thereby improving the electrical efficiency from 30% to 40%.

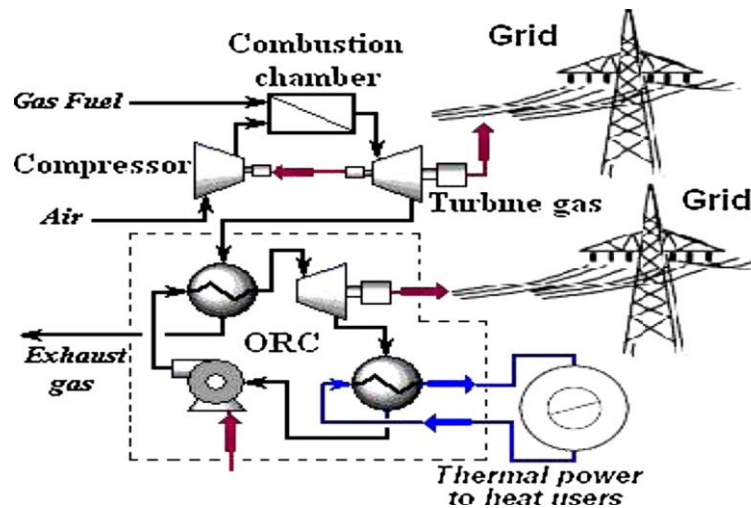


**Figure 2.74:** Combined cycle turbine/microturbine of gas – ORC [15]

In addition, a 30kW of low temperature ( $\approx 100^{\circ}\text{C}$ ) can be realised from the output gases of the ORC, which can serve cogeneration purposes. Nevertheless, these combined mini-cycles are mainly fitting for plants where cogeneration (the heat) has little significance compared to electricity generation. The projected cost for the whole system, according to these authors, is around 4000€/kWe [261]. The evaluation after combining gas microturbines and ORC has been performed by other researchers [262, 263], who revealed the payback time for such investment to be less than three years for the complete system.

#### 2.2.9.2. Steam turbines

A large fraction of the world's electricity is produced with steam turbines, mostly with steam generated from conventional fossil fuel or nuclear heat resources. One of the benefits of CSP is the simplicity with which a new source of heat can be applied to the dominant power production technology. Consequently, the vast majority of CSP systems currently in operation use steam turbines. All the concentrator types have been applied to steam generation for deployment in steam turbine energy [15].

A plant integrating a Rankine cycle using a steam turbine includes the following processes:

- Pure feedwater is compressed to high pressure (e.g., over 10MPa)
- Boiling and superheating the steam in a boiler may be in the focal point or employing a heat exchanger with another heat transfer fluid.
- Expansion of the steam to low pressure through a series of turbine stages coupled to a generator.

- The expansion process ends with condensing the low-pressure steam with the help of a cooling tower and then repeating the cycle.

The Rankine cycle has a higher conversion efficiency for higher steam temperature and pressure at the turbine inlet (common with all heat engine cycles). The main characteristic that enhances efficiency includes different stages of steam bleed from the turbines that can be employed to increase heat feedwater prior to the use in boilers [4].

The fraction of liquid condensing within the turbine must be maintained to a low value to prevent blade erosion. This can be accomplished by ensuring that the vapour is sufficiently superheated before expansion. Increased boiler pressure to improve efficiency can imply that the material will not allow vapour to be superheated far enough to prevent condensation in the turbine. This problem is addressed by re-heating the vapour after partial expansion. All the characteristics are typically combined in a large-scale steam turbine-based power plant, and the overall configuration is typically some variation of that shown in Figure 2.75.

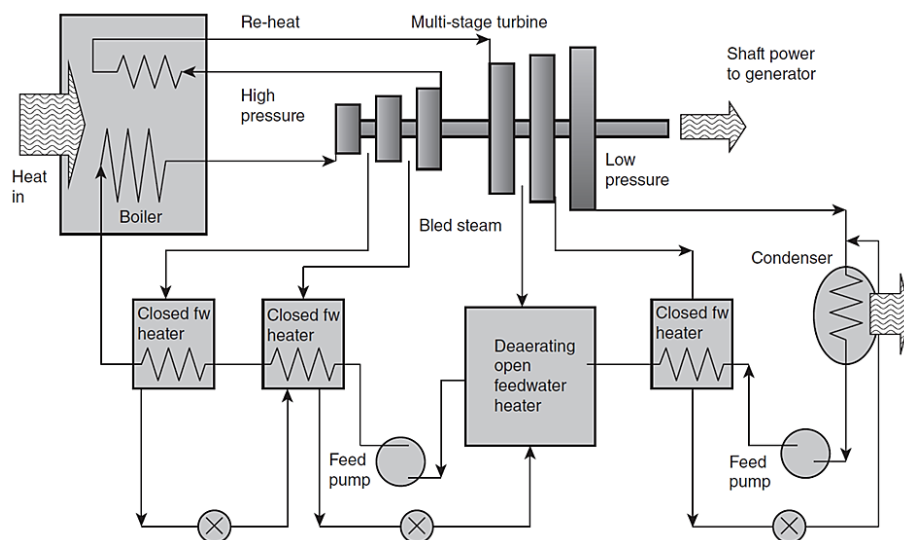


**Figure 2.75:** Indicative configuration for a large-scale steam turbine power plant [4]

Managing the chemical composition of the cycle water is an important part of the project on a more realistic basis. To maintain the amount of impurities such as dissolved salt within reasonable limits, a fraction of the water is regularly blown down (expelled from the system). The direct mixing of bled steam and feedwater occurs in an open feed-water heater. It operates at ambient pressure, and the heating process eliminates any dissolved air before sending the feedwater to the boiler [4].

When systems are designed as larger units and operate at full capacity, they tend to be more efficient. At the 50 to 100MWe range, the bulk, but not all, of the size efficiency advantage is

realised. Per unit power, larger systems are less expensive. Larger-scale power generation turbines used in coal power stations are usually about 500MWe. A larger turbine needs a larger area, which results in extended thermal line losses, so there is a trade-off against turbine size, with many analysts recommending a 250MWe unit as providing the lowest-cost electricity. As of 2012, no CSP plant systems of this scale had been installed, though some are in the planning stages.

The most efficient state-of-the-art steam turbines operate at steam inlet temperatures of up to 700°C. However, if a thermal oil heat transfer fluid is used, trough and linear Fresnel concentrators are restricted to about 400°C, and up to 500°C for an alternative such as direct steam generation (DSG). The temperature needed for the maximum possible steam turbine inlet temperatures and pressures can be achieved by tower and dish systems; the constraint in this case is the survival of materials in the turbine or solar receiver [90].

For optimum conversion efficiency, state-of-the-art supercritical steam turbines are now being manufactured. At high temperatures, supercritical steam is steam at pressures and temperatures beyond the critical point (22MPa, 374°C); at these pressures and temperatures, the phase shift takes place continuously rather than nucleate boiling. These turbines, which are only viable at very large scales, have yet to be applied to CSP.

A major area of variation between solar and fossil operation of steam turbines is the intermittent and varying nature of solar output [4]. This has two potential impacts:

- The wish to vary turbine speed high and low more often and more rapidly than in steady-state fossil-fuel operations;
- The desire to operate at part-load more often.

Although energy storage can help to alleviate some of these effects, directly moving technologies and practices from the traditional generation does not always yield the best results. With these concerns in mind, turbine manufacturers are now designing steam turbines specifically for CSP applications. Such steam turbines will achieve full power in 30 minutes from a cold start and in less than 30 minutes from a warm start. At maximum load, typical steam turbine heat-to-AC-electricity conversion efficiencies for existing CRSs are about 40% gross.

#### **2.2.9.3. Stirling engines**

Stirling engines comprise an external combustion engine with a reciprocating piston engine that runs on a fixed volume of gaseous working fuel, typically hydrogen or helium, but also air. A combination of constant temperature and adiabatic (zero heat transfer) processes make up the ideal cycle. It can achieve the maximum thermodynamically feasible conversion efficiencies between two constant temperatures in the ideal limit [4].

While large fossil-fuel systems for marine propulsion exist, the Stirling engines contemplated for CST applications to date have all been small (in the tens of kWe range). Stirling engines mounted on a dish integrate the receiver, engine, and generator into a single unit at the focus.

Stirling engines have long been deployed in dish concentrators. Despite the fact that dishes have been applied to direct steam generation, photovoltaics, and other systems, many in the CSP sector refer to dish systems in general as 'Dish-Stirling'. Stirling engines have not yet been seriously applied to collector types [264].

Stirling engines can be categorised into two types: piston-crankshaft engines, which are similar to internal combustion engines, and free-piston engines, which have an oscillating piston connected to a linear generator but no actual restraining connection. However, both styles have been employed.

With a total solar AC to electric efficiency of around 30% at design point DNI, Dish-Stirling systems continue to hold the record for the highest solar to the electric conversion efficiency of any technology. The Stirling system is much smaller in comparison to the Rankine cycle, but thermal storage in the Dish-Stirling configuration is yet to be established [37].

#### **2.2.9.4. Brayton engine**

Jet engines and turbo generators deployed in gas turbine stations are based on the Brayton cycle. It is a common misconception that a gas turbine is named for the fact that it burns gas; however, the name refers to the fact that the operating fluid is a gas (usually air). To achieve the necessary heating in the fuel-fired mode, any hydrocarbon fuel, such as diesel, LPG, propane, or biogas, could be burned. Solar heat may also be used to increase the temperature of compressed air until it is expanded. With temperatures before the expansion of around 1000 °C needed for efficient operation, tower systems or dishes are the most appropriate choice. Demonstration CSP systems based on the Brayton cycle's solar heating have been put to the test [265].

A combined-cycle power plant uses a gas turbine to generate high-temperature exhaust gases, which are then guided to a 'heat recovery steam generator', which generates steam for a steam turbine cycle in a fossil-fuelled application. The combined performance could be in excess of 50%, making it the most efficient thermal to electric conversion system currently available commercially [265]. The ability to incorporate combined cycle operation with either steam or ORC bottoming cycles in a similar high-efficiency manner is a major benefit of using the Brayton cycle in CSP applications.

The Brayton cycle presents the potential of lower operation and maintenance (O&M) cost compared to the Stirling-dish system for dish application. Supercritical carbon-dioxide Brayton cycles (s-CO<sub>2</sub> cycles) are presently gaining interest in the area of solar thermal research. Since CO<sub>2</sub> has different thermodynamic properties than air, it can achieve higher overall cycle efficiencies.

Other methods of converting solar radiation into electricity that may become competitive in the future can be described as follows [265]:

- The Kalina cycle is a modified Rankine cycle involving varying concentrations of ammonia and water that provides high efficiency for temperatures between 200 and 300 °C degrees. It is being sought for commercial purposes, as well as for geothermal energy applications.
- Thermoelectric converters use heat to generate electricity. Semiconductor-based systems operate similarly to photovoltaic cells, with the exception that thermal excitation rather than individual photon absorption is used to excite electrons into the conduction band.
- Thermionic converters, which excite electrons from an active surface through an evacuated region to a collector, often generate electricity directly from heat.
- Thermo-photovoltaics transform the radiation re-emitted from heated surfaces using PV cells tailored to thermal radiation wavelength.

#### **2.2.9. Future growth, cost and value of CSP**

CSP is becoming more commercially viable. CSP global capacity, for example, was 400 MW in 2006 and increased to 4800 MW in 2017 [266]. The capacity, however, grew just 1.6% in 2020 to 6.2 GW [267]. The reduced market growth comes on the back of several challenges encountered by the CSP sector over the years, including increased cost competition from solar



PV, the expiration of CSP incentive programmes, and a variety of operational issues at existing installations. Construction delays also hampered market growth.

Spain and the United States are the world leaders in CSP plants, with power generation capacities of 2300MW (48%) and 1738MW (36%), respectively [266]. These capacities had remained the same in 2020, with the only increment coming from China, with a single 100 MW parabolic trough project coming [267]. Figure 2.76 shows that the rest of the planet contributes 762MW (16%). Furthermore, the beginning of the commercialization period has had a major impact on CSP systems. Site selections, technical reviews, performance analysis, economic investigations, and advances in the CSP method and materials are all topics of recent CSP study.

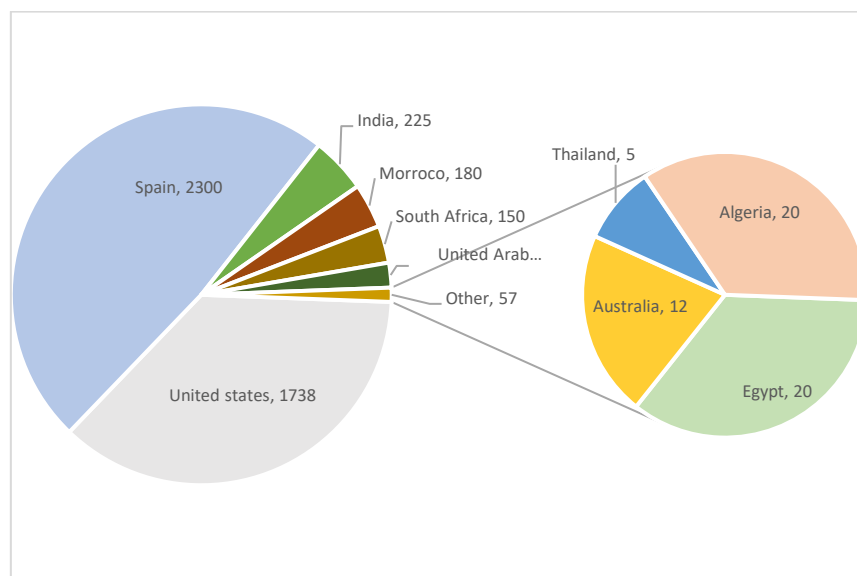


**Figure 2.76:** Status of concentrated solar power (CSP) plants worldwide [11]

In the United Arab Emirates, China, Chile, and India, more than 1GW of CSP projects was under construction in 2020, despite the fact that no new projects began construction during the year. Spain, the market leader in cumulative operating CSP capacity, had no new CSP capacity come online for the seventh year in a row. In the last five years, the United States, which ranks second in cumulative capacity, has seen no new capacity increases. The bulk of projects scheduled for completion in 2020 used parabolic trough technology. At the end of the year, there were little over 1GW of trough systems, just under 0.3GW of tower systems, and a 14 MW Fresnel system under construction around the world. All of these plants, with the exception of two hybrid CSP-natural gas plants, will have thermal energy storage (TES) [11].

The IEA 2010 and 2019 roadmap envisions a rapid expansion of CSP capacity in countries or regions with high DNI and estimates electricity output as a percentage of total demand in IEA

climate-friendly scenarios in these areas (Table 2.12). CSP power, which combines local output and electricity from surrounding sunnier areas, is projected to contribute less in neighbouring but less sunny regions [268, 269].

Plants constructed prior to 2020 primarily respond to intermediate and peak loads, while the first collection of HVDC lines is being constructed to link some of the CSP plants in sunny areas to large demand centres. As costs and performance improve, CSP deployment will begin with base-load plants from 2020 to 2030, maximising CO<sub>2</sub> emission reductions. Solar fuels will join the global energy mix after 2030, while CSP continues to grow. CSP will account for about 11% of global electricity output by 2050 [270].

**Table 2.12:** Electricity from CSP plants a shares of total electricity consumption [268]

Countries	2020	2030	2040	2050
Australia, Central Asia,4 Chile, India (Gujarat, Rajasthan), Mexico, Middle East, North Africa, Peru, South Africa, United States (Southwest)	5%	12%	30%	40%
United States (remainder)	3%	6%	15%	20%
Europe (mostly from imports), Turkey	3%	6%	10%	15%
Africa (remainder), Argentina, Brazil, India (remainder)	1%	5%	8%	15%
Indonesia (from imports)	0.50%	1.50%	3%	7%
China, Russia (from imports)	0.50%	1.50%	3%	4%

The main concern for developers of the technology as well as research and development practitioners within this field is the cost of CSP energy. Despite the exclusion of fuel cost, the cost of CSP energy is overshadowed by the payback of the high initial investment cost over the lifetime of the project. A regime of accelerated growth in installed capacity, in addition to a rapid decay in the cost of energy generated, is confidentially anticipated by the industry. The trend of reduction in the cost of installed capacity increases is reasonably linked to the following [271]:

- Technical improvements, as experiences are gained from plants installed and parallel R&D efforts identify performance improvements.
- Scaling to larger installed plant size, which provides for more efficient and cost-effective large turbines and other components deployed.
- Volume production that facilitates fixed costs of investments in production efficiency to spread across large production runs.

Analytically these practical effects result in a commonly observed development for a new technology of cost reduction of an approximately fixed fraction for every doubling of deployed capacity.

The overall estimated growth of CSP electricity output is represented in Figure 2.77 in comparison with three other scenarios: the BLUE Map scenario of ETP 2008, and the Advanced and Moderate scenarios of Global CSP Outlook 2009. Figure 2.78 shows the growth of CSP electricity production by region according to this roadmap, as is further detailed below. This projection takes into account a significant amount of electricity transportation.

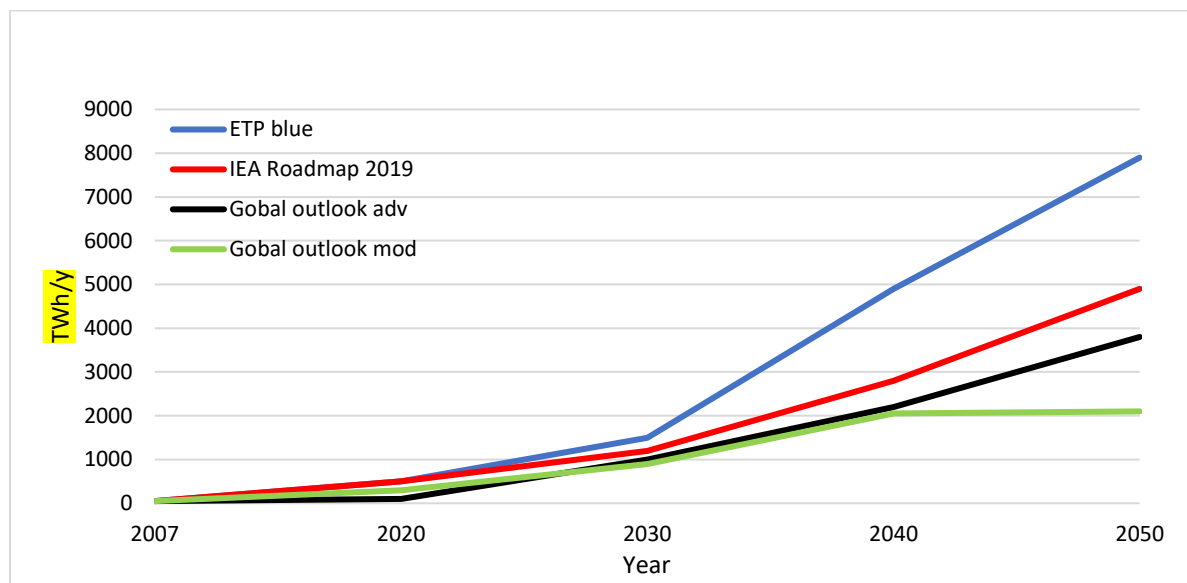


**Figure 2.77:** Growth of CSP production under four scenarios (TWh/y) [269]

Long-distance electricity transportation is a key component for rising CSP's capacity. Large countries, including Brazil, China, India, South Africa, and the United States (Figure 2.78) would need to set up large internal transmission systems for CSP-generated electricity. In other situations, high-voltage transmission lines would cross national boundaries, allowing CSP producers to expand their export markets while ensuring energy protection for importing countries. Australia could feed Indonesia; Central Asian countries could feed Russia; Northern African countries and Turkey could power the European Union; northern and southern African countries could feed equatorial Africa, and Mexico could provide CSP energy to the United States [11].

Because of the abundance of sunlight in the Middle East and North Africa, prices would be lower, offsetting the additional transmission costs and electricity losses anticipated. Furthermore, existing feed-in tariffs for large-scale, ground-based solar energy in Spain or

France will effectively cover the costs of electricity production in North Africa, estimated at \$209 (€150)/MWh on best sites, as well as transportation to the south of Europe, estimated at \$21 (€15)/MWh to \$63 (€45)/MWh [11].

AT Kearney (2010) was contracted by European and Spanish CST industry associations to conduct a study of CSP energy cost predictions. A range of major areas for decreasing the costs of manufacture and increasing annual output was identified. Together, these actions are recommended to result in an overall energy cost reduction in 2025 relative to 2012 of 40–50%. Around the same period of time, they indicate global installed capacity could extend between 60 to 100 GW depending on policy frameworks in place [265].

The global rollout of CSP, which began before 2010, is expected to accelerate between 2010 and 2020, thanks to ongoing industry activities and the introduction of appropriate CSP incentives in sunny countries. Due to planned advances in satellite algorithms, which give higher spatial resolution and better DNI maps, the global solar resource capacity will be investigated more precisely from 2010 to 2020. Many high-quality solar radiation measurement stations back up these figures. All countries and regions interested in CSP, including those that currently lack sufficient coverage, such as China, India, Turkey, Africa, the Middle East, and Latin America, have such reference stations built [11, 267].

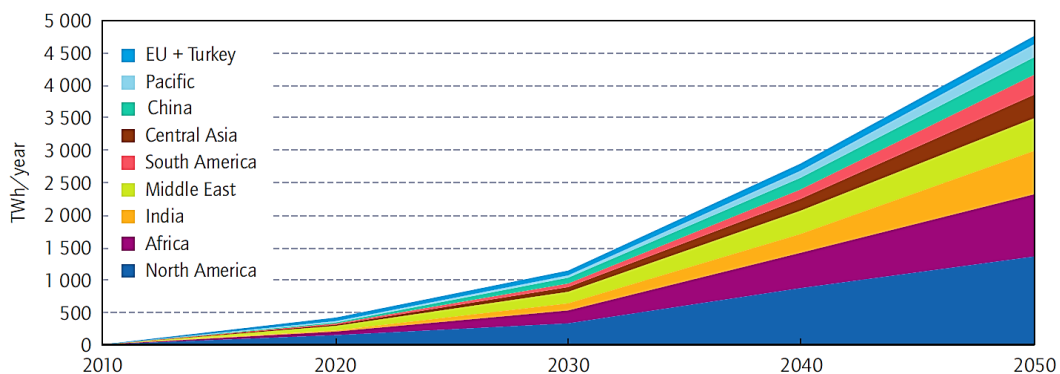


**Figure 2.78:** Growth of CSP production by region (TWh/y)

By 2020, global installed capacity will hit 148GW, with a capacity factor of 32% (2800 hours per year), generating 414TWh per year. Primary energy from fossil-fuel backup or hybridization in CSP plants accounts for 18% of this total; hence, the "solar share" of CSP electricity is 82%, or 340TWh. By 2020, this will account for 1.3% of global electricity output. The industry's global capability, which must rapidly increase from around 1GW per year in 2010 to more than 20GW per year by 2020, is the limiting factor for deployment during this period [11, 266].

As CO<sub>2</sub> prices rise and solar fields and storage costs fall due to higher temperature technologies (540°C and above), CSP technologies will become competitive with coal-fired base-load capacity, maximising CO<sub>2</sub> reductions around 2020. Many newly constructed CSP plants would have larger solar fields and storage systems, allowing them to generate electricity continuously for the majority of the year. Incentives would quickly disappear in most countries because they are no longer needed to support the implementation of CSP capacity. [11, 266].

Furthermore, investors in CSP plants constructed after 2010 will gradually reach the end of their reimbursement duration and will begin to reap much greater benefits, as CSP electricity costs will now be derived solely from operating and maintenance costs. With an average capacity factor of 39% (3400 hours per year), global installed capacity totals 337GW, generating 1140 TWh per year. Thanks to advances in storage, solar would account for 85% of total energy or 970TWh. By 2030, this will account for 3.8% of global electricity output. By 2040, global installed CSP capacity would have increased to 715GW, with a capacity factor of 45% (3900 hours per year), generating 2790TWh annually. Solar energy accounts for 85% of global electricity production or 2370TWh.

By 2050, CSP electricity will be generated and consumed in the locations depicted in Figure 2.79. Africa, India, and the Middle East will be the top producers, followed by North America. Africa would be the leading exporter, while Europe would be the leading importer. However, when the Middle East and North Africa are combined, they generate almost as much as North America (the United States and Mexico). When all solar products are considered, including gaseous and liquid fuels, the Middle East-North Africa region is by far the largest producer.

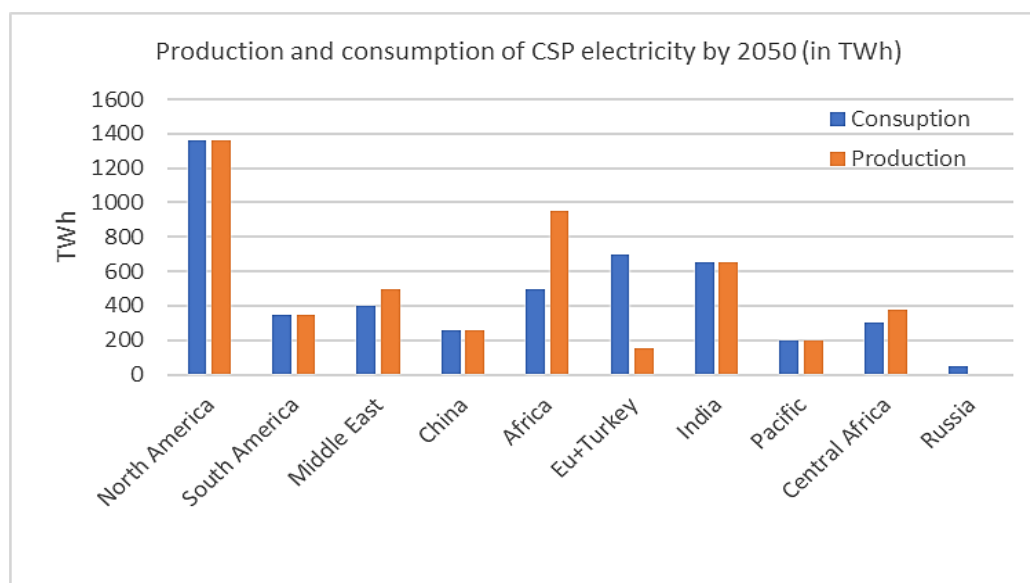


**Figure 2.79:** Production and consumption of CSP electricity by 2050 (in TWh) [11]

As variable renewable technologies such as wind and PV compete for a larger share of energy production, the capacity to provide dispatchable power will become more significant. CSP has the advantages of the integration of thermal energy storage being cost-effective, enhancing the performance, and having very little influence on the overall cost of energy. Several studies [272, 273] have analysed the extra value that can be offered by energy storage capacities of CSP systems, and it can be 30% or more valuable than average market prices. Thus, CSP can look forward to a growing recognition of the value of its energy in parallel with future cost reduction [265].

### **2.3. General discussion on concentrated solar power technologies**

In this section, a review of concentrating solar thermal power plants was presented. The literature review constitutes the state-of-the-art in the various concentrating thermal solar power plant technologies based on a variety of thermal prime movers and taking into consideration key areas such as the designs, components, configurations, modelling and experiments. The prospects of concentrating solar technologies in the context of utility-scale power plants, their performance, technical challenges are discussed. Moreover, the application and future development of the concentrating solar power technologies were presented. Next to that, a critical evaluation and discussion on the facts and information obtained from various resources are put forward.

The provision of sustainable, cost-effective and environmentally friendly energy for consumer societies and industrial economies has been a major concern for both industrialized and developing countries. For that reason, there is a renewed interest in the generation of energy with various solar technologies. Among others, Concentrated Solar Power (CSP) technologies have the potential to meet such demands. However, most recent solar energy harnessing technologies require substantial energy to attain efficient power generation with compact plant size and the least payback time. CSP may prove to be a promising choice due to its potential to overcome environmental and techno-commercial constraints associated with conventional energy generating technologies.

Generally, concentrating solar power technologies deploy mirrors or reflectors to focus large solar radiation or thermal energy onto a small area known as the receiver. Electrical power is produced when the concentrated light is converted to heat which drives a heat engine (usually a steam turbine) integrated with an electrical power generator. During off-peak sun hours or at night-time, integrated thermal storage can serve as a backup. This can be achieved by over

scaling the solar field with respect to the power block in order to store the excess heat produced during the sunniest hours.

Presently, concentrated solar power (CSP) technologies can be grouped into four types: parabolic trough collectors, linear Fresnel reflectors, parabolic dish collectors, and central receiver systems. The parabolic dish CSP technology drives a compact Stirling or Brayton engine to produce electrical power and is more suitable for modular power generation, mostly on the scale of 1-30 kWe. The other three combine with a utility-scale power deploying Organic Rankine Cycle turbine to produce electricity and can be improved with large-scale thermal storage to increase the supply of a solar power plant.

Early research work focussed on the parabolic dish and parabolic through collector types. Later advancement saw the development of a central receiver technology that successfully operated between the early 80s and late 90s. Development on Linear Fresnel Reflector came at a later stage, and since then, no meaningful progress was made until in the mid-80s due to low oil prices. However, there has been renewed interest LFR technologies as an attractive choice for energy generation to meet both thermal and electrical needs over recent years.

Presently, parabolic trough power plants dominate the solar thermal power technologies. These collectors are usually aligned in north-south orientation using a single-axis tracking mechanism to track the sun in the southeast direction to get the required output level. The design of such a collector constitutes inside reflector surface, which concentrates the solar beam radiation on a linear absorber placed at the focal line to absorb the energy. The large collector fields supply the thermal energy used to drive a steam turbine, which, on its part, integrates an electric generator.

The advancements were made on the parabolic trough CSP systems in the last few decades because the technology deployed in their production was well advanced, matured, and attained a commercial state. PTC are deployed in power generation in various countries due to their high concentration ratio and high-temperature capability. The parabolic trough collector is also regarded as the lowest cost large-scale solar power technology available today.

In addition, the parabolic trough collectors can be used in an Integrated Solar Combined Cycle System (ISCCS), which has the potential to lower costs and improve overall solar to electric performance. Since parabolic trough systems are deployed in the traditional Rankine steam cycle to generate electricity, they can easily be hybridised, which means they can be set up to



use fossil fuel (typically natural gas) as a backup fuel to generate electricity during off-peak sun hours or at night-time.

Nonetheless, at this time, operational power plants are faced with some challenges that increase considerably capital and maintenance costs. The receivers of parabolic troughs are coupled to the collector; hence both track the sun through the configuration of rotating joints. High temperatures and pressures of the heat transfer fluid can result in leakages through these rotating joints, with negative environmental impact and on the operators' health as well as reducing the plant reliability.

Moreover, the metal glass welds at the end of each module are subject to failures along the collector lifetime. Replacing such a long tube will be at the expense of significant economic consequences. PTCs require heavy structures in order to hold nearly the 6-m in the length aperture. In addition, mirrors are notably curved, and vacuum receivers require metal glass seals, which are more expensive to manufacture.

A parabolic dish is a point focusing solar concentrator integrated with a full point dual-axis solar tracker. Concentrated solar radiation is collected on a single focal point comprising of the assembly of a turbine or Stirling engine; hence no external heat transfer fluid is required. Their modular collector and receiver units can either function independently or be integrated with a larger system of dishes. Compact size and the possibility of hybridization are key features for its competitiveness with other CSP technologies.

Furthermore, Parabolic Dish systems offer the highest potential solar conversion efficiencies compared to the other CSP technologies because they always present their full aperture directly towards the sun and avoid the 'cosine loss effect' that the other approaches experience when the sun is out of the reference position. They are highly efficient at thermal-energy absorption and power conversion systems, thus achieving a concentration ratio of 600-2000 capable of attaining temperatures more than 1500 °C. They are, however, the least commercially mature.

Unfortunately, the proof-of-reliability operation phase of parabolic dish systems has yet to be completed. Only a few numbers of prototypes have been tested globally, and maintaining annual availability above 90% remains a major difficulty. Given that autonomous operation and off-grid markets are among this technology's top priorities, more long-term test references are required. Parabolic dish systems technology investment costs, which are twice as high as those of the parabolic troughs [22], would have to be dramatically reduced by mass production

of specific components, like the engine and the concentrators. Their system and industries, and initiatives are basically confined to the US and Europe.

Central receiver systems with the field of heliostats as collectors can be used for very high inputs of radiant energy to redirect impinging solar radiation onto a common focal point known as the receiver. This is known as the heliostat field or central receiver collector. By deploying modified concave mirror segments on the heliostats, large amounts of thermal energy can be concentrated into the cavity of a steam generator to generate steam at high pressure and temperature. The impinging heat energy absorbed by the receiver is transferred to a circulating fluid that can be stored and later used to generate power.

Generally, central receiver systems can achieve concentration ratios of 300-1500 and are highly efficient, both in collecting energy and converting it to electricity. Solar energy collected optically can be transferred to a common focal point (receiver), reducing thermal-energy transport requirements and storing thermal energy easily. In addition, they are quite large (generally more than 10MW) and thus gain from economies of scale.

Central tower systems are, however, land-intensive. The receiver's central location provides a universal benefit of collecting all energy in one spot and saving on transportation networks. In contrast to a parabolic concentrator, the constant position of such a central receiver limits flux concentration: heliostats are always oriented at an angle to the direct beam; therefore, the amount of energy gathered is reduced. As a result, in order to achieve the required flux concentration efficiency, the area of the collecting field must be increased, which result in challenges such as land use, environmental implications, and capital expenses.

Due to the high expectations on CSP technologies to play a major role in the utility-scale power supply market, the quest to cost reduction the CSP is therefore open to other technologies other than the parabolic trough and parabolic dish collectors. Current SOTA Linear Fresnel technology is being targeted at high-temperature power cycles alternative to the other CSP technologies. Fresnel reflectors are a modified form of a parabolic trough; hence the curvature of the mirrors being so small and relatively narrow aperture results in compact plant size and easier manufacturing, in addition to the lower prices compared to parabolic trough.

The challenges associated especially with the trough and central receiver systems are the main reasons for the renewed interest in Fresnel reflectors. The very first industrial Linear Fresnel CSP (EP1-Solnova, Spain) based on a simplified technology has drawn a lot of attention. Based on these advancements, recent studies have shown that the life cycle analysis of the cheapest

solar field compared to the trough systems has greatly improved and can be built in less time. Fresnel systems offer benefits such as reduced cost, simplicity on plant design and maintenance, compact plant size and avoidance of heavy steel structures and rotating joints associated with trough and central tower systems. Every single element has been studied to be found as standard good available at a low price on the market.

In comparison with the central tower technology, in which thousands of heliostats are designed separately with a three-dimensional tracking system, Linear Fresnel Mirrors can share the same drive system, as all of them rotate around their separate axis at the same speed. Such a single-axis tracking system is more cost-effective and much simpler than for central towers plants. In addition, the wind torque load is roughly proportional to the square of the mirror height, and the low-profile reflector architecture allows increasing concentration ratio without increasing wind loads, which is otherwise the case for parabolic troughs and large-sized heliostat mirrors for central-receiver systems.

However, the LFR technology is generally faced with the challenge of total thermal power variation, concentrated on to a receiver and its flux map over a given time of the day. This issue results from the solar field's optical efficiency and change in total radiation falling within the field, initiated by the zenith angle. In addition, LFR is said to have low average concentration factors. The variation in radiation qualities, i.e. thermal fluxes concentration onto the receiver, results in various exergy efficiencies. However, concentration factors as low as ten suns are enough to preheat the fluid up to 300 °C with adequate performance.

The new age in CSP technologies began in 2006. The PS10 11MWe installed in Sevilla, Spain, by Abengoa Solar was historically the first central receiver tower plant erected as an industrial process. Major industrial realizations quickly dovetailed this new accomplishment as Nevada Solar One came up in 2007 (solar trough, 64MWe, USA), PS20 in 2009 (central tower, 20MWe, Sevilla Spain), Andasol in 2009 (parabolic trough, 50MWe, Granada Spain) and several others and also various projects throughout different countries of high solar irradiance. One of the last innovative projects is probably PE1. This Linear-Fresnel industrial CSP plant is regarded as the pioneer in the form of a modular (1.4MWe) DSG system built to use only low-cost standard components and dry cooled power block. Subsequently, additional advancements have been recorded in the 20MWe Gemasolar solar tower plant (Spain, 2011) based on the Themis/Solar-Two technology. Thus, operating a 15-hour storage allows 24 hours of continuous electricity generation per day.

Over the recent years, drivers of CSP technologies have acknowledged the significance of solar energy resource evaluation and energy demand/needs assessment. Quite a number of academic or industrial advancements have been achieved, but however, there are still challenges associated with properly estimating the direct solar resource available to a location at the ground level. Recently, at the international Solar Pace conference, worldwide key specialists were again convinced that significant advances are still to be achieved.

In this context, the development of high-quality meteorological measurement devices is vital to enhancing the deployment of the CSP system. In addition, it is imperative to provide access to conduct a local energy demand assessment of the various users (household, public buildings, and industries) in order to optimize the scale and the operation of the CSP plant. Therefore, governmental agencies and industrial organisations in possession of such data should make them readily accessible to promoters of CSP technologies. These data sets are often very difficult to access, especially if patented by top companies.

The solar field constitutes a fundamental part of CSP plants. Generally, CSP solar fields constitute mirror surfaces supported by steel structures or metallic frames. Recent advancements in solar field design have led to the adopting best optical properties resulting in high optical performances. Such achievements are realized at the expense of an increased cost. The weight of the primary mirrors and the surface they offer to the wind load require heavy frame and steel structures for their support and the concrete foundations that bear the whole system. Thus, the solar field represents roughly 50% of the investment cost of a CSP plant.

It would be highly recommended to adopt innovative reflective surfaces mounted on all kinds of light rigid or flexible supports. Those modern reflective materials have already their commercial markets at cost-effective prices for application in CSP solar field. This has led to further innovative concentrating systems such as the Linear Fresnel Reflectors, which offer lower initial cost, compact plant size and simplicity in plant design, running and maintenance. It is projected that this trend could extend to other CSP technologies.

As CSP systems require DNI to attain the desired output, the solar field will consume a large land area. Parabolic trough and central tower systems need adequate spacing between lines, resulting in solar field density of about 26% and 35%, respectively, to minimise shading and blocking. Whereas Linear Fresnel Reflectors have higher solar field density due to parallel rows of mirrors sharing the same tracking unit, shading, blocking, and the resistance to the

wind is minimised. It is suggested that the solar field density needs to be optimized in the case of the trough collectors and central tower systems.

Solar field maintenance can also be regarded as an important issue. As CSP applications are mostly implemented in drylands with high solar irradiance potential, the collector surfaces are usually covered by sand or dust. Despite the high DNI impinging on the reflective surfaces, the deposits of sand/dust and debris can considerably reduce the overall optical efficiency of the solar field.

There are recommended techniques for cleaning solar field reflector surfaces, such as the use of compressed air or demineralized water. The most recent approach, in the case of Fresnel reflectors, is the deployment of automatic motorized dry brushes. This, however, results in additional operating and water costs, which could be not avoided. Next to that, R&D efforts are deployed in finding state-of-the-art techniques or specific coating to reduce the dust deposit is gone unnoticed.

Receivers and absorber tubes form part of the critical components in CSP systems. Receiver tubes for low-temperature applications, in the case of Linear Fresnel, and high temperatures for trough collectors usually have a selective coating to improve absorbance of impinging solar radiation and lowest infrared emitted flux. This selective property deposited on the receiver's surface minimizes thermal losses and consequently enhances the overall thermal efficiency of the solar field. To improve this effect, the receiver tube is usually surrounded by a glass tube that is evacuated to block its infra-red radiations and to reduce the losses due to convection.

As an additional enhancement, the evacuated volume between the two tubes is usually deployed to reach very low thermal losses and very high thermal efficiency. Currently, selective coatings are produced by electrolytic deposition of heavy metals containing species. The costs of such a process are rather high both from the economic and environmental points of view. Hence, there is a need for further research on how the cost of such a process can be reduced with lower environmental impact and to increase life expectancy (30 years).

At high-temperature ranges between 600 to 1000°C, the central tower and dish engine will require receivers that constitute high-temperature materials capable of withstanding thermal constraints as well as oxidative environments. Studies are currently ongoing in this field, and ceramic materials such as SiC or metals like Inconel are currently used at laboratory or pilot scales [14]. It is projected that these materials in the near future will emerge cost-effective and provide excellent properties that can reduce thermal losses and enhance overall system

efficiency. Consequently, for such systems, there is a need to focus on selective properties for absorber surfaces and receivers glazing, taking into account the shock and compatibility with high-temperature HTF.

In CSP systems, the thermal energies are usually supplied via conduction and convection to the Heat Transfer Fluids (HTF). The multi-functional HTF needs to gather, transport, and exchange heat gained from solar radiation and is, therefore, an essential part of a CSP system. In order to generate electricity, the hot HTF can also be stored in an insulating tank if no sun is available, in addition to heat transfer from the receiver to the steam generator. Since a significant amount of HTF is needed to operate a CSP plant while maximising its performance, it is necessary that HTF costs are minimised.

Given the functionality of the HTF, their performance is determined by a wide range of constraints, both practical and fundamental. Because of their stability over a relatively large temperature range, synthetic and mineral oils are the HTF choice for most solar thermal plants. Molten salts, on the other hand, promise higher efficiencies as operating temperatures have attracted a lot of interest. These efficiency gains are, however, combined with the challenges of melting the salts and higher pumping costs.

In the context of low to medium temperature ranges, the best available fluid would remain water/steam, taking into consideration cost and environmental criteria, among others. Moreover, to drive the penetration of the direct steam generation, there is a need to invest more in R&D to improve current receiver tube designs. The first industrial Linear-Fresnel plants, the PE1 and PS10, are industrial solar central tower plants based on DSG. The former has a secondary reflector housing the receiver tube, thereby minimizing drift in ray concentration and enhancing the concentration ratio. In addition, the glazing on the lower side reduces losses due to infra-red radiation.

The desired characteristics of an HTF include a high boiling point and thermal stability, high-temperature vapour pressure ( $<1$  atm), a low melting point, low viscosity, low metal alloy corrosion, high thermal conductivity, high thermal capacity for energy storage and low cost. The freezing point of the HTF is another important element regarding its temperature stability; hence, safety measures should be integrated into the system so that the HTF does not freeze in the plumbing, which can cause damage and speedy wear.

The toxicity, environmental danger, stability, material compatibility (e.g., metals, effect of impurities and cost) are also factors not to be ignored in practical applications. Another

important issue that needs to be examined experimentally is the long-term durability of different HTFs. The HTFs are categorized into six main groups based on material types: (1) molten salts, (2) water/steam, (3) air and other gases, (4) thermal oils, (5) organics, and (6) fluid metals.

A range of various solar to electric energy conversion systems can be deployed to the different concentrator types. A large fraction of the world's electricity is produced with steam turbines, mostly with steam generated from conventional fossil fuel or nuclear heat resources. One of the benefits of CSP is the simplicity with which a new source of heat can be applied to the dominant power production technology. Consequently, the vast majority of CSP systems currently in operation use steam turbines. All the concentrator types have been applied to steam generation for deployment in steam turbine energy.

The most efficient state-of-the-art steam turbines operate at steam inlet temperatures of up to 700 °C. However, if a thermal oil heat transfer fluid is used, trough and Linear Fresnel concentrators are restricted to about 400°C, and up to 500°C for an alternative such as direct steam generation (DSG). The temperature needed for the maximum possible steam turbine inlet temperatures and pressures can be achieved by tower and dish systems; the constraint in this case, is the survival of materials in the turbine or solar receiver.

For optimum conversion efficiency, state-of-the-art supercritical steam turbines are now being manufactured. At high temperatures, supercritical steam is steam at pressures and temperatures beyond the critical point (22 MPa, 374 °C); at these pressures and temperatures, the phase shift takes place continuously rather than nucleate boiling. These turbines, which are only viable at very large scales, are yet to be applied to CSP. A major area of variation between solar and fossil operation of steam turbines is the intermittent and varying nature of the solar output.

Although energy storage can help to alleviate some of these effects, directly moving technologies and practices from the traditional generation does not always yield the best results. With these concerns in mind, turbine manufacturers are now designing steam turbines specifically for CSP applications. Such steam turbines will achieve full power in 30 minutes from a cold start and less than 30 minutes from a warm start. At maximum load, typical steam turbine heat-to-AC-electricity conversion efficiencies for existing CRSs are about 40% gross.

Stirling engines have long been deployed in Dish Concentrators. Despite the fact that Dishes have been applied to direct steam generation, photovoltaics, and other systems, many in the CSP sector refer to Dish systems in general as 'Dish-Stirling'. Stirling engines have not yet

been seriously applied to collector types. The Stirling system holds the record for the highest solar to the electric conversion efficiency of any technology and is much smaller in comparison to the Rankine cycle; however, thermal storage in the Dish-Stirling is yet to be established.

The Brayton cycle presents the potential of lower operation and maintenance (O&M) cost compared to the Stirling-dish system for dish application. Supercritical carbon-dioxide Brayton cycles (s-CO<sub>2</sub> cycles) are presently gaining interest in the area of solar thermal research. Since CO<sub>2</sub> has different thermodynamic properties than air, it can achieve higher overall cycle efficiencies. With temperatures before the expansion of around 1000 °C needed for efficient operation, tower systems or dishes are the most appropriate choice. Demonstration CSP systems based on the Brayton cycle's solar heating have been put to the test.

An Organic Rankine cycle turbine (ORC) is fundamentally similar to a steam Rankine cycle; however, it employs a lower boiling point organic fluid, which makes it compatible and suitable for low-temperature applications. For smaller systems, ORC may achieve higher efficiencies than steam turbines (in the form of a few kWe). However, compared to water/steam systems, capital and operational maintenance (O&M) costs are higher per built MWe. ORC has been employed in various forms of low-temperature heat sources, including solar energy, geothermal energy, biomass energy and waste heat energy.

With a total installed capacity of 4,950 MW, the ORC's market capacity in the 1-100 kW range is small. The high specific cost of technology is currently not competitive with other existing technologies despite the large market potential for small-scale ORC (e.g., wind, solar). In order to maximise the power generation of such power plants, efficiencies of the ORC components should be improved while maintaining the lowest possible cost. For the future development of ORC for decentralised power, a compromise between these two parameters is essential.

Concentrated Solar Power (CSP) have emerged among the top contenders that may play a major role in the future energy mix, particularly in regions with a substantial annual global direct irradiation, where it appears to be a more cost-effective technology compared to other solar technologies for electricity generation. The uncertainty in the prices of fossil fuels and increasing demand for energy which was first experienced in the early 70s prompted the search for alternative energy from sustainable sources. Since then, the provision of sustainable, cost-effective and environmentally friendly energy for consumer societies and industrial economies has been the top agenda for industrialized and developing countries. This experience has led to immense scientific work on various ways of electricity generation from CSP systems.



Spain and the United States have dominated the chart of installed CSP power plants. Other countries with declared CSP projects or currently under control include the Middle East (Egypt, Israel) and North Africa (Morocco, Algeria), Greece, Portugal, Italy, Cyprus, Australia, Malta, China, India and South Africa. India took a major initiative in 2015 by setting up the Jawaharlal Nehru National Solar Mission, with a target of 20 GWe of combined CSP and PV capacity to be installed by 2022.

This activity has combined to provide a rate of growth that is similar to that which was witnessed by wind energy and PV during its first regime of modern commercial deployment. Despite the industry still being in its nascent stages and vulnerable to sudden policy amendments in key countries, the continued robust growth in the global installed capacity is projected.

The continuing challenges for CSP in the past and more recently emanate from the reliance on the economies of scale afforded by large steam turbines, resulting in a large degree of risk capital per project for relatively new technology. Moreover, necessary investment in this field is expected to increase, given the rapid growth in the size of renewable energy projects.

Future research in this subject is expected to work in this trend to progress properly in the learning curve for CSP, which can address some design and optimization for optical and thermal processes that can be combined for a more accurate understanding of the process that will present a more reliable and improved system for an integrated period, in order to get a substantial reduction in the cost of electricity.

A regime of accelerated growth in installed capacity, in addition to a rapid decay in the cost of energy generated, is confidentially anticipated by the industry. The trend of reduction in the cost of installed capacity will be driven by technical improvements, as experiences are gained from plants installed, and parallel R&D efforts identify performance improvements. In addition, scaling to a larger installed plant size, which provides for more efficient and cost-effective large turbines and other components deployed, is a major factor.

Furthermore, CSP can immerge cost-competitive as a result of volume production that facilitates fixed costs of investments in production efficiency that spreads across large production runs. Analytically these practical effects result in a commonly observed development for a new technology of cost reduction of an approximately fixed fraction for every doubling of deployed capacity.

## 2.4. Summary and Conclusion (knowledge gaps)

This Chapter presents a literature review on the state-of-the-art in thermal solar power plants based on various thermal prime movers: this focussed on key areas such as the designs, components, configurations, modelling, and experiments. Critical evaluation and discussion on the facts and information obtained from various resources are presented.

Concentrating solar power technology is a very promising research area for energy generation to meet both electrical and thermal needs. Thus, it was necessary to conduct a compressive literature review on this topic and in addition, putting together facts and information related to several components and subsystems of the linear Fresnel reflector solar field and the organic Rankine turbine is an area that has been previously overlooked.

In recent years, several research works have been conducted on Linear Fresnel reflector systems, focusing mainly on the design, modelling, and optimisation of the solar field. While most of these studies deployed several variables, there is very little work where the optimisation of the mirrors is performed using key variables such as the mirror curvature, width, distance between mirror centre lines and receiver height. In the present study, however, the flat mirror is modified by slightly giving it a curvature which gives an optimal shape, and this was achieved by the optimisation of the whole system, which significantly improves the optical efficiency. In addition, the secondary reflector shape and position were also optimised and the combination of the two was looked together for the first time.

Furthermore, for the first time, we studied a very small axial ORC turbine, and for that, we were able to carry out a full 3-dimensional simulation of the complete turbine, taking into account the variation of the properties of the refrigerants and incorporating them into the CFD format using the material property database.

In addition to the above, several reviews have been conducted on the separate CSP technologies. However, a combined review of CSP technologies, including plant sub-components, is an area that has been overlooked. Hence, the present literature constitutes a detailed review of CSP technologies bringing together plant sub-components such as the primary mirrors, secondary reflectors, receivers, heat transfer fluids, organic working fluids and thermal prime movers and analysing them based on the designs, configurations, modelling and experiments.

## Chapter 3 : Linear Fresnel Reflector Solar Field

### 3.1. Introduction

Linear Fresnel Reflector (LFR) CSP technology is considered an attractive alternative for energy generation to meet thermal and electrical needs. LFR, however, is regarded as a low-efficiency technology, which is mainly due to very little previous research in this field. Unlike trough collectors, LFRs have fixed receivers; hence when the sun is out of the reference position, mirrors struggle to track the sun while concentrating solar flux on the focal line on the receiver. This results in variation and drift in ray concentration, which significantly impacts the optical efficiency and concentration factor of the primary mirrors and the performance of the receiver tube.

The renewed interest in LFR technology as a promising choice for thermal and electricity generation results from its performance, simplicity of implementation, operation and maintenance, compact plant size and lower cost. For this reason, various research efforts are ongoing to improve the performance of Linear Fresnel Reflectors technology and the development of concentrating solar thermal power plants based on such an approach.

In this Chapter, the modelling, optimization and the Monte Carlo Raytracing of the proposed LFR solar field are performed in an attempt to minimize the drift and variation in ray concentration and improve the optical performance of the solar field. In order to accomplish this objective, the study is split into several sections. A detailed description and features of the proposed solar field is discussed in Section 3.2. Simulations were performed using the Innova MicroSolar power plant design and configuration.

Section 3.3 presents the approach and methods adopted in the modelling, optimization and Monte Carlo Raytracing of the proposed LFR solar field. Based on the literature review conducted on concentrating solar power systems, previous research was leveraged to define processes with embedded CSP technologies that support appropriate concept development, design, modelling and optimization. This is very useful in understanding the research process, and it forms the basis for the entire approach and methods, tools and models deployed.

Using the mirror elements as variables, the mirror profile is modified by a simple optimization approach proposed. Next to that, a Monte Carlo Raytracing Technique is deployed to determine the performance of the optimized solar fields. The raytracing is performed using the chosen location's daily and monthly solar irradiance data for both east-west and north-south solar field

orientation. In the case of the central LFR configuration, the performance of the optimized mirrors is compared with flat and uniform mirror curvatures.

Section 3.4 presents the thermal analysis of the LFR solar field. A steady-state analysis of thermal performance is carried out, taking into account the receiver tube's main features and optimum operating condition for various concentrated heat fluxes (in  $\text{W/m}^2$ ) by deploying the results from MCRT in ANSYS Fluent (R2020) CFD solver. From this model, the fluid outlet temperatures and thermal efficiencies are computed for a range of values of the variables such as the inlet temperature, fluid speed, and thermal flux concentrated on the absorber. The approach and methods deployed in the flow model and heating of the Heat Transfer Fluid are defined.

The validation of the numerical heat transfer model was conducted, taking into account the inlet, outlet temperatures and thermal efficiency. The numerical results were compared with the test data from the Innova MicroSolar plant using Therminol 62 as the heat transfer fluid. The detailed model applies a combination of ray tracing and CFD (ANSYS/Fluent) model. The influence of the model optimization of the solar field and raytracing on the thermal output is in good compliance with the results of the experimental tests.

The modelling and optimization deployed are to determine the optical and thermal performance of the systems. Results analysis and discussion are presented in section 3.4. The optical simulation results show minimized drift in ray focusing and improved concentration ratio by the optimized mirrors deploying north-south and east-west solar field orientations. Also, the computed optical efficiency for separate mirror elements and the overall solar field shows improved optical performance for the optimized mirrors. Results from the theoretical model are validated with optical and thermal experimental data gathered from a Linear Fresnel Plant Innova MicroSolar erected in Almatret, Spain. The last section constitutes the conclusions from the study and impact on the future of Linear Fresnel technology in the Concentrated Solar Power industry.

### **3.2. Innova MicroSolar project**

The Innova Micro Solar Project studied in this project is a Linear Fresnel Reflector demonstrational solar power plant designed and installed in the town of Almatret, Lleida, Catalonia, Spain, on bearing lat. 41.30, long. 0.42. The plant is expected to meet domestic and small business scale heat and power demands and consider the possibility of mounting the component on flat/pitched roofs or surrounding ground.

The solar field constitutes two adjacent LFR modules (see Figure 3.1). Each module comprises of 9 primary reflector units and 5 receiver tube units. The total length is about 20m, and it requires a ground area of around 140m<sup>2</sup>. The net mirror surface area is 73m<sup>2</sup> whilst the total solar field mirror area is about 146m<sup>2</sup>, which at nominal conditions (DNI) – equal to 900 W/m<sup>2</sup> delivers a nominal peak thermal power of 80kW. The two LFR collector modules are connected to form a single hydraulic loop.

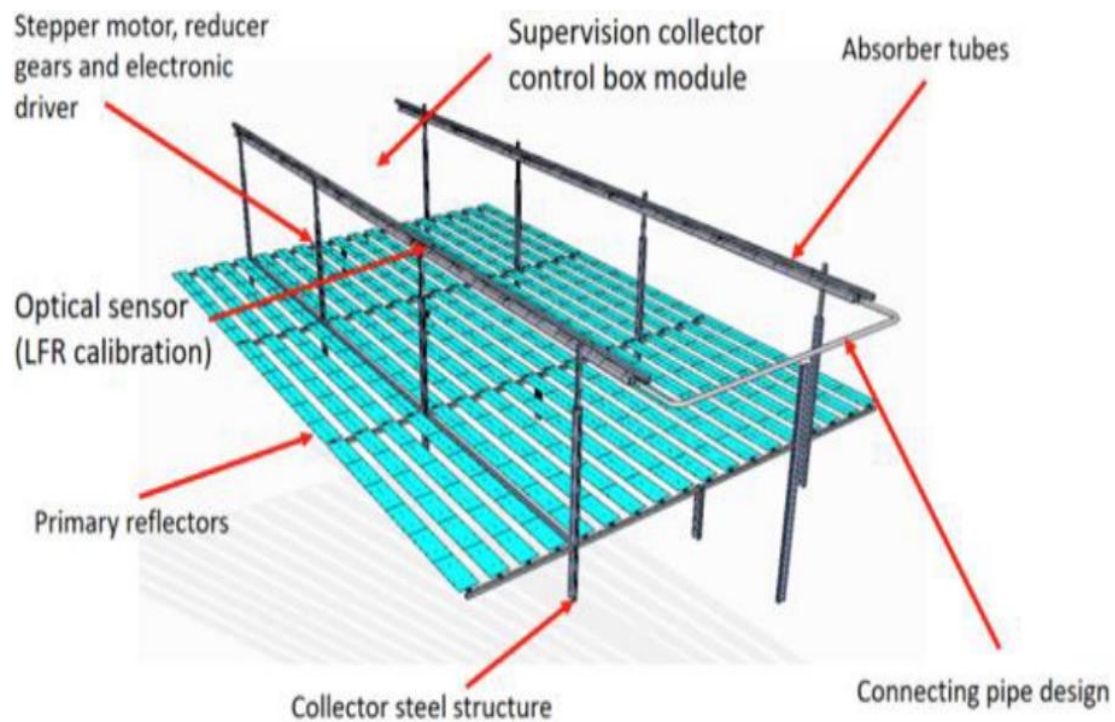


**Figure 3.1:** Innova MicroSolar Project LFR solar field layout

The 3D optical model of the solar field was developed and optimised using LighTools optical software. The model was validated using an approach presented in Zhu, Shi [59] and experimental data obtained from the Innova MicroSolar Project power plant. The sketch of the proposed solar field and environs are presented in Figure 3.2.

The solar field forms a significant part of the Innova MicroSolar pilot plant. The primary objective for the modelling activity was to achieve a high concentration factor of the LFR collector by obtaining the highest efficiency of the most critical and expensive component, which is the evacuated absorber tube (the receiver). This objective has been achieved by optimizing the primary mirrors and placing the receiver closer to the mirrors, such that almost all impinging sunrays on the primary mirrors directly hit the receiver. A secondary effect of this design choice is that the secondary reflector recovers and redirects towards the receiver a very small portion of incident sun power.

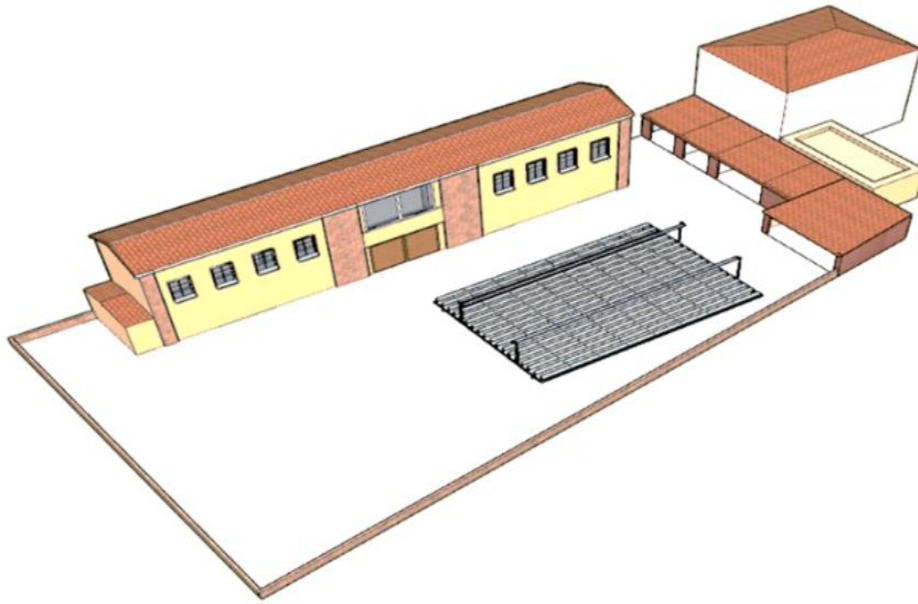


**Figure 3.2:** The 3D model of the LFR solar field in the Innova MicroSolar Project and its surroundings. East-west orientation, Lat 41.30, long. 0.42. Almatret, Spain

An appropriate receiver tube with a maximum operating temperature of  $550^{\circ}\text{C}$  was selected, taking into account the operating temperature chosen for the Innova MicroSolar project, which is  $280^{\circ}\text{C}$ ; this component achieves a very high efficiency (nearly 90%) for transferring sun irradiation to Heat Transfer Fluid (HTF). Therminol 62 synthetic oil, which can reach temperatures of over  $340^{\circ}\text{C}$  was selected as the heat transfer fluid.

### 3.3. Numerical approach and optical modelling of the LFR

The optical design of a solar concentrator is based not only on identifying and evaluating specific solutions in time but also on the integrated performance over a range of time. Different locations and different seasons are additional important factors to evaluate. The primary aim of optical design is to obtain a reflector profile that concentrates the solar flux distribution emitted by a source onto a prescribed focal point of a receiver, thereby minimizing lateral drift in ray concentration and operation at optimum through the year.

#### 3.3.1. LightTools Illumination Design Software Applications

LightTools is a 3D optical engineering and design software product that supports virtual prototyping, simulation, optimisation, and photorealistic renderings of illumination applications. Its complete design and analysis capabilities, combined with ease of use, support for rapid design iterations, and automatic system optimisation, help to ensure the delivery of accurate, timely, and cost-effective illumination designs.

The modelling of the linear Fresnel reflector solar field is performed using an optical simulation tool, LightTools 8.7 version. This provides us with the option of developing the visual prototype of the solar field, design, optimisation and analysis of the key elements that have a greater influence on optical efficiency, as well as performing a Monte Carlo Ray Tracing of the solar rays. Also, this does not eliminate the requirement to develop prototypes or the need to characterise physical parameters but rather provides the flexibility that allows the designer to adjust parameters and study the influence of parameters on the output performance.

### 3.3.2. Solar field configuration

Linear Fresnel Solar Field can be aligned in a north-south direction for east-west tracking and in an east-west direction. The north-south orientation is commonly deployed in industry, as it results in a higher annual energy collection. For horizontal fields, nevertheless, east-west fields lead to a more uniform energy production throughout the year [23]. For this study, the primary mirrors aligned both in north-south and east-west orientation can be analysed and configured for a one-axis tracking system such that the projected solar rays' incident on the mirrors is concentrated on the receiver tube placed at the common focus of all the primary mirrors. Figure 3.3 shows the schematic of the solar field, which was used in this study.

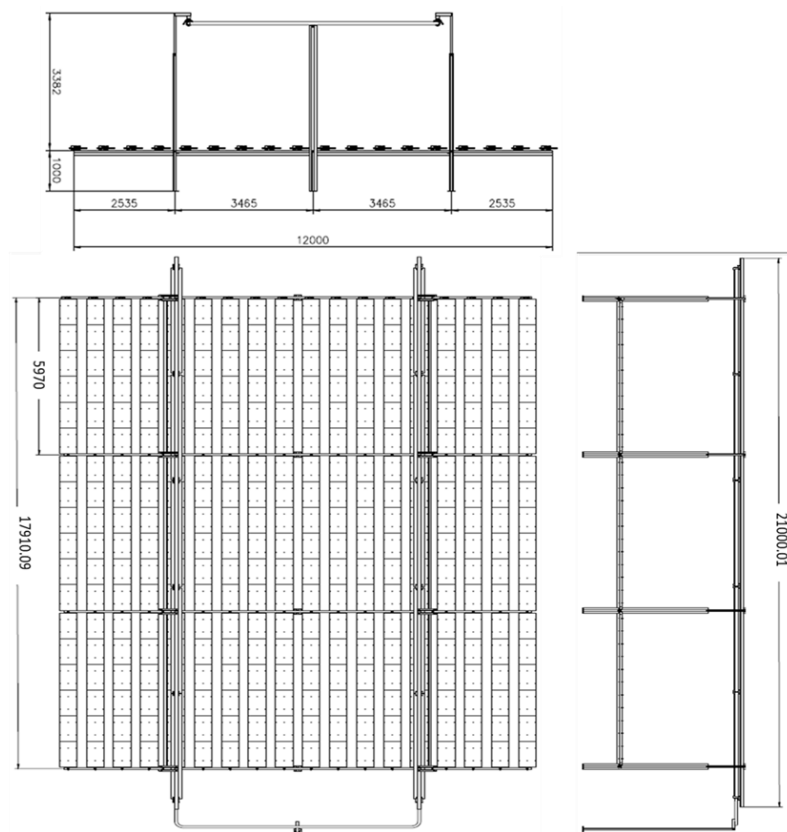


**Figure 3.3:** Solar Field configuration for the proposed study



The solar field design considered the configuration and specification adopted for the Innova Micro Solar pilot plant. For the solar field, a single unit was considered, comprising of an array of 9 long, parallel mirrors with a total width of 4.05m, length of 18m and effective collector area of about 73m<sup>2</sup>. A single evacuated tube absorbing receiver of 70mm diameter, enclosed by an evacuated absorbing glass of 125mm in diameter, is placed 3m above the primary mirrors. The receiver is placed inside a secondary reflector linear cavity of 25 cm wide. The schematic of the solar field can be seen in Figure 3.4.

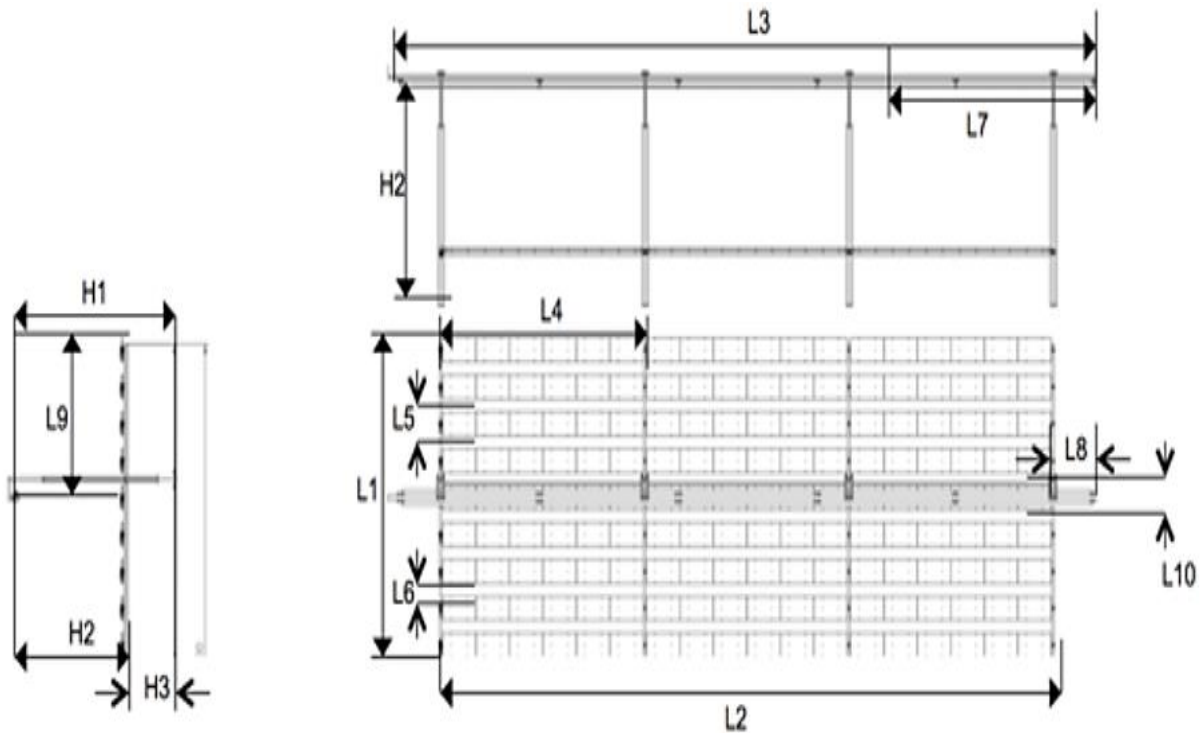


**Figure 3.4:** Modelling layout and schematic representation of the InnovaMicro Solar pilot plant

In this study:

- i. Flat mirrors were initially deployed. However, using the LightTools optimization tool, the mirrors were modified.
- ii. Mirrors with equal width are considered for both optimization and simulation.
- iii. The mirrors are aligned in east-west orientation for a single-axis tracking of the sun and vice versa.
- iv. The rotating joint of each mirror matches with the centre line of the mirror; hence, it is always focused on the central point of the receiver tube.
- v. An adequate distance must be kept between two consecutive mirrors so that a mirror does not block or shade its nearest neighbour.



- vi. A central LFR with a single absorber tube was preferred. Two of which were connected to form a single hydraulic loop.
- vii. The secondary reflector design specifications of the Innova MiroSolar were considered. However, these design specifications were used to modify the secondary reflector using LightTools optimisation in order to attain higher efficiency from the optimised mirrors.

Table 3.1 presents main design parameters of the solar field, which were used in the simulation process.

**Table 3.1:** Dimensional input data for the raytracing Monte Carlo software to optimize the design of the LFR collector

Geometrical data	Value	Units
Total LFR aperture, L1, $W_{field}$	5	m
Total LFR length, L2	18	m
Total receiver tube length, L3	18	m
Primary reflector unit length, L4	Not less than 6	m
Primary reflector aperture, L5	0.45-0.65	m
Offset distance between two adjacent primary reflectors, L6	0.3-0.2	m
Absorber tube unit length, L7	Fixed at 4.06	m
Offset length primary mirrors – receiver line, L8	1-2	m
Number of primary reflectors, N,	07-10	
Height of the receiver tube from the ground level, H1,	3.5-5.5	m
Height of the receiver tube from the primary mirror's plane, H2, $h_{rec}$	2.5-3.5	m
Height of the primary mirrors from the ground level, H3,	Greater than	m
	0.5	
Aperture of the secondary reflector, $A2_{ref}$	0.15-0.25	m <sup>2</sup>
LFR total ground area, $A_{tot}$ ,	100-200	m <sup>2</sup>
Total LFR weight to mirror area ratio, $W_{ratio}$	Less than 23	kg/m <sup>2</sup>

### 3.3.3. Modelling primary mirrors

The position of the primary mirrors can be defined by the tilt angle ( $\delta_n$ ), such that the incident ray (impinging at an angle  $hf$ ) concentrates on the receiver tube, the distance between two consecutive mirror centre lines ( $S_n$ ), and distance from the central point ( $Q_n$ ). The focal plane is positioned at a distance ( $f_n$ ) from the mirror element placed in the centre of the LFR ( $S_o = 0$ ). The pivoting point of each mirror corresponds with the central point of the mirror; hence, it is always focused on the central point of the receiver.

The  $n_{th}$  mirror in the LFR array is defined by three parameters notably, position, ( $Q_n$ ), tilt ( $\delta_n$ ) and space ( $S_n$ ) as presented in Figure 3.5. These parameters can be obtained using simple geometrical optics expression [78] as follows.

The tilt angle of the  $n_{th}$  mirror on the horizontal plane is obtained by

$$\tan 2\delta_n = Q_n/f_n \quad (3.1)$$

The position  $Q_n$  of the  $n_{th}$  mirror is computed from the centre of the solar field using the expression.

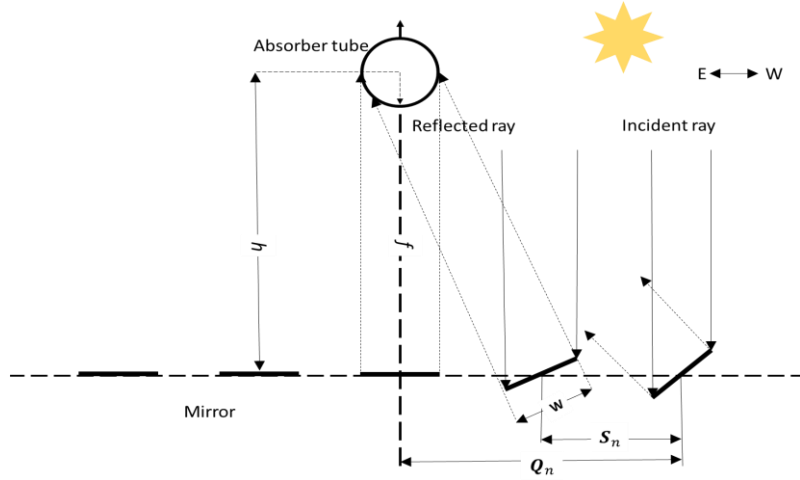


**Figure 3.5:** Schematic design showing layout of reflectors (mirrors)

$$Q_n = Q_{n-1} + S_n \quad (3.2)$$

Here,  $n \geq 1$ .

For the initial iteration  $S_0 = Q_0 = 0$  and;  $S_1 = Q_1 = 0.75$ ,  $W = 0.45$ ,  $f_n = 3$ .

To obtain the focal length ( $f_n$ ) of the  $n_{th}$  mirror and the circular radius of curvature ( $r_{nc}$ ) the following expressions can be applied.

$$f_n = \text{sqrt}(h^2 + Q_n^2) \quad (3.3)$$

$$r_{nc} = 2 \frac{f_n}{\cos \delta_n} \quad (3.4)$$

Optionally, a secondary reflector of a suitable geometry recovers and redirects on the absorber tube the portion of the light which does not directly hit the tube. This component increases the optical efficiency of the whole system. The measured length of the secondary reflector deployed for this study is 18 m, the Lamina width is not less than 0.5 mm and the aperture width is 0.33mm

### 3.3.4. The efficiency of LFR solar field

Generally, for a Linear Fresnel Solar field, a comparative study of the obtainable efficiency can be performed by identifying the relevant parameters. Various studies [45] have analyzed the energy efficiency of LFR; however, most of them are made up of the same relationships, in general. Using the Monte Carlo Ray Tracing technique, analyses are performed based on a

given month's average daily irradiance data. The energy and optical efficiency (ratio between incident rays on the target and the total number of rays) are computed using the expressions in equation 2.3 and 2.4 of section 2.2.4.2 [3]:

### 3.3.5. Optimization and Monte Carlo Ray Tracing (MCRT)

Generally, optimization requires identification of one or more parameters (dimensions, angles, curvatures, coefficients of surface shape or texture polynomials, etc.) that can be changed in the attempt to improve the performance [274]. Other authors (Abbas, Montes in [9]) have used variables such as the filling factor, number of mirrors, width, and receiver height. Similarly, Boito and Grena [14] has performed optimization of the geometry of LFR using positions, widths and focal length of mirrors as variables. For this study, which mainly focuses on modifying the mirrors to enhance concentration factor, the curvature, tilt (Alpha) angle, mirror aperture (width), and height were used as optimisation variables. For the merit function, NS-ray fans pointing to the mirror's aperture were used.

**Parameterization:** One critical aspect when using optimization for solar concentrating applications is to find an efficient system parameterization. In the optimization procedure it is necessary to list parameters in the model which can be varied in order to improve system performance. The choice of variables can influence both how long it takes to find the improvements and whether the optimisation can improve performance. The more variables are used in the optimisation, the longer it generally takes to find a solution. Parameterization can be used to reduce the number of variables. This is imperative because the convergence time strongly depends on a number of variables, and in addition, poorly selected variables could increase the possibility of the search becoming trapped in the local bare minimum.

**Merit function:** One of the fundamental components for robust illumination (solar radiation) optimization is the introduction of the merit function, which allows optimization algorithms to compare whether changes in the illumination system can enhance performance [275]. This merit function randomly traces selected rays and predicts performance measures by binning rays within identified areas and/or angles. From Figure 3.6, at the initial stages, the solar field geometry was defined and through parametric control, system boundaries and variables were assigned. If the optimization does not meet the required target, the merit function is checked for improvements until the specified target is achieved.

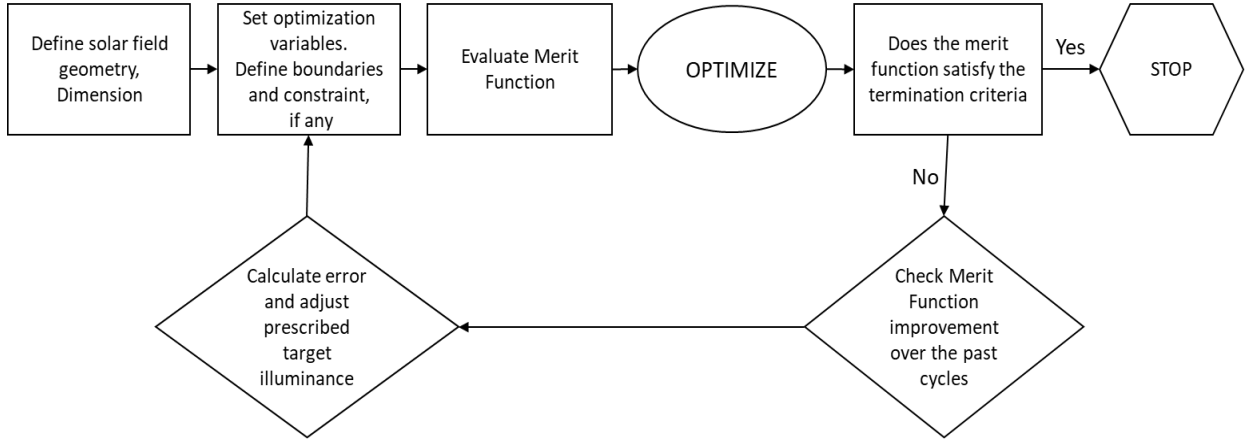


**Figure 3.6:** Flow chart of the iterative algorithm.

A flexible illumination merit function for a bundle of rays can be developed using a sum of the squares method that effectively aims at the individual rays [275, 276]. Such merit function (Eq. 3.7) provides robust performance for a wide variety of systems. Of course, other merit function groups can be included to tailor the optimizer for a specific system. The ray aiming merit function is;

$$MF_{group} = \sum_i^{N_{rays}} \sum_j^{N_{items}} w_{i,j}^2 (V_{i,j} - T_{i,j})^2 + w_{loss} \frac{\sum_i^{N_{rays}} \sum_j^{N_{items}} w_{i,j}^2 (V_{i,j} - T_{i,j})^2 + w_{loss}}{1 + N_{ReceiverRays}^2} \quad (3.4)$$

where  $V_{ij}$  is value of  $j^{th}$  parameter of  $i^{th}$  ray,  $T_{ij}$  is the target for  $j^{th}$  parameter of  $i^{th}$  ray,  $w_{ij}$  is the weight of  $j^{th}$  parameter of  $i^{th}$  ray,  $w_{loss}$  is the weight of efficiency penalty term,  $N_{ReceiverRays}$  is a number of rays that hit the receiver,  $N_{Rays}$  is the total number of rays traced, and  $N_{Items}$  is a number of different parameters for each ray used in merit function.

Using the optimized mirrors, a Monte Carlo Ray tracing is performed to check the optical performance of the modified mirrors. The result is compared with the performance of two separate mirror shapes (flat and uniform-curvature mirrors). Whilst the ray-tracing was being performed, the concentration factor in the form of irradiance, radiant intensity and rays density for different times of the day of the various mirror shapes was obtained. The location for this study was Almatret, Lleida, Spain.

The main parameters used in the ray-tracing Monte Carlo numerical simulations are presented in Table 3.2. These parameters were adopted from the Innova Micosolar linear Fresnel plant configuration in order to compare with the simulation results. In addition, several studies [63, 66, 277] have deployed similar value ranges for key parameters such as reflectance, transmittance, and absorbance in the solar field ray-tracing.

**Table 3.2:** Main parameters used in the raytracing- Monte Carlo numerical simulations

Monte Carlo Data	Value	Units
Mean value sun shape angle, $\mu_{\text{sun}}$	0.53	degrees
Primary mirror RMS of the reflector specularity distribution, $\sigma_{\text{primary\_mirror}}$	4	mrاد
External receiver glass Gaussian deviation, $\sigma_{\text{abs\_glass\_ext}}$	1	mrاد
Internal receiver glass Gaussian deviation, $\sigma_{\text{abs\_glass\_int}}$	2	mrاد
Secondary reflector Gaussian deviation, $\sigma_{\text{primary\_mirror}}$	4	mrاد
Average value of the primary reflector specularity $\eta_{\text{primary\_reflector}}$	0.88	%
Average value of the secondary reflector specularity, $\eta_{\text{secondary\_reflector}}$	0.88	%
Solar transmittance receiver glass with AR coating, $\eta_{\text{tau\_abs\_glass}}$	96.7	%
Receiver absorbance, $\alpha_{\text{abs}}$	96.1	%
Receiver emissivity black body at 400 °C, $\eta_{\text{abs\_400}}$	7.1	%
Ratio of AR coated area to total glass tube area, SAR/S <sub>glass,tot</sub> ,	96	%
Receiver glass type	Borosilicate glass	
Absorber tube thermal losses at 400 °C, Th <sub>abs_loss_300</sub>	90	W/m
Maximum HTF operating temperature, T <sub>abs_max</sub>	400	°C
Nominal pressure in the vacuum annulus, P <sub>abs_vacuum</sub>	< 1.0 x 10 <sup>-4</sup>	mbar
Maximum allowable temperature of bellows, T <sub>bellows</sub>	450	°C

**Modelling The Sun:** When it comes to solar design and analysis, the radiation that strikes the earth from the sun is complicated; thus, modelling assumptions and simplifications are frequently made. The spectral distribution and atmospheric absorption, as well as the direction of impingent solar insolation, weather influences, and how these factors change over the year, are all significant factors to consider. In the present work, however, emphasis is primarily on the direct normal insolation element of the sun's radiation and did not take into account the spectral distribution since the focus is purely on reflective concentrators.

A ray sensitivity analysis was conducted since the precision of the Monte Carlo predictions is subject to the number of rays traced [275]. Monte Carlo predictions require more rays to be traced and this may necessitate a longer to compute compared to ray aiming. For a given output efficiency, the average number of reflections (Hits) experienced by a ray can be approximated by;

$$\eta = (R_{\text{sphere}})^{Hits_{\text{avg}}}, \quad (3.5)$$

$$Hits_{\text{avg}} = \ln(\eta) / \ln(R_{\text{sphere}})$$

Since  $\ln(1 - \Delta) \approx -\Delta$  for small  $\Delta$ , the required number of hits increases as the sphere reflectivity increases. Table 3.3 shows the results of the ray sensitivity analysis. The rays are project with default wavelength of 550nm and a flux of approximately 1000W/m<sup>2</sup> [278]. The rays are parameterized with 100% transmissivity to travel in the air.

The primary and secondary reflectors are assigned with reflectivity of 92 and 0.95 per cent. The variation in power concentrated on the receiver after  $8 \times 10^5$  rays were traced was found to be negligible and thus  $1 \times 10^6$  number of rays were chosen for the simulation.

**Table 3.3:** Main parameters used in the ray-tracing Monte Carlo numerical simulations

No. of rays	Power (kW)
$6 \times 10^5$	497189.07
$7 \times 10^5$	497208.72
$8 \times 10^5$	497333.51
$9 \times 10^5$	497412.39
$1 \times 10^6$	497444.19

A sun source model comprising of a distant disc source is configured as a Lambertian emitter aimed towards the solar field aperture. The amount of the solar flux impinging within the aim region is calibrated to correspond to the direct normal insolation that strikes the specified location. Additionally, an AM1.5 is used to weigh the rays.

Figure 3.7 illustrates how this solar concept works. The solar field's rectangular aperture comprising nine (9) mirrors oriented east-west is shown surrounded by a red circular aim region. Also in red is a vector joining the origin to the solar disc, which is far away from the ground.

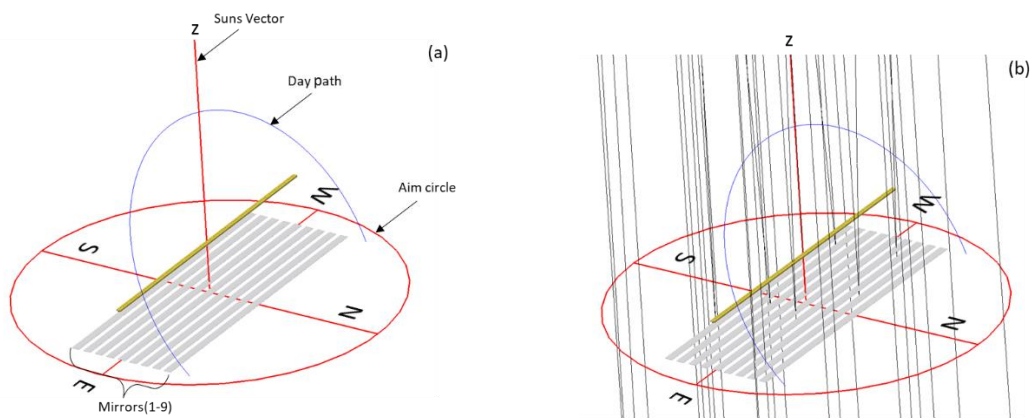


**Figure 3.7:** Sun Model and Solar Field. (a) Shows the Solar field with direction indicators. Additionally, a vector to the Lambertian sun disc (not shown) is indicated in red, along with the aim circle. (b) Rays trace from sun towards aim circle and strike the solar field

On the same figure, the sun is oriented directly overhead, and the vector is lined up with the z-axis of the coordinate system. Furthermore, North, South, East, and West are also indicated. Figure 3.7b depicts a set of rays traced from the solar disc towards the aim circle that then strikes the primary reflectors.

The solar irradiance data used for this study was obtained from PVGIS 5.2, a metrological data tool developed by the Photovoltaic Geographical Information System, European Union. The study was carried out by deploying the monthly average irradiance data for two locations, Spain (July and December) and the USA (May and December). The separate locations were selected in order to analyse the influence of physical parameters such as the solar field orientation, mirror shapes, end losses, shading and blocking of the sun's path and different seasons in a year. The monthly average irradiance for the two chosen locations is presented in Figure 3.8 below;

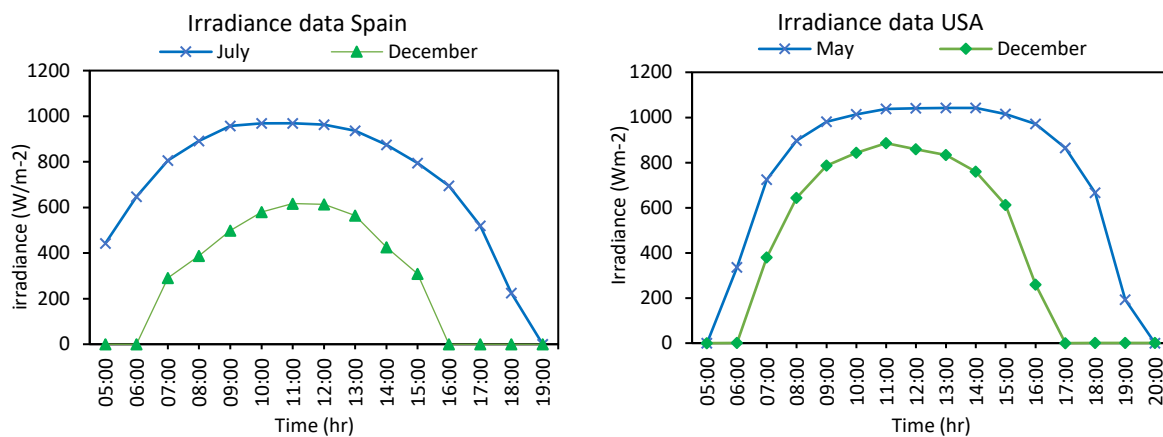


**Figure 3.8:** Monthly average irradiance data for Spain (July and December) and the USA (May and December)

### 3.4. Thermal modelling – receiver tube

A steady-state numerical simulation of the thermal performance is carried out to analyse the influence of the optimized solar field on the outlet temperature of the heat transfer fluid. This considers the main features and optimum operating condition of the receiver tube for various concentrated heat fluxes (in W/m<sup>2</sup>) and a range of values of the main variables (inlet temperature, fluid speed, thermal flux onto the absorber, etc.).

The thermal analysis is performed using Therminol 62 as the heat transfer fluid. The receiver tube has an outer external diameter of 70 mm while the thickness is about 2 mm, and its length single unit tube length is 4060 mm. Thermal losses are around 100 W/m at a temperature of about 300 °C. The absorber modules are connected to form a single hydraulic loop with a maximum temperature of 400 °C. The analysis is conducted with ANSYS Fluent (R2020) model.

Two different radiation profiles have been deployed in the analysis. These profiles imply the intensity of solar radiation on the circumference of the pipe after concentration. The first profile constituted direct normal radiation intercepted by the primary mirror and concentrated on the bottom side of the receiver, whilst the second profile consisted of drifted rays that are redirected on the receiver by a secondary reflector.

### 3.4.1. Receiver tube

A commercial evacuated tube specifically designed for CSP solar plants working at medium/high-temperature levels was selected due to the general project's requirements. The component already satisfies two of the Innova MicroSolar Project's primary requirements, mainly supporting Therminol 62 oil and having high efficiency at such a temperature level. Figure 3.9 depicts the appearance of a conventional Therminol 62 oil evacuated receiver tube. Around 96% of the aperture length is defined as the ratio of the length of the absorber ( $L_{abs}$ ) to the total length of the receiver ( $L_{HCE}$ ).

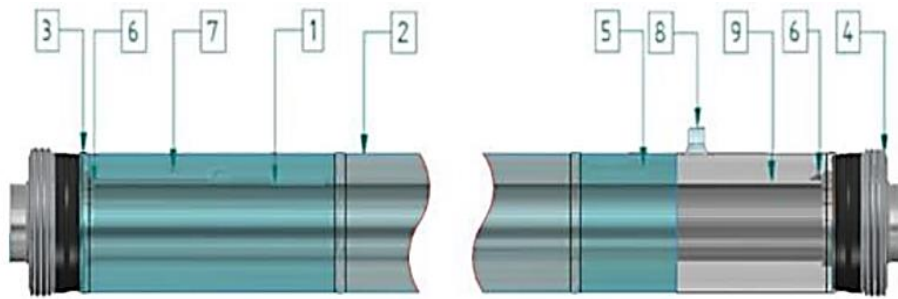


**Figure 3.9:** Stainless steel absorber tube with spectrally selective coating; 2. Glass jacket with Anti Reflective (AR) coating; 3. Glass to metal seals; 4. Thermal expansion compensators; 5. Vacuum annulus; 6. Not Evaporable Getter (NEG) pills; 7. Barium getter; 8. Pump nipple; 9. Serial number.

A spectrally selective coating is deposited on the steel tube in the specified evacuated absorber tube technology. This is a multilayer thin film construction with an interior metal layer that reflects infrared radiation and a superior antireflective ceramic substance. At the solar receiver's operational temperature (up to 400 °C), a graded ceramic-metallic material ensures a strong absorptance in the solar wavelength range and a low emittance behaviour. The tube getter absorbs the residual gases desorbed by the metal and glass surfaces inside the annulus, allowing for safe and efficient operation throughout the predicted receiver's lifespan.

The envelope glass tube has an outside diameter of roughly 125 mm. The active length is roughly 3,920 mm, and the thickness is 3 mm. The steel absorber tube has an outside diameter of 70 mm, a thickness of roughly 2 mm, and a length of 4,060 mm. The bulk glass has a solar transmittance of roughly 92%, but with the AR coating, it has a solar transmittance of around



97%. The AR coating to total glass tube area ratio (SAR/S glass tot) is approximately 96%. Solar transmittance is approximately 97%. At a temperature of 300 °C, thermal losses are roughly 100 W/m<sup>2</sup>. The maximum temperature for such a receiver is 550 °C, with a projected lifetime of more than 25 years.

### 3.4.2. Mesh details and sensitivity analysis

The quality of the discretization utilised has a direct impact on the accuracy of the steady-state approach. Structured hexahedral meshes were employed in this work since they are known to produce improved accuracy and reduce demand for CFD computational effort. Figure 3.10 shows a structure hexahedral medium mesh (3,026,340 elements) and fine mesh (3,291,392 elements). However, the refined mesh with 3,544,576 elements was selected after a thorough grid independence analysis was performed considering the computational expense time and in addition to determining the impact of mesh resolution on the results and reducing numerical impacts induced by mesh size and distributions. Figure 3.11 shows the results of the sensitivity analysis for the refined mesh, while Figure 3.12 depicts the schematic of the physical domain of the receiver pipe.

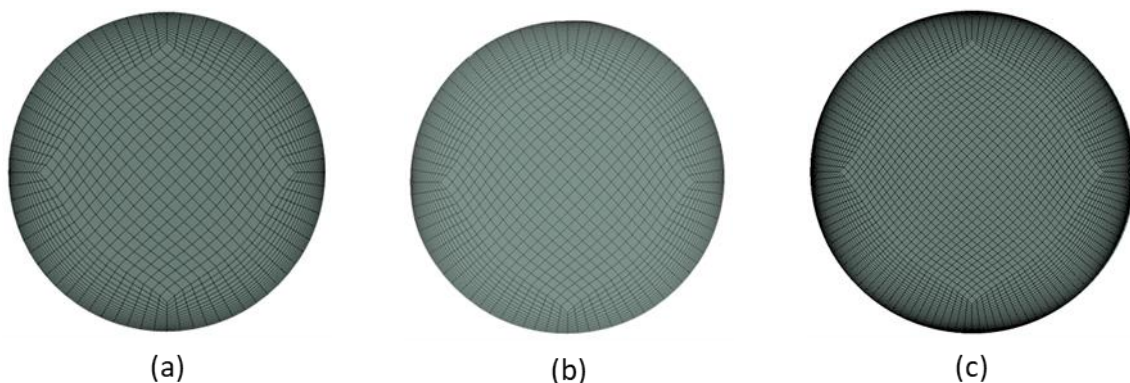


**Figure 3.10:** View of the deployed computational meshes (a) Medium mesh, (b) fine mesh and (c) refined mesh

The computational grid was created utilising hexahedral elements closest to the heat pipe's surface in order to accurately solve the flow and heat transfer in the vicinity of the surface at the wall in the pipe. In this case, the elements on the heat pipe's surface had a side length of 0.05 m. (Figure. 3.11). As a result, the computational grid's dimensions for the global number of grid points were 3 544 576, and it is observed that the variation in the numerical outcomes after 3 544 576 elements is negligible, and the Y-plus (Y+) was 12.1.

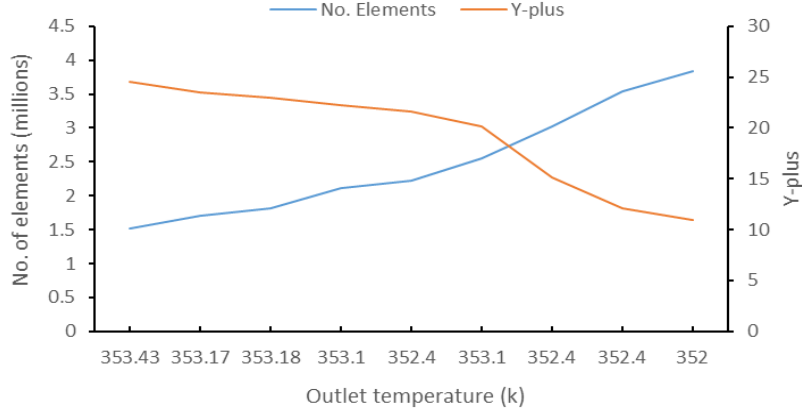


**Figure 3.11:** Mesh details and sensitivity analysis

### 3.4.3. Model governing equations

The physical model to be studied constitutes two receiver pipes connected by a hydraulic loop to form a u-shape. The hot fluid enters the pipe via the inlet with a uniform mass flow rate and different temperatures. The outer surface of the region connecting pipes is thermally insulated (Figure. 3.12) and considered adiabatic. The assumption is made in order to simplify the problem; namely, the fluid is considered compressible and steady-state with no internal heat generation and neglecting viscous dissipation. The thermo-physical properties of the fluid are temperature dependent. The receiver pipe constitutes two parts, mainly the upper part exposed to constant solar flux by the secondary reflector and the bottom part, which receives concentrated radiation from the primary reflectors. The phenomenon of flow in a conventional pipe duct is governed by the continuity, momentum, and energy equations presented in Section 5.4.2. of Chapter 5.

The useful heat generation ( $Q_u$ ) is computed using the energy balance in the fluid volume.

$$Q_u = M \cdot C_p \cdot (T_{out} - T_{in}) \quad (3.6)$$

The thermal efficiency ( $\eta_{th}$ ) of the linear Fresnel reflector is defined as the ratio of the useful heat to the available solar energy:

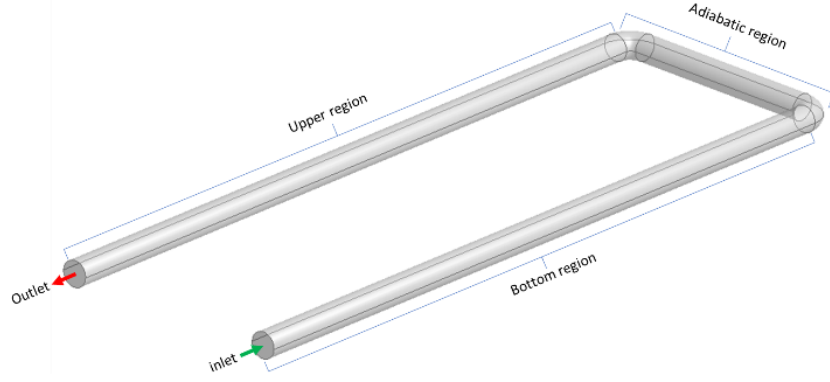


**Figure 3.12:** Schematic of the physical domain of receiver pipe

$$\eta_{th} = Q_U / Q_S \quad (3.7)$$

The mean fluid temperature ( $T_{fm}$ ) is estimated as:

$$T_{fm} = \left( \frac{T_{in} + T_{out}}{2} \right) \quad (3.8)$$

Typically, the thermal losses are by convection and radiation and expressed are as follows:

$$Q_{conv} = h_{conv} S_a (T_{tube} - T_{\infty}) \quad (3.9)$$

$$Q_{rad} = \varepsilon \sigma S_a (T_{tube}^4 - T_{\infty}^4) = h_{rad} S_a (T_{tube} - T_{\infty}) \quad (3.10)$$

Where;

$$h_{rad} = \varepsilon \sigma (T_{tube} - T_{\infty})(T_{tube}^2 + T_{\infty}^2) \quad (3.11)$$

Because it is difficult to determine the temperature of the receiver, the convection and radiation coefficients can be obtained relative to the ambient temperature in the proposed model. Furthermore, rather than the surface of the absorber  $S_m$ , the entire surface of the mirrors  $S_m$  can be deployed [54].

Hence.

$$Q_{loss} = Q_{conv} + Q_{rad} = h_{conv}' S_a (T_{tube} - T_{amb}) + h_{rad}' S_a (T_{tube} - T_{amb}) \quad (3.12)$$

$$Q_{loss} = (h_{conv}' + h_{rad}') S_a (T_{tube} - T_{amb}) = U S_m (T_{tube} - T_{amb}) \quad (3.13)$$

U is defined as;

$$U = (h_{conv}' + h_{rad}') \frac{S_a}{S_m} \quad (3.14)$$

The result from this analysis is to check the best design configuration and impact of the solar field optimization on the thermal performance of the receiver tube.

#### 3.4.4. Material properties: heat transfer fluid (HTF)

The HTF chosen is Therminol 62 (T62), a synthetic diathermic oil manufactured by Eastman in the United States. At a very low operational design pressure, T62 can reach the requisite design temperature of 280°C (maximum 6 bar). As a result, all valves and pumps in the facility can operate with lower-class gaskets, and piping does not need to be thick-walled. This is a critical element for the solar field, as it ensures the highest level of safety protection by preventing HTF leakage. This HTF is not damaging to the environment, nor does it provide any additional health hazards or danger to the surrounding area, resulting in lower plant construction and management costs. HTF's key feature is its low viscosity at low temperatures, which implies it can be pumped readily at those temperatures as well. Other features of HTF are presented in Table 3.4.

FLUENT provides a standard materials database as well as the ability to create a custom database. Depending on the physical models deployed, numerous materials may be required; in addition, the material physical and thermodynamic properties are determined.

**Table 3.4:** Features of Therminol 62 heat transfer fluid

Appearance	Water-white liquid
Composition	Isopropyl biphenyl mixture
Moisture Content, Maximum (ASTM E203-75)	200 ppm
Flash Point, PMCC (ASTM D-93)	160 °C (320 °F)
Flash Point, COC (ASTM D-92)	171 °C (340 °F)
Autoignition Temperature (ASTM E-659)	407 °C (765 °F)
Kinematic Viscosity, at 0 °C 103.	mm <sup>2</sup> /s (cSt)
at 40 °C	10.7 mm <sup>2</sup> /s (cSt)
at 100 °C	2.52 mm <sup>2</sup> /s (cSt)
Liquid density at 25 °C	951.1 kg/m <sup>3</sup> (7.94 lb/gal)
Average Molecular Weight	252
Normal Boiling Point	333 °C (631 °F)
Heat of Vaporization at Maximum Use Temperature (325 °C / 620 °F)	263.9 kJ/kg (113.6 Btu/lb)

Temperature, mass fraction, and pressure can all be used to tailor material properties. In this study, temperature-dependent options, which include the definition of properties as piecewise linear functions, were preferred. Temperature-dependent fluid properties of Therminol 62 are presented in Figure 3.13 [279].

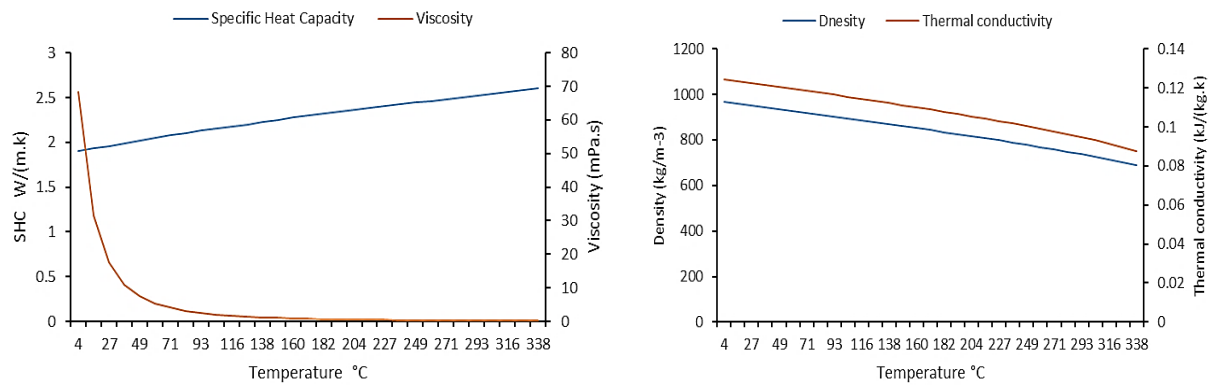


**Figure 3.13:** Temperature-dependent fluid properties of Therminol 62: specific heat capacity and viscosity (Left) and Thermal conductivity and density (Right)

### 3.4.5. Boundary Conditions

Boundary conditions and material properties form an integral part of the formulation of the task for all CFD simulations. The correctness of the simulation results is determined by how well these parameters are defined. The upper and lower bounds of the field variables are defined by the boundary conditions of any problem. These are the operating conditions that determine how variables interact and behave. There are different types (combinations) of boundary conditions. The number of boundary conditions in a fluid flow simulation can be modified to ensure that the entire balance is maintained in system forces. This can be achieved by applying the appropriate boundary condition.

**Inlet boundary condition:** To give a regulated mass flow rate at the inlet, mass flow boundary conditions are used. This is computed for a range of values of the variables (inlet temperature, fluid speed, thermal flux concentrated on the absorber, etc.). The k- $\epsilon$  turbulence model was chosen for this study due to the high Reynolds number ( $3.5 \times 10^5$ ) with a turbulent intensity of 5% [280].

**Outlet boundary condition:** a pressure-based outlet boundary condition was prescribed at the outlet. This boundary condition defines an outflow based on the flow pressure at the outlet. This option is selected because we have a value for the flow rate (or velocity), assigned at the inlet.

**Wall boundary condition:** A stationary no-slip wall condition with 0.5% surface roughness is specified. The top and bottom walls of the absorber tube are subjected to constant wall heat fluxes from the solar field discussed in Section 3.3. Heat is transferred to the fluid through the walls of the receiver tube.

### 3.4.6. Solver setting

All solution variables were initialized prior to starting iterations. The standard initialization model was selected with an inlet boundary to automatically set values that are specified at the inlet boundary. The solver for steady-state simulations was configured to perform enough iterations to attain a converged solution. Tolerances are set for all discrete conservation equations (momentum, energy, etc.) in all cells (Residual). The residue momentum (in all three coordinates) and mass flow rate as well as the energy and k-epsilon ( $k$ - $\epsilon$ ) convergence criteria are set at  $10^{-6}$ . Figure 3.14 shows the converged residuals.

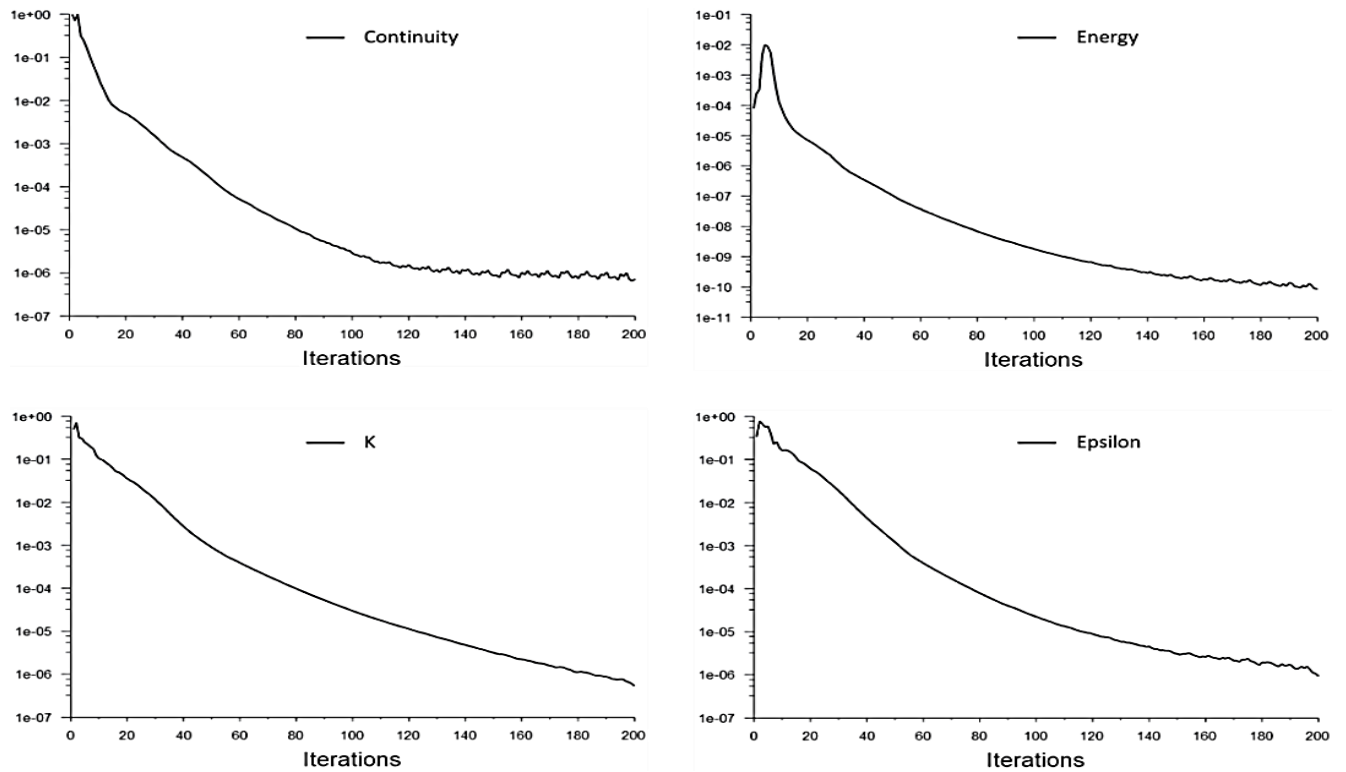


**Figure 3.14:** The converged residuals momentum, energy, mass, turbulence, and mass flow rate

### 3.5. Analysis of results and discussion

For the initial optimization, flat mirror profiles were used. NS-ray fans were added such that each ray hits a strategic point of the mirror aperture since the optimisation with NS-Rays is effective and creates a quick and stable starting point [274]. This ray constitutes a fan of five rays comprising three points, the starting point, width of fan and fan direction (all rays will be parallel). This considers the global source radiation used in the latter part of this study for Monte Carlo Raytracing of the solar field.

In Figure 3.15(a), flat mirrors were initially deployed. The receiver tube was made non-ray traceable; instead, a dummy plane with the Y-axis sharing the length of the cylinder was used.

An NS-ray fan merit function was defined to aim each ray to the local coordinate  $Y = 0$ . Figure 3.15 (b) presents the results after the optimization. Note that the radius has been converted to its reciprocal curvature since this is a more appropriate parameter to use in the optimisation procedure:

$$c = \frac{1}{r} \quad \text{where } c \text{ is curvature, } r \text{ is radius} \quad (3.9)$$

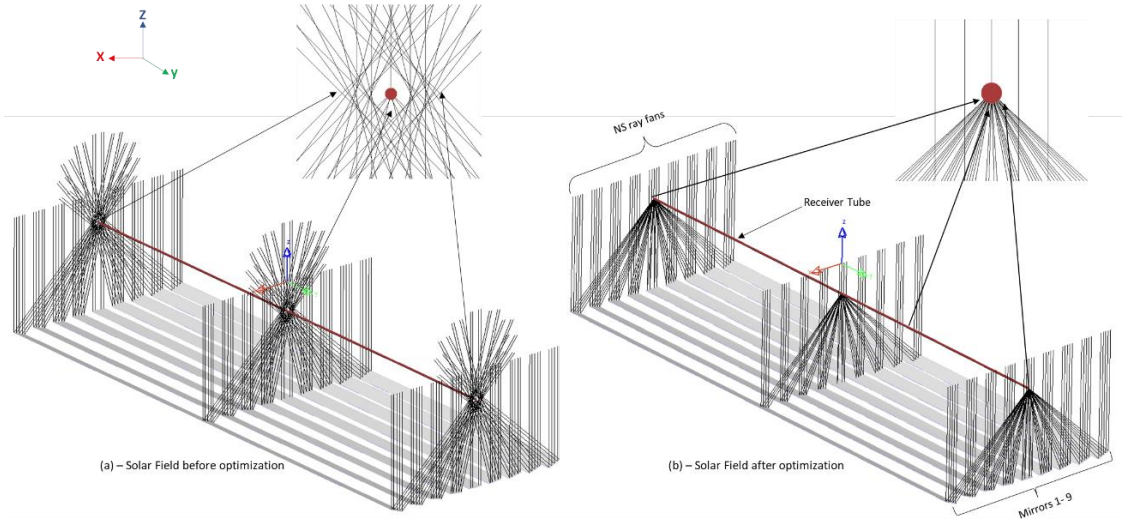


**Figure 3.15:** Solar field before (right) and after optimization (left)

From the results, variation in the curvatures and tilt (Alpha) angles can be observed from charts in Figure 3.16 and Table 3.5, respectively. The optimization proceeds iteratively in a series of steps that gradually improve the performance. Having modified the curvature to concentrate the rays on the central point of receiver tube, the mirrors horizontally align to revolve about east-west axes relative to the sun; hence only the projections of the NS-ray fans (solar radiation) in the y-z plane are reflected on to the receiver tube.

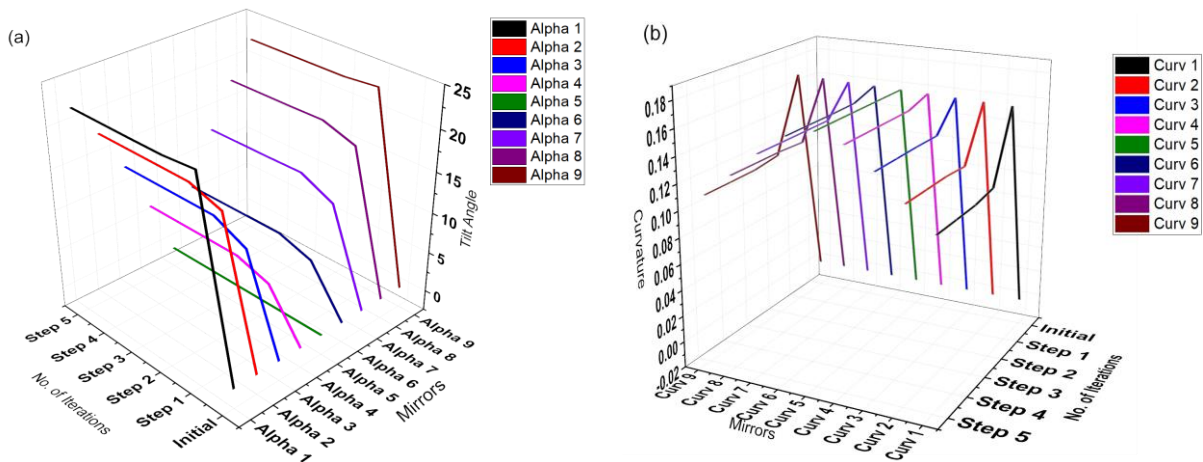


**Figure. 3.16:** Results from optimization of solar field: (a) left - the tilt angle of mirrors at the reference point and (b) right - is the alterations in mirror curvatures.



The results of the modelling and optimization obtained from the LightTool optical program were compared with the data from Innova Microsolar and the approach proposed in [59]. Table 3.5 shows the comparison of the results. The optimization simulations were performed in five (5) iteration circles, and if to assume the results for one of the mirrors, “Curv 1” (mirror 1), to be precise, it can be observed that the optimization initially starts with the value zero (0). However, as the procedure progresses, the value increases to 0.16 and iteratively declines to 0.109 after five (5) circles of iterations. As mentioned earlier, the radius has been converted to its reciprocal curvature, hence for a curvature of 0.109, the corresponding radius would be 9.19 m.

In addition, constant parameters were maintained for the receiver height ( $h$ ), the distance between consecutive mirror centre lines ( $S_n$ ) and their distance from the central mirror ( $Q_n$ ) and focal lengths ( $f_n$ ). Moreover, the variation in the curvatures ( $c$ ) of all the nine optimized mirrors for the Innova Microsolar and analytical approach can be seen. These variations can have a significant effect on the efficiency of the primary mirrors during the solar field ray-tracing.

**Table 3.5:** Result of optimization showing curvature and corresponding radius for 5 iteration steps: r-radius, c-curvature

Mirrors	$h$	$S_n$	$Q_n$	$f_n$	$\delta_n$ (°)		$C$ ( $m^{-1}$ )			$R$ (m)		
					Optimized	Ref. 59	Optimized	Innova	Ref. 43	Optimized	Innova	Ref. 43
Mirror 1	3.00	0.75	3.00	4.24	22.49	19.47	0.109	0.104	0.111	9.19	9.64	9.00
Mirror 2	3.00	0.75	2.25	3.75	18.42	16.70	0.126	0.120	0.128	7.90	8.35	7.83
Mirror 3	3.00	0.75	1.50	3.35	13.27	12.60	0.145	0.132	0.145	6.89	7.6	6.87
Mirror 4	3.00	0.75	0.75	3.09	7.01	6.91	0.160	0.148	0.161	6.23	6.77	6.23
Mirror 5	3.00	0.75	0.00	3.00	0.00	0.00	0.167	0.148	0.167	6.00	6.77	6.00
Mirror 6	3.00	0.75	0.75	3.09	7.01	6.91	0.160	0.148	0.161	6.23	6.77	6.23
Mirror 7	3.00	0.75	1.50	3.35	13.27	12.60	0.145	0.132	0.145	6.89	7.6	6.87
Mirror 8	3.00	0.75	2.25	3.75	18.42	16.70	0.126	0.120	0.128	7.90	8.35	7.83
Mirror 9	3.00	0.75	3.00	4.24	22.49	19.47	0.109	0.104	0.111	9.19	9.64	9.00

Optimization employing Monte Carlo simulation performance predictions can be exceedingly computer-intensive for non-imaging problems, as the number of rays to trace to assess the output distribution with appropriate precision is often above  $10^6$ . Furthermore, the parameterization of the reflector surface may necessitate a high number of variables, hence expanding the solution space and increasing optimization time, and increasing the likelihood of entrapment in a local minimum.

In LightTools, to determine whether or not the results of the optimization meet the set target is defined by the outcome of the Merit Function. For the initial parametrization, the value of the Merit Function item (e.g., output value, ray, ray fan, ray grid, test point, or intensity slice) for



that iteration process was assigned a specific target such as hitting local coordinate  $Y=0$  (central point on the receiver) and the weighing value of 1 (highest importance). Ideally, the Merit Function value should be very close to zero; the closer the values get to the target during the optimization, the better the system performs. The computed contribution for each Merit Function item results after optimisation are presented in Figure. 3.17.

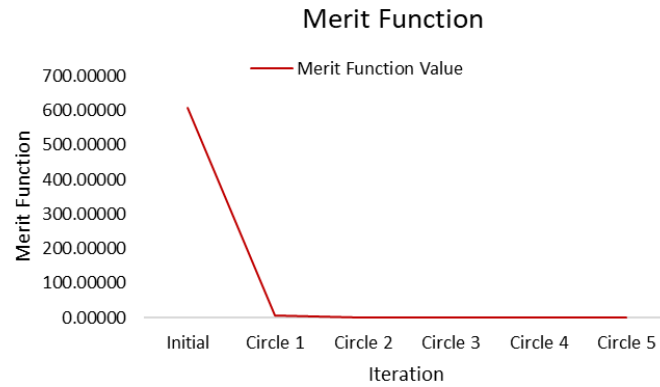


**Figure 3.17:** The result of merit function of the optimised solar field

Since the optimization takes into consideration the orientation of the mirrors relative to the sun position, in this case, NS-ray fans and the distances from the receiver tube, each mirror appear to vary in curvature as depicted in Figure 3.18.



**Figure. 3.18:** Pictorial (symmetrical) representation of optimised mirror curvatures – M- mirrors 1- 9

### 3.5.1. Monte Carlo Ray Tracing – analysis of simulation results

Monte Carlo ray tracing was used for obtaining numerical data on the performance of the solar fields, and results for the optimized solar field are compared with results obtained for the Innova MicroSolar solar field. In addition, a comparative analysis between three (3) mirror profiles is conducted, namely flat, uniform mirror curvature and the optimized mirrors. A

uniform value of  $0.166\text{m}^{-1}$  for the curvature is assigned to mirrors with a uniform curvature obtained from partial optimization. The raytracing is performed deploying average daily irradiance data for the months of July and December considering north-south and east-west solar field orientations and annual average monthly irradiance data.

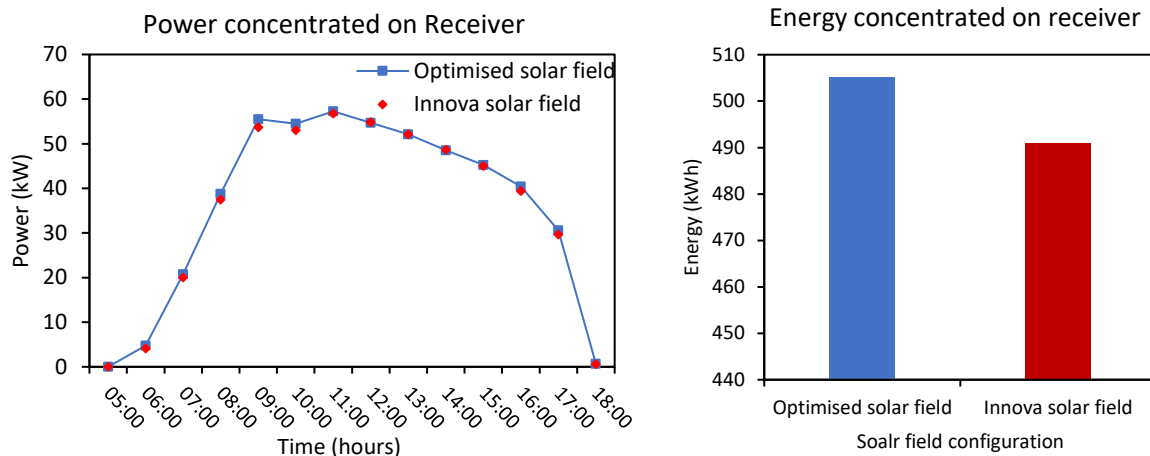


**Figure. 3.19:** Raytracing results - power concentrated on the receiver in July (left) and annual harnessed energy (right)

Figure. 3.19 (left) shows diagrams of power concentrated on the receiver, and there is a close correlation between the optimised and the modified Innova solar field, with slightly higher performance observed in the optimised mirrors. Also, it can be seen from the diagram for the total daily energy collected (Figure. 3.19 (right)) that the optimised mirrors harnessed approximately 505 kW compared to the 490 kW from the Innova MicroSolar solar field configuration. Furthermore, the diagrams of monthly average and annual energy harnessed (Figure. 3.20) show an improved performance in the optimised solar field configuration.

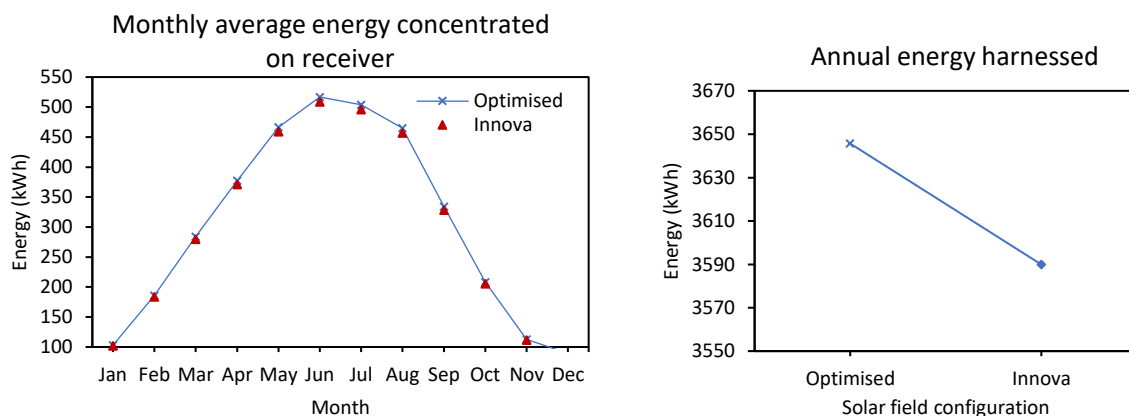


**Figure. 3.20:** Monthly average energy (left) and annual harnessed energy (right) from the solar fields

The scatter Charts in Figure 3.21 - 3.23 show the raw ray data collected by the receiver from the various mirrors' profiles (flat mirrors, uniform mirror curvature, and the optimized mirrors)

for average daily irradiance data in the month of July. The analysis is performed for both north-south (NS) and east-west (EW) solar field orientations. The Y-axis represents the length of the receiver (18m), while X-axis donates not only the width but also shows the receiver model is cylindrical and horizontally oriented. The scatter chart does not depict anything about the energy or power; however, it can show the density of ray concentration on regions on the receiver tube.

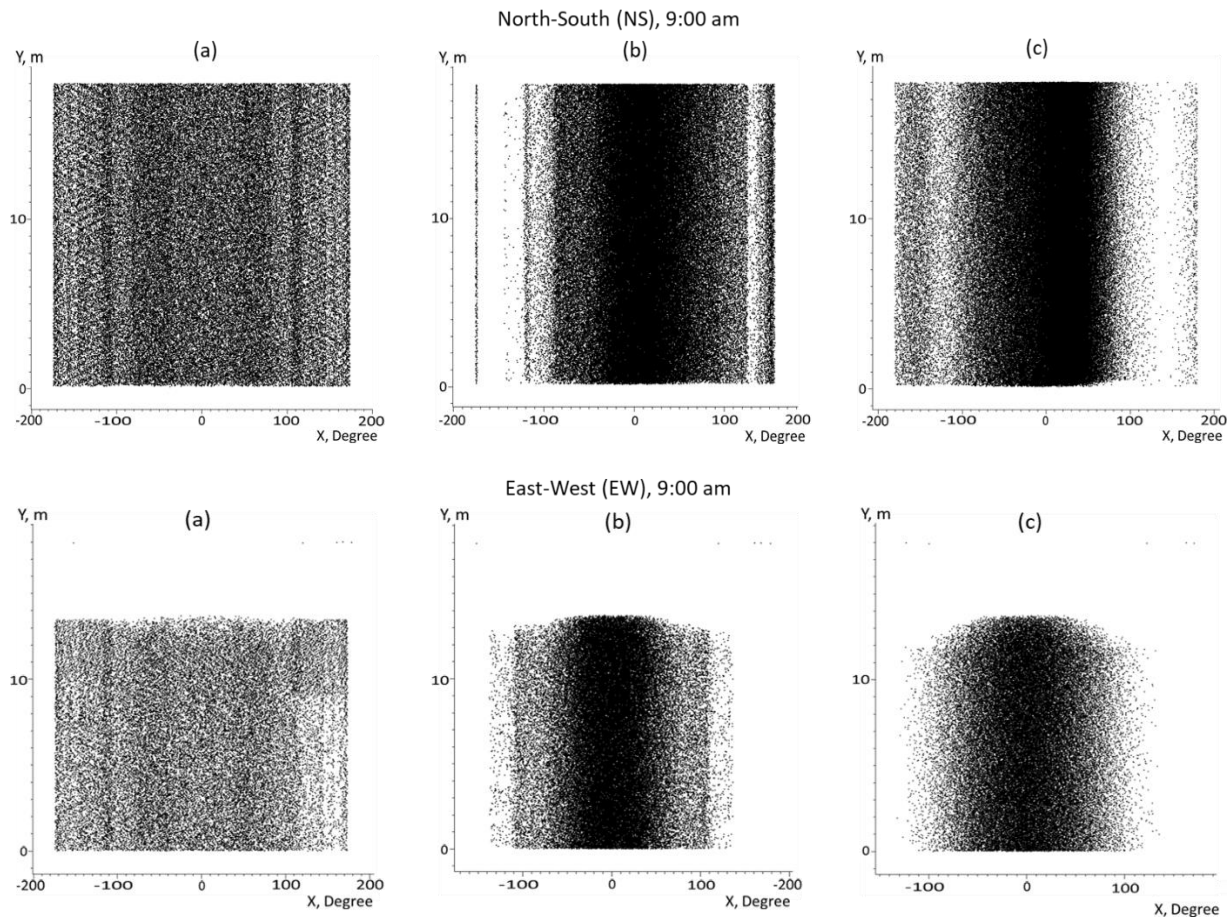


**Figure 3.21:** The concentration density of irradiance impinging on the receiver at 9:00 am in July considering north-south (NS) and east-west (EW) orientations (a) Flat, (b) Uniform curvature, (c) Optimised mirrors

With over 1,000,000 rays selected for initial tracing, the scatter chart is not very dense for the flat mirrors at 9:00am, 12:00noon and 3: 00pm for both north-south and east-west orientations, respectively, as depicted in Figure 3.21-3.23. This indicates a lower concentration compared to the uniform curvature and optimized mirrors. However, the significance of deploying a secondary receiver can be observed from the results of the flat and uniform-curvature mirror. The uniformity in the scattering of rays impinging on receivers in both cases is due to drifted rays being redirected onto the receiver by a secondary reflector. This further justifies the drifts and variation in concentrated rays in both cases as the secondary reflector refocuses drifted rays resulting in wider width ( $180^0$ - $200^0$ ) of the receivers covered with redirected rays.

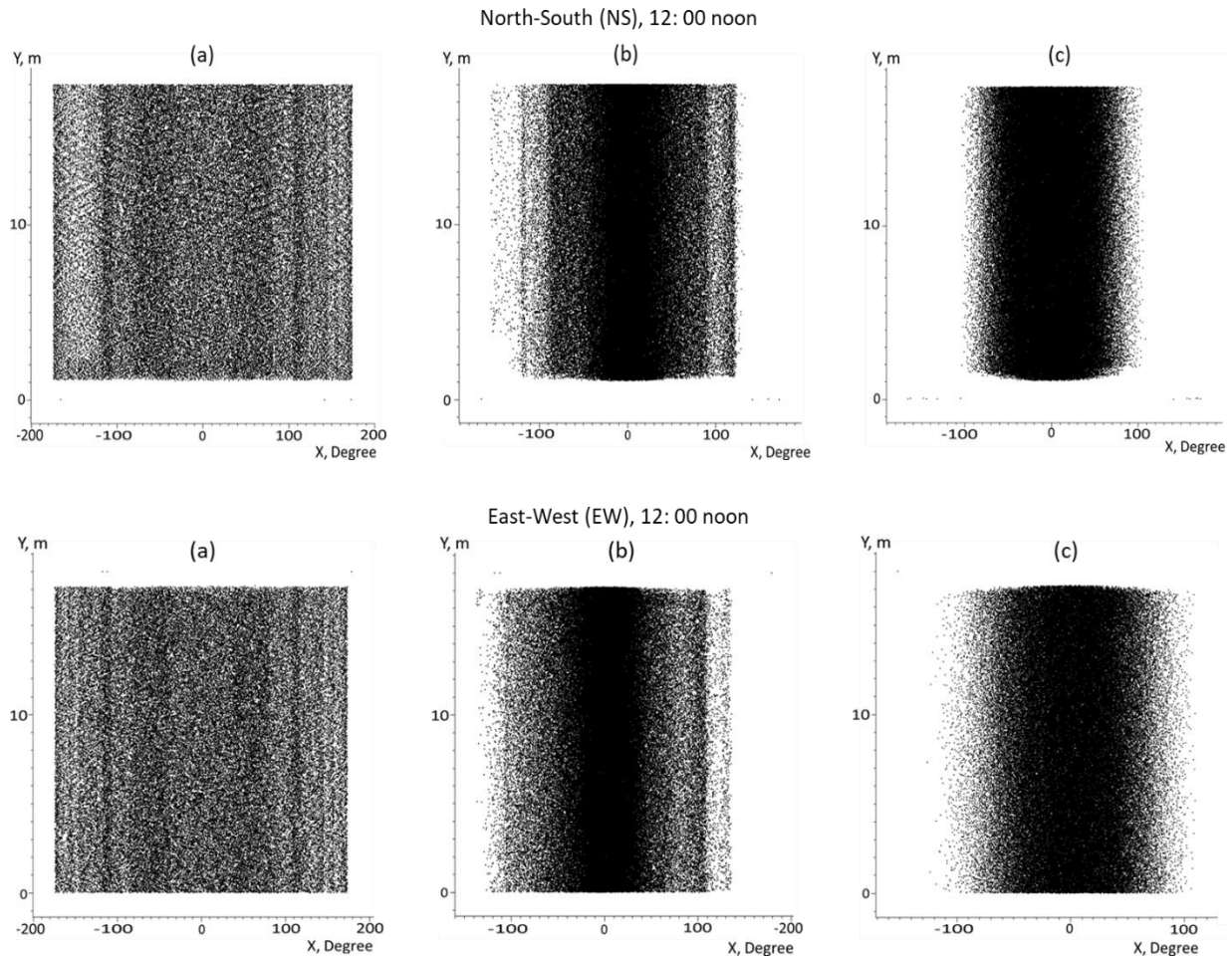


**Figure 3.22:** The concentration density of irradiance impinging on the receiver at 12:00 noon in July considering north-south (NS) and east-west (EW) orientations (a) Flat, (b) Uniform curvature, (c) Optimised mirrors

The ray concentration tends to be denser in the case of the optimised mirrors, especially between 12:00noon and 01:00pm. In addition, from the orientation point of view, the concentration tends to be denser and precise in the case of the north-south orientation. The scattering being narrow implies the rays impinging on a common focus on the receiver; hence the variation in reflection rays reaching the receiver is greatly reduced. This implies an improved performance from the optimised mirrors, which can enhance the overall output of the solar field.

In a Linear Fresnel reflector solar system, some portion of the collector aperture remains unused as a result of end losses and inter-row shading/blocking. With regards to the former, it can be observed from the scatter chart in Figure 3.21 and the picture of the solar field in Figure 3.24 that the east-west orientation compared to the north-south suffers from end losses at 9:00am. This is due to the non-zero angle incidence of sunbeams in the axial path. The intensity of solar radiation is mainly a function of the angle of incidence, the angle at

which the Sun's rays strike the earth's surface. This greatly affects the overall output of the solar field, which is discussed in the subsequent sections.

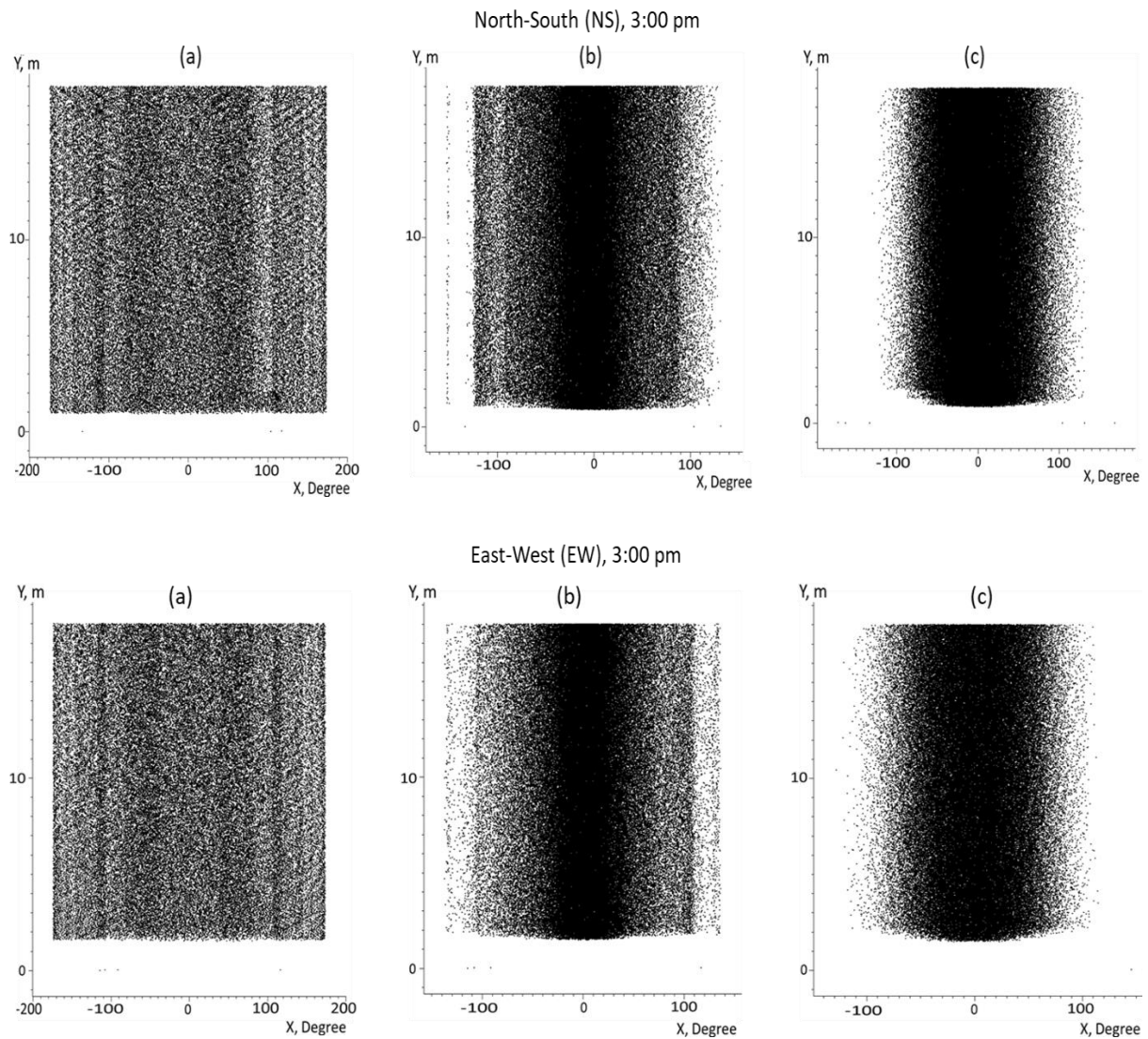


**Figure 3.23:** The concentration density of irradiance impinging on the receiver at 3:00 pm in July considering north-south (NS) and east-west (EW) orientations (a) Flat, (b) Uniform curvature, (c) Optimised mirrors

The amount of direct radiation received varies throughout the day due to the angle subtended by the mirrors (as seen by the sun) changes. The quantity of solar radiation varies with the cosine of the angle; hence the amount of solar radiation received is maximum when the cosine is equal to 1. The scattering of ray concentration on the receiver tube can be further analyzed on the lumber viewer in Figures 3.25 - 3.27.

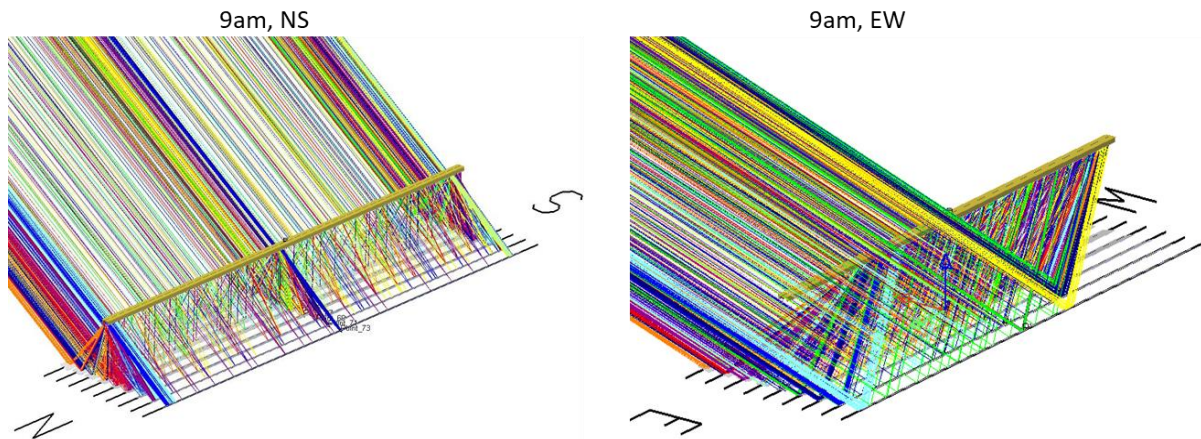


**Figure 3.24:** Solar field ray tracing at 9: 00 am: north-south (NS) – Left and east-west (EW) solar field – Right showing the effect of end losses

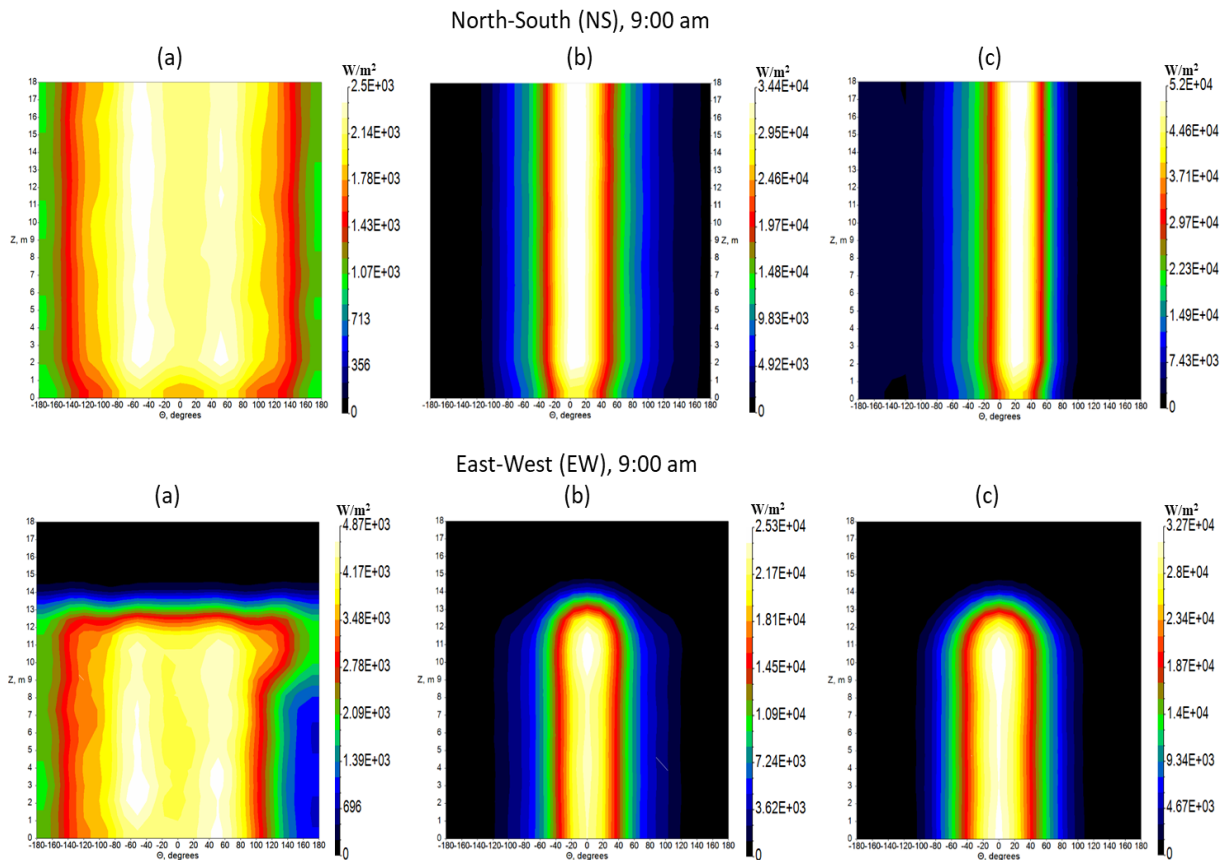


**Figure 3.25:** The concentration of irradiance impinging on the receiver at 9:00 am in July considering north-south (NS) and east-west (EW) orientations (a) Flat, (b) Uniform curvature, (c) Optimised mirrors

The Lumber plots graphically show the pseudo-colour map of irradiance (spatial) concentration on the receiver. Black regions indicate zero intensity, and other coloured regions, from blue to white (centre), indicate the low to the highest concentration of irradiance. In addition, the pseudo-colour map depicts how accurate data is concentrated on a specific region of the receiver surface. The legend to the right of the main colour grid shows statistics on the amount



of power at different irradiance levels. The Z-axis represents the length of the receiver (18 m) while the width being cylindrical, is in degrees starting from the central point and varies from 0 to  $\pm 180$  degrees.

The flat mirror configurations in the north-south and east-west orientation in all three (3) cases, as shown in Figures 3.25a - 3.27a, recorded lower irradiance concentrations. The fact that the mirror profiles are flat and specularly reflecting when the sun is out of its reference position thus precluding the possibility of getting a common focus or illumination over the entire surface of the absorber. The contribution of this mirror element to the concentration on the surface of the receiver is reduced. This challenge results in modest energy efficiency (50%) of the solar field and variation in total radiation falling within the field.

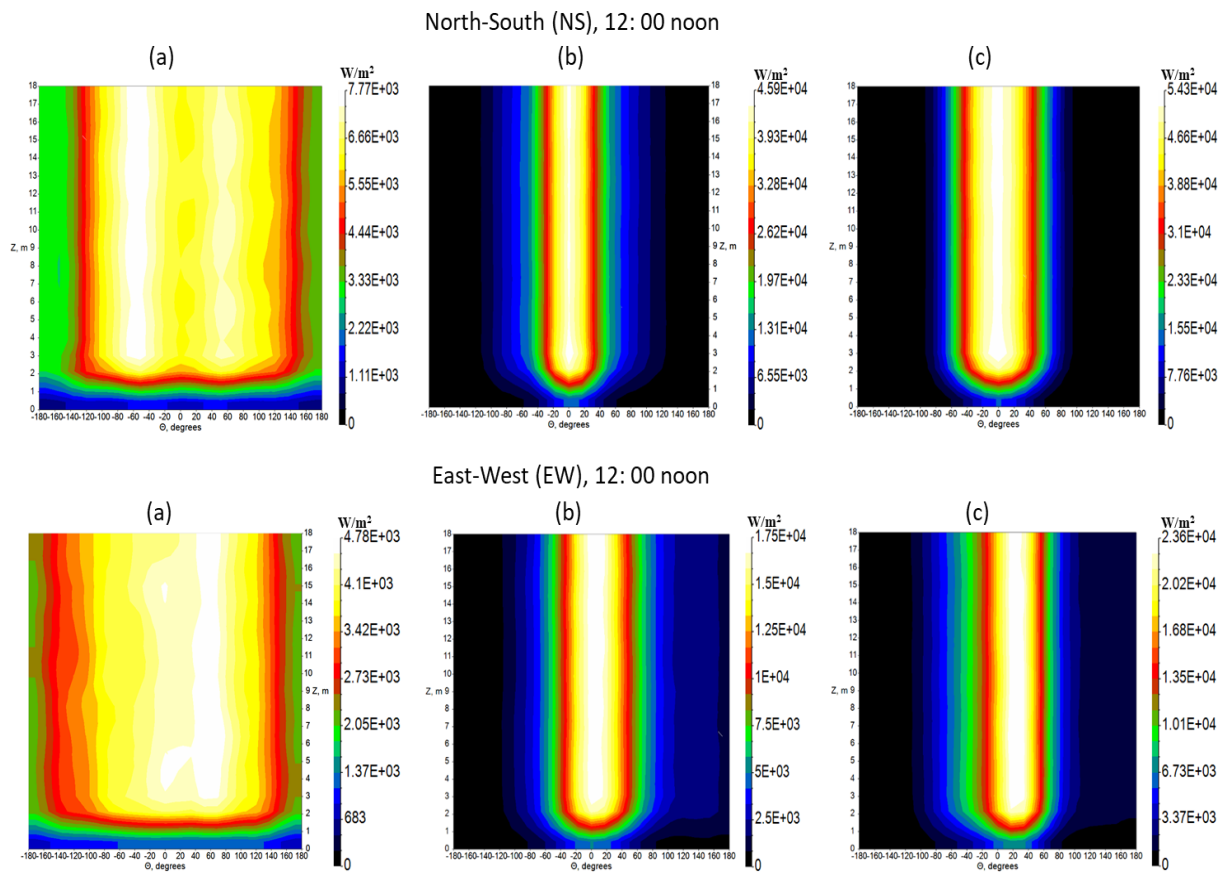


**Figure 3.26:** The concentration of irradiance impinging on the receiver at 12:00 noon in July considering north-south (NS) and east-west (EW) orientations (a) Flat, (b) Uniform curvature, (c) Optimized mirrors

It can be observed that the best configuration is the one that has the mirror elements optimized (Figures 3.25c - 3.27c). The reason for this is the mirror profile being modified, drifts in ray concentration are greatly minimized, and after reflection, illuminates a common focus on the absorber. This eventually improves the concentration factor and results in greater energy impinging on the absorber. Also, an average performance can be seen from the configuration

with uniform mirror curvatures (Figures 3.25b - 3.27b). The partial modification (optimization) of the mirror profiles has improved the concentration compared to the flat mirrors, however lower than the optimized.

The effect of end losses can be noticed at 9:00am and 3:00pm in the case of the east-west orientation compared to the north-south, which is somewhat marginal. The variation on the focal area of the receiver at 9:00am is approximately one-third of the length of the receiver length. With the change of solar altitude angle and azimuth angle, the loss at the end of the receiver, however, is marginal at 3:00pm. The concentration ratio tends to be higher for the optimized mirrors in both orientations, with a very little variance at 3:00pm.

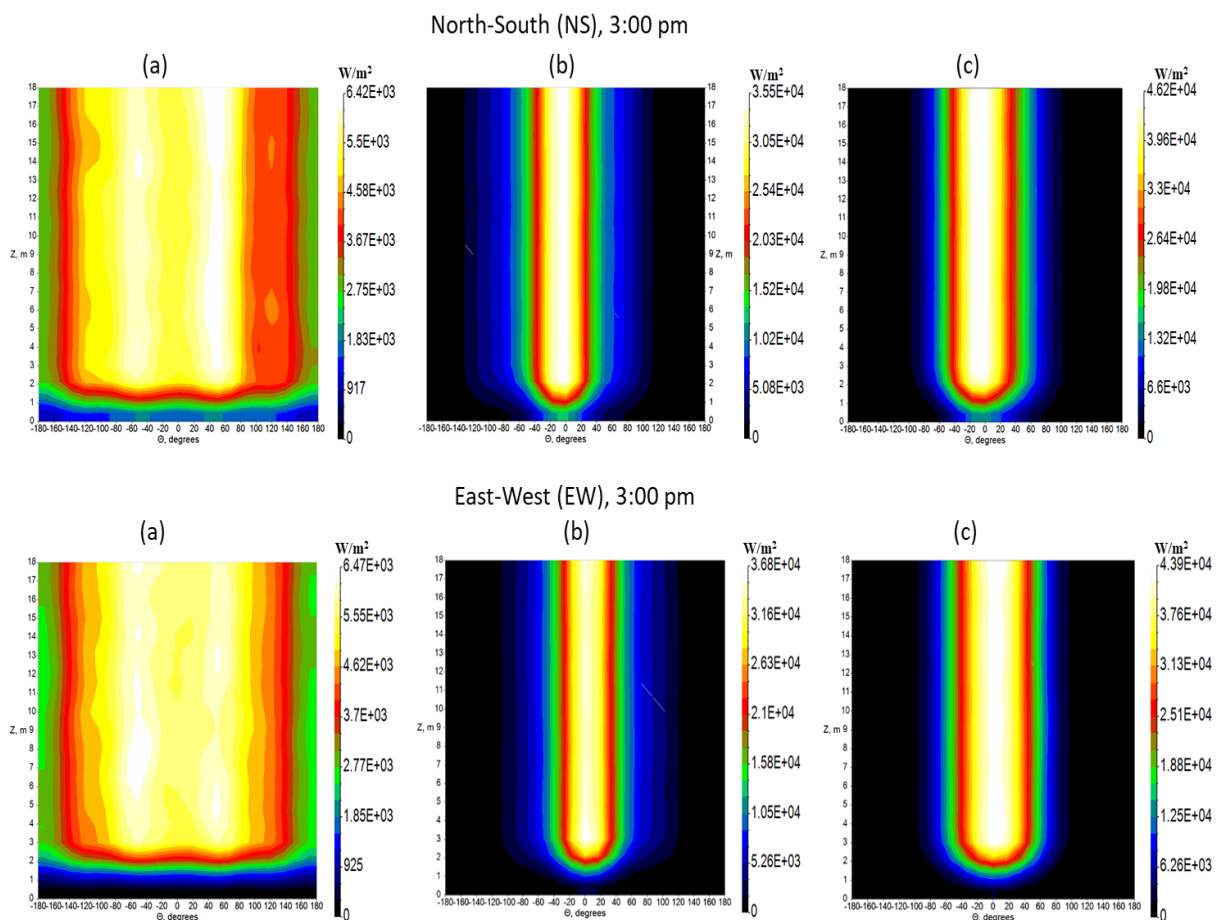


**Figure 3.27:** The concentration of irradiance impinging on the receiver at 3:00 pm in July considering north-south (NS) and east-west (EW) orientations (a) Flat, (b) Uniform curvature, (c) Optimised mirrors

Furthermore, additional observations can be drawn from Figures 3.25 - 3.27. The symmetrical axis of the plots, which represent ray concentration on the absorber, ranging from black to white, indicating lower to higher concentration, vary in pseudo-colour for the three configurations. The black region represents a portion of the receiver not covered by rays. One may notice a greater portion of the receiver concentrated with rays in the case of the flat mirrors.



The symmetrical axis is wider in width ( $180^0$ ) since the colours that make up the chart indicate active regions on the absorber. Note, this does not denote higher concentration or efficiency; however, it shows that a considerable amount of ray drifts occurred, which were redirected back on the absorber by the secondary reflector, resulting in somehow uniform distribution across the length of the receiver.

Deploying a similar approach, it can be observed that the symmetrical axis highlighting the active portion on the receiver tends to be narrower in the width for both uniform mirror curvatures and optimized mirrors. With the latter slightly narrower ( $60^0$ -width) than the former ( $100^0$ -width) and compared to the ( $180^0$ -width) flat mirrors. Also, since the black region of the symmetrical axis, which appears to have a wider width, highlights portion on the absorber not hit by rays, the drifts and variation in ray concentration are said to be greatly minimized, hence reflected rays in both cases illuminate a common focus.

A similar study was conducted to determine the influence of the sun path on the performance of the solar field deploying average daily irradiance data for the month of December, considering both north-south and east-west solar field orientations. Figures 3.28 - 3.30 illustrate the density of raw ray data intercepted by the receivers at 9:00am, 12:00noon and 3:00pm, respectively, for the three (3) mirror configurations.

Furthermore, the received concentration characteristic is a little different in the east-west direction in December compared to in July, showing an improved concentration. This is because the north-south variation in sun angle predominates over the east-west variation (which is what is being tracked here).

Factors such as blocking effects, shading, and the end-loss effect play a significant role in the performance of the solar field. This is noticeable repeating the preceding simulation with the east-west direction. Slight nearest-neighbour blocking can be noticed from all three (3) cases in the results obtained at the start and end of the day, due mainly to the low sun position. This effect is indicated by the stripes (angles greater than  $180^0$ ) on the receiver observed in 'b' and 'c' in all three (3) circumstances from Figures 3.28 - 3.30. The north-south orientation, on the other hand, exhibits much less blocking by the nearest neighbour.

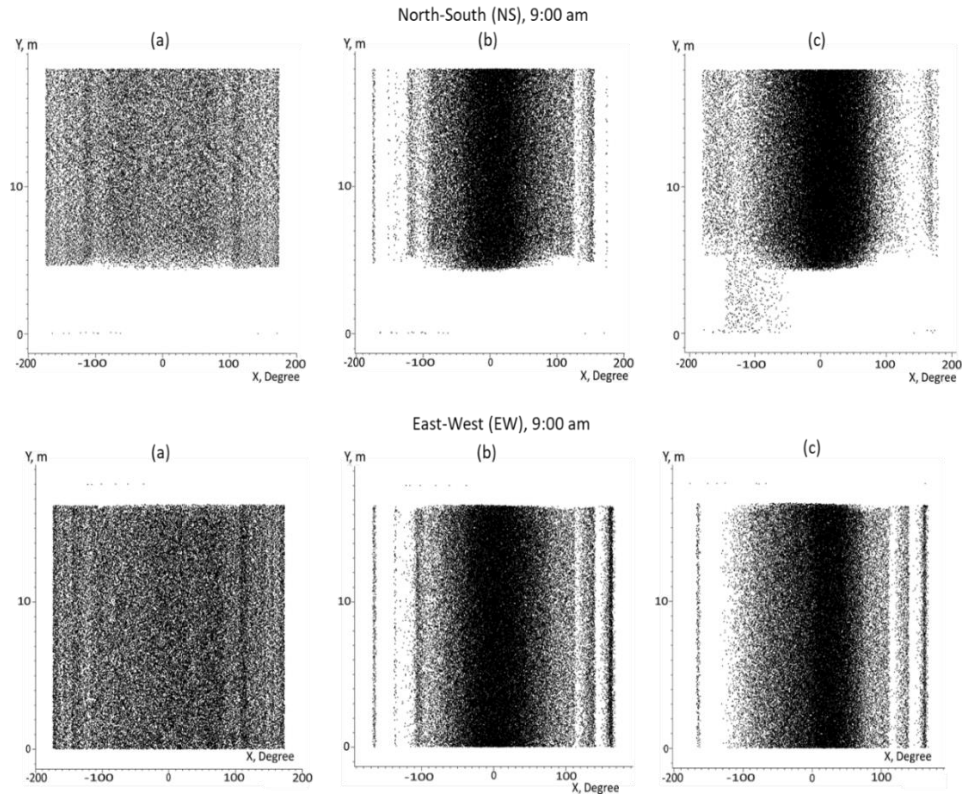


**Figure 3.28:** The concentration density of irradiance impinging on the receiver at 9:00 am in December considering north-south (NS) and east-west (EW) orientations (a) Flat, (b) Uniform curvature, (c) Optimised mirrors

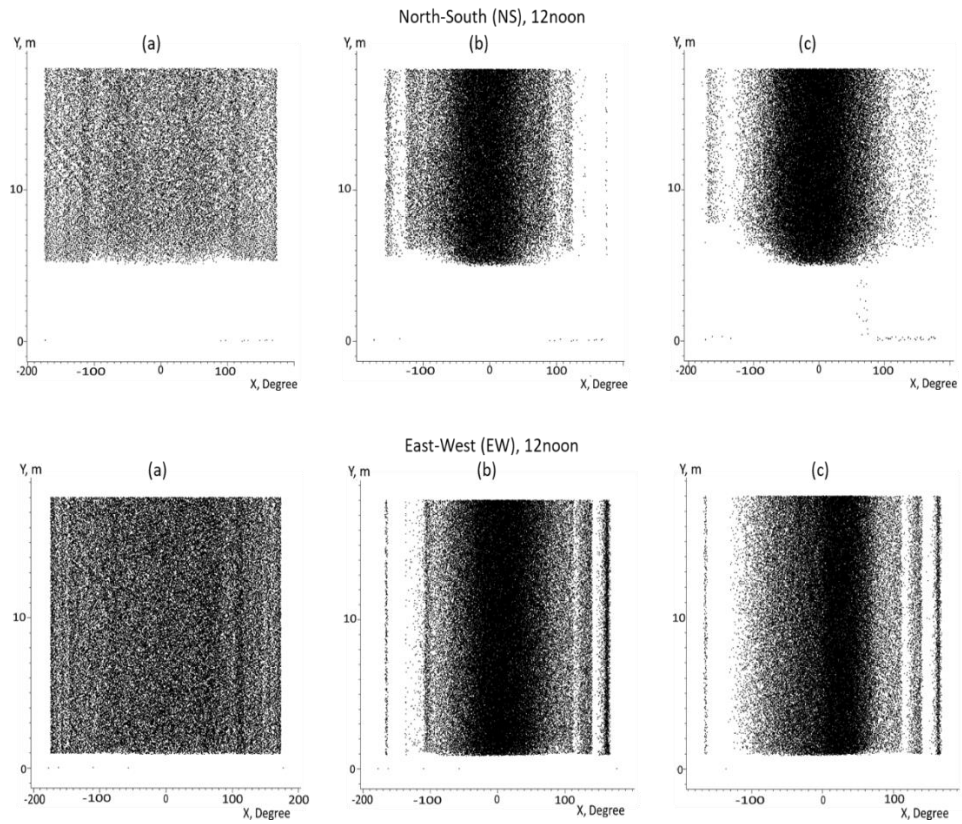


**Figure 3.29:** The concentration density of irradiance impinging on the receiver at 12:00 noon in December considering north-south (NS) and east-west (EW) orientations (a) Flat, (b) Uniform curvature, (c) Optimised mirrors

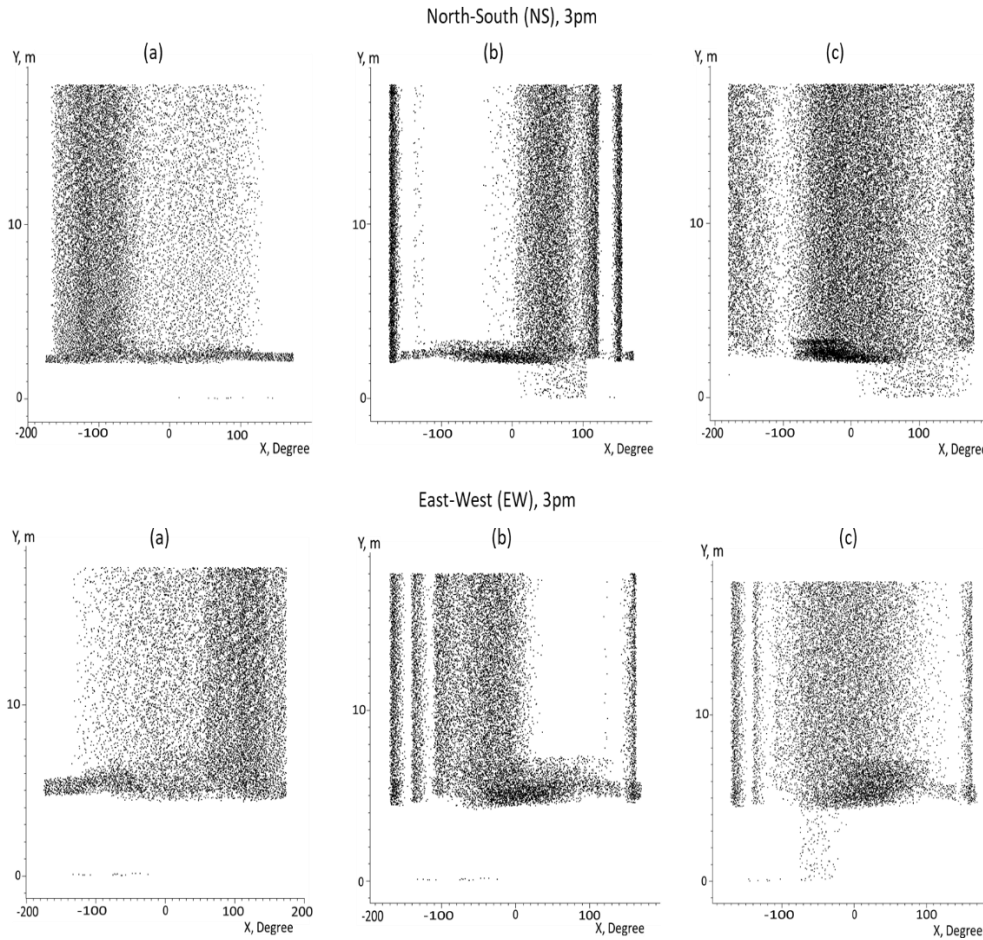


**Figure 3.30:** The concentration density of irradiance impinging on the receiver at 3:00 pm in December considering north-south (NS) and east-west (EW) orientations (a) Flat, (b) Uniform curvature, (c) Optimised mirrors

The shape of the primary mirror is an important feature of a linear Fresnel reflector since it is one of the features that determine the degree to which reflected rays conform to the law of reflection, where the reflected angle equals the incident angle. The reverse is a diffuse reflector, which scatters reflected rays in a broad range of directions. This effect can be observed in the performance of the flat mirrors. The mirror profile being flat, impinging sun flux struggled to concentrate on the focal line of the receiver; hence drifted rays are redirected onto the receiver surface by the secondary reflector resulting in a uniform and wider ray concentration on the surface of the receiver tube. Blocking and end losses effects are further observed from rays traced at 3:00 pm (Figure 3.29).

It can be drawn from the result of the July raytracing that the sun shape depends on location and varies with time; hence, this greatly influences the reflector's optical performance. The lumber charts in Figures 3.32 - 3.34 depict the power intercepted by the receiver in December,

considering the two (2) solar field configurations by deploying a similar approach used in the July raytracing of the solar field.

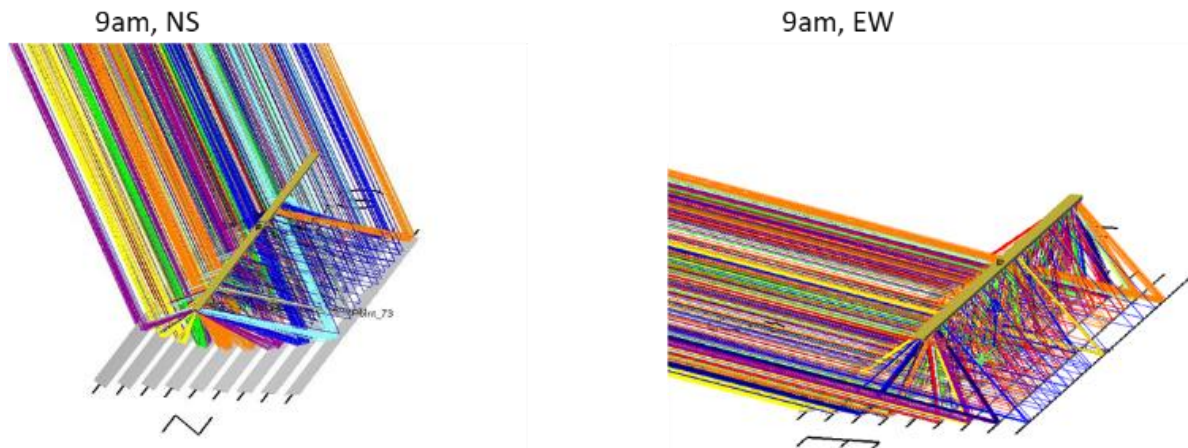


**Figure 3.31:** Solar field ray tracing at 9: 00 am: north-south (NS) – Left and east-west (EW) solar field – Right showing the effect of end losses

The trend of the results for the rays traced December depicted in Figures 3.32 - 3. 34 exhibits similar behaviour to the solar field performances traced in July such that the variations and lateral drifts in ray concentrations are significantly decreased in the uniform curvature and optimized mirrors for data obtained at different times of the day. However, from the intercepted power point of view, it can be drawn from the statistics on the amount of power at different irradiance levels that the east-west harnesses more power than the north-south orientation in December. Furthermore, the effect of end losses encountered in ray-traced July is marginal in December.

End losses are common to parabolic trough and linear Fresnel reflectors concentrators. The decline in power harnessed by the north-south (Figure 3.32) orientation results from the impinging sun rays that are reflected from the mirror but which, as a result of the sun not being directly overhead of the mirrors and longitudinal incidence angle of the mirror as seen by the sun path, drifts away from the receiver, and instead is concentrated beyond the end of the receiver. Depending on the orientation (north-west or east-south), these losses might be experienced all year round, or else only in the morning and evenings.

If the flat mirrors were considered in all three (3) cases of rays traced, we would find the irradiance levels shown in Figures 3.32 - 3.34. One may observe that the maximum concentration factor is very low, around  $4.7 \text{ kW/m}^2$  at peak (at 12 noon); in addition, after the general shape, one may deduce that an important part of the radiation is lost on the sides of the receiver.

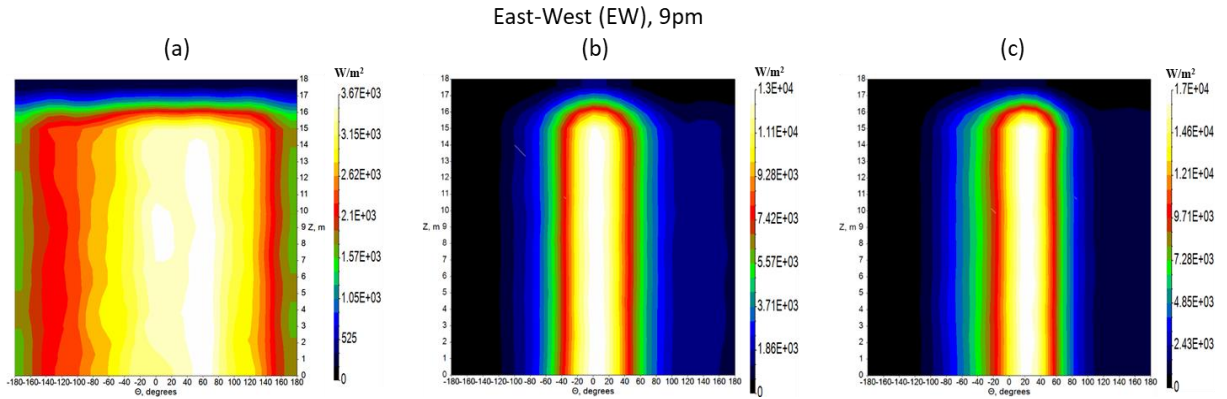
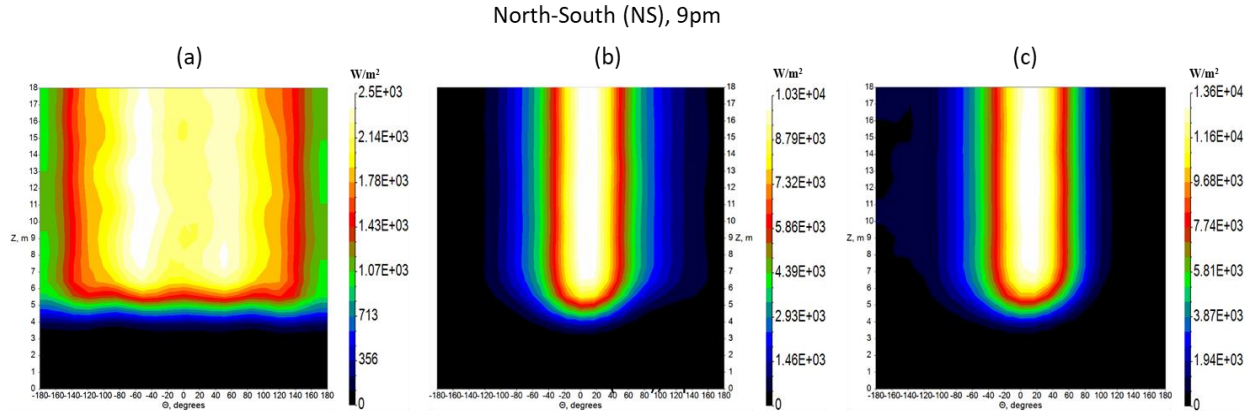


**Figure 3.32:** The concentration of irradiance impinging on the receiver at 9:00 am in December considering north-south (NS) and east-west (EW) orientations (a) Flat, (b) Uniform curvature, (c) Optimised mirrors

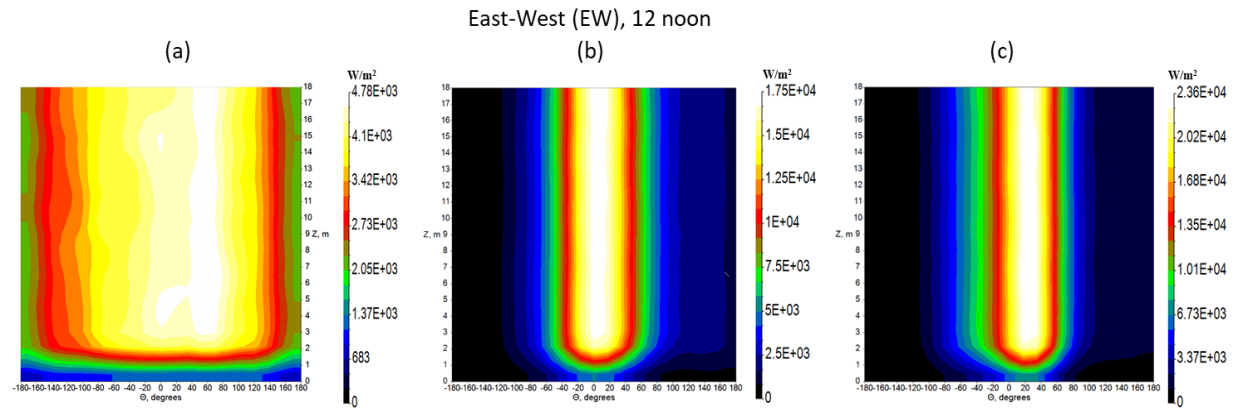
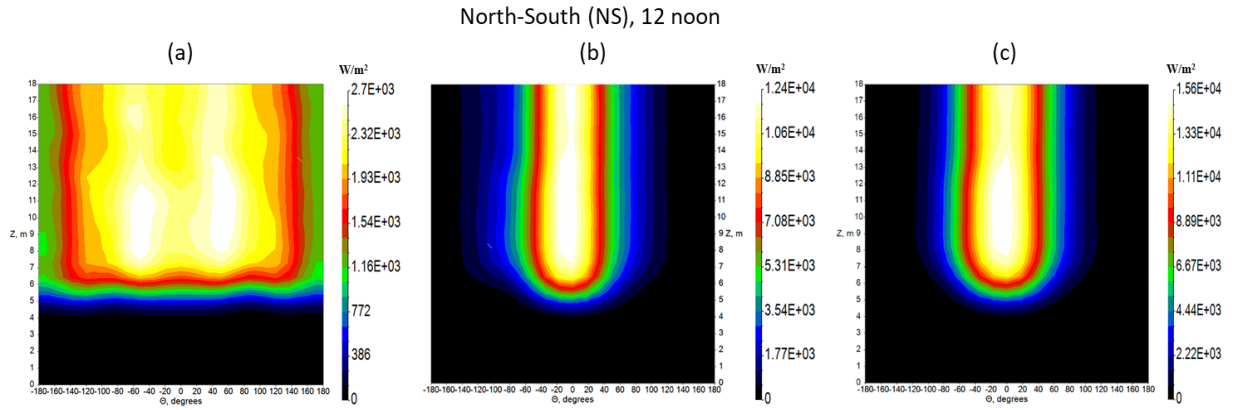


**Figure 3.33:** The concentration of irradiance impinging on the receiver at 12:00 noon in December considering north-south (NS) and east-west (EW) orientations (a) Flat, (b) Uniform curvature, (c) Optimized mirrors



This makes sense, as mirrors are flat, they do not imply an extra concentration, and they are wider than the receiver itself. If the number of mirrors were doubled, their width being only 45 cm (same total surface), the concentration features would be improved, achieving close to the concentration recorded by the uniform curvature and optimized mirrors.

Due to the receiver design and configuration concept, the mirrors of both north-south and east-west orientations suffer blocking effect from nearest their neighbours. Whilst farthest mirrors which turn to be almost perpendicular, suffer major blocking effect by their nearest neighbour. Generally, all mirrors may also suffer shadowing from the receiver to which they are concentrating. This effect can be observed in the raytracing results recorded at 3:00pm in December for both solar field orientations.

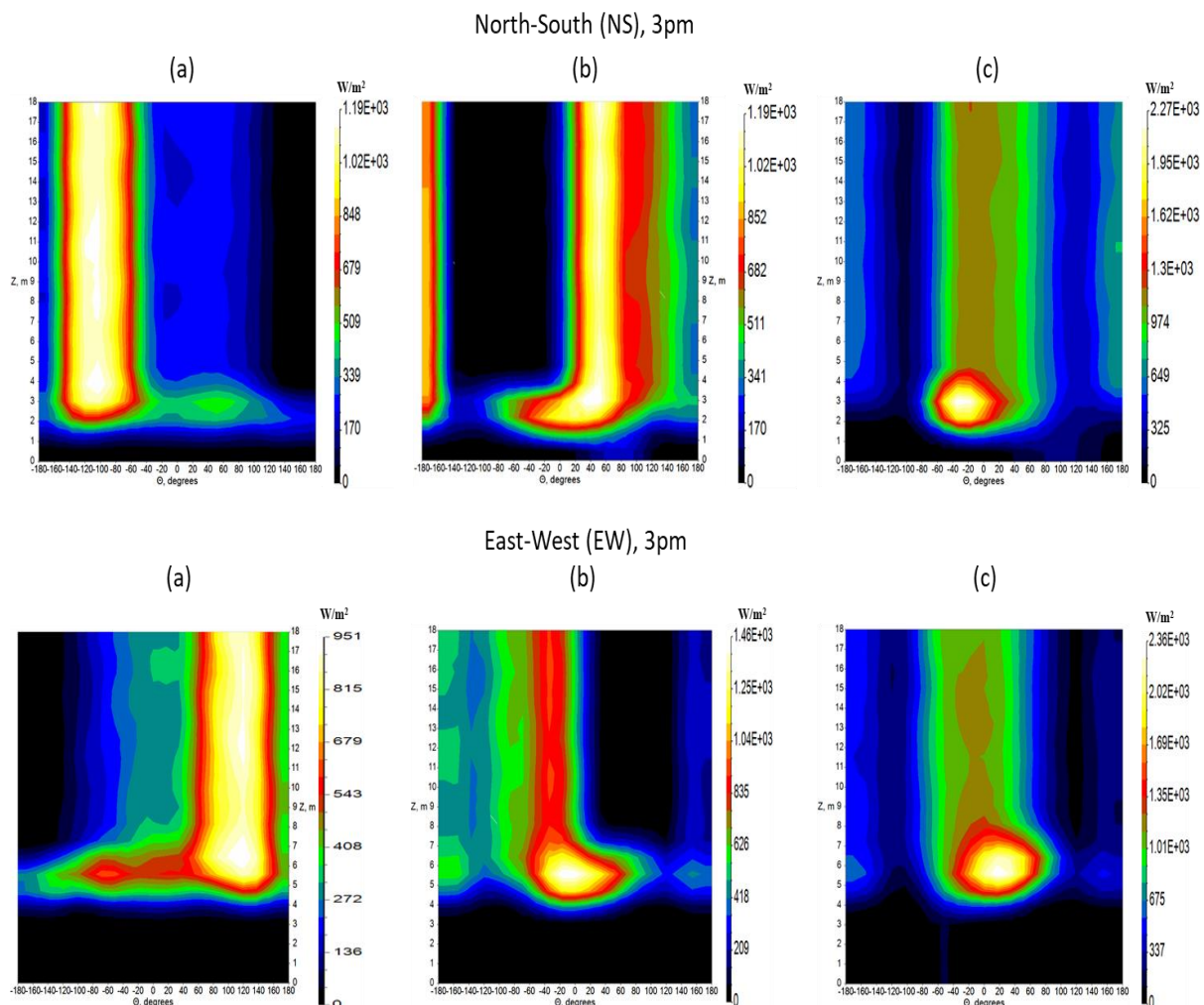


**Figure 3.34:** The concentration of irradiance impinging on the receiver at 3:00 pm in December considering north-south (NS) and east-west (EW) orientations (a) Flat, (b) Uniform curvature, (c) Optimised mirrors

The energy efficiency of LFR solar field is determined by computing the ratio of flux intercepted by the receiver to the amount of radiation that is incident on the LFR primary reflectors. This is conducted at different average Direct Normal Irradiance (DNI) conditions

for the months of July and December, taking into account the different mirrors profiles and solar field orientations. In addition, the total power harnessed by the separate mirror elements within the prescribed times is determined. The power (irradiance) as a function of time varies considerably across the average Direct Normal Irradiance (DNI) conditions. Figure 3.35 shows the power striking the receiver as plotted over average daily irradiance data for the month of July, considering the two solar orientations.

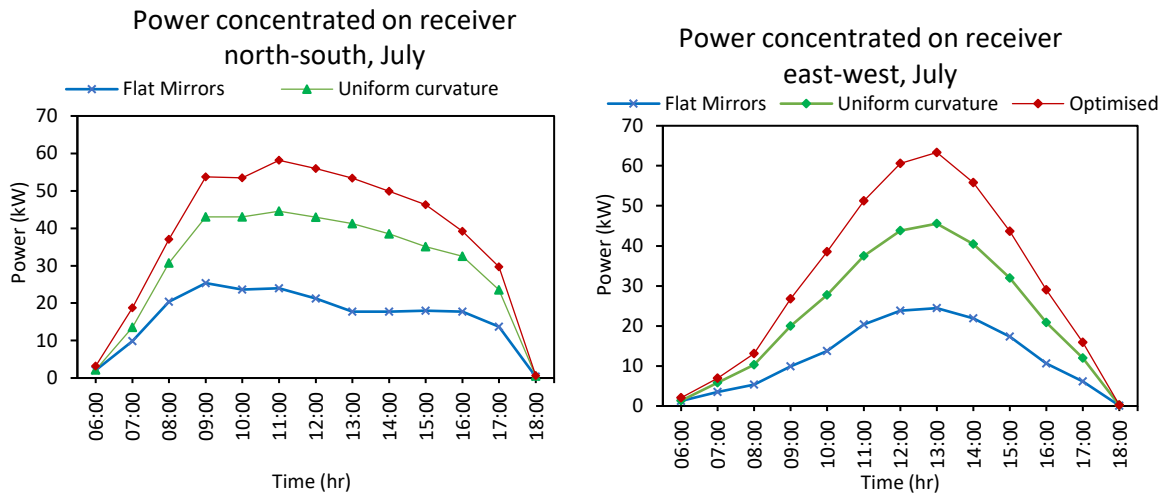


**Figure 3.35:** Power concentrated on receiver by different mirror profiles: flat mirrors, uniform mirror curvature and optimized mirrors for north-south (Left) and east-west (Right) in July.

Considering that this is a one-axis tracking system, it can be observed that generally, the north-south tracker offers the biggest payoff. This, however, depends upon the shape and size of the collectors as well as other factors. Because tracking collectors are invariably used in multiple units, the interaction between neighbouring collectors becomes one factor. Another factor is the blocking effect resulting from the receiver assembly. A slight decline in power impinging on the receiver at 10:00am caused by the blocking effect of the receiver due to the transverse movement of the sun can be seen in Figure 3.35(left). The effect is experienced by most collectors as long as the sun moves, and the receiver gets in between the mirrors and the sun. In this case, however, it was marginal during the other times of the day.

Furthermore, the mirrors aligned in east-west orientation suffer less blocking effect from the receiver assembly due to the longitudinal path of the sun as seen by the mirrors aligned in the east-west direction; hence, the east-west orientation attains a peak power of about 63kW at noon compared to about 59 kW of the north-south. Nonetheless, the energy efficiency and total power harnessed in Figure 3.36 show that overall, the north-south orientation leads to a more uniform energy production along the day in all three cases.

The energy efficiency and power harnessed show significant variation during raytracing for the separate mirror elements and their orientations (Figure 3.36). With the maximum energy value of about 500kWh and a daily efficiency of 88% (north-south) and 400kW, and a daily efficiency of 82% reached (east-west) in July, the best configuration is the one that has the mirror elements optimized.

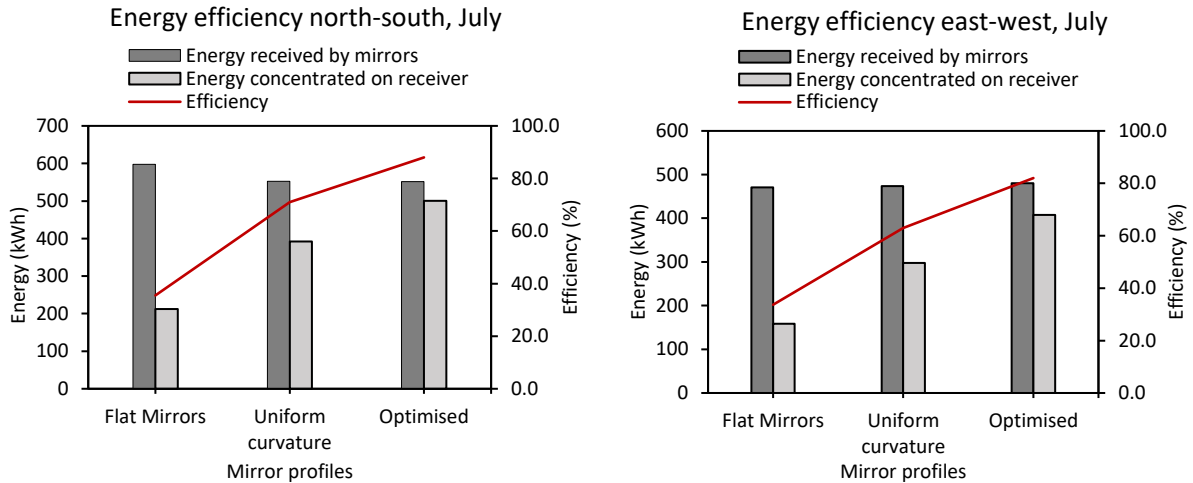


**Figure 3.36:** Energy efficiency of the different mirror profiles: flat mirrors, uniform mirror curvature and optimized mirrors for north-south (Left) and east-west (Right) in July

The reason for this is the mirror profile being modified, drifts in ray concentration are greatly minimized, and after reflection, illuminates a common focus on the absorber. This eventually improves the concentration factor and results in greater energy impinging on the absorber.

Moreover, from the results of rays traced in December as presented in Figure 3.37 and 3.38, respectively, it can be observed that the mirrors aligned in the east-west direction are more efficient and harness more power compared to the north-south.

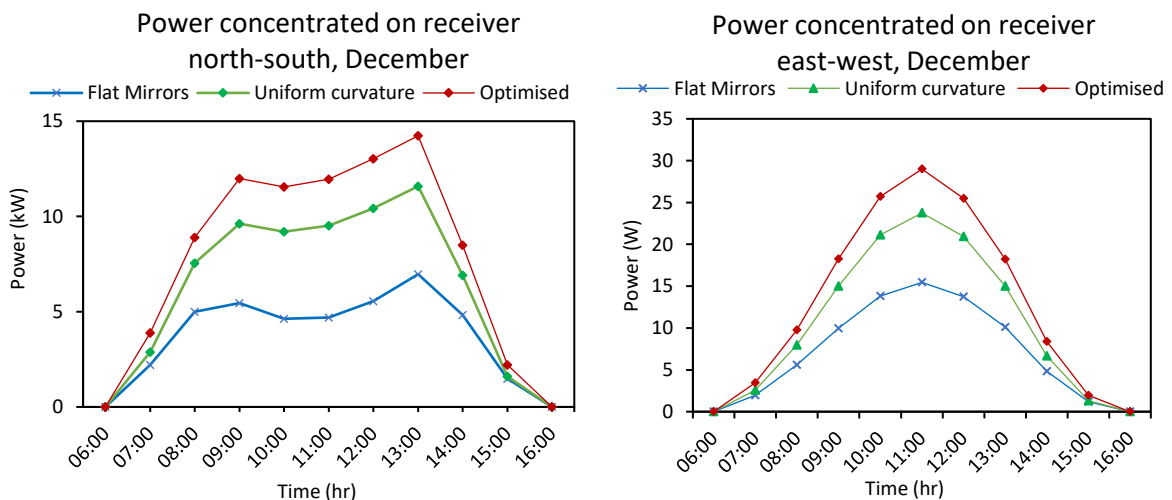


**Figure 3.37:** Power concentrated on receiver by different mirror profiles: flat mirrors, uniform mirror curvature and optimized mirrors for north-south (Left) and east-west (Right) in December



The optimized mirrors, for instance, reached 140 kW with an efficiency of 85% compared to the 85kW and 62% attained when mirrors are aligned in a north-south direction. The sun path plays a significant role in this case. The transverse direction as seen by the mirrors aligned north-south combined with the lower position of the sun result in cosine and end losses.

An average performance can be seen from the configuration with uniform mirror curvatures from both figures. The partial modification (optimization) of the mirror profiles improved the concentration and efficiency to 69% (north-south) and 62% (east-west) in July and in December 52% (north-south) and 64% (east-west) compared to the flat mirror profiles.

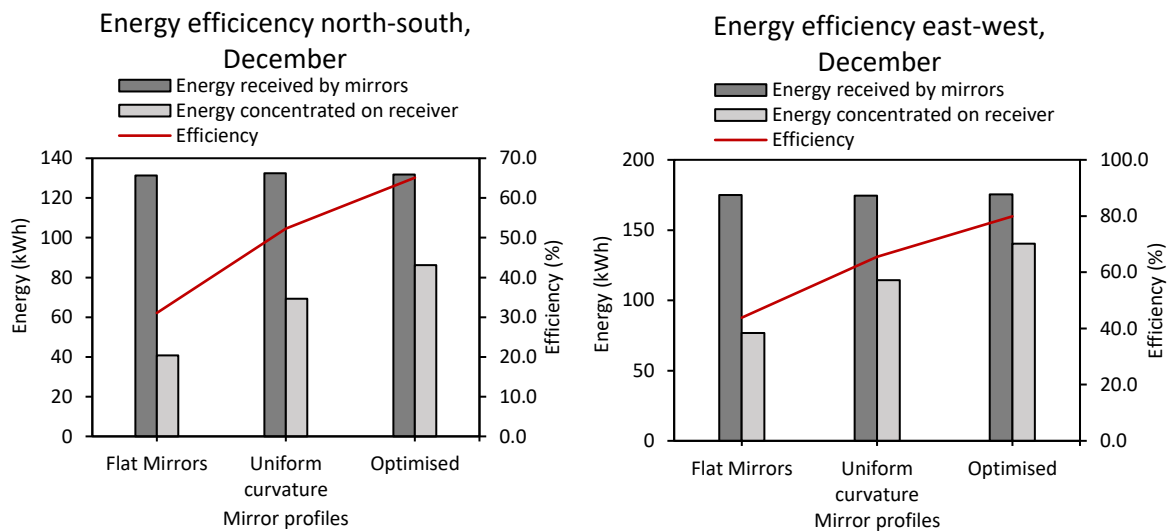


**Figure 3.38:** Energy efficiency of the different mirror profiles: flat mirrors, uniform mirror curvature and optimized mirrors for north-south (Left) and east-west (Right) in December.

The energy efficiency provides comprehensive information since it only takes into consideration the energy irradiance beyond a certain threshold. However, concentration factors as low as 10 suns are enough to preheat the fluid up to 300 °C with adequate performance.

From the average monthly energy harnessed point of view, it can be observed from Figure 3.39 (left) that from January to February and October to December, the east-west orientation produces more energy 987kWh compared to the north-south 699kWh. Again, this is mainly attributed to the sun angle as seen by the mirrors aligned in north-south resulting in end losses leaving significant portion of the mirror aperture not receiving solar radiation as seen in Figure 3.31. Subsequently, the north-south orientation produces more power, 2947kWh, than the east-west, 2421kWh, between February and October. Overall, annual energy harnessed show higher

performance achieved deploying the north-south orientation 3646kWh than the east-west 3590 kWh.

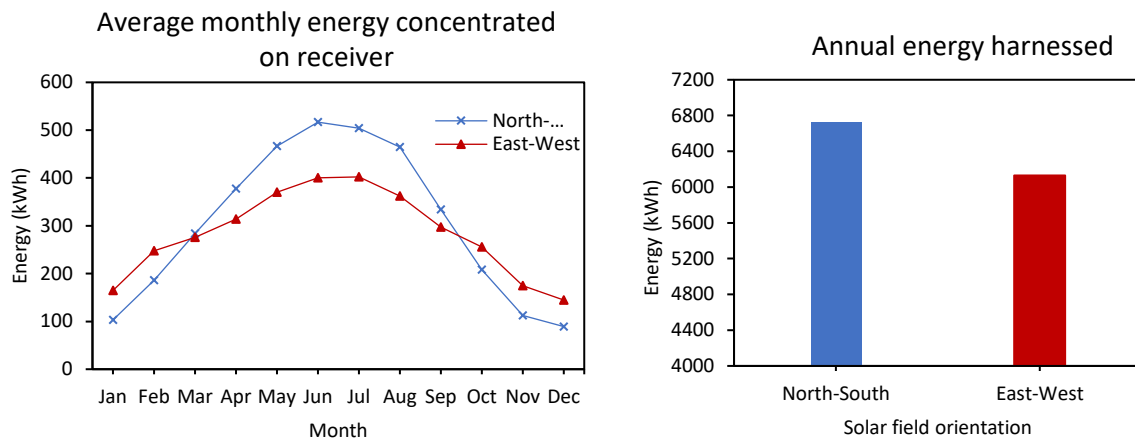


**Figure 3.39:** Monthly average energy concentrated on the receiver (left) and annual energy harnessed (right) by north-south and east-west solar field configurations

It can be deduced from the raytracing results that the mirrors shadowing effect and blocking losses have been minimized. However, mirrors that appear in front of the receiver relative to the sun's position tend to be closer to the sun; hence, their tilt (almost horizontal) allows the mirrors to reflect solar radiation without shadowing/blocking effect from their nearest neighbours. On the other hand, mirrors that appear farther from the sun and behind the receiver tend to suffer from the shadowing effect and blocking losses from their nearest neighbours. This situation often occurs before 9:00am and after 3:00pm.

The deployment of a secondary reflector was able to minimize the variation in ray concentration for the flat and uniform curvature mirrors. However, in the case of the flat mirrors, as shown in Figure 3.40, in spite of the presence of a secondary reflector, a substantial drift in ray concentration by the flat mirror is noticed. With the optimised mirrors, the drift in ray concentration is hardly noticed.

Concentrating system such as Linear Fresnel is effective only with direct solar energy because diffuse radiation cannot be focused. Also, unless combined with a tracking system, you are limited to low values of concentration.

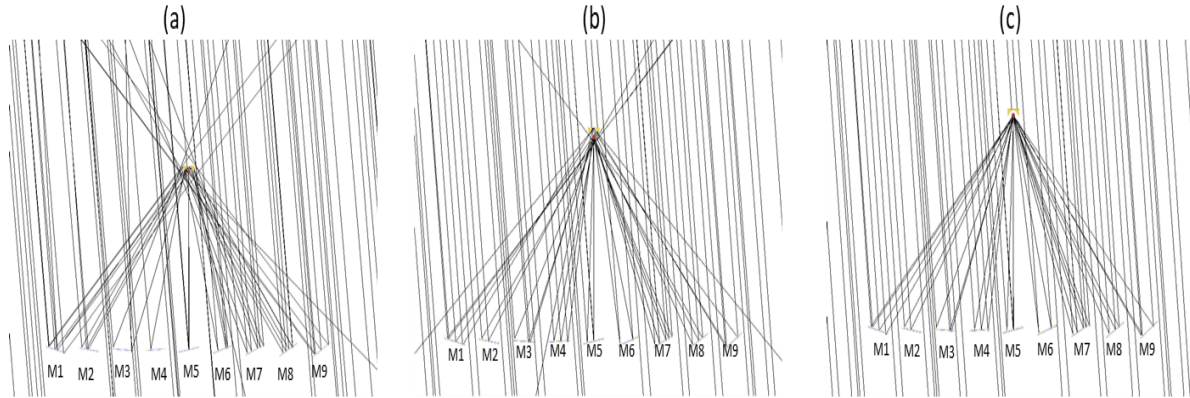


**Figure 3.40:** Solar fields showing ray concentration of various mirror shapes (a) – Flat mirrors, (b) – uniform curvature mirrors, (c) – optimized (different curvature) mirrors

### 3.5.2. Thermal performance

The thermal investigation analyses the performance of the collector for different ranges of inlet temperatures using the Therminol 62 as heat transfer fluid in every temperature region. The analysis was conducted in two stages. Test one commenced at 11:03 hours and ended at 12:52 hours, while the second test started at 13:03 hours and elapsed at 13:12 hours. Figure 3.41 compares the results of the solar field's oil inlet and outlet temperatures from the simulation model and values obtained from the experimental investigation. The results obtained from the simulation model corresponds with the general behaviour of the first measurement results showing a very good correlation for the temperature difference with a very negligible variance.

Figure 3.42 exhibits the thermal efficiency obtained from the experimental investigation and the simulation model. Higher values of the inlet temperature result in lower thermal efficiency. The decline in thermal efficiency with the inlet temperature shows a decreasing rate due to the high temperature. Moreover, it should be taken into account that the heat transfer from the selective coating of the absorber tube to the heat transfer fluid relies largely on the diameter of the tube and the heat flux focussed onto the tube; hence, high fluid temperatures indicate high tube surface temperatures and thus high thermal losses due to conduction, convection and radiation. It is apparent that thermal losses increase as the receiver temperature rises.

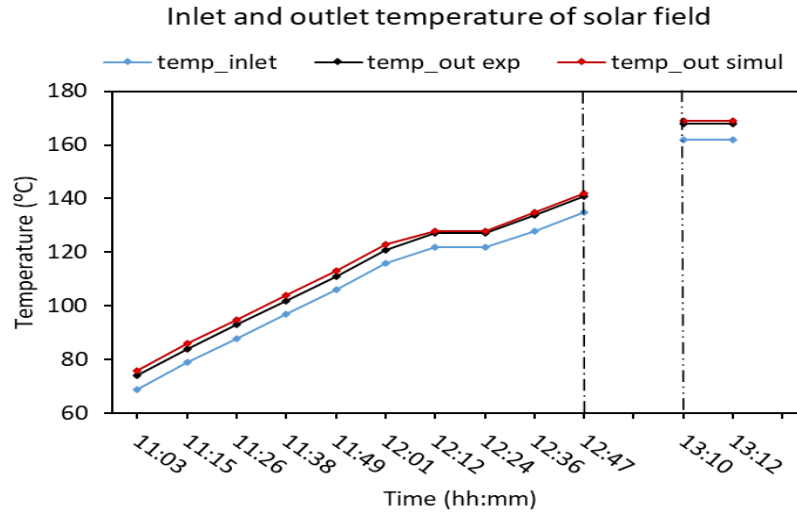


**Figure 3.41:** Comparison between theoretical and experimental results for values of temperature inlet and outlet

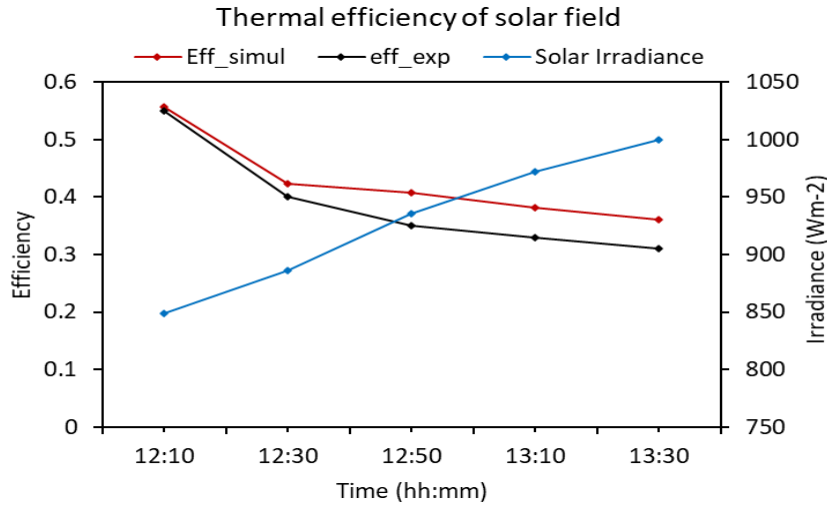


**Figure 3.42:** Comparison between theoretical and experimental results for values of thermal efficiency.

The maximum energy efficiency can be found at the outlet temperature, which is higher for higher fluxes of radiation concentration. This is due to the fact that the outlet temperature is an integral parameter of determining the energy; thus, it is imperative to note that peak outlet temperature may not always be the maximum temperature allowed by the heat transfer fluid. In addition, for different sensitivity analyses, the absorbed radiation would be governed not only on the DNI and sun position but also on the collector geometry, tracking mechanism, and the optical properties of the interacting surfaces.

### 3.6. Summary and conclusion

Linear Fresnel Reflectors are believed to have a very low concentration factor. The drift and uncertainty of reflected rays' direction, increased by the long distance between the mirrors and the fixed receiver, are the main elements that confine the concentration factor in LFR. To avoid this variation and maximize the amount of direct radiation received, the mirrors need to be constantly re-oriented so that the sun's rays are always approximately normal to it. This is achieved best by modifying the mirror elements and solar field design and configuring a single-axis tracking system.

This chapter discussed the results of a study carried out on the optical and thermal performance of a solar field based on linear Fresnel reflectors. The mirrors of the solar field were optimized in an attempt to minimize the drift of reflected rays and maximize the amount of direct radiation received. In addition, the primary mirrors were aligned in a north-south direction for east-west tracking and in an east-west direction for north-south tracking, with each panel configured to rotate about its axis individually.

Through a Monte Carlo ray-tracing technique, the optical performance of optimised mirrors was compared with that of flat mirrors and uniform curvature mirrors deploying an average daily irradiance data for the months of July and December for Almatret, Spain. Thus, the power harnessed by the receiver and the energy efficiency of separate mirror elements were analysed. A steady-state analysis of thermal performance was carried out, taking into account the receiver tube's main features and optimum operating condition for various concentrated heat fluxes (in  $\text{W/m}^2$ ) by deploying the results from MCRT in ANSYS Fluent (R2020) CFD solver. From this model, the fluid outlet temperatures and thermal efficiencies are computed for a range of values of the definition variables such as the inlet temperature, fluid speed, and thermal flux concentrated on the absorber.

Optimizing key mirror elements such as the curvature, width, length, receiver height from the mirror plane, and the distance between two consecutive mirror centrelines can significantly impact the LFR solar field optical performance. Results from the study show that the optimised solar produced more power than the Innova solar field configuration. Furthermore, the computed average monthly energy produced shows the former harnessed approximately 505kW compared to the 490kW from the latter configuration. The optimization of these key elements results in an improved concentration which can enhance the energy conversion efficiency of LFR plants and greatly minimize the cost of thermal storage, which results in low

Levelized cost of electricity (LCOE) and offers LFR with the economic potential to compete with other CSP power plants.

When a north-south of east-west solar field orientation is deployed with a clear annual sun model, it was observed that the efficiency of the system is influenced by key factors such as sun path, mirror profile, optical errors (shading, blocking), end losses, the inclination of the receiver and the solar field orientation. Findings from the study show that north-south orientation produces more energy of approximately 2947kWh from March to October compared to an east-west solar field orientation, which produces approximately 2421kWh. However, tracing from January to March and October to December shows that the east-west orientation produces more energy of about 987kWh than 699kWh by the north-south orientation. Therefore, the north-south orientation offers higher performance and leads to more uniform energy production throughout the year.

As for the factors influencing solar field performance, it was found that mirror fields experience end losses at certain times of the day. As the distance from the mirrors to the receiver increases, the dispersion of the rays caused by the effective sun-shape and path (optical and sun-shape errors) also increases. The effect is significant in December, especially with the north-south orientation due to the sun's angle and transverse direction as seen by the mirrors. However, depending on the orientation (north-west of east-south), these losses might be experienced all year round, especially during the morning and evening.

Furthermore, prospects of linear Fresnel technology in the context of utility-scale power plants can be assured with the right technological advancement. Since the reflector accounts for nearly 50% of total plant construction cost, any enhancement in the technology would be a step forward. Presently there is a need for technological advancement in the manufacturing of reflectors to address concerns of reflectors degradation and modest returns in the efficiency of the LFR plant. Maintenance-free, self-cleaned, lightweight and extended life span are the key areas for future development in reflectors to further cut down the LCOE of LFR technology.

The present study forms the basis for future research, where the optical and thermal processes will be combined for a more accurate understanding of the process, taking into consideration the map of radiation flux. Moreover, having a better LFR solar field producing more concentrated radiation fluxes, would have a positive effect on the overall energy output and efficiency of the plant.

## **Chapter 4 : Comparative Analysis of Linear Fresnel Reflector Configurations**

### **4.1. Introduction**

Compact plant size, simplicity in plant design and lower capital cost are features that have renewed the interest in linear Fresnel reflector concentrating solar power technology to meet both thermal and electrical needs. However, Linear Fresnel Reflectors are also faced with significant challenges of lower optical efficiency, mainly attributed to their average concentration ratio.

This Chapter analyses the design and modelling of a solar field based on Central and Compact linear Fresnel reflector configurations. For a detailed comparative analysis, the profiles of the mirrors are first modified by a simple optimization approach proposed. This takes into account the mirror curvature, width, focal length, tilt angle and distance between two consecutive mirror centre lines as optimization variables.

As a second step, a Monte Carlo Raytracing Technique is deployed to analyze the optical performance of the optimized mirror configurations. The raytracing is performed using daily average monthly, and yearly solar irradiance data of the chosen location. The model of the Innova MicroSolar Linear Fresnel Reflector demonstrational solar power plant designed and installed in the town of Almatret, Lleida, is slightly modified for the comparative analysis between the Linear Fresnel Reflector configurations.

The results of the comparative analysis show minimized drift in ray concentration, and the computed energy efficiency for separate mirror elements and the overall solar field show improved optical performance for the central configuration. Despite the blocking and shading effect being greatly minimized in the compact configuration, findings show lower optical efficiency, mainly due to the fixed receiver and distance from the primary mirrors.

### **4.2. Linear Fresnel reflector solar field – comparative analysis**

The full details of the Innova MicroSolar Fresnel Reflector demonstrational solar power plant studied in this project are described in Section 3.2 of Chapter 3. The plant, as highlighted previously, is expected to meet domestic and small business scale heat and power demands and consider the possibility of mounting the component on flat/pitched roofs or surrounding ground.

### 4.3. Numerical approach and optical modelling of the LFR

LightTools 8.7 illumination design by Synopsis was used for the modelling and optimization of the proposed solar field configurations. The simulation is performed with the flux transmission based on the Monte Carlo Raytracing Technique. As previously mentioned in section 3.3.5, one million rays from the sun source are projected on the LFR solar field with a constant wavelength of 550 nm with a flux of 1000 W/m<sup>2</sup> [278]. The rays are parameterized with 100% transmissivity to travel in the air. The primary and secondary reflectors are assigned with a reflectivity of 92 and 0.95 %, as adopted by the Innova Microsolar solar field design.

#### 4.3.1. Solar field configuration

The configuration of an LFR solar field may vary according to the mirror array, receiver position, and architecture. The receiver architecture may be vertical, horizontal, or triangular in configuration. For the central linear Fresnel reflector solar field, as shown in Figure 4.1, the receiver is mounted in the centre of the mirror array whilst in the Compact Linear Fresnel Reflector type (Figure 4.2), two receivers are deployed at either end of the mirror array such that consecutive mirrors concentrate to a different receiver.

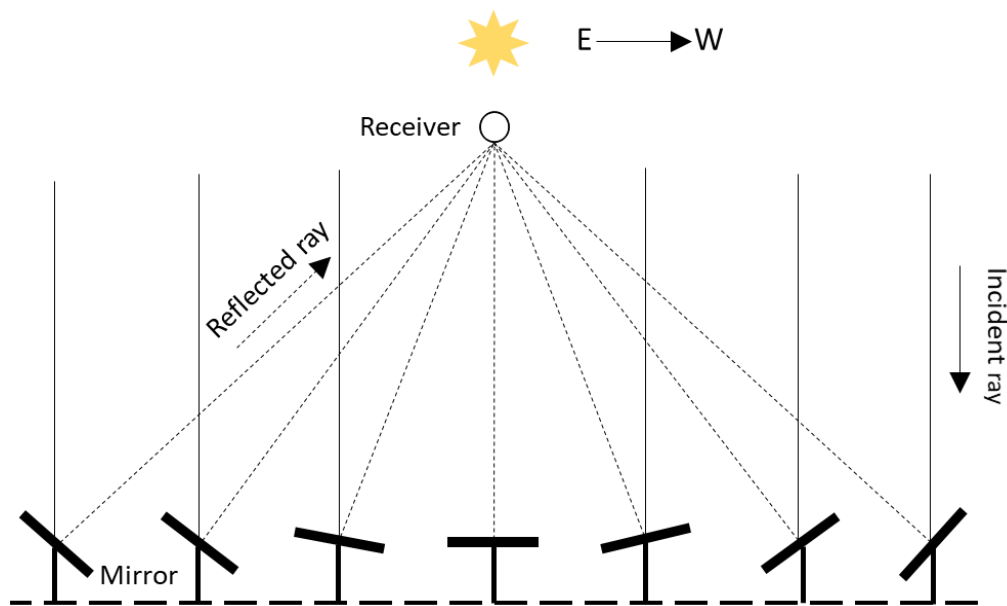


**Figure 4.1:** Central LFR solar field configuration

Various researchers have studied the different features of both configurations. These characteristics could be either in terms of mirror design (flat or modified), receiver architecture (single-tube or multi-tube receiver) and secondary reflector design (with or without secondary reflector). The compact LFR plant in Kimbarlina, for instance, consists of a multi-tube receiver



and without a secondary reflector, while the central LFR power plants Puerto Errado 2 in Spain and Dhursar in India are configured with single-receiver tubes and secondary reflectors deployed.

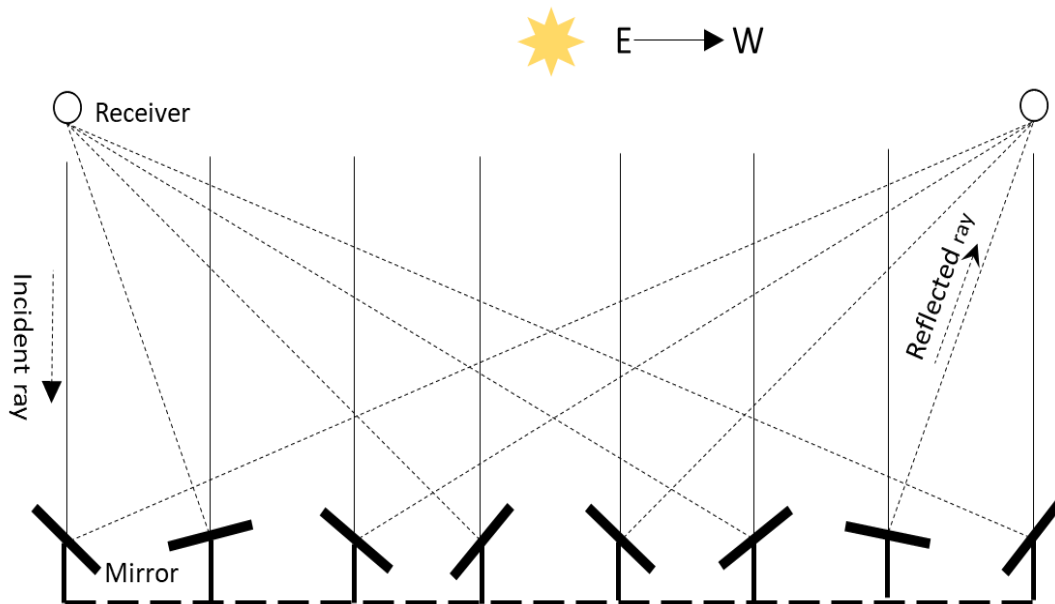


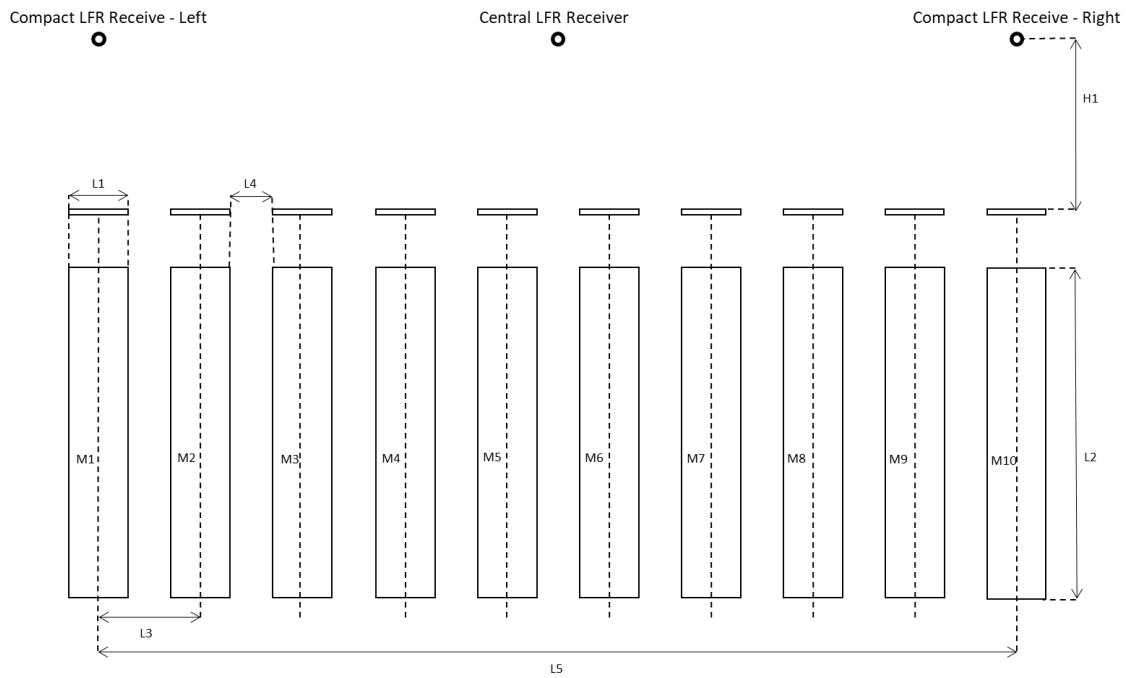
**Figure 4.2:** Compact LFR solar field configuration

A similar approach deployed in the geometrical modelling performed for the central LFR solar field of the Innova MicroSolar demonstrational plant is adopted for the comparative analysis between Central LFR (CenLFR) and the compact LFR (ComLFR). As depicted in Figure 4.1 & 4.2, the LFR solar field constitutes two units. The primary reflector system and the receiver assembly. The primary reflector system consists of mirror apertures configured in rows on a fixed frame. The mirrors are aligned for a single axis east-west tracking of the sun.

The receiver assembly comprises the receiver tube placed at a certain height, slightly above primary reflectors. The central LFR configuration receiver is placed 3 m above the primary mirror's plane, while due to the increased distance of the farthest mirrors a height of 3.5m was obtained after the optimisation of the two compact LFR receivers' positions at either end of the solar field (Figure 4.3). The geometrical parameters of the solar field are presented in Table 4.1.

**Table 4.1:** Geometric parameters of the proposed LFR solar field

Parameter	Measurement	Unit
Primary mirror width, L1	0.45	m
Primary mirror length, L2	18	m
Distance between two consecutive mirror centre lines, L3	0.75	m
Offset distance between two adjacent primary reflectors, L4	0.35	m
Primary mirror unit length, L5	6.75	m
Total number of mirrors	10	
Receiver Length	18	m
Height of receiver tube from the primary mirror's plane, H1	3, 3.5	m
Receiver Diameter	70	mm
Net mirror area	81	m <sup>2</sup>
Ground area	137	m <sup>2</sup>

**Figure 4.3:** Modelling layout and schematic representation of the Innova Micro Solar pilot plant

#### 4.3.2. Modelling primary mirrors

A similar approach deployed in section 3.3.2 of Chapter 3 describes details of equations used in calculations and modelling of the primary mirrors in this section. The position of the primary mirrors can be defined by the tilt angle ( $\delta_n$ ), such that the incident ray (at an angle  $\alpha$ ) is concentrates on the receiver tube, the distance between two consecutive mirror centre lines ( $S_n$ ), and distance from the central point ( $Q_n$ ). The focal plane is positioned at a distance ( $f_n$ ) from the mirror element placed in the centre of the LFR ( $S_o = 0$ ). The pivoting point of each mirror corresponds with the central point of the mirror; hence, it is always focused on the central point of the receiver.

The  $n_{th}$  mirror in the LFR array is defined by three parameters notably, position, ( $Q_n$ ), the tilt ( $\delta_n$ ) and space ( $S_n$ ) as shown in Figure 4.4.

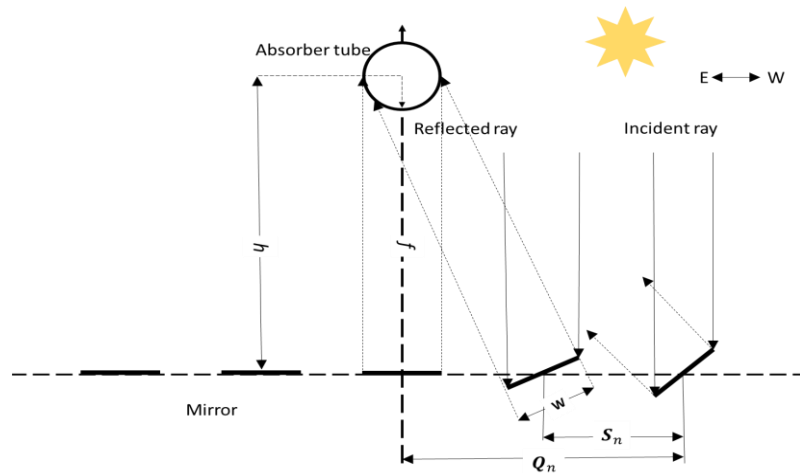


**Figure 4.4:** Design and geometrical parameters of primary mirrors

Note that each mirror's rotation axis must be aligned with its reflecting surface, a requirement that must be met by the mechanical nature of the mirror supporting structure. The study thus, developed an optical design process based on this principle to minimize the variance of the concentration factor during the day.

#### 4.3.3. Optimization and Monte Carlo Ray Tracing (MCRT)

The geometric parameters of LFR may differ from one solar field to another. Optimizing most or all of these relevant parameters can be an extremely challenging task, particularly when coupled with the reflector's optical features. Generally, the ideal approach constitutes experiential baseline linear Fresnel design optimizing the very few selected parameters considered most relevant to the overall optical and/or economic performance.

For a detailed comparative analysis, first, the optimization of the solar field was performed to determine the appropriate mirror elements and geometries. The optimization variable defined include the mirror curvature, which determines the concentration of solar radiation that impinges on the receiver, the height of the receiver from the mirror plane, mirror width and length, distance between the consecutive mirror centre lines.

The optical performance of a linear Fresnel reflector can be analysed based on the ray-tracing technique by deploying various forms of computer methods. The solar field ray-tracing was performed using LightTools 8.7 illumination design by Synopsys. Ray tracing allows various collector elements such as reflectors and receivers with defined optical properties and

mechanical features to interact with the actual or specified sun data. The accuracy of the simulation results depends on the density of the sun rays traced; in other words, the number of sun rays needs to be large enough to produce results with the required precision.

Furthermore, the modified primary mirrors are configured to focus intercepted sun rays onto the receiver tube; hence the main receiver consists of a one-tube without a secondary reflector. However, the purpose of the study was the optical process, and the receiver was horizontally placed, with no discussion on whether it is a multi-tube or one-tube, and with or without a secondary reflector.

For the aforementioned studies, the following assumptions were made.

- The primary mirrors were modified by a simple optimization approach proposed.
- The demonstrational plant solar field configuration is aligned in North-South orientation is used in the comparative analysis.
- In terms of location data, solar irradiance data for Phoenix, USA, were used for this study. Information on this data is given in section 3.3.5.” in the sun ‘**Modelling Subsection**’
- The receiver tube with a diameter of 70 mm was positioned at 3m (central LFR) and 3.5m (compact LFR) above the plane of the primary reflector.
- The rotating joint of each mirror matches with the centre line of the mirror; hence, it is always focused on the central point of the receiver tube.
- An adequate distance of 0.35 m was assigned between two consecutive mirrors so that a mirror does not block or shade its nearest neighbouring mirror.
- The design of the receiver tube and the secondary reflector cavity discussed in sections 3.3.3 and 3.4.1 were considered in this section.
- In order to have equivalent configurations, the orientation of the receiver has been chosen horizontal in all the cases. Besides, the receiver surface must be the same, and also the primary mirror surface focusing on each receiver.

Further details on the Optimization and Monte Carlo Ray Tracing (MCRT) approach, such as sun modelling, merit function and main parameters used in the raytracing Monte Carlo numerical simulations, are presented in Section 3.3.4 of Chapter 3.

#### 4.3.4. The efficiency of LFR solar field

For a proper comparative study, it is necessary to define a comparison criterion. that sense, a new variable is defined, namely the useful energy efficiency, which only accounts for the radiation that reaches the receiver with irradiance close to the reference value of 1000W/m<sup>2</sup>. In this case, as a result, the expression given for the energy and optical efficiency (ratio between rays reaching the target and the total number of rays) are computed using Equations 2.3 and 2.4 in section 2.2.4.2.

#### 4.4. Analysis of results and discussion

Flat mirror profiles were employed during the initial optimization. Each ray hits a precise spot of the mirror aperture with NS-ray fans preferred. This considers global source radiation, which will be employed in the Monte Carlo Raytracing of the solar field in a subsequent section. A dummy plane with the Y-axis sharing the length of the cylinder was employed instead of the receiver tube, which was made non-ray traceable. Each ray was targeted to the local coordinate  $Y = 0$  using an NS-ray fan merit function. Note that the radius has been converted to its reciprocal curvature since this is a more appropriate parameter to use in optimization:

$$c = \frac{1}{r} \text{ Here } c \text{ is the curvature; } r \text{ is radius}$$

In addition to the mirror curvature, other key parameters used for the optimization include the mirror tilt angle, mirror width and height, and receiver height. The mirror width and height are parameters used to define the mirror positions. Figure 4.5 shows the optimized solar fields of the two configurations. Furthermore, it can be observed Figure 4.6 and 4.7 that the iteration process follows the same trend as the initial solar field model of the Innova project in section 3.4 of chapter 3. In the case of the compact configuration, however, fewer iterations are observed (Figure 4.7) due to the smaller number of mirrors focussing on two separate receiver tubes positioned at either end of the solar field.

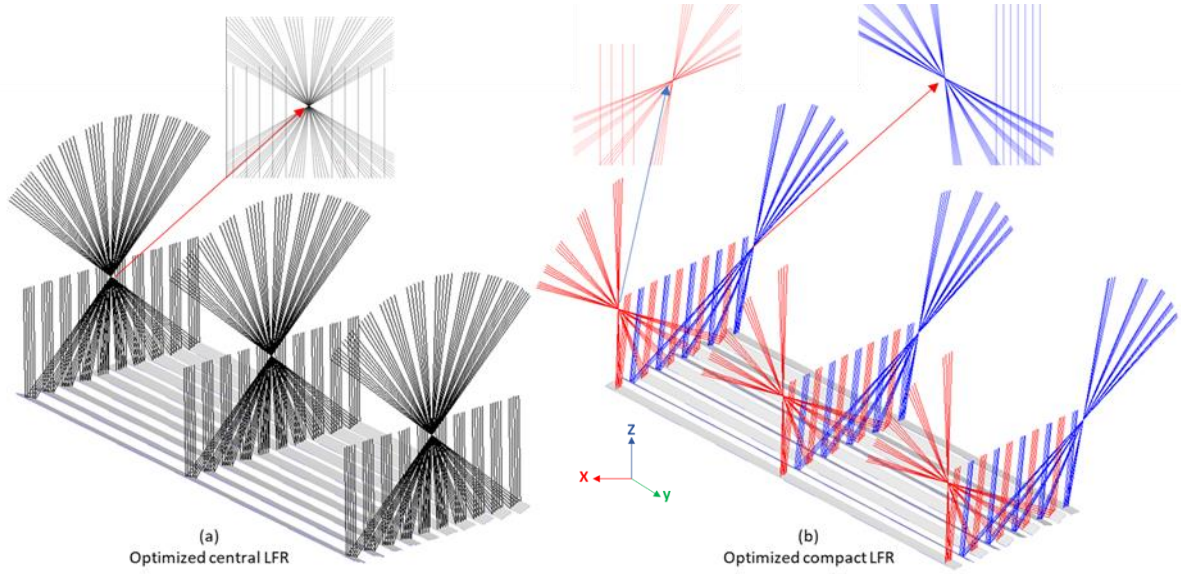


**Figure 4.5:** Optimized central (a) and compact (b) LFR solar field configurations

Furthermore, due to the increased distances of the farthest mirror of the compact configuration, the optimised receiver height was 3.5m compared to the 3m of the central configuration. The optimization proceeds iteratively in a series of steps that gradually improve the performance. The mirrors are horizontally aligned to revolve about east-west axes relative to the sun; thus, only the projection of the NS-rays fan (solar radiation) in the y-z plane is reflected on to the receiver tube after the curvature has been modified to concentrate the rays on the central point of the receiver tube.

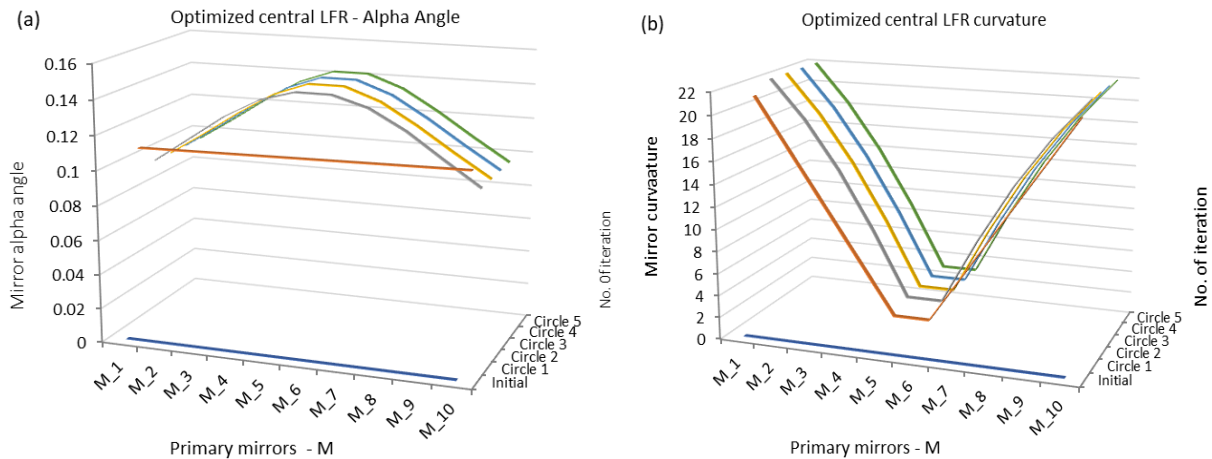


**Figure 4.6:** Results from optimization of primary mirrors of the central LFR (a) tilt angle (b) curvature

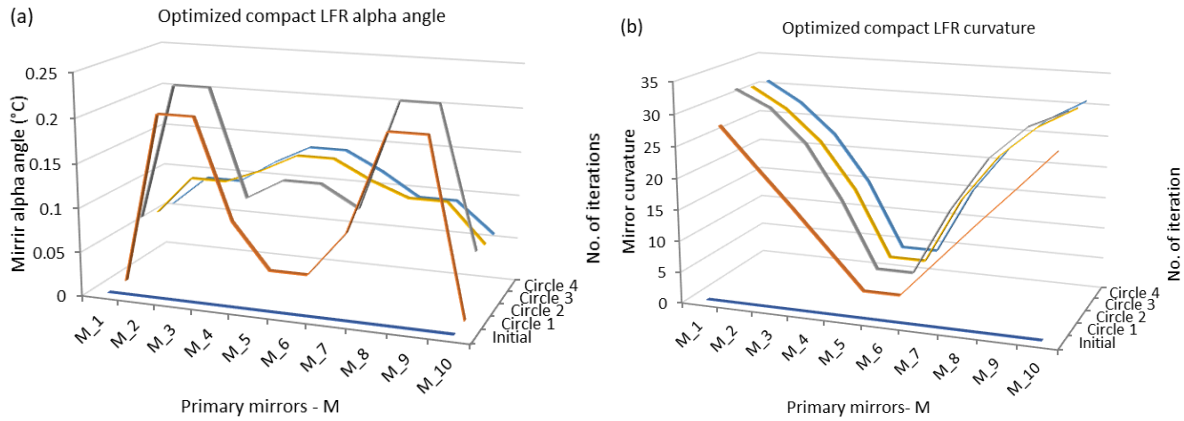


**Figure 4.7:** Results from optimization primary mirrors of the compact LFR (a) tilt angle (b) curvature

The value of the Merit Function is used to determine whether or not the outcome of an optimization achieves the given target. The value of the Merit Function item (e.g., output value, ray, ray fan, ray grid, test point, or intensity slice) for the iteration is assigned a specific target (local coordinate  $Y=0$ ) during the initial parametrization. The Merit Function value is expected to be as close to zero as possible, and the closer the values are to the target during optimization, the better the system operates. Figure 4.8 shows the computed contribution for merit function item outcome after optimization.

#### 4.4.1. Monte Carlo Ray Tracing – analysis of simulation results

The solar radiation concentration in LFR systems relies on the mirror shapes and their configuration. When fixed mirrors are used, maximum concentration can be attained at a certain time in the day and will decline over time. To minimize this variation in concentration, the system can be configured to track the sun.

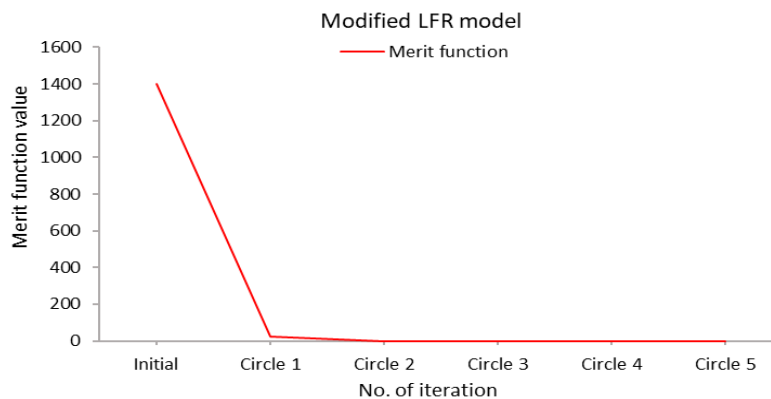


**Figure 4.8:** The result of merit function of the optimised solar field

Hence the orientation is designed to optimize the position of the reflecting surface relative to the sun. As the sun's position is characterized by two values: the height extending from  $0^\circ$  at sunrise to  $90^\circ$  when the overhead at noon, and azimuth ranging from south (zero) and east (positive), ranging from  $-180^\circ$  to  $+180^\circ$  [281], two orientation axes of the mirrors meet the monitoring purpose.

For linear concentrator, only one coordinate needs to follow the sun with an optimized collector adjustment with the collectors configured in the north-south direction; a simple orientation tracking is done in the east-west direction over given hours of the day to concentration solar radiation on the receiver tube laid out on the focal of the concentrator. The solar concentration obtained varies according to the hour and season.

The optical analysis is performed by means of a detailed raytracing program since this is the most preferred approach to analysing the optical performance of a solar field. Raytracing allows various collector elements such as reflectors and absorbers with defined optical properties and mechanical features to interact with the actual or specified sun data. The results of the study illustrate the performance recorded over the course of an average daily data of a selected month and year, taking into consideration: the DNI (Direct Normal Irradiance).

In the Monte Carlo raytracing, the two solar field configurations (central and compact) were considered. The raytracing was performed deploying average daily irradiance data for the months of May and December, considering a north-south solar field orientation. The accuracy of the simulation results depends on the density of the sun rays traced; in other words, the number of sun rays needs to be large enough to produce results with the required precision. The sun shape depends on location and varies with time; hence this greatly influences the reflector's optical performance.

The density of rays collected by the receiver from the two mirror configurations for average daily irradiance data in the months of May is presented in Figure 4.9. The data is recorded at three selected times of the day; namely, 9:00am, 12:00noon and 3:00pm. The central LFR receiver represents 'a' while 'b' and 'c' denote the compact LFR receivers on the left and right. The Y-axis denotes the length of the receiver (18m), while X-axis represents not only the width but also shows the receiver model is cylindrical and horizontally oriented.



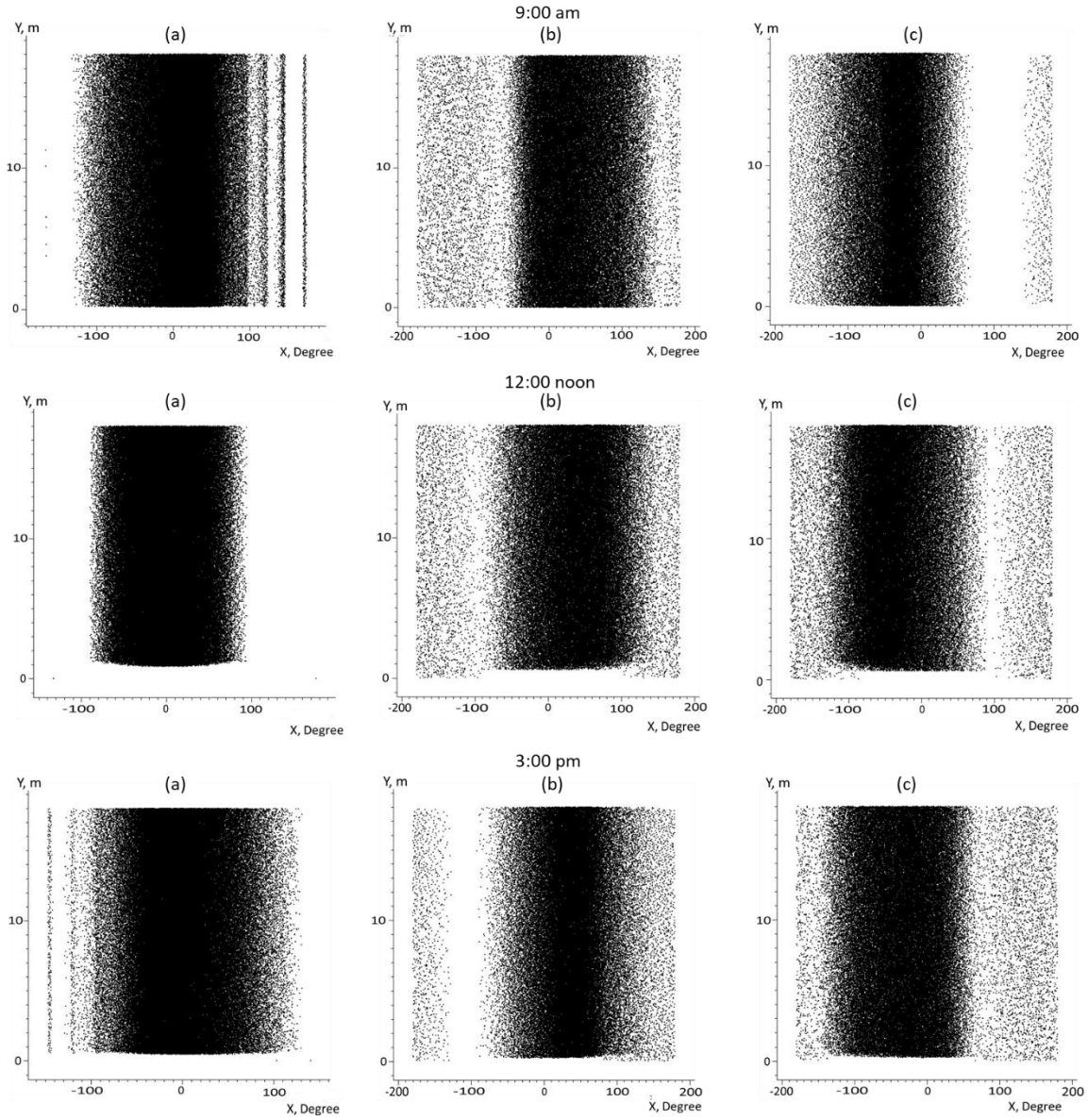


**Figure 4.9:** The concentration density of irradiance impinging on the receiver in May considering north-south orientations (a) Central LFR receiver (b) Compact LFR right receiver, (c) Compact LFR left receiver

In Figure 4.9 one may observe that the density of rays reaching the receivers ‘b’ and ‘c’ of the compact configuration is concentrated only on the half of the receiver from either side. However, because this design is anticipated to contain consecutive mirror arrays concentrating on either receiver at the separate ends, the receiver ‘b’ would receive identical radiation to that reaching the receiver ‘c’ from the left side. When the compact solar field is simulated, the radiation flux on each receiver equals to the sum of the radiation received by the solar field, as in the case ‘a’ (central LFR).

The primary aim of the compact LFR is to minimize losses due to shading and blocking while utilizing less space. It is worthy of note that losses due to shading and blocking can result in economic losses due to the fraction of mirrors not utilised. Such incidents occur either as a result of the reflective surfaces being shaded by nearest neighbour mirrors (shading) or as a result of reflected solar radiation from one mirror not concentrating on the receiver as it is interrupted on its way by another mirror (blocking).

Moreover, from Figure 4.9a, it can be observed that the ray concentration appears to be denser on the central LFR receiver compared to the two compact receivers in all three (3) cases. This indicates higher concentration realised. Nonetheless, the central configuration suffers from a slight shading effect by nearest neighbour mirrors. This effect is experienced at 9:00 am and 3:00 pm, as depicted in Figure 4.9a, indicated by the stripes on the non-shaded region of the receiver tube.

It is important to note the minimised shading and blocking realised in the compact LFR. However, due to the concept of receiver design and configuration, the mirror rays of the compact LFR configuration suffer shading effect from receivers at both ends. Whilst farthest mirrors suffer minor shading by the receiver to which they are concentrating, they may also suffer shading from the second receiver. This effect can be observed on the non-active parts of receiver 'c' at 9:00am and receiver 'b' at 3:00pm in Figure 4.9.

The concentration factor of irradiance obtained at selected times of the day is presented in Figure 4.10. It can be observed that the central configuration harnesses more power in all three cases, with a peak  $65 \text{ kW/m}^2$  at noon compared to the compact configuration with a combined peak of  $52 \text{ kW/m}^2$ . The contribution of errors to the optical performance of the primary mirrors is greatly influenced by the distance between the collectors and the receiver. Hence the greater the distance, the lower the concentration factor and more reduction in the optical performance.

In the case of the compact configuration, the drift and uncertainty of reflected rays' direction, increased by the long distance between the mirrors and the receiver, which are the main elements that confine concentration factors in LFR. The decline in peak power by the compact receivers b at 9 am & c at 3 pm compared to noon results from the increased distances between the primary mirrors and the receiver leading to a greater dispersion in rays' concentration.

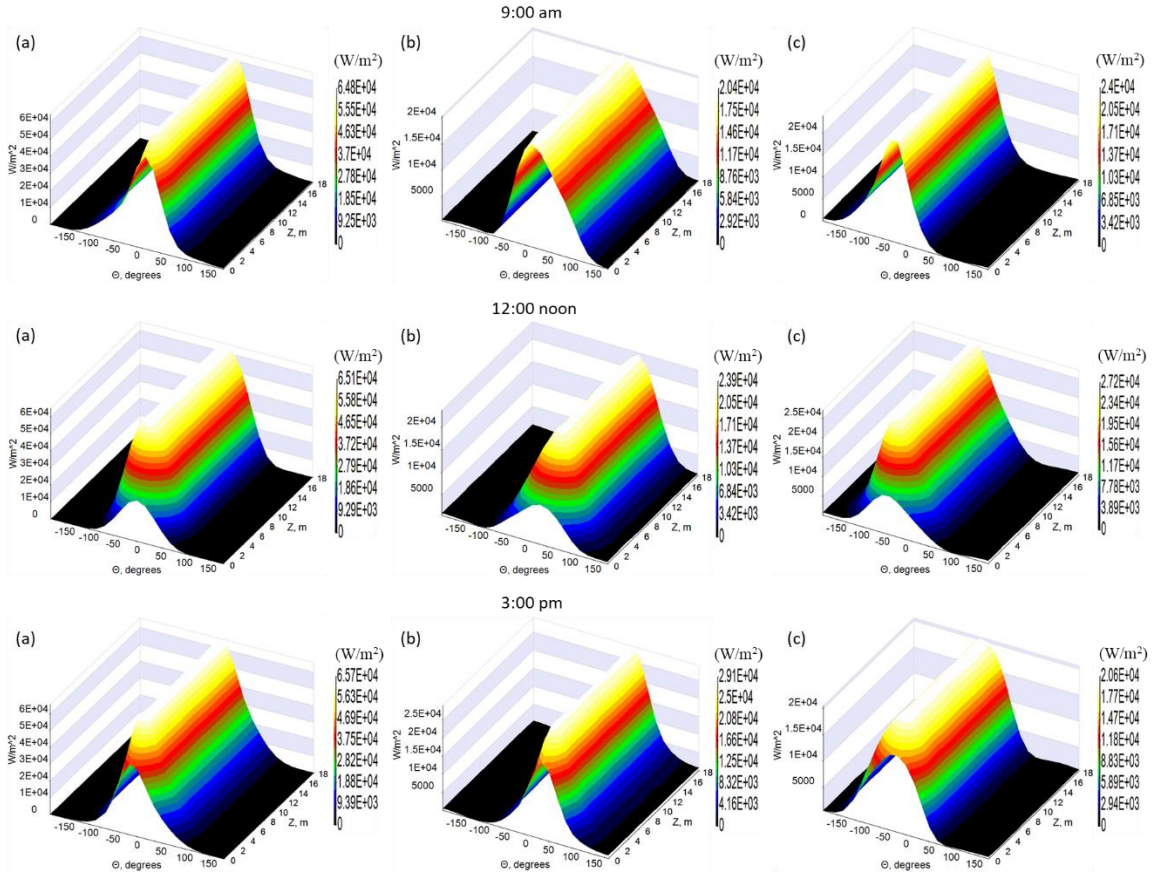


**Figure 4.10:** The concentration of irradiance impinging on the receiver in May considering north-south orientations (a) Central LFR receiver (b) Compact LFR right receiver, (c) Compact LFR left receiver

As presented in Figure 4.11, a thorough characterization of the raytracing process, comprising not only different average fluxes but also their distributions, along with different irradiance conditions, would significantly impact the optical performance. Hence the impact of the sun angle/path on the solar field configuration deploying average daily irradiance data in the month of December is investigated.

Comparing Figure 4.9 & 4.11, it can be noted that the intensity of solar radiation impinging on the receiver is greatly dependent on climate and season of the year, as well as the optical performance of the solar field. It is also imperative to note that the solar radiation flux concentration on a receiver surface by the Fresnel reflectors is far from uniform, as all reflectors are generally focused onto the central line of the receiver in order to harness higher radiation concentrations.

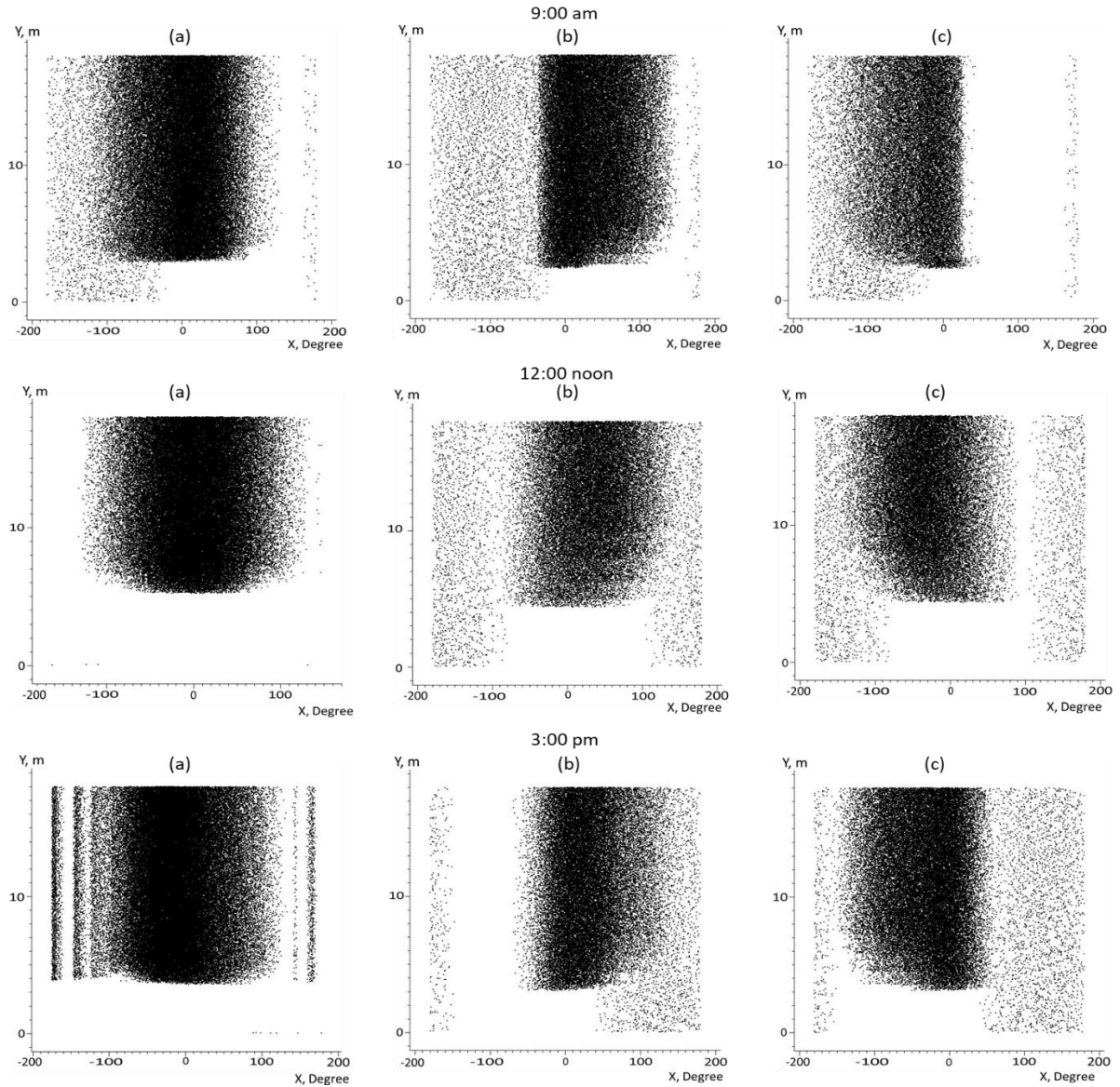


**Figure 4.11:** The concentration density of irradiance impinging on the receiver in December considering north-south orientations (a) Central LFR receiver (b) Compact LFR right receiver, (c) Compact LFR left receiver

Furthermore, the low density in concentration in December can be observed compared to May in both solar field configurations across all three cases. The variation in the distribution along the day can be noticed, and this applies to other days of the year. This is as a result of the effect of the tracking errors and natural aperture and mirror profile in addition to the variation in ray concentration and distance travelled by concentrated rays along the day and year with changes in irradiance source position.

The flux ( $\text{W/m}^2$ ) intercepted by the receivers in the month of December is presented in Figure 4.12. The ray intercepted show a similar trend to the results obtained in May (Figure 4.10) in the sense that the central LFR harnesses more power compared to the compact configuration. However, it can be observed that overall, the concentration factor is higher in May compared

to December in all three cases. In addition, the decline in power noticed from the central LFR receiver at 3 pm in Figure 4.12 is due to the shading and blocking effect experienced by the farthest mirrors from their nearest neighbours due to the sun's position. However, in the compact LFR configuration, this effect is minimised due to the mirrors concentrating rays on the two receivers located at either end of the mirrors array.

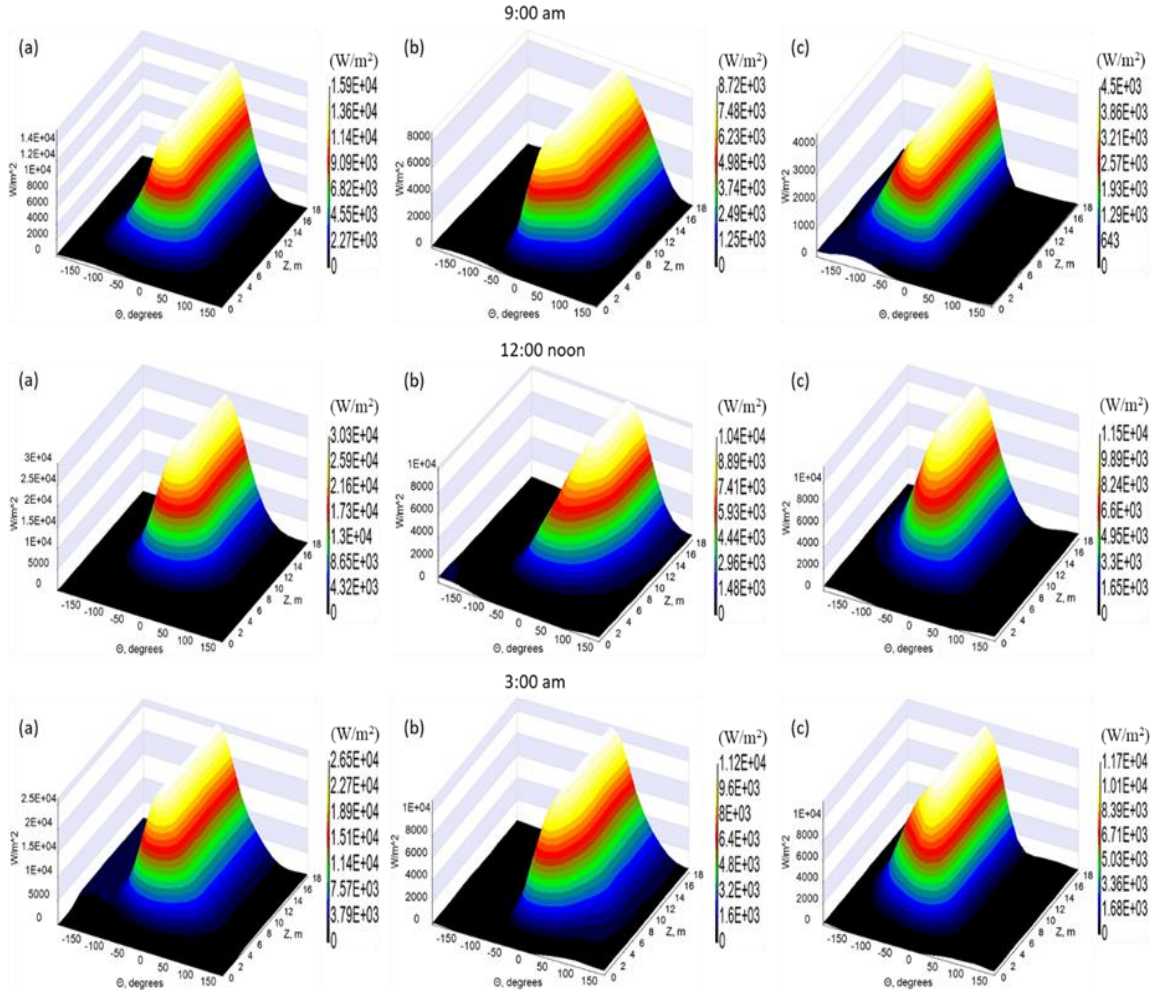


**Figure 4.12:** The concentration factor of irradiance impinging on the receiver in December considering north-south orientations (a) Central LFR receiver (b) Compact LFR right receiver, (c) Compact LFR left receiver

As for the end and lateral losses, since the black regions on the charts shown in Figure 4.12 indicate zero intensity and other coloured regions, ranging from blue to white (centre), indicate the low to highest concentration (irradiance level), the effect of end and lateral losses can be noticed from the non-active parts of the receiver in December compared to May. The effect, however, appears to be slightly higher in the case of the compact configuration as the distance from the mirrors to the receiver is increased, the dispersion of the rays caused by the effective sun-shape (optical and sun-shape errors) is also increased.



Generally, the end losses happen when a portion of reflected rays is drifted away from the receiver as a result of the slanted incidence of incoming sunbeams, which results in reduced efficiency of the LFR solar field. The incidence of end losses in the solar field configurations at 12 noon in December is depicted in Figure 4.13.

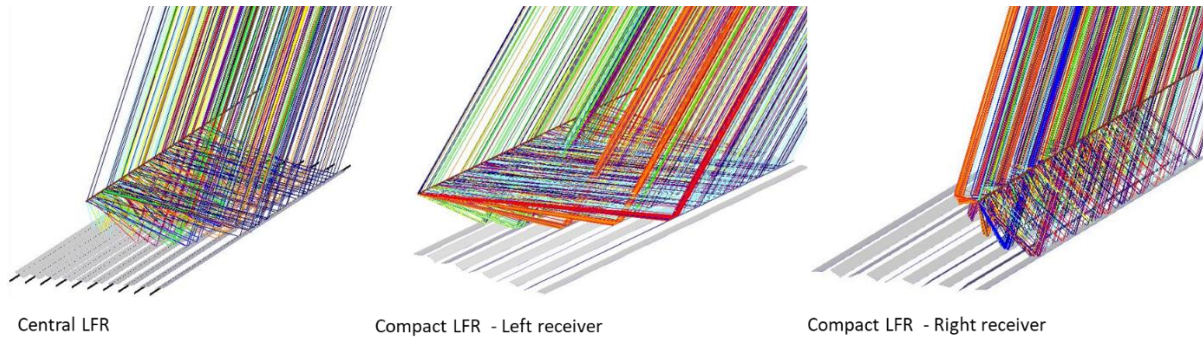


**Figure 4.13:** Solar field ray tracing showing the effect of end losses on the central and compact LFR configurations

Each mirror's total power and useful energy efficiency relative to the sun's position and their distance from the receiver were investigated. This is significant in determining the performance and contribution of each mirror to the total power harnessed. It can be observed in Figure 4.14 that in both configurations, mirrors M1 that appear in front of the receiver relative to the sun's position tend to be closer to the receiver; hence their tilt (almost horizontal) allows the mirrors to reflect solar radiation with minimised drifts and less shading/blocking effect from their nearest neighbours. Thus, the minimised dispersion of the ray's concentration, as a result, leads to improved efficiency and energy harnessed.

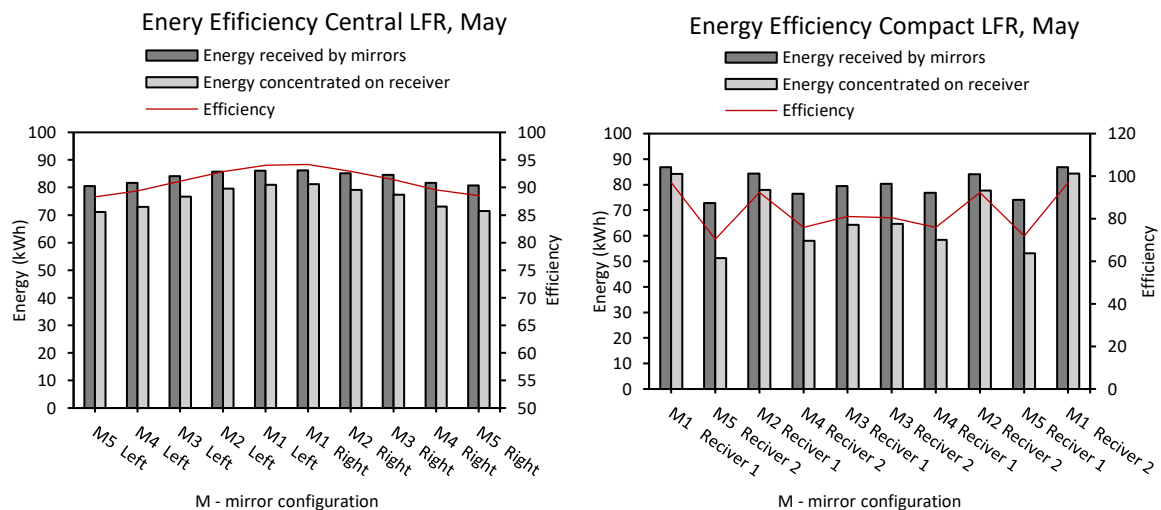


**Figure 4.14:** Energy efficiency of primary mirrors of the two solar field configurations in May: Central LFR (right) and Compact LFR (left)

On the other hand, mirrors that appear farther from the sun and behind the receiver tend to suffer from shading and blocking losses from their nearest neighbours. This impact is

experienced most by mirrors of the central configuration farthest from the receiver. Despite this improvement, it is not sufficient to overcome other challenges faced by compact Fresnel Reflectors. Thus, with the receiver being fixed and the distance away from the mirror array, mirrors suffer from drifts and variation in ray concentration resulting in lower power and energy efficiency compared to the central configuration.

It is imperative to note from Figure 4.15 that the significant decline in energy and efficiency in the month of December is mainly due to the low sun position and the direction of the suns vector on the east-west path. This causes the mirror to reflect sun rays beyond the receiver aperture as a result of a wider incident angle of the rays reaching the primary mirrors. These lead to combined cosine and end losses.

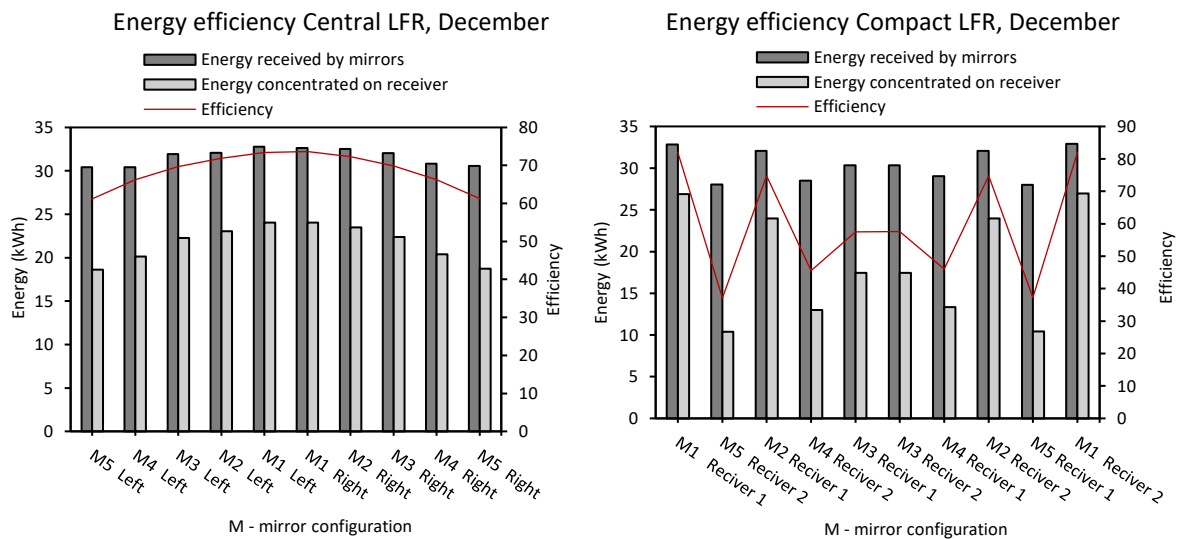


**Figure 4.15:** Energy efficiency of primary mirrors of the two solar field configurations in December: Central LFR (right) and Compact LFR (left)

From the point of view of the average monthly power harnessed (Figure 4.16), the best configuration is the one employing a single receiver.

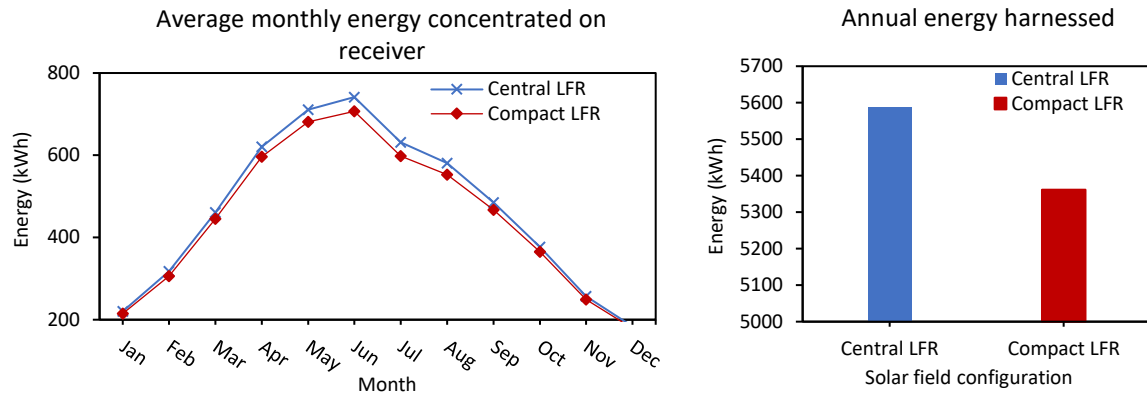


**Figure 4.16:** Energy produced by Central and compact LFR configurations – average monthly energy (Left) and annual energy (Right)

The difference in power harnessed appears to be marginal between the two configurations from October to February. However, from March, we start to notice higher performance from the central LFR configuration. The lowest performance was recorded in December, with the central LFR generating 183 kWh while the compact type harnessed 178 kWh. Peak power was achieved in June, with the former generating 741 kWh and the latter 705 kWh. Furthermore, the computed annual energy value demonstrates that the Central configuration produces approximately 230 kWh more energy than the compact LFR configuration.

#### 4.5. Summary and conclusion

Linear Fresnel collector arrays present some relevant advantages in the domain of concentrating solar power because of their simplicity, robustness and low capital cost. However, they also present important drawbacks and limitations, notably their average concentration ratio, which seems to significantly limit these systems' performance. This challenge can be overcome by characterizing the mirror field configuration selecting key variables that can influence the primary mirrors' performance.

In this chapter, the solar radiation concentration of two LFR solar field configurations, central LFR and Compact LFR was investigated. In the initial approach, the modelling and optimisation of the solar field are conducted to minimise ray concentration variation and improve concentration factor. In addition, a detailed Monte Carlo Raytracing Technique is deployed for the comparative study between central linear Fresnel reflectors and compact linear Fresnel reflectors configurations. In that sense, two variables were defined, the energy efficiency and total energy harnessed by the solar fields. The simulation performed is to present a detailed analysis of how design parameters influence the performance of the two LFR configurations.



Finding from the energy efficiency and power shows overall better performance from the central LFR configuration. Power harnessed from November to February, nonetheless, is very close between the two configurations. Next to that, the computed energy efficiency for separate mirror elements indicates that in both configurations, mirrors that appear in front of the receiver relative to the sun's position tend to be closer to the receiver, focussing solar radiation with less shadowing/blocking effect and attaining the higher efficiency compared to the farthest mirrors.

Furthermore, subsequent analysis shows that the compact linear Fresnel reflectors minimize blocking and shading losses compared to a central configuration. However, this is not enough to overcome other challenges, such as the greater dispersion of the rays reaching the receiver, caused by the fact that mirrors must be located farther from the receiver, which yields lower efficiencies.

In addition, it has also been found that both LFR configurations are subject to losses such as the end and lateral losses, which significantly impact the optical performance of the compact LFR configuration compared to that of the central LFR. However, depending on the orientation (north-west or east-south), these losses might be experienced all year round. In the case of the north-south orientation, the losses were higher in December. Increasing the length of the mirror aperture to minimize the end losses has been suggested, however, this might result in much more consumption of materials and cost.

## Chapter 5 : Organic Rankine Cycle Turbine

### 5.1. Introduction

In the last few decades, the increasing world energy demand has given rise to profound economic challenges and environmental concerns. The generation of energy using unconventional technologies that offer sustainability, reliability and environmental benefits is, without a doubt, imperative to achieving central policy goals on energy security, climate change mitigation and greenhouse emission reduction in a most cost-effective way.

Limiting the reliance on conventional energy sources has led to the renewed interest in studies related to the use of residual heat rejected by the industry, which makes up more than half of the heat generated in the industry's installations. However, as conventional steam power cycles struggle to improve on the recovery of low-grade heat, it is imperative to seek alternative means that can present a better performance, exploring low-temperature heat sources such as biomass, geothermal and solar energy to meet electrical and thermal needs.

Organic Rankine Cycle (ORC) systems are enabling technology that can play a significant role in this regard due to their ability to convert low-temperature heat sources into useful energy and potential integration in future distributed generation systems. Small-scale ORC systems based on axial or radial-outflow turbines are an attractive choice for various electricity generation applications, mainly domestic and rural situations, under-served and unserved locations with a high degree of poverty and a lack of opportunities for socio-economic development.

In this Chapter, a small-scale Organic Rankine Cycle turbine developed by a French company, Enogia, as a part of Innova MicroSolar Project and used for low-temperature applications capable of generating electrical power was theoretically investigated and numerical results were compared to experimental results provided by the company. A single-stage axial turbine expander deploying R365fmc, and the new environmentally friendly Novec649 organic working fluids were selected. The effect of the range of inlet definition variables such as temperature, pressure and rotational speed on the work output and isentropic efficiency as well as the influence of rotor tip clearance (rotor gap) on the turbine power were investigated and analysed. Results from the study show a good correlation between the theoretical and experimental studies.

## 5.2. The Organic Rankine cycle turbine (ORC) Turbine

An Organic Rankine cycle (ORC) is fundamentally similar to a steam Rankine cycle; however, it employs a lower boiling point organic fluid, which makes it compatible and suitable for low-temperature applications. For smaller systems, ORC turbines may achieve higher efficiencies than steam turbines (in the form of a few kWe). The principle of operation of the ORC is the same as the conventional Rankine Cycle, with the most important alteration being the working fluid. An organic compound of low boiling point is preferred in the case of the ORC instead of water, thus reducing the temperature needed for evaporation. The schematic of the ORC driven by the LFR solar field is shown in Figure 5.1.

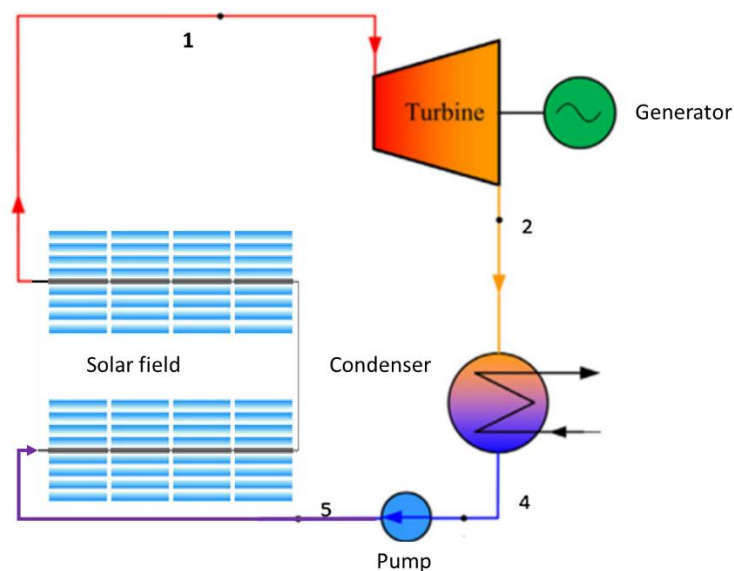


**Figure 5.1:** Organic Rankine cycle driven by the LFR solar field

The liquid fluid, which is pressurized by a pump, is channelled into an evaporator (heat source) to generate a vapour that is expanded in a turbine connected to a generator. Finally, the vapour, after the expansion in the turbine, is condensed in the condenser and returned back to the evaporator by the pump to repeat the cycle. To enhance the use of energy in the cycle, an internal heat exchanger can be deployed to preheat the fluid after the pump that will enter the evaporator [15].

The ORC turbine model adopted in the current study is depicted in Figure 5.2 below. The model constitutes a small-scale axial-outflow ORC turbine with a power output of a few kW capable of transforming the energy from a low-temperature heat source into useful power employing an appropriate organic working fluid. The axial turbine adopts a single-stage fitted on the same

disc, hence, low-temperature heat source, low mass flow range, and thus, a target application generating only a few kW (1 - 5 kW).

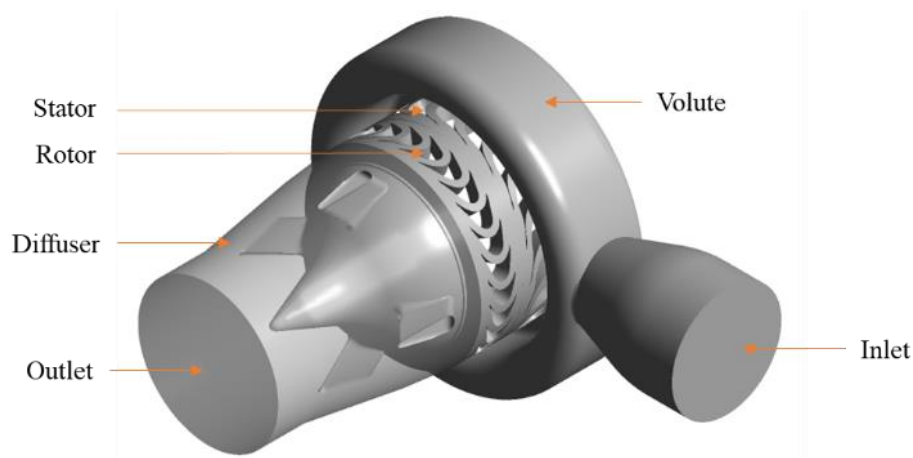


**Figure 5.2:** Organic Rankine Cycle (ORC) turbine

The liquid fluid which is pressurized by a pump is channelled into an evaporator (heat source) to generate a vapour that is expanded in a turbine connected to a generator. Finally, the vapour at the turbine output is condensed and injected back into the pump to repeat the cycle. In order to enhance the use of energy from the expanded vapour, an internal heat exchanger can be deployed to preheat the pump fluid that will enter the evaporator. The key features of the turbine and its dimensions can be seen in Table 5.1.

**Table 5.1:** The key features of the turbine and dimensions

Component/Domain	Dimension	Unit
Number of stator blades	19	-
Number of rotor blades	27	-
Stator blades clearance	~ 0.1	mm
Rotor blades clearance	~ 0.08	mm
Inlet diameter	25	mm
Diffuser outlet diameter	32	mm

### 5.3. Organic working fluids selection

The selection of a suitable working fluid is imperative to the performance of the organic Rankine Cycle. Depending on the application, the source, and the amount of heat to be deployed, the fluid must demonstrate excellent thermodynamic properties at the lowest possible temperatures and pressures and also meet some criteria, such as being economical, non-toxic, non-flammable, environmentally friendly and tolerating a high use of the available energy from the heat source. This limits the list to just a few fluids if all aspects that can restrict their use are considered.

The new environmentally friendly Novec649 and the R365fmc are the two fluids proposed for this study considering the properties mentioned above. The properties of these fluids are presented in Table 5.2. The thermo-physical properties of organic fluids considerably affect the cost and availability, system efficiency, turbine size and performance, environmental issues such as ozone depletion potential (ODP), global warming potential (GWP) and safety (critical pressure and temperature).

**Table 5.2:** Thermo-physical properties of organic fluids

Property	Novec	R365fmc
Boiling Point(°C)	322	314
Molecular Weight (g/mol)	316	148
Critical Temperature (°C)	442	500
Critical Pressure (MPa)	1.88	3.2
Absolute Viscosity (cP)	0.64	0.4
Ozone Depletion Potential	0	0
Global Warming Potential (GWP)	1	0

The choice of dry and isentropic working fluids in a low-temperature heat source application are more favourable for ORC since expansion in the turbine will be in the superheated regime. This will ease challenges resulting from the existence of droplets of organic liquid in the rotor stage, compared with wet fluids' expansion in the wet regime, which requires preheat equipment. This element considerably lessens turbine maintenance and evaporator size requirements, which results in reduced capital cost of the ORC system.

#### 5.4. CFD methodology and numerical approach

The CFD application presents an imperative step to study the turbines' performance and combines initial single-stage design due to the actual flow field in axial turbines' being a strongly 3D, viscous and turbulent flow. Consequently, this section presents the 3D CFD analysis deployed in determining the aerodynamic performance of the axial turbines by performing the analysis through the stator and rotor blade passage and the complete turbine configuration.

The important geometric features of the proposed turbines, as presented in Table 5.1, are used to generate the 3D geometry of the turbine stage (stator and rotor), which constitute an essential part of the complete turbine in Figure 5.2, employing the ANSYSR20-Turbo grid tool. The pressure and angle/thickness modes are used to characterize the curves for the hub, shroud and blade profile for the stator and rotor blades.

#### 5.4.1. Mesh details and sensitivity analysis

The ANSYSR20 Turbo Grid meshing tool was employed to generate the computational mesh configured for CFD analysis through the hexahedral mesh and based mainly on an O-H grid. The quality of the discretization utilised has a direct impact on the accuracy of the steady-state approach. Thus, to obtain a sufficient mesh size, a detailed grid independence study was performed for the complete turbine taking into account the computational expense time and accuracy of results.

The preliminary mesh was constructed, and the 3D CFD modelling was carried out. The dimensionless distance  $y^+$  and the turbine outlet temperature and pressure were computed. The mesh was then refined, and the simulation was repeated until the grid-independent solution was attained. The outcome of the mesh independence study revealed that the variation in the numerical outcomes was found to be negligible for the meshes with  $10 \times 10^6$  elements and more. Hence the mesh with a number of elements  $10.27 \times 10^6$  was selected for further modelling. The grid independence study results are presented in Table. 5.3. The computational meshes of the blade passage for both the stator and rotor blades are presented in Figure. 5.3.

**Table 5.3:** A detailed grid independence mesh study

No. of Elements[ $10^6$ ]	Outlet P [Pa]	Outlet T [K]	Torque [N-m]	Power (kW)
3.10	207000	444.247	-2.071	1.573
4.48	207000	444.221	-2.094	1.590
5.40	207000	444.192	-2.122	1.611
7.50	207000	444.177	-2.134	1.620
10.27	207000	444.159	-2.148	1.632
14.60	207000	444.150	-2.152	1.635

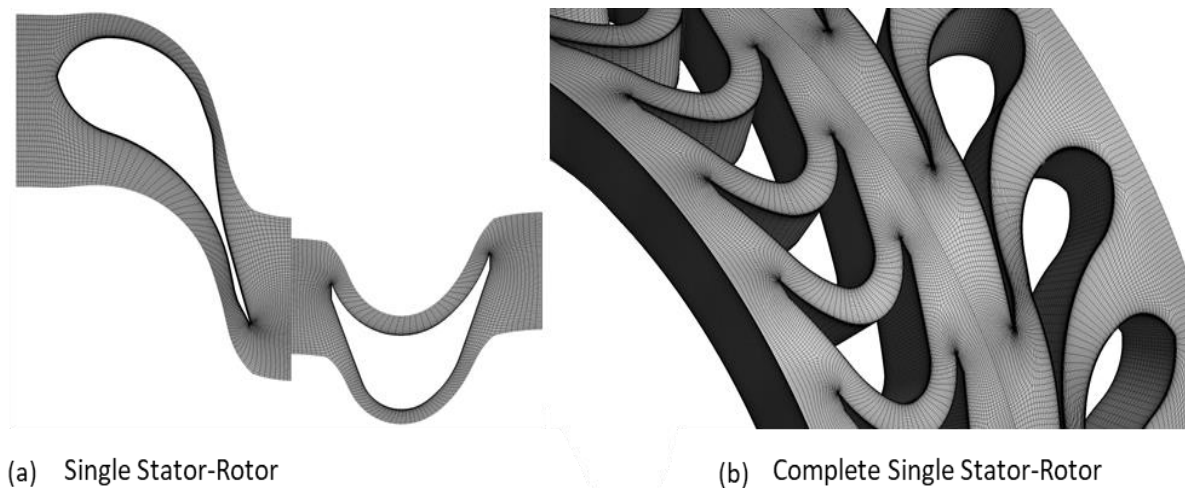


**Figure 5.3:** Computational meshes of the blade passage for stator and rotor blades

The chosen topology is generated using the H-type and O-type grids combined to improve the grid orthogonality around the blade. For the purpose of mesh resolution, nodes were added in the blade passage (blade-to-blade) hub-to-tip to increase the computational mesh due to the deviation of  $y^+$ . This is used to determine the first node away from the wall and is denoted as boundary layer mesh size, which is a dimensionless distance from the wall. Figure 5.4 depicts the generated meshes for the turbine Volute and Diffuser.

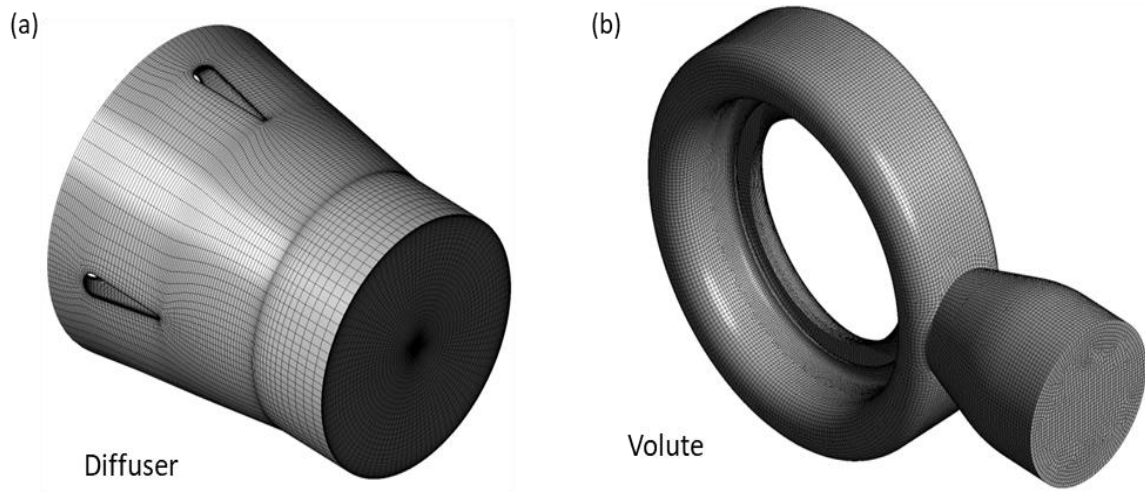


**Figure 5.4:** Generated meshes for the turbine Volute and Diffuser

#### 5.4.2. Model governing equations

The fluid is considered compressible and steady-state flow condition. A standard k-epsilon was selected as the turbulence model due to high Reynold number of around  $3.5 \times 10^5$ . By determining  $y^+$ , the turbulence model k-epsilon is capable of automatic near-wall treatment to capture turbulence closure. Based on the k-epsilon model proposed in the CFX user's manual, the value of  $y^+$  must be around unity. For flow separation under an unfavourable pressure gradient, the k-epsilon accounts for the turbulent shear stress transfer. The turbulence intensity at the inlet was kept at the recommended value of 5%. The governing equations for mass, momentum and turbulent kinetic energy are as follows [282]:

**Mass conservation equation:** The mass conservation equation, often known as the continuity equation, is written as follows:

$$\frac{\partial}{\partial t} + \nabla \cdot (\rho \vec{v}) = S_m \quad (5.1)$$



where  $S_m$  represents is the mass added to the continuous phase from the dispersed second phase. In this case, no mass is added, hence  $S_m = 0$ .

**Momentum Conservation Equation:** In an inertial reference frame, momentum conservation is represented as

$$\frac{\partial}{\partial t}(\rho \vec{V}) + \vec{V} \cdot \nabla (\rho \vec{V}) = -\nabla p + \nabla \cdot (\bar{\bar{\tau}}) + \rho \vec{g} + \vec{F}'_b \quad (5.2)$$

The static pressure is denoted by  $p$ , the stress tensor is given by  $\bar{\bar{\tau}}$ , and  $\rho \vec{g}$  and  $\vec{F}'_b$  are the gravitational body force and external body forces, respectively.

**Turbulence:** By solving two independent transport equations, two-equation turbulence models can determine both the turbulent length and time scale. The following are the k-epsilon transport equations used to calculate the turbulent kinetic energy and specific dissipation rate:

$$\frac{\partial}{\partial t}(\rho k) + \frac{\partial}{\partial x_i}(\rho k u_i) = \frac{\partial}{\partial x_j} \left[ \left( \mu + \frac{\mu_t}{\sigma_k} \right) \frac{\partial k}{\partial x_j} \right] + G_k + G_b + \rho \epsilon - Y_m + S_k \quad (5.3)$$

The rate of dissipation  $\epsilon$  of the turbulence kinetic energy  $k$  is obtained from the following transport equation.

$$\frac{\partial}{\partial t}(\rho \epsilon) + \frac{\partial}{\partial x_i}(\rho \epsilon u_i) = \frac{\partial}{\partial x_j} \left[ \left( \mu + \frac{\mu_t}{\sigma_\epsilon} \right) \frac{\partial \epsilon}{\partial x_j} \right] + C_{1\epsilon} \frac{\epsilon}{k} (G_k + C_{3\epsilon} G_b) - C_{2\epsilon} \frac{\epsilon^2}{k} + S_\epsilon \quad (5.4)$$

Here  $\mu_t$  represents the eddy viscosity;  $G_k$  represents turbulence kinetic energy generation resulting from mean velocity gradients;  $G_b$  denotes turbulence kinetic energy generation due to buoyancy;  $Y_m$  is the contribution of fluctuating dilatation in compressible turbulence to the overall dissipation rate, and  $C_{1\epsilon}$ ,  $C_{2\epsilon}$  and  $C_{3\epsilon}$  are constants in these equations. The turbulent Prandtl numbers for  $k$  and  $\epsilon$ , are  $\sigma_k$  and  $\sigma_\epsilon$ , respectively. In this case, no source terms were defined, therefore,  $S_k$  and  $S_\epsilon$  user-defined source terms are not applicable.

**Energy equation:** the energy equation in ANSYS is solved by deploying the following equation:

$$\frac{\partial}{\partial t}(\rho e_t) + \nabla \cdot \left( p \vec{V} \left( e_t + \frac{p}{\rho} \right) \right) = \nabla \cdot [k \nabla T + (\bar{\bar{\tau}} \cdot \vec{V})] + S_g \quad (5.5)$$

The total internal energy is represented by  $e_t$  and  $k$  denotes the thermal conductivity while  $\nabla T$  is the temperature gradient.  $(\bar{\bar{\tau}} \cdot \vec{V})$  is the viscous dissipation term for work done by viscous shear stresses.  $S_g$  is the source term.

**Performance of the turbine:** The organic fluid's output vapour is expanded through a turbine. The turbine's performance is calculated as follows:

$$\eta_{ST} = \frac{h_1 - h_2}{h_1 - h_{2,s}} \quad (5.6)$$

$$\dot{W}_{ST} = \dot{m}_{WF} (h_1 - h_2) \quad (5.7)$$

Here  $\eta_{ST}$  denotes isentropic efficiency of the turbine,  $h_1 - h_2$  are the input and output enthalpies of the turbine (kJ/kg) and  $\dot{m}_{WF}$  is the inlet mass flow rate to the turbine (kg/s) while  $\dot{W}_{ST}$  is the turbine produced power (kW).

#### 5.4.3. Material properties: organic fluid

The ORC turbines 3D CFD analysis requires an accurate thermodynamic model to take into account the variations in the thermodynamic properties of organic fluids. Therefore, NIST Reference Fluid Thermodynamic and Transport Properties Database (REFPROP - Version 10) was used to obtain the thermodynamic properties of the selected organic fluids, R365FMC and NOVEC649, respectively, as a function of the pressure and temperature. The boundary conditions such as inlet pressure and total temperature, rotational speed, and mass flow rate are used from experiments to carry out the 3D CFD simulations using ANSYSR20-CFX.

#### 5.4.4. Boundary conditions

In order to obtain a unique solution from specifying a problem, the information on the dependent (flow) variable at the domain boundaries such as mass, momentum, energy etc. were specified. The boundary conditions were carefully defined, identifying the location of the boundaries (e.g., inlets, outlets, walls, symmetry), assigning the appropriate information at the boundaries and the data necessary at the boundary condition type and the physical models employed. The precision of the simulation results is determined by how well these conditions are defined.

**Inlet boundary condition:** Pressure and temperature inlet boundary conditions are used to specify the fluid pressure and temperature at flow inlets since the values are known from experiments.

**Outlet boundary condition:** a pressure outlet boundary condition was defined, and a static (gauge) pressure at the outlet boundary is specified.

**Domain Interface:** A general connection-type interface was used to connect the volute and the stator, while a standard mixing interface is employed between the stator and rotor and between the rotor and diffuser.

**Wall boundary condition:** A stationary no-slip wall condition with 0.5% roughness is specified.

#### 5.4.5. Solver setting

The solver input parameters dictate how problems are solved by introducing the models of accuracy, stability and convergence. An upwind scheme was used for the numerical discretization methods. More emphasis is given to convergence, which is critical for the CFD simulation. Appropriate solver settings are selected for this simulation and monitored from solution convergence. Figure 5.5 shows the workflow for solver simulations.

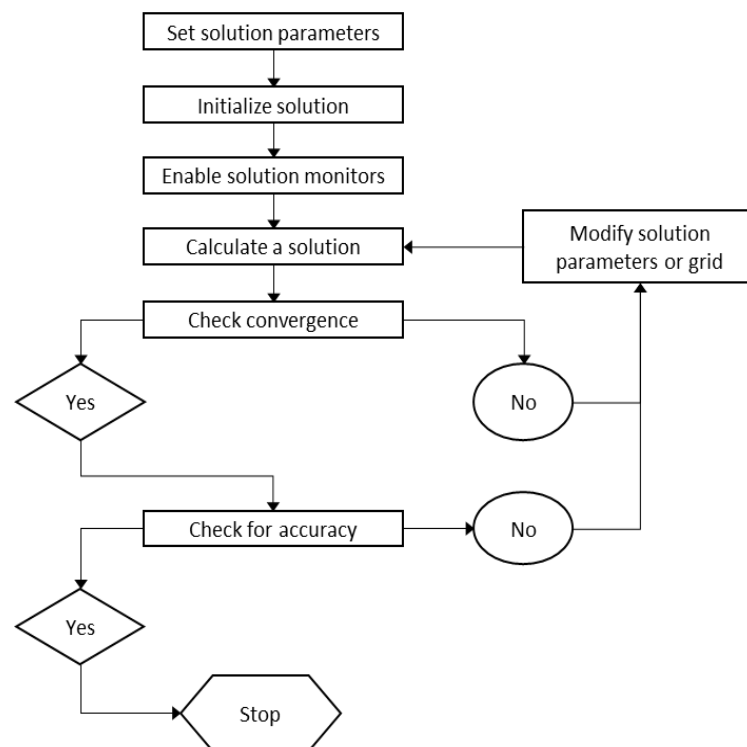


**Figure 5.5:** Basic workflow for solver simulation

All solution variables were initialized prior to starting iterations. The standard initialization model was selected with an inlet boundary to automatically set values that are specified at the inlet boundary. The solver was configured to perform enough iterations to attain a converged solution. Tolerances are set for all discrete conservation equations (momentum, energy, etc.) in all cells (Residual). The residue momentum (in all three coordinates) and mass flow rate as

well as the energy and k-epsilon ( $k-\epsilon$ ) convergence criteria, are set at  $10^{-6}$ . The converged residuals can be observed in Figure 5.6.

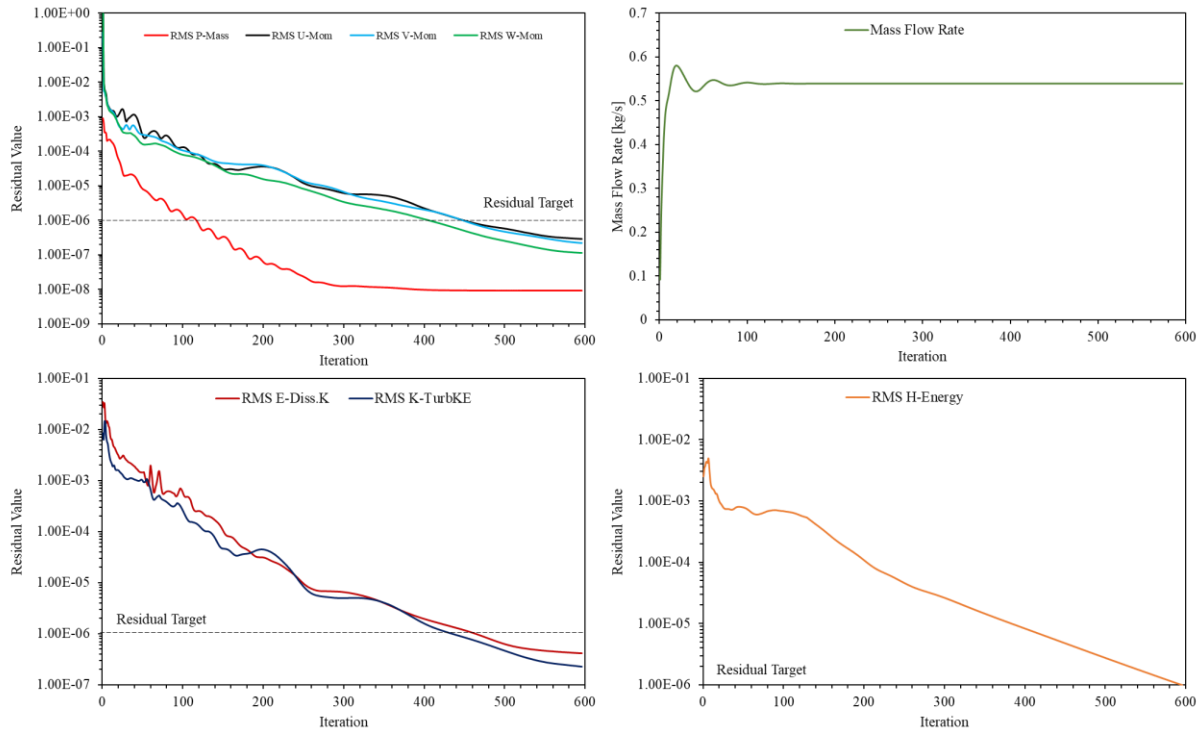


**Figure 5.6:** The converged residuals for momentum, energy, mass, turbulence and mass flow rate

## 5.5. Results and discussion

Generally, several parameters influence the performance of an ORC turbine. Normally, these parameters simultaneously result in an increase or decrease in the performance parameters or costs. In this section, the effects of temperature, pressure, rotational speed, velocity and rotor gap on the performance of an axial turbine are considered. The input parameters for the experimental and numerical investigation of the ORC turbine are presented in Table 5.4. The experiment is performed for various input variables such as temperature, pressure, and rotational speed deploying two working fluids, mainly Novec649 and R356mfc.

**Table 5.4:** Input parameters for the experimental and numerical simulation for investigation of the ORC turbines

Experimental numerical simulation inputs					
Parameters	Test. 1 values	Test. 2 values	Test. 3 values	Test. 4 values	Test. 5 values
Inlet pressure [Pa]	1389000	1314000	1373000	1389000	1371000
Outlet pressure [Pa]	207000	196000	209000	209000	208000
Inlet Temperature [K]	460	461.91	448.6	443.07	439.92
Rotational speed [rpm]	7253	6908	6782	6814	6720

To begin, the effects of each of the parameters listed in Table 5.4 on the ORC turbine performance are investigated to see how each variable affects turbine performance independently. A pressure-based inlet and outlet boundary conditions were assigned. For this purpose, a variable is altered in a specific range, with the assumption that the other variables are also changed, and their influences on turbine performance, such as the outlet temperature, mechanical power, work output, and isentropic efficiency of the turbine, are studied and analysed. The investigation was conducted in five (5) different stages. Table 5.4 shows all the cases studied and the values such as the rotational speed, inlet and outlet temperatures and pressures specified on boundaries, and Table 5.5 shows boundary conditions employed.

**Table 5.5:** the boundary conditions employed in numerical simulation for investigation of the ORC turbines

<b>Boundary Conditions</b>	
Inlet	pressure [Pa] & Temperature [K]
Outlet	pressure [Pa] & Temperature [K]
Turbulence	K-epsilon
Domain Interface	General connection-type for volute and stator
	Standard mixing interface for stator and rotor
	Standard mixing interface for rotor and diffuser
Wall	no-slip wall
Solver setting (residue)	convergence criteria, are set at $10^6$ .

The variations in outlet temperatures for the different ranges of the input parameters are shown in Figure 5.7. and temperature contours in Figure 5.8. It is observed in these Figures that the results of the CFD simulation are in good correlation with the data obtained from the experiment. The organic fluid Novec649 records a slightly higher temperature at the outlet compared to the R365mfc. This is due to the lower molecular weight of the R365mfc, which causes a lower transition in temperature. In addition, Novec exhibits properties such as low latent heat and high density compared to R365fmc.

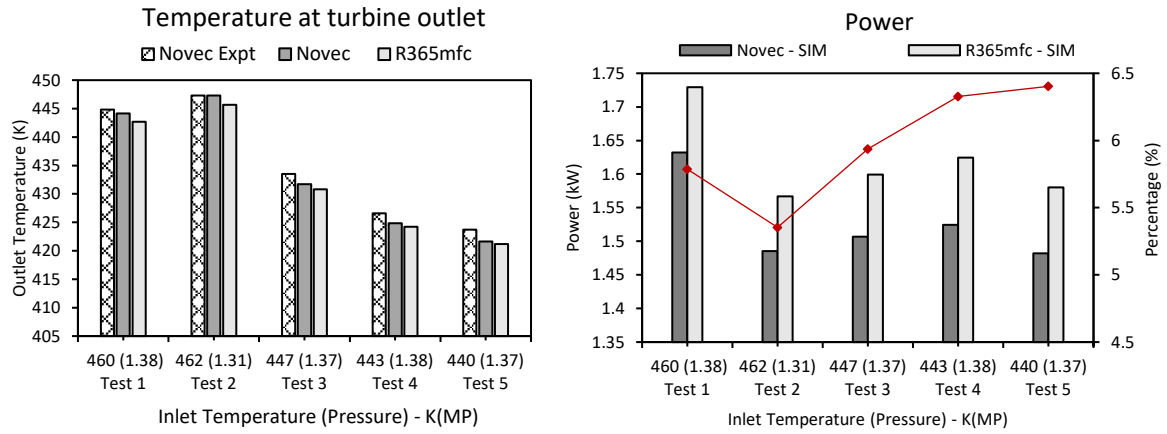


**Figure 5.7:** Fluid temperatures at turbine outlet (Left) and turbine power for various inlet temperatures and pressures (Right)

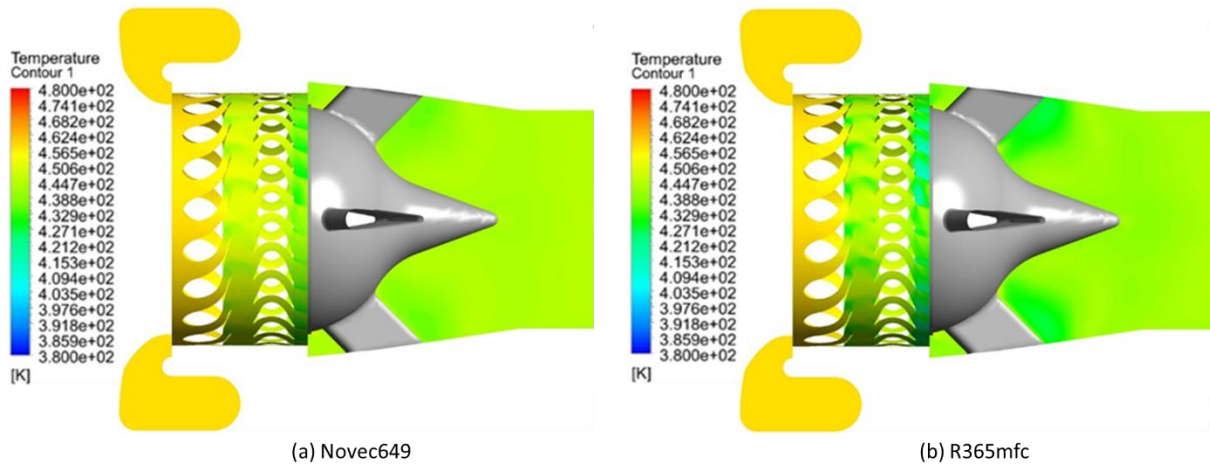


**Figure 5.8:** Temperature contours in the complete turbine (a) Novec649 (b) R365mfc

From the graph in Figure 5.7 (Left), it can be noted that as the input pressure increases with an increase in the temperature, as expected. The performance of the ORC turbine is very sensitive to the inlet temperature. The higher the inlet temperature, the better the performance of the turbine.

Furthermore, the results show that, in all five (5) test phases, the influence of the parameters' inlet turbine temperature and pressure on the turbine power is much more than other parameters. This trend can be observed from the result obtained at test 2; despite the fact that the higher rotational speed compared to test 3 and 5, a lower turbine power was realised due to lower inlet pressure.

Furthermore, comparing the performance of the two working fluids, Novec649 and R365mfc, enhanced performance from the R365mfc is observed compared to Novec69 for different inlet temperatures, pressure and rotational speed. The R365mfc is a lighter fluid, with a light molecular weight (148 g/mol), hence can produce substantially higher power outputs compared

with the high molecular weight of Novec (316 g/mol). In addition, Novec649 has high-density and lower specific volumes compared to R365mfc, thus requiring a higher-pressure ratio and rotational speed to achieve the same power output as the R365mfc fluids.

The effect of the tip clearance (rotor gap) of rotor blades on the performance of the single-stage axial turbine was investigated. A number of steady-state viscous flow simulations were run for the tip clearance effect for a range of values, namely 0, 50, 100, 150 and 200  $\mu\text{m}$ , deploying both organic fluids. The effects investigated include the distribution and variation of the pressure, the velocity, and the turbine power. It is observed that larger tip clearance has a negative effect on the stage pressure gradient and power output of the turbine. Contours of pressure in the tip clearance (rotor gap) on the turbine stage for 0 and 200  $\mu\text{m}$  deploying Novec649 are presented in Figure 5.9. For the 200  $\mu\text{m}$  rotor gap a secondary flow is induced across the rotor blade. The leakage flow can also be considered to have a higher pressure, thus, reducing the performance of the turbine.

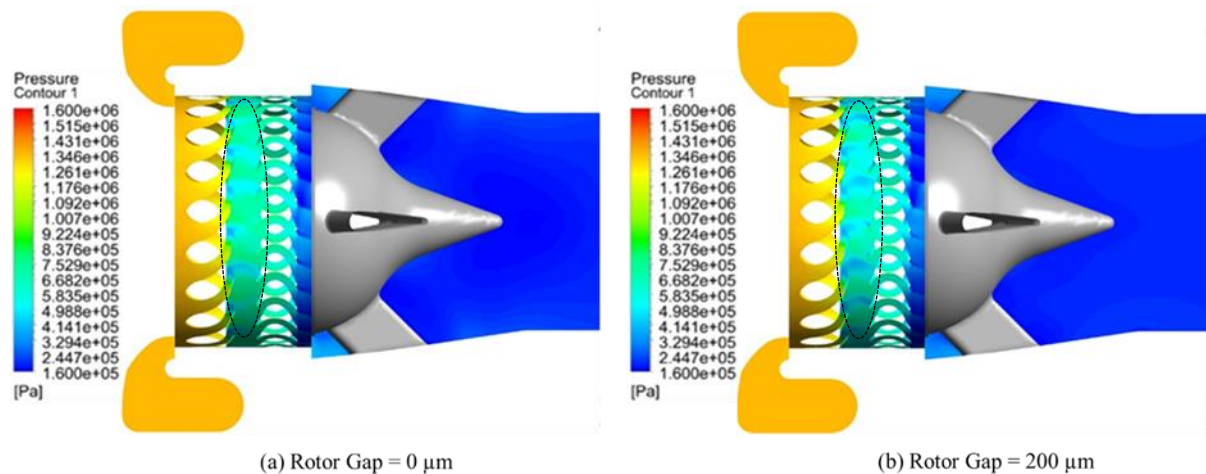


**Figure 5.9:** Contour of pressure characteristics on complete turbine (a) 0  $\mu\text{m}$  gap contour (b) 200  $\mu\text{m}$  gap contour

The increase in tip clearance (rotor gap) has a detrimental impact on the overall performance of an axial turbine. Figures 5.10(left) and 5.10(right) depict the effect of increasing tip clearance on the output power of the turbine and organic fluids (Novec649 and R365mfc). Using Novec649 as working fluid, it has been observed from Figure 5.10(left) that an increase in tip clearance results in a decrease in turbine power with increasing percentage difference compared to 0  $\mu\text{m}$  rotor gap. Subsequently, a similar trend is noticed in Figure 5.10(right); however, the effect appears to be substantial using Novec649 compared to R365mfc due to the variance in thermo-physical properties. These result in secondary flow due to pressure gradients and leakage through tip clearance caused by pressure difference.



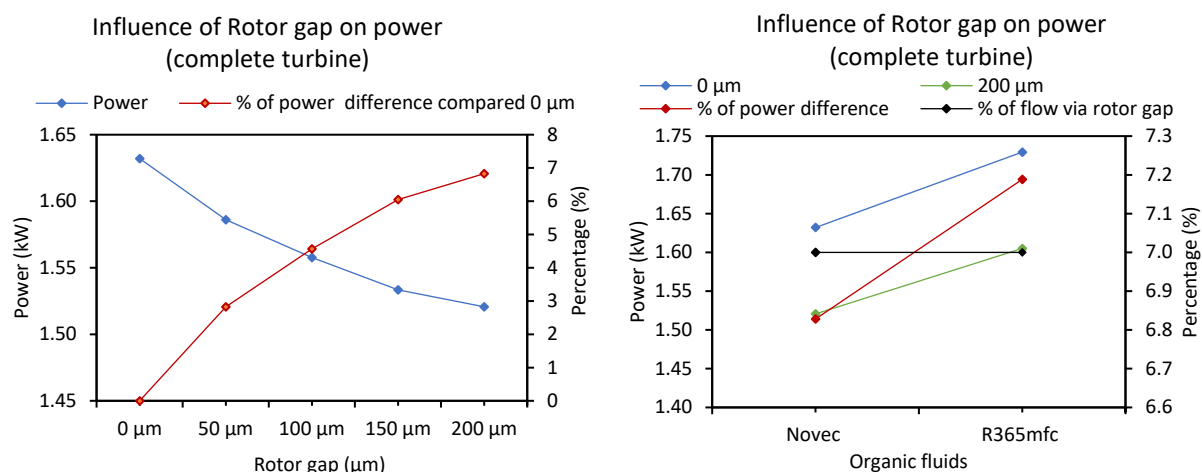


**Figure 5.10:** Effect of tip clearance (rotor gab) under steady state condition using Novec649 on turbine power output (Left), and comparison of the effect of tip clearance (rotor gab) on Novec649 and R365mfc (Right)

The turbine tip clearance loss is part of the overall blade loss because the fluid bypasses the blades and so does not contribute to the turbine power output and interacts with the outer wall boundary layer. The relative motion between the turbine blades and the casing wall depicted in Figure 5.11 results in a velocity field in the tip region. In the case of the rotor with 200  $\mu\text{m}$  tip clearance, the fluid near the casing wall experiences a considerable velocity difference across the tip. The highest and the lowest velocities were both observed in the region of the tip leakage vortex. Thus, resulting in about 7 % of the fluid not following through the passage as shown in Figures 5.11b and 5.11d.

Turbines, unlike compressors, operate in a favourable pressure gradient; there is much pressure drop taking place during the fluid flow. The tip leakage flow expands to the same back pressure as the passage flow.

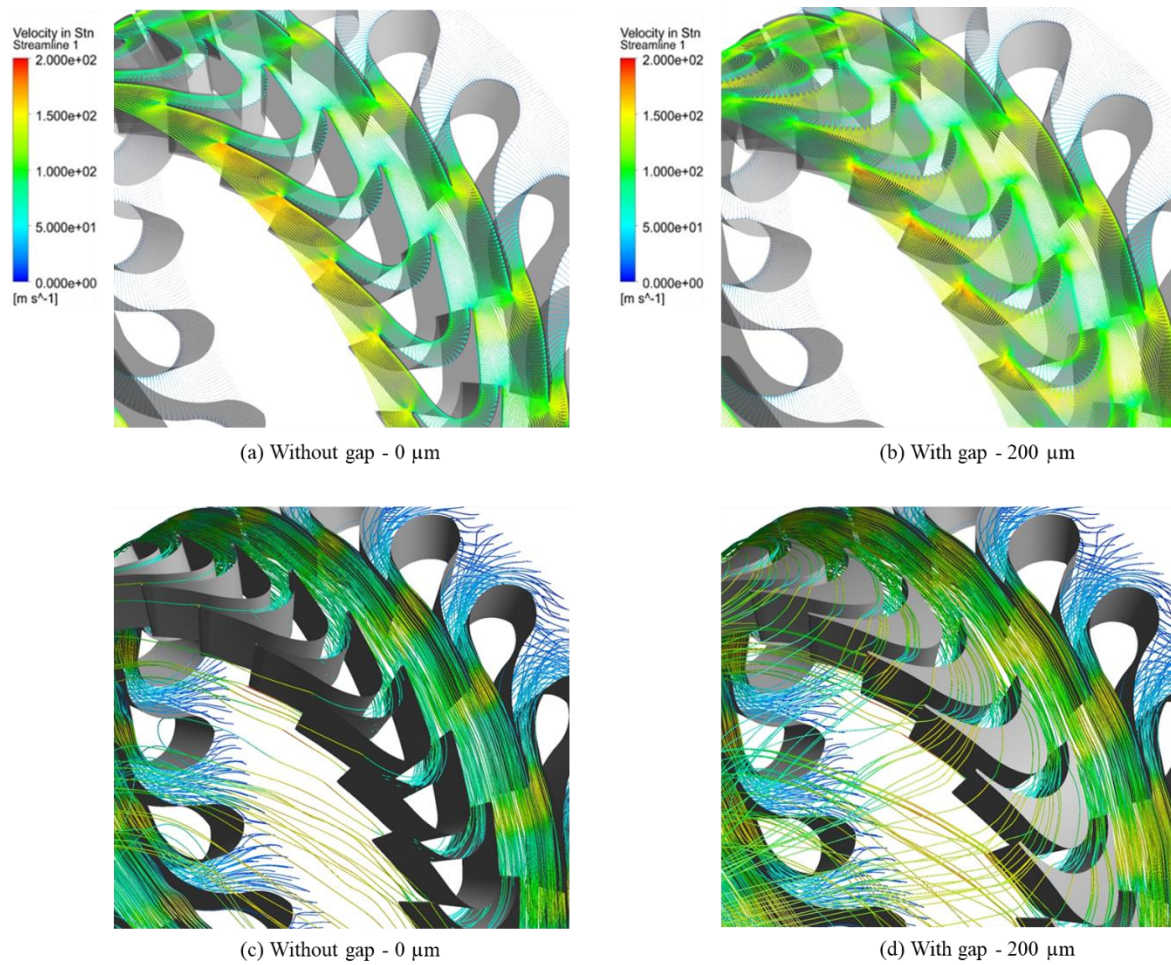


**Figure 5.11:** Effect of tip clearance (rotor gap) on turbine blades (a) 0  $\mu\text{m}$  gap contour (b) 200  $\mu\text{m}$  contour (c) 0  $\mu\text{m}$  gap streamline (b) 200  $\mu\text{m}$  gap streamline

This causes a higher axial velocity in the tip region and a slightly lower axial velocity across the remaining blade span. The leakage flow can also be considered to have a higher pressure than the passage flow. Hence, this constitutes a significant effect on the flow stability, pressure rise, and turbine work output. It is generally accepted that the tip leakage flow should be kept to a minimum as recommended.

Figure 5.12(left) depicts the graphs for inlet temperatures and isentropic efficiency at varying inlet pressure for different tests performed using Novec649 and R365mfc organic fluids. From Figure, it can be seen that by increasing the inlet temperature, the isentropic efficiency also increases. In axial turbines, increased turbine pressure results in greater enthalpy differences between the inlet and outlet of the turbine, thus increasing the isentropic efficiency and the work output of the turbine. As the flow passes through the stator, it increases the kinetic energy of fluid that impinges on the blades.

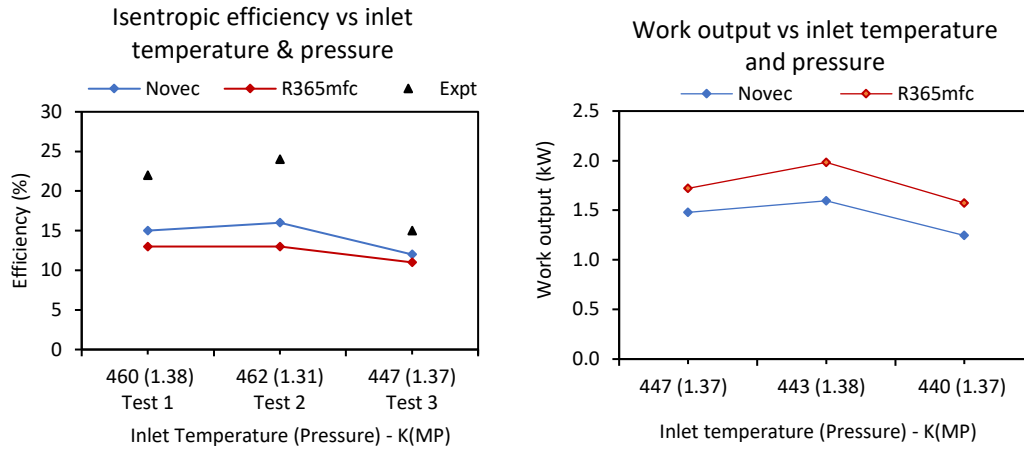


**Figure 5.12:** Isentropic efficiency (Left) and turbine work output (Right) for different inlet temperature-pressure

Moreover, Figure 5.15(right) depicts the dependence of the turbine work (kW) on the different turbine inlet temperatures under superheated vapour conditions for varied inlet pressure for the different tests conducted. In the case of both fluids, the turbine work significantly increases with an increase in the turbine inlet temperature and pressure. As a result of pressure increase at the inlet, the value of enthalpy is increased, which formulates the turbine work output to become enlarged. In axial turbines, increased turbine pressure results in greater enthalpy differences between the inlet and outlet of the turbine. As the flow passes through the stator and rotor, the rotor is required to add energy to the system by extracting high kinetic energy that impinges on the blades, thus increasing enthalpy, thus resulting in higher work output of the turbine. From R365mfc point of view, fluid properties such as higher enthalpy compared to Novec649 result in higher work output.

Choosing the appropriate working fluid is vital for the ORC. The fluids Novec649 has a higher temperature output as well as the isentropic efficiency compared to R365mfc. However, in terms of useful power production and work output at the turbine outlet, these fluids act quite contrariwise. In power generation, the R365mfc fluid generates a higher power in all test points. This trend suggests the significance of the preferred objective in cycle design. In cases where there are no boundaries in terms of the need for power, the fluid Novec649 would be the good choice; however, when a specific power is required, the R365mfc is preferred.

## 5.6. Summary and Conclusion

In this Chapter, the parametric evaluation of an axial ORC turbine for the range of parameters, notably, inlet turbine temperature and pressure, rotational speed for different test points, is performed and analysed. The effects of the defined parameters on the turbine power, isentropic

efficiency and work output are considered. In addition, the impact of varying the rotor tip clearance (rotor gap) on the turbine power output is examined. The investigation was carried out deploying two organic fluids, namely, Novec649 and R365mfc. A comparative analysis of the characteristics and behaviours of these working is performed between results obtained from numerical approach and experimental data.

It was observed that the inlet turbine temperature and pressure have the greatest effect on the power, work output and isentropic efficiency. Increasing the turbine inlet temperature and pressure result in increased isentropic efficiency and power output. However, material limitations most times lead to challenges when using high temperatures. High temperature also results in stress on the rotor blades and rotational speed. Nowadays, there are emerging technologies that deploy artificial cooling techniques to keep the blades cooler and permit the use of high temperatures. There are also studies to identify and develop newer materials that can withstand higher temperatures and stress.

The selection of a suitable working fluid and its application in ORC turbine is a very crucial aspect mainly due to the dependence of its categorization on the temperature of the heat source, defined by the fluid thermodynamic and/or thermophysical properties such as temperature and critical pressure, chemical stability, and safety. Considering the thermodynamic design point for each working fluid, the Novec649 offers the best performance in terms of isentropic efficiency. However, with such properties as lower viscosity, a higher and more stable specific heat, a higher thermal conductivity, R365mfc experiences lesser temperature drops and turbulent flow regime than with than Novec649, thus producing higher turbine power.

In addition to its higher power output, the R365mfc is exhibit excellent properties terms of safety and environmental impact. Both fluids (Novec 649 and R365mfc) are non-flammable and ecologically friendly, with an ozone depletion potential of 0 [283, 284]. However, compared to Novec649, which has a global warming potential of 1, R365mfc has a global warning potential of 782 [283, 284]. Next to that, Novec649 allows for a lower pressure, which reduces design limitations and simplifies manufacturing.

The presence of moving blades in ORC turbine turbines needs a limited annular tip clearance between the rotor blade tip and the shroud. Although mechanically essential, this clearance could be a significant cause of loss in a turbine. The gap height can be a fraction of a millimetre, yet it can have a disproportionately large impact on the performance of the stage. When there

is a large gap between the blades and the shroud, leaks occur, and contact between them can harm the blades.

As a result, independently evaluating the sources of performance decline provides useful information that can aid in maintenance action. The turbine tip clearance loss is part of the overall blade loss because the fluid does not follow the expected path at the blade tip and so does not contribute to the turbine power output and interacts with the outer wall boundary layer. The study performed on the impact of varying rotor tip clearance revealed that increasing turbine tip clearance reduces gas turbine performance (power) and, as a result, will require increased inlet temperature and pressure.

## Chapter 6 : Solar Field Shading Analysis

### 6.1. Introduction

Shading analysis is a fundamental step in the design, installation and operation of a solar field. Shading of any form results in a negative impact on the performance of an entire solar field [285]. The shadow cast on collector surfaces implies obstruction of solar radiation projection, and this may reduce the efficiency of the collector in direct proportion to the area shadowed at any time.

Generally, shading of solar field can occur from various sources, mainly nearest neighbour collectors, buildings and vegetation, and is likely to happen during some period of the day, mostly close to sunrise and sunset; hence, it is preferred that any form of shadow be minimised all through the day.

The estimation of the impact of shading from nearest neighbour collectors is best performed at the modelling and design stage of a solar field, and this takes into consideration multiple variables such as the spacing between reflectors, their height, the tilt angle, the latitude, row length, the type of solar field configuration and the time of year [286]. In this section, shading resulting mainly from structures such as buildings and vegetation is considered.

The process of precise shading study involves making on-site measurements, which are then used to design the surrounding of the chosen location for installation, either as a 3D or 2D model. There are a few different approaches to create these 3D or 2D models, while nearly most of the methods consist of mapping the horizon and then merging it with sun path data, each method has its different approach.

SolMetric is a tool that deploys a special camera that captures images of the entire background of a specified location. The sketch of a sun path is then spread across the image, which generates the solar data of the site. The data can then be analysed further using additional software [3].

Another tool that offers a cheaper alternative but without direct estimation or analysis of generation losses is the SunPathFinder. The system constitutes a highly polished, transparent; convex plastic dome merged with an analogue sun path chart [287]. The resulting image will show both the surrounding area together with the sun path diagram.

T\*SOL launched a professional simulation software tool for the design and planning of solar thermal systems. The tool estimate temperatures and energy performance over a given duration with a wide choice of systems and components. The results show a precise graphical representation of the solar element, collector temperature and heat transfer, whereas a detailed report depicts all data and variables.

There are few shading estimation applications developed for smartphones, notably, the SolmetriciSV for IOS and the Sunshades for android. Both deploy different methods such as GPS, and compass for mapping the surroundings and also greatly vary in other aspects. However, one possible setback of these approaches is the considerable margin of error, especially when used together.

In this study, the shading analysis was performed using computer software tools, namely, shadow-analyses, sketch-up and LightTools. With google sketch-up, a rough shade estimation can be performed simply by measuring distances either in reality or creating the 3D model of the site and the surrounding environment using the tool.

However, for precise analyses, additional software, Shadow-Analysis, can be linked with sketch-up. The combination supports sun tracking and shadow effects that can be easily and dynamically improved or even animated within the program to evaluate the timing and effect of obstructions. In addition, LightTools is used to analyse the optical performance of the solar field.

The first step involves identifying the appropriate distance between a solar field and the surrounding building with the aim of analysing the shading factor. Besides, the distance and height of the surrounding buildings from the solar field were considered as the shading phenomenon. The study considers aligning the solar field in north-south and east-west orientation, both for east-west tracking of the sun. The proposed design is installed in Almatret, Spain, with the coordinate of 41°18'17.1"N 0°25'37.2"E. The proposed solar field orientation and the sounding layout can be seen in Figure 6.1.

## **6.2. Sun Path**

A sun path chart is mainly a plot of the sun's position, or path, in the sky at various times over the day and seasons. The sketch comprises the solar azimuth angle (the angle between the sun's horizontal direction and a reference path, generally north or south) and the solar altitude (the



sun's vertical position or elevation over the horizon). The sun path chart of the proposed location is presented in Figure 6.2 below.

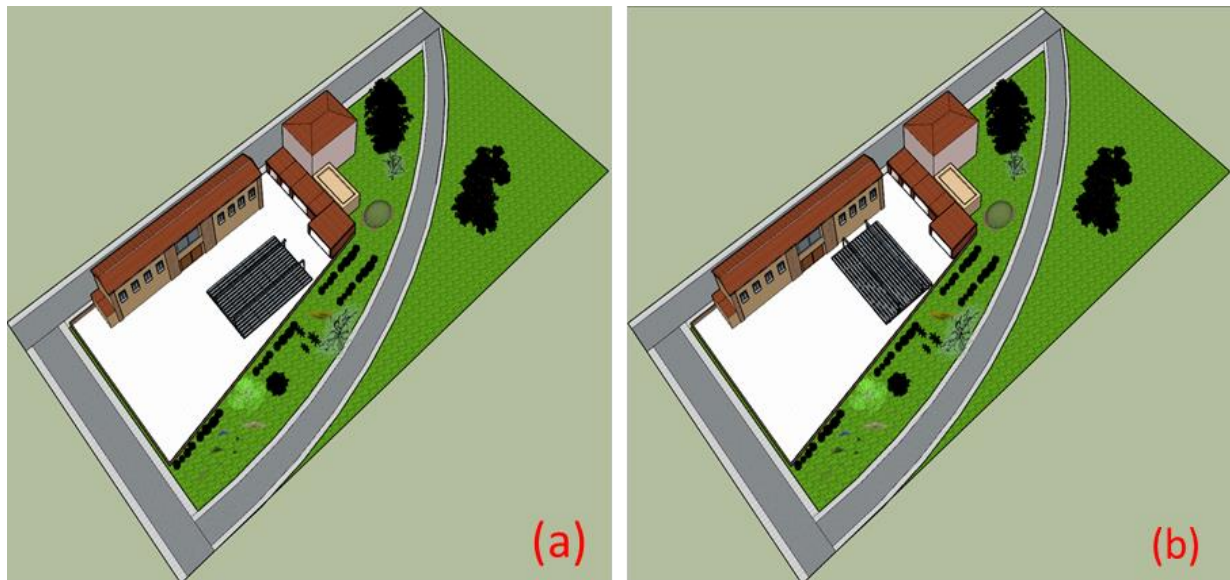


**Figure 6.1:** Building layout with east-west (a) and north-south (b) solar field orientation

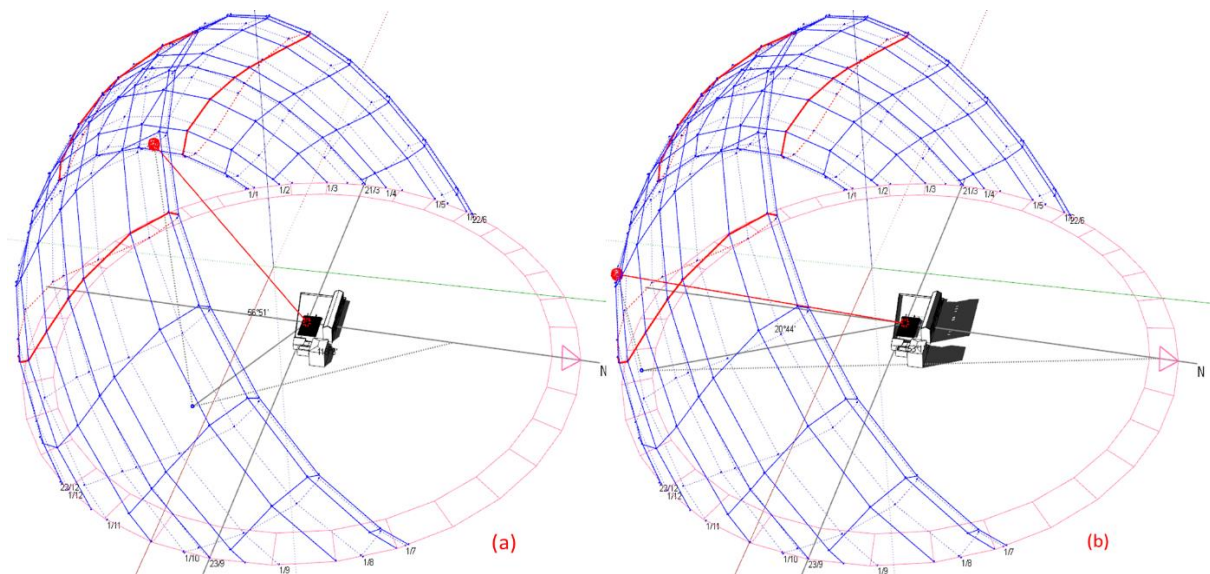


**Figure 6.2:** Sun path during summer (July) season (a) and Sun path during winter (December) season (b)

Sun often does not rise from the east every day. The Sun deviates a few degrees from precise east over the year. Different parts of the sky affect the radiation altitudes at different times of the day and seasons. The latitude of a site has a major impact on the altitude of a sun path. Hence every installation site comes with its challenges. These challenges need to be taken into consideration in the design, installation and operation of a solar field in the desired location. As a result, this study is performed for the two main seasons: summer (July) and winter



(December). The complex relationships are best studied by deploying computer simulation tools.

### 6.3. Assessing the impact of shading

The optical performance of a Linear Fresnel reflector collector is highly dependent on weather conditions. More precisely, the shading of the solar field is a common phenomenon that can affect the performance of such a system. Studies show that critical shading can prevent solar fields from reaching their design potential, which would not always have been the case if the shading had been analysed in the design stage.

Assessing the impact of shading on the proposed LFR solar field was performed for the two main seasons in a year, summer (July) and winter (December), considering a north-south and east-west orientation.

Figures 6.3 and 6.4 depict the impact of shading analysed in December, considering two north-south and east-west orientations configurations, respectively.

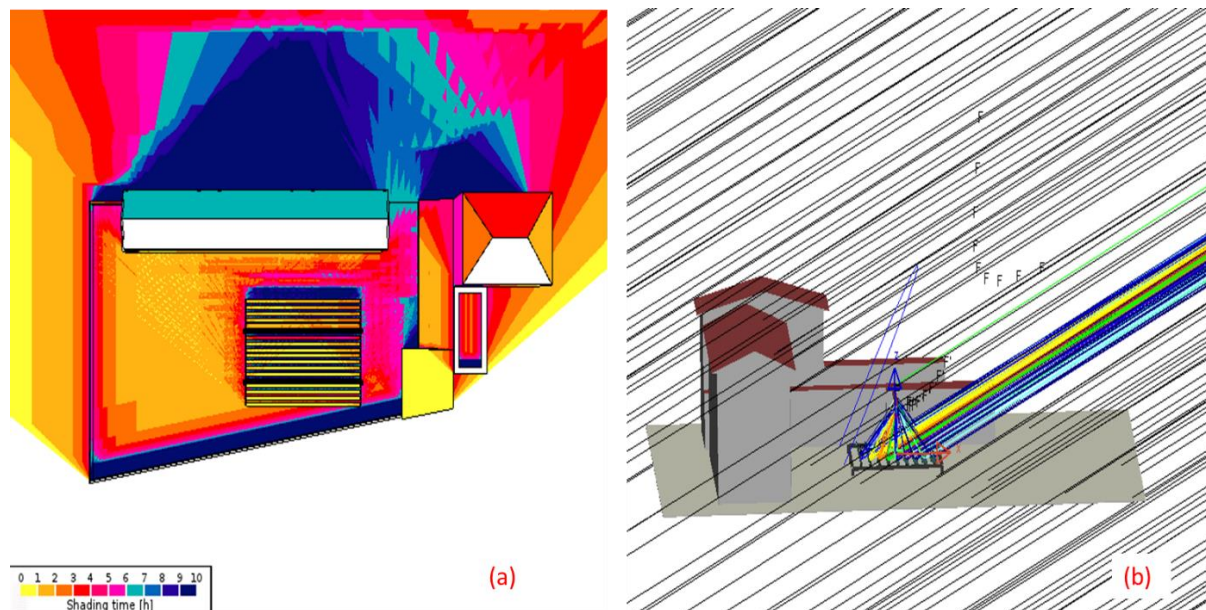


**Figure 6.3:** Pseudo-colour shading analysis (a) and Raytracing (b) in winter (December) season for east-west solar field orientation

While 6.3a and 6.4a show the pseudo-colour chart of shading impact across the solar field and surrounding, 6.3b and 6.4b depict solar irradiance harnessed by the mirrors and concentrated on the receiver tube.

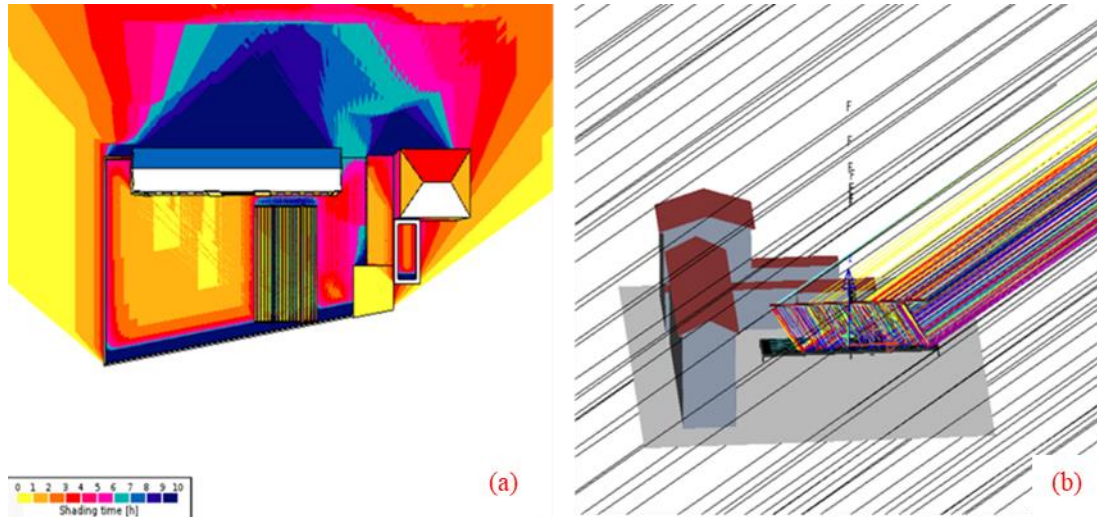


**Figure 6.4:** Pseudo-colour shading analysis (a) and Raytracing (b) in winter (December) season for north-south solar field orientation

The charts exhibit almost similar characteristics for both orientations. It can be deduced from the shading hour (h) indicator that overall, the shading impact of the surrounding on the solar field is marginal. The charts are further clarified in Figure 6.5 with the irradiance graph using MCRT in LightTools. This is achieved by modelling the solar field and its surrounding (including all possible obstructions). The east-west orientation harnesses more power but produces 5% less power (on average) due to the shading observed between 6:00 am to 8:00 am compared to the conventional solar field considered without abstraction.

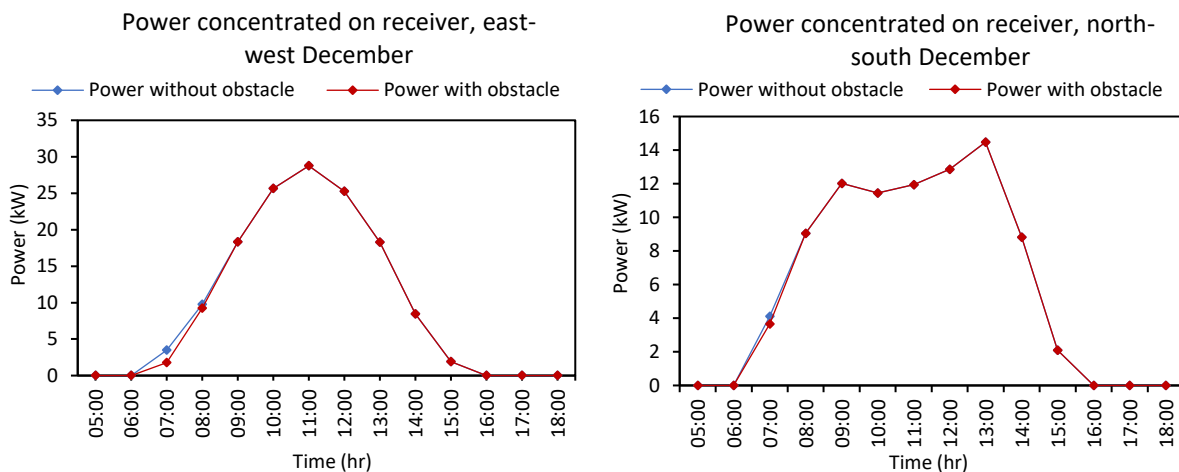


**Figure 6.5:** Power produced by solar field in December - east-west orientation (Left) and north-south orientation (Right)

Conversely, the north-south configuration suffers a negligible loss of 2% because of shading (Figure 6.5b) as compared to power recorded without obstruction from the surrounding. The variance is largely due to the angle intended by the sun and the position and orientation of the

solar fields. The east-west orientation tends to be closer to the buildings, which is in between the sun path and the solar field, hence suffering from the shadowing effect between 6:00 am to 8:00 am. However, in terms of the total power harnessed, the north-south configuration produces 30% less power than the former.

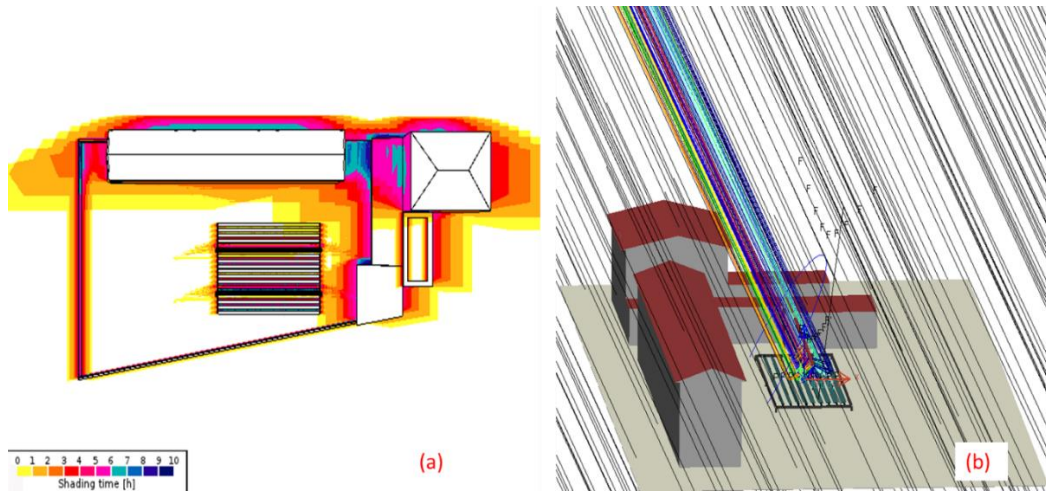


**Figure 6.6:** Pseudo-colour shading analysis (a) and Raytracing (b) in summer (July) season for east-west solar field orientation

Deploying a similar approach, the impact of shading on the solar field during the summer season (July) was investigated. The investigation shows that the shadow pattern varies across the year. During the winter months, the sun rises from a lower position compared to other seasons. While the impact of shading largely depends on the solar field layout, when combined with variation in sun path, it can have a significant impact on the performance of a solar field. This can be observed by comparing either Figures 6.3b and 6.6b or 6.4b and 6.7b, respectively. From these figures, it can be noticed that the sun path greatly varies. It rises at a higher elevation in summer and at a lower position in winter.

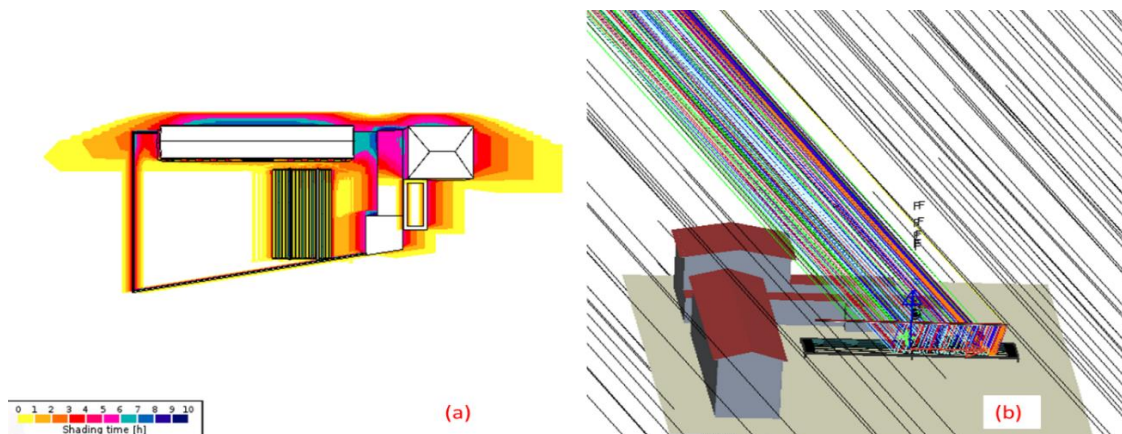


**Figure 6.7:** Pseudo-colour shading analysis (a) and Raytracing (b) in summer (July) season for north-south solar field orientation

Furthermore, despite the sun rising from a higher elevation in summer, the impact of shading on the solar field is observed to be higher compared to the winter season. This setback is largely attributed to the height and position of the building surrounding the solar field for both north-south and east-west orientation. Figures 6.6b & 6.7b show the portion of the solar fields that suffer shading effect from the surrounding buildings.

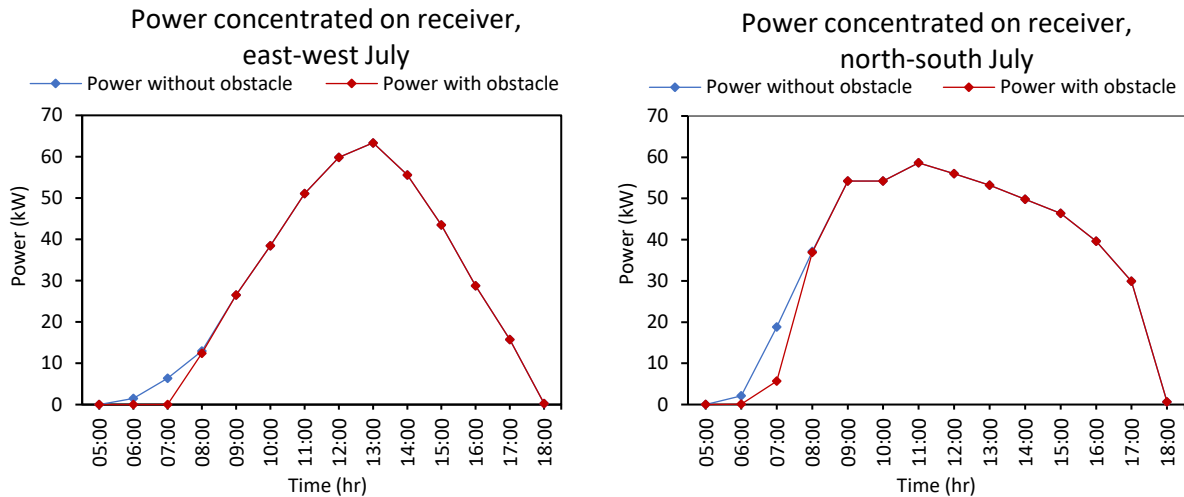


**Figure 6.8:** Power produced by solar field in July, east-west orientation (Left) and north-south orientation (Right)

Comparing the total power harnessed through ray tracing using the daily average monthly data of July in summer and December in winter seasons, it can be seen in Figures 6.5 and 6.8 that the shading effect tends to be slightly higher in the former, 6% (east-west) and 9% (north-south). In addition, it is important to note that due to the sun angle and building the layouts with regards to the solar field orientations, the impact of shading tends to be higher in the north-south orientation in July compared to the east-west in December.

#### 6.4. Conclusions

Shading analysis is a fundamental step in the phase of design, installation and operation of a solar field. Shading of any form can have a negative influence on the performance of an entire solar field. Therefore, it is imperative to minimise any hard shading resulting from objects such as buildings, trees, and objects by taking all the angles into consideration and ensuring that any form of shading should only occur during the start and end of the day as in the case in the present study.

In the present study, despite the shading effects being negligible and occurring during the morning, it is imperative to conduct shading analysis to determine its impact on LFR solar

fields. Such estimations are significant, especially when designing collectors for places where the available land strip does not align with a particular orientation, as in the case of the north-south configuration. Where the impact is detrimental to the performance of the solar field, measures had to be taken to resolve such. These might include considering the various orientations, installation on roof-tops, removing the obstruction or increasing the mirror field. The primary aim is to maximize energy collection and minimize the cost of electricity.



## Chapter 7 : General Discussion

In the last few decades, the world energy demand has increased by more than 40%, which has led to profound economic challenges and environmental concerns [17]. The main motives behind the transition to sustainable and environmentally energy technologies are the lessening of the conventional fossil fuel resources and the adverse effect of CO<sub>2</sub> emission on the global environment.

Concentrated solar power will undoubtedly play a vital role in the near future as a means of providing sustainable and environmentally friendly energy to meet both thermal and electrical needs. Concentrated solar power systems are among the most cost-effective clean and sustainable energy generation technologies. They can contribute significantly towards international commitments to greenhouse gas emission reduction and climate change mitigation.

Solar energy is the most readily available renewable energy source in both direct and indirect forms. The harnessed energy is mostly deployed in solar power plants for both thermal and electrical energy generation. In order to achieve this, solar power plants use concentrating technologies. Presently, four possible concentrated solar power technologies vary according to configuration, ranging from linear Fresnel reflectors, Parabolic through collectors, Parabolic Dish/Engine, and the central receiver systems.

Most concentrating solar fields consist of the primary mirrors (reflectors) and a receiver placed at a certain height above the mirror plane. The concentration largely depends on the mirror apertures and receiver area [45]. Impinging solar radiation intercepted by the primary mirrors is concentrated on the receiver tube. Depending on the technology employed, either line or point focus, heat transfer fluid in the receiver is heated to high temperatures to either directly run a thermodynamic power cycle or generate another working fluid at high temperature through a heat exchanger to run the cycle to produce electrical power [45].

Parallel rows of mirrors (reflectors) curved in one dimension intercept the solar radiation in parabolic trough systems. The mirror arrays can be over 100 metres long, with a curved surface that is 5 to 6 metres wide. Heat collectors are stainless steel pipes (absorber tubes) with a selective coating. The coating is designed to allow pipes to absorb solar energy while emitting relatively little infrared energy. An evacuated glass envelope insulates the pipes. As the sun moves across the sky, the reflectors and absorber tubes move with it [7].

Most commercial parabolic trough plants deploy synthetic oil as the heat transfer fluid, which transports heat from collector pipes to heat exchangers, where water is preheated, evaporated, and then superheated. The superheated steam powers a turbine, which in turn powers a generator that produces electricity. The water returns to the heat exchangers after being cooled and condensed.

Being the most established of the CSP technologies, parabolic troughs make up the majority of present commercial facilities. However, most existing facilities lack thermal storage and rely on combustible fuel as a backup to maintain consistent capacity [268]. In Spain, for example, all CSP plants rely on natural gas to generate 12 % to 15% of their annual electricity. Some of the newer facilities have large thermal storage capacities.

Parabolic dishes concentrate the sun's rays at a focal point propped above the centre of the dish. The entire apparatus tracks the sun, with the dish and receiver moving in tandem. The sun's rays are focused on a focal point propped above the dish's centre in parabolic dishes. Most dishes have an independent engine/generator (such as a Stirling machine or a micro-turbine) at the focal point. This design eliminates the need for an external heat transfer fluid [11].

The highest solar-to-electric conversion efficiency of any CSP system is achieved by parabolic dishes [31]. Parabolic dishes compete with PV modules, especially concentrating photovoltaics (CPV), as well as other CSP technologies, due to a number of factors, including their small size, lack of cooling water and hybridization. The exception is very large dishes that have been proven to be compliant with thermal storage and fuel backup. Dishes, according to proponents, would be able to cope with larger solar thermal systems due to mass production [11, 268].

Solar towers, also known as central receiver systems (CRS), focus the sun's rays on a central receiver at the top of a fixed tower using hundreds or thousands of relatively small reflectors (called heliostats). DSG is used in the receiver in some industrial tower plants, while molten salts are used as both the heat transfer fluid and the storage medium in others. Central receivers can typically achieve concentration ratios of 300 –1500 and are highly efficient in collecting energy and converting it to electricity [9].

CRS are quite large (generally more than 10 MW) and thus gain from economies of scale, and they can easily store thermal energy [9]. The extremely high temperatures enhance the efficiency with which heat is converted into energy and lower the cost of thermal storage. Furthermore, the model is highly adaptable, with designers having access to a broad range of



heliostats, receivers, transfer fluids, and power blocks. Several towers feed one power block in some plants.

Linear Fresnel Reflector (LFR) solar field create a linear focus on the downward-facing stationary receiver installed on a series of small towers. Parallel rows of flat or slightly curved mirrors rotate independently on a single axis to reflect the solar radiation onto to fixed receiver mounted at a certain height above the mirror apertures [288]. From a thermal systems point of view, the stationary receiver avoids the requirement for rotary joints for the heat transfer fluid and can aid in minimising losses due to convection from a thermal receiver because it has a permanently down-facing cavity [4].

The promoters of the LFR systems claim that the technology offers simplicity in plant design with near-flat mirrors and fewer supporting structures, which is closer to the ground, compensating for the lower overall optical and thermal efficiency. To enhance optical efficiency and ground use efficiency, compact Linear Fresnel Reflectors employ multiple receivers for each mirror so that adjacent mirror elements have different inclinations in order to focus on different receivers. This allows a higher packing density of mirrors which improves optical efficiency and minimize land use. In addition, blocking and shading resulting from nearest neighbour mirrors are greatly reduced.

The solar field design is a curial factor in concentrating solar technologies. Depending on the concentrating type employed, the solar field can either be oriented in a north-south or east-west direction for tracking the sun, in a single or dual-axis tracking mechanism with single or multiple receiver configurations. In addition, the type of coupling technology deployed (direct steam generation or heat exchanger) can play a significant role in the kind of power cycle (steam turbine, organic Rankine cycle, Brayton or Stirling engines) to be considered for the plant.

Linear Fresnel Reflectors and parabolic trough collectors are line focussing concentrators. Both systems' primary mirror (reflector) design can use either parabolic or cylindrical (circular) type. Parabolic mirrors are more efficient at the expense of design complexity, while cylindrical mirrors are cheap and easily manufactured, however less efficient. Their solar field configurations can either be in a north-south or east-west direction. The north-south orientation is commonly deployed in industry, as it results in a higher annual energy collection. Whereas for horizontal fields, east-west field orientation leads to a more uniform energy production throughout the year.

Parabolic dish and the central receiver systems are point focussing concentrators. The central receiver solar configuration constitutes a cylindrical central receiver tower, with an exterior heat-transfer surface completely surrounded by heliostats (reflectors). Alternatively, the heliostats are stationed north of the receiver tower (in the northern hemisphere), and the receiver constitutes an enclosed heat transfer surface. As for the parabolic dish collectors, both the receiver and the dish follow the sun in both azimuth and elevation.

Recent Advances in solar field design, modelling and optimization have led to adopting the best optical properties (reflectivity of 95%, wide wavelength reflectance), resulting in high optical performances. Such achievements are realized at the expense of an increased cost. The weight of the primary mirrors and the surface they offer to the wind load require heavy frame and steel structures for their support in addition to the concrete foundations to bear the whole system. Thus, the solar field represents roughly 50% of the investment cost of a CSP plant. Several attempts have been made to avoid this extensive use of metallic supports like concrete structures but without extensive industrial achievements.

Nowadays, innovative reflective surfaces deposited on all kinds of light rigid or flexible supports have been proposed. Those modern reflective materials have already their own commercial markets at cost-reflective prices for application in CSP solar field. These have led to further innovative concentrating systems, as in the case of Linear Fresnel Reflectors, which offer lower initial cost, compact plant size, and simplicity in plant design, running, and maintenance.

As opposed to the parabolic dish and central tower, in which a complex dual-axis tracking mechanism is integrated, Linear Fresnel and trough mirrors can share the same drive system, as all mirrors rotate around their separate axis at the same time speed [23]. Such a single-axis tracking system is more cost-effective and simpler, eliminating the complexity, maintenance, and cost associated with the parabolic dish collectors and central receiver tower systems. Currently, there is a mean line between two approaches proposed, increasing the size of concentrating units to minimize the number of tracking components or deploying compact concentrating units configured on common racks shared sub-systems.

Regarding the receiver configuration, Linear Fresnel Reflectors provide more designed options than the other concentrating systems. LFR receivers can be single tube or multitube (evacuated or non-evacuated – vertical, horizontal, or triangular) and with or without a secondary reflector [45]. However, Linear Fresnel is faced with the challenge of drifts and variation of ray

concentration due to their fixed receiver assembly resulting in lower optical efficiency. On the other hand, trough collectors constitute a single receiver that tracks the sun collectively with the reflector, leading to minimised variation in ray concentration and improved optical efficiency.

Moreover, both LFR and PTC receivers usually have a selective coating to improve the absorbance of impinging solar radiation and the lowest infrared emitted flux. This selective property deposited on the receiver's surface minimizes thermal losses and consequently enhances the overall thermal efficiency of the solar field [5, 289]. To improve this effect, the receiver tube is usually surrounded by a glass tube that is completely evacuated to block the losses due to convection. Currently, the costs of such receiver design are high both from economic and environmental points of view. Hence, further research is needed on how the cost of such a process can be reduced with lower environmental impact and increased lifetime.

External receivers and cavity receivers are the two types of receiver geometries that can be used for central receiver systems and parabolic dish collectors. Only cavity receivers have been used in dish/Stirling systems. External receivers, on the other hand, have been used in lower-temperature parabolic dish applications. At high operating temperatures, heat losses at unprotected external receivers are very high, especially radiative heat losses. However, in a cavity receiver, a large portion of the released radiation stays within the cavity and is absorbed again, resulting in a lower overall radiative heat loss.

At the high-temperature range between 600 to 1000 °C, the central tower and dish engine will require receivers that constitute high-temperature materials capable of withstanding thermal constraints as well as oxidative environments [289]. It is projected that the materials for such receivers in the near future will emerge cost-effective and provide excellent properties that can reduce thermal losses and enhance overall system efficiency. Consequently, for such systems, there is a need to focus on selective properties for receiver surfaces and glazing, taking into account the shock and compatibility with high-temperature heat transfer fluid (HTF).

The multi-functional HTF needs to gather, transport, and exchange heat gained from solar radiation and is, therefore, an essential part of a CSP system. Given the functionality, the performance of an HTF is determined by a wide range of constraints, both practical and fundamental. HTFs are required to exhibit key features such as being environmentally friendly, stable, able to withstand the effect of ambient temperatures (solidification) and available at low

cost without conflict of use. Because of their stability over a relatively large temperature range, synthetic and mineral oils are the HTF choice for most solar thermal plants.

On the other hand, molten salts promise higher efficiencies as operating temperatures have attracted much interest. At higher temperature ranges (up to 600°C), molten salts have proved to be very efficient HTF. However, these efficiency gains are combined with the challenges of melting the salts and higher pumping costs [37]. In addition, major challenges associated with the application of molten salt is mainly crystallization temperatures which are significantly above the ambient temperature leading to possible freezing and clogging. Significant advancements are being recorded today to reduce the freezing point of this HTF [289]. Also, several new approaches are being investigated to address deficient oils and molten salts using ionic fluids, fluids containing nanoparticles and liquid metals.

Overall, in the context of low to medium temperature ranges, the best available fluid would remain water/steam, taking into consideration cost and environmental criteria, among others. Moreover, to drive the penetration of the Direct Steam Generation (DSG), there is a need to invest more in R&D to improve on current receiver tube designs. The first industrial Linear-Fresnel plant PE1, and the first industrial solar central tower plant PS10 are based on DSG. The former has a secondary reflector housing the receiver tube, thereby minimizing drift in ray concentration and enhancing the concentration ratio. In addition, the glazing on the lower side reduces losses due to intra-red.

The most widely used fluid for Parabolic Trough Collector solar fields with a temperature of around 400°C degrees is Solar Oil. This synthetic oil, biphenyl oxide, is rather expensive (about 6 euros/L), highly flammable and not environmentally friendly. The fluid is also subjected to industrial monopoly and strictly limited temperatures below 400°C. According to the Life Cycle Analysis carried out for the parabolic trough CSP plant, the manufacturing, operation, and disposal of the Solar Oil accounts for 21.4%, 22% and 24% GHG content of the whole process [289]. Parabolic dish systems, requiring very high temperatures between 600 and 1000 °C use air (He, CO<sub>2</sub> or H<sub>2</sub>) as the working fluid.

A range of various solar to electric energy conversion systems deployed to the different concentrator types have been discussed. A large fraction of the world's electricity is produced with steam turbines, mostly with steam generated from conventional fossil fuel or nuclear heat resources. One of the benefits of CSP is the simplicity with which a new source of heat can be applied to the dominant power production technology. Consequently, the vast majority of CSP

systems currently in operation use steam turbines. All the concentrator types have been applied to steam generation for deployment in steam turbine energy.

The most efficient state-of-the-art steam turbines operate at steam inlet temperatures of up to 700 °C [4]. However, suppose a thermal oil heat transfer fluid is used. In that case, trough and linear Fresnel concentrators are restricted to about 400 °C, and up to 500 °C if an alternative heat transfer fluid such as direct steam generation (DSG) is used [4]. The temperature needed for the maximum possible steam turbine inlet temperatures and pressures can be achieved by tower and dish systems; the constraint in this case is the survival of materials in the turbine or solar receiver. Rankine cycle is mostly preferred because of its higher conversion efficiency for higher steam temperature and pressure at the turbine inlet (common with all heat engine cycles).

Stirling engines have long been deployed in dish concentrators. Despite the fact that dishes have been applied to direct steam generation, photovoltaics, and other systems, many in the CSP sector refer to dish systems in general as 'Dish-Stirling'. Stirling engines have not yet been seriously applied to collector types. With a total solar AC to electric efficiency of around 30% at design point DNI, Dish-Stirling systems continue to hold the record for the highest solar to the electric conversion efficiency of any technology. The Stirling system is much smaller in comparison to the Rankine cycle, but thermal storage in the Dish-Stirling configuration is yet to be established.

An organic Rankine cycle turbine (ORC) is fundamentally similar to a steam Rankine cycle; however, it employs a lower boiling point organic fluid, which makes it compatible and suitable for low-temperature applications [15]. For smaller systems, ORC systems may achieve higher efficiencies than steam turbines (in the range of a few kWe). However, compared to water/steam systems, capital and operational maintenance (O&M) costs are higher per built MWe. Because of its better fit for low-temperature sources, ORC technology is being aggressively sought for geothermal power applications [15, 226]. A few small Linear Fresnel CSP systems have been fitted with ORC systems.

The choice of a suitable working fluid is essential to the performance of the Organic Rankine Cycle. Depending on the application, the source and the amount of heat to be deployed, the fluid must demonstrate excellent thermodynamic and physical properties at the lowest possible temperatures and pressures and also conform to some criteria, such as being economical, nontoxic, non-flammable, environmentally friendly and tolerating a high use of the available

energy from the heat source. This limits the list to just a few fluids if all aspects that can restrict their use are considered.

The Organic Rankine Cycle investigated in this study comprises a micro axial turbine. R365fmc, and the new environmentally friendly Novec649 Organic working fluids were selected. The parametric evaluation of the turbine considered the effect of the range of inlet variables such as temperature, pressure and rotational speed on the work output and isentropic efficiency and the influence of rotor tip clearance (rotor gap) on the turbine power was investigated.

Findings from the study show a good correlation between the theoretical and experimental studies. It was observed that the turbine performance is very sensitive to inlet temperature and pressure. The higher the inlet temperature, the better the performance of the turbine. Furthermore, it was noticed that the performance of an organic fluid could be greatly influenced by key thermophysical properties such as molecular mass, critical pressure, density, viscosity and thermal conductivity. Next to that, an increase in the rotor tip clearance (rotor gap) decreases turbine power output.

Although most of the present solar thermal power plants are parabolic troughs, Linear Fresnel reflectors have emerged as an option that can serve both thermal and electrical needs. LFR compact plant size implies that they require up to 3 times less space for the same generated energy compared to PTCs, in addition to the operation and maintenance benefits. Furthermore, LFR is cheaper to produce, thanks to the very narrow reflectors and nearly flat, with a very small curvature. Easy maintenance and reduced water usage are added advantages.

Linear Fresnel Reflectors, however, are regarded as a low-efficiency technology, which is mainly due to very little previous research in this field. Unlike trough collectors, LFRs have fixed receivers; hence when the sun is out of the reference position, mirrors struggle to track the sun while concentrating solar flux on the focal line on the receiver. This results in variation and drift in ray concentration, which significantly impacts the optical efficiency and concentration factor of the primary mirrors and the performance of the receiver tube.

It has been found in the course of this study that the optimization of key parameters of a solar field can have a great influence on optical performance. The modelling, optimization and Monte Carlo Raytracing was conducted to investigate the thermal and optical performance of the Linear Fresnel Reflector solar field. The optimization variables considered were the mirror curvature, height, width and distance between consecutive mirror centre lines. Finding from

the investigation showed an improved performance from the optimized solar field compared to experimental data.

Therefore, the quest to cost reduction in the CSP is open to other technologies other than the parabolic trough collectors. Both Linear Fresnel collectors and central towers deploy fixed receivers, which entails no limit in the pressures of the heat transfer fluid (HTF) and a more efficient system to drain molten salts. Thus, the Levelized Cost of Electricity (LCOE) is estimated to be lower for LFCs, as reported in some studies. Parabolic dish systems are modular and have the highest concentration factor but face competition from cheap photovoltaic systems due to lack of storage systems.

CSP is becoming more commercially viable, and global installed capacity is projected to increase in the near future. By 2030, CSP is anticipated to account for 3.8% of global electricity output. By 2040, global installed CSP capacity would have increased to 715 GW, with a capacity factor of 45% (3900 hours per year), generating 2790 TWh annually. As costs and performance improve, CSP will account for about 11% of global electricity output by 2050 [11, 27].

Spain and the United States are the world leaders in CSP plants, with power generation capacities of 2,300 MW (48%) and 1,738 MW (36%), respectively [8]. Because of the abundance of sunlight in the Middle East and North Africa, prices would be lower, offsetting the additional transmission costs and electricity losses anticipated. Other countries and regions interested in CSP, including those that currently lack sufficient coverage, such as China, India, Turkey, Latin America, are expected to commence demonstrational and pilot plants [11, 27, 30].

The main concern for developers of the technology as well as research and development practitioners within this field is the cost of CSP energy. Despite the exclusion of fuel cost, the cost of CSP energy is overshadowed by the payback of the high initial investment cost over the lifetime of the project. A regime of accelerated growth in installed capacity, in addition to a rapid decay in the cost of energy generated, is confidentially anticipated by the industry.

The trend of reduction in the cost of installed capacity to the increase is reasonably linked to the technical improvements, as experiences are gained from plants installed, and parallel R&D efforts identify performance improvements, scaling to larger installed plant size, which provides far more efficient and cost-effective large turbines and other components deployed,



and volume production that facilitates fixed costs of investments in production efficiency to spread across large production runs.

## Chapter 8 : Conclusions and Recommendations for Future Work

### 8.1. Conclusions

In this research, the theoretical and experimental studies were performed to improve the design of the solar field and organic Rankine cycle turbine in a small Linear Fresnel Reflector solar thermal power plant. In the preliminary section, the thesis introduction was dovetailed by a review of concentrating solar thermal power plants. The review focussed on the state-of-the-art in the various concentrating thermal solar power plant technologies based on a variety of thermal prime movers: taking into consideration key areas such as the designs, components, configurations, modelling and experiments performed. The prospects of concentrating solar technologies in the context of utility-scale power plants, their performance, technical challenges were put forward. The subsequent section discussed the application and future developments of the concentrating solar power technologies. Next to that, a critical evaluation and discussion on the facts and information obtained from various resources were put forward.

Subsequently, the numerical approach and the results of a study carried out on the optical and thermal performance of a solar field based on linear Fresnel reflectors are presented in Chapter 3. In an attempt to minimize the drifts and variations in ray concentration and maximize the amount of direct radiation received, the modelling and optimization of the LFR solar field were carried out. In addition, the primary mirrors were aligned in a north-south direction for east-west tracking and in an east-west direction for north-south tracking, with each panel configured to rotate about its axis individually.

Through a Monte Carlo ray-tracing technique, the optical performance of optimised mirrors was compared with that of flat mirrors and uniform curvature mirrors deploying an average daily irradiance data for selected months. Thus, the power harnessed by the receiver and the energy efficiency of separate mirror elements were analysed. A steady-state analysis of thermal performance was performed, taking into account the receiver tube's main features and optimum operating condition for various concentrated heat fluxes (in  $\text{W/m}^2$ ) by deploying the results from MCRT in ANSYS Fluent (R2020) CFD solver. From this model, the fluid outlet temperatures and thermal efficiencies are computed for a range of values of the definition variables such as the inlet temperature, fluid speed, and thermal flux concentrated on the absorber.

In Chapter 4, the solar radiation concentration of two LFR solar field configurations, central LFR and Compact LFR, was performed. By adopting a similar approach presented in Chapter

3, the modelling and optimisation of the solar field are conducted to minimise ray concentration variation and improve concentration factors. In addition, a detailed Monte Carlo Raytracing Technique is deployed for the comparative study between central linear Fresnel reflectors and compact linear Fresnel reflectors configurations. In that sense, two variables were defined, the energy efficiency and total energy harnessed by the solar fields. The simulation performed is to present a detailed analysis of how design parameters influence the performance of the two LFR configurations.

Furthermore, the CFD modelling and parametric evaluation of an axial ORC turbine for the range of parameters, notably, inlet turbine temperature and pressure, rotational speed for different test points, were performed and analysed in Chapter 5. The effects of the defined parameters on the turbine power, isentropic efficiency and work output are put forward. In addition, the impact of varying the rotor tip clearance (rotor gap) on the turbine power output is examined. The investigation was carried out deploying two organic fluids, mainly, Novec649 and R365fmfc. A comparative analysis of the thermo-physical properties and behaviours of these working fluids is performed between results obtained from numerical approach and experimental data.

In Chapter 6, shading analysis of the solar field and environs is performed using different approaches proposed. In this context, shading resulting mainly from structures such as buildings and vegetation is considered. The analysis considers sun and shadow effects that can be easily and dynamically improved or even animated within the program to evaluate the timing and effect of obstructions and the resulting consequence on the optical performance of the solar field. A general discussion was presented in Chapter 7.

Presently there are high expectations on CSP technologies to play a major role in the utility-scale power supply market. Despite the commercial success and advancements attained by the other three (3) CSP technologies. The quest to cost reduction the CSP is open to linear Fresnel reflectors. Current State of the Art linear Fresnel technology is being targeted at high-temperature power cycles alternative to the other CSP technologies. Fresnel reflectors are a modified form of a parabolic trough; hence, the mirror's curvature being so small and relatively narrow aperture results in compact plant size and easier manufacturing, in addition to the lower prices compared to parabolic.

On the other hand, Linear Fresnel reflectors are regarded as a low-efficiency technology, which is mainly due to very little previous research in this field. Unlike rough collectors, LFRs have

fixed receivers; hence when the sun is out of the reference position, mirrors struggle to track the sun while concentrating solar flux on the focal line on the receiver. This results in variation and drift in ray concentration, which significantly impacts the optical efficiency and concentration factor of the primary mirrors and the performance of the receiver tube.

However, findings from the present study show that the optimization of key mirror elements such as curvature, width, length, receiver height from the mirror plane, and the distance between two consecutive mirror centrelines can significantly impact the LFR solar field optical performance. The optimization of these key elements results in an improved concentration which can enhance the energy conversion efficiency of LFR plants and greatly minimize the cost of thermal storage, which results in low Levelized cost of electricity (LCOE) and offers LFR with the economic potential to compete with other CSP power plants.

The raytracing conducted deploying an average daily solar radiation showed a close correlation between the optimised and the Innova MicroSolar Project solar field with slightly higher performance observed from the optimised solar field. It was found that the total energy harnessed by the optimised mirrors over an average daily ray tracing was approximately 505 kWh compared to the 490 kWh from the Innova solar field configuration. Furthermore, from annual energy harnessed point of view, it was observed that the optimised mirrors produced 3,646 kWh in comparison to 3,590 kWh from the Innova MicroSolar Project solar field configuration. Overall, it can be concluded that improved performance was realized from the optimised solar field.

The study conducted to compare the performance of the separate mirror profiles, flat, uniform and optimised mirror curvatures revealed that the best results were obtained from the optimised mirrors. Findings from the study showed the following production of energy: 212 kWh from the flat mirrors, 392 kWh from the uniform curvature mirrors and 505 kWh from the optimised mirrors. The flat and uniform mirror curvatures are mostly deployed in the solar field for their simplicity in production and to minimise cost, however, at the expense of reduced optical efficiency. In addition, this could also result in the possible addition of mirror arrays and increased plant size. Conversely, optimised mirrors can enhance the solar field optical efficiency and compact plant size.

Assuming the mirrors are aligned in a north-south orientation to track the sun in an east-west direction and applying a clear day model throughout the year, it was observed that this solar field configuration produces more energy of approximately 2,947 kWh from March to October

compared to an east-west solar field orientation, which produces approximately 2,421 kWh. However, tracing conducted from January to March and October to December shows that the east-west orientation produces more energy of about 987 kWh compared to 699 kWh by the north-south orientation. These findings show that the performance of solar field is influenced by key factors such as mirror profile, optical errors (shading, blocking etc.), end losses, the inclination of the receiver and the solar field orientation. Overall, the present design demonstrates that the north-south orientation offers the biggest payoff and leads to a more uniform annual energy production of around 6,719 kWh than the east-west orientation, which produces 6,130 kWh. Given the physical condition and improvement realised through the optimization of the solar field, the north-south orientation was implemented.

As for the end losses, it was found that as the distance from the mirrors to the receiver increases, the dispersion of the rays caused by the effective sun-shape and path (optical and sun-shape errors) also increases. The effect is significant from October to February, especially considering the north-south orientation due to the angle and the transverse direction of the sun as seen by the mirrors and east-west orientation from March to October. However, depending on the orientation (north-west or east-south), these losses might be experienced all year round, especially during the morning and evening hours.

The comparative analysis between the LFR configuration shows overall better performance from the central LFR configuration considering the energy efficiency and annual energy harnessed. From the energy efficiency point of view, the central LFR configuration was 89% and 68% efficient compared to 82% and 60% of the compact LFR in the months of May and December, respectively. Next to that, the computed energy efficiency for separate mirror elements indicates that in both configurations, mirrors that appear in front of the receiver relative to the sun's position tend to be closer to the receiver, focussing solar radiation with less shadowing/blocking effect and attaining higher efficiency compared to the farthest mirrors.

Furthermore, the computed annual energy shows that the Central configuration produce approximately 230 kWh more energy than the compact LFR configuration. However, energy harnessed from November to February, nonetheless, is very close between the two configurations. Subsequently, analysis shows that the compact linear Fresnel reflectors minimize blocking and shading losses compared to a central configuration, which indicates that distances between consecutive mirror centre lines can be minimized to optimise space. However, this is not enough to overcome other challenges, such as the greater dispersion of the

rays reaching the receiver, caused by the fact that mirrors must be located farther from the receiver, which yields lower efficiencies.

It has also been found that both LFR configurations are subject to losses such as the end and lateral losses, which has a significant impact on the optical performance of the compact LFR configuration compared to that of the central LFR. Depending on the orientation (north-west of east-south), however, these losses might be experienced all year round. In the case of the north-south orientation, the losses were higher in December. Increasing the length of the mirror aperture to minimize the end losses has been suggested. However, this might result in much more consumption of materials and costs.

Organic Rankine Cycle (ORC) systems are enabling technology that can play a significant role in solar to electric power generation to their ability to convert low-temperature heat sources into useful energy and potential integration in future distributed generation systems. Small-scale ORC systems based on axial or radial-outflow turbines are an attractive choice for various electricity generation applications, mainly domestic and rural situations, under-served and unserved locations with a high degree of poverty and a lack of opportunities for socio-economic development.

The study on the parametric evaluation of an axial ORC turbine demonstrates that the inlet turbine temperature and pressure have the greatest effect on the power, work output and isentropic efficiency. Increasing the turbine inlet temperature and pressure result in increased isentropic efficiency and power output. However, material limitations most times lead to challenges when using high temperatures. High temperature also results in stress on the rotor blades and rotational speed. Nowadays, there are emerging technologies that deploy artificial cooling techniques to keep the blades cooler and permit the use of high temperatures. There are also studies to identify and develop newer materials that can withstand higher temperatures and stress.

The selection of a suitable working fluid and its application in ORC turbine is a very crucial aspect mainly due to the dependence of its categorization on the temperature of the heat source, defined by the fluid thermodynamic and/or thermophysical such as temperature and critical pressure, chemical stability and security. Considering the thermodynamic design point for each working fluid used in this study, both Novec649 and R365mfc are promising working fluids that can be deployed in Organic Rankine Cycle.

However, finding from this study shows that the R365mfc produced more turbine power for the various inlet temperature and pressure levels (Test1-1.7 kW, Test2-1.56 kW, Test3-1.59 kW, Test4-1.6 kW, Test5-1.58 kW) than the Novec649 (Test1-1.6 kW, Test2-1.4 kW, Test3-1.5 kW, Test4-1.5 kW, Test5-1.4 kW). With such properties as lower viscosity, a higher and more stable specific heat, a higher thermal conductivity, experiences lesser temperature drops, and the turbulent flow regime will be attained at reduced fluid velocities with R365mfc than Novec649, thus producing higher turbine power.

Moreover, thermodynamical performances are not the only parameter for fluid selection. In addition to its higher power output, the R365mfc exhibits excellent properties in terms of safety and environmental impact. Both fluids (Novec 649 and R365mfc) are non-flammable and ecologically friendly, with an ozone depletion potential of 0. However, compared to Novec649, which has a global warming potential of 1, R365mfc has a global warming potential of 782. Next to that, Novec649 allows for a lower pressure, which reduces design limitations and simplifies manufacturing.

The study performed on the impact of varying rotor tip clearance revealed that increasing turbine tip clearance reduces ORC turbine performance (power) and, as a result, will require increased inlet temperature and pressure. The recorded power at 50  $\mu\text{m}$  gap was 1.7 kW. However, when the gap was increased to 200 $\mu\text{m}$ , the turbine power declined to 1.6 kW. Although mechanically essential, this clearance could be a significant cause of loss in a turbine. The gap height can be a fraction of a millimetre, yet it can have a disproportionately large impact on the performance of the stage.

As a result, independently evaluating the sources of performance decline provides useful information that can aid in maintenance action. The turbine tip clearance loss is part of the overall blade loss because the fluid does not follow the expected path through the blades and does not contribute to the turbine power output and interacts with the outer wall boundary layer. The presence of moving blades in ORC turbine turbines need a limited annular tip clearance between the rotor blade tip and the shroud, and as a result, for this study, exceeding a 200  $\mu\text{m}$  tip clearance would critically deteriorate the turbine performance.

Shading analysis is a fundamental step in the phase of design, installation and operation of a solar field. Shading of any form can have a negative influence on the performance of an entire solar field. Therefore, it is imperative to minimise any hard shading resulting from objects such as buildings, trees and objects by taking all the angles into consideration and ensuring that any



form of shading should only occur during the start and end of the day as in the case in the present study.

In the present study, despite the shading effects being negligible and occurring during the morning times it is imperative to conduct shading analysis to determine its impact on LFR solar fields. Such estimations are significant, especially when designing collectors for places where the available land strip does not align with a particular orientation, as in the case of the north-south configuration. Where the impact is detrimental to the performance of the solar field, measures had to be taken to resolve such negative impacts. These might include considering the various orientations, installation on roof-tops, removing the obstruction or increasing the mirror field. The primary aim is to maximize energy collection and minimize the cost of electricity.

## **8.2. Recommendations for future work**

The present study forms the basis for future research, where the optical and thermal processes will be combined for a more accurate understanding of the process, taking into consideration the map of radiation flux. Moreover, having a better LFR solar field producing more concentrated radiation fluxes would have a positive effect on the overall energy output and efficiency of the plant.

Furthermore, prospects of linear Fresnel technology in the context of utility-scale power plants can be assured with the right technological advancement. Since the reflector accounts for nearly 50% of total plant construction cost, any enhancement in the technology would be a step forward. Presently there is a need for technological advancement in the manufacturing of reflectors to address concerns of reflectors degradation and modest returns in the efficiency of LFR plant. Maintenance-free, self-cleaned, lightweight and extended life span are the key areas for future development in reflectors to further cut down the LCOE of LFR technology.

As for the future perspective of LFR design, research in this subject will address some transient analysis of receivers, with emphasis on the effects generated by rapid deviations of the reflected radiation and by thermal energy storage, which presents a more reliable system for an integrated period. The deployment of the multi-tube receiver can significantly enhance the thermal efficiency of LFR, with fewer challenges on the pumping power requirement. They also have other benefits, such as operational flexibility and greater heat gains with fewer lateral tubes.

Future studies should work in this trend to progress properly in the learning curve for CSP, in order to get a substantial reduction in the cost of electricity. In this new quest, an alternative on the position of the receiver should be studied in depth for assessing the potential improvement in the optical connection between the mirror arrays and the receiver. Furthermore, the concept behind the design of a secondary reflector remains open. For a conventional central LFR solar field, a single receiver tube plays a very significant role in the harnessing of solar radiation, and the secondary reflector geometry also requires detailed study.

In a broad sense, the implementation of a CSP project will require the evaluation of the performance of the entire process by deploying various simulation approaches for several years. It has been shown that for such complex solar processes, it might take approximately seven years of study to ascertain the relevant results. Furthermore, it is imperative to conduct a local energy demand assessment of the various users (household, public buildings, and industries) in order to optimize the scale and the operation of the CSP plant. These data sets are often very difficult to access especially if patented by top companies.

The Organic Rankine cycle plays a dominating role in solar to electric power generation. However, very few research works can be found where the actual design and 3D analysis of turbines expander that can be employed in Organic Rankine Cycles (ORC) for power generation with a low-temperature heat source. Organic Rankine Cycle compatibility with low-temperature use makes the cycle's overall efficiency highly sensitive to inefficiencies in heat transfer, which relies largely on the fluid thermodynamic properties and its operating conditions.

Therefore, choosing the appropriate working fluid is very important for the ORC. Several research works have been carried out to find a suitable fluid for such systems and meet all safety standards and environmental criteria. The efficiency of the turbine has a great influence on the overall efficiency of the ORC because the turbine is considered a key component of the system. Hence, with a high turbine efficiency and power output, high cycle efficiency can be achieved.

Although significant progress has been made in recent years, most of the modelling methodologies and efficient systems can be predicted in high-temperature ranges, while low-grade thermal energy recovery should be considered in its infancy, according to the literature study. The design of efficient expanders, modelling and analysing heat transfer and system losses, and other areas still have a lot of research potential. The choice of the expander

selections, for instance, can be further improved by employing specially designed turbines to work with organic fluids in the organic Rankine cycle, and further research on new working fluids can have a great impact to increase the application of organic Rankine cycle in low-temperature applications.

From a broad perspective, several challenges faced by the CSP sector in recent years, including increasing cost, competition from solar PV, the expiry of CSP incentive programmes and a range of operational issues at existing facilities, have influenced its market growth. Hence, it is highly recommended that the relevant bodies and promoters of CSP technologies provide incentives for electricity production deploying solar thermal or hybrid solar power plants without any restrictions on the solar share. In addition, future research in R&D should primarily focus on improving the cost-effectiveness of the most cost-sensitive components, such as tracking systems, mirrors facets and receivers, as well as the implementation of new power supply and communication systems to bring down capital and operational costs.

## References

1. Beltagy, H., et al., *Sizing Analysis of Linear Fresnel Solar Thermal Power Plant in Algeria*. Energy Procedia, 2016. **93**: p. 19-24.
2. Kumar, V., R.L. Shrivastava, and S.P. Untawale, *Fresnel lens: A promising alternative of reflectors in concentrated solar power*. Renewable and Sustainable Energy Reviews, 2015. **44**: p. 376-390.
3. Abbas, R., et al., *High concentration linear Fresnel reflectors*. Energy Conversion and Management, 2013. **72**: p. 60-68.
4. Lovegrove, K. and W.S. Csiro, *Introduction to concentrating solar power (CSP) technology*, in *Concentrating Solar Power Technology*. 2012, Elsevier. p. 3-15.
5. Jebasingh, V.K. and G.M.J. Herbert, *A review of solar parabolic trough collector*. Renewable and Sustainable Energy Reviews, 2016. **54**: p. 1085-1091.
6. Gharbi, N.E., et al., *A comparative study between parabolic trough collector and linear Fresnel reflector technologies*. Energy Procedia, 2011. **6**: p. 565-572.
7. Fernández-García, A., et al., *Parabolic-trough solar collectors and their applications*. Renewable and Sustainable Energy Reviews, 2010. **14**(7): p. 1695-1721.
8. Foster, R., M. Ghassemi, and A. Cota, *Solar energy: renewable energy and the environment*. 2009: CRC press.
9. Chu, Y. and P. Meisen, *Review and comparison of different solar energy technologies*. Global Energy Network Institute (GENI), San Diego, CA, 2011.
10. Sawin, J., *Renewable energy policy network for the 21st century: Renewables 2012 Global Status Report*. REN21 Secretariat, 2011.
11. IEA, *Technology Roadmap - Concentrating Solar Power*. 2010, IEA: Paris.
12. Barbón, A., et al., *Theoretical elements for the design of a small scale Linear Fresnel Reflector: Frontal and lateral views*. Solar Energy, 2016. **132**: p. 188-202.
13. Zhu, G., et al., *History, current state, and future of linear Fresnel concentrating solar collectors*. Solar Energy, 2014. **103**: p. 639-652.
14. Boito, P. and R. Grena, *Optimization of the geometry of Fresnel linear collectors*. Solar Energy, 2016. **135**: p. 479-486.
15. Vélez, F., et al., *A technical, economical and market review of organic Rankine cycles for the conversion of low-grade heat for power generation*. Renewable and Sustainable Energy Reviews, 2012. **16**(6): p. 4175-4189.
16. Al Jubori, A.M., et al., *Modelling and parametric analysis of small-scale axial and radial-outflow turbines for Organic Rankine Cycle applications*. Applied Energy, 2017. **190**: p. 981-996.

17. Pu, W., et al., *Experimental study on Organic Rankine cycle for low grade thermal energy recovery*. Applied Thermal Engineering, 2016. **94**: p. 221-227.
18. Quaschnig, V., *Technical and economical system comparison of photovoltaic and concentrating solar thermal power systems depending on annual global irradiation*. Solar Energy, 2004. **77**(2): p. 171-178.
19. Vant-Hull, L. *Central tower concentrating solar power (CSP) systems*. 2012.
20. Günther, M., et al., *Parabolic trough technology*. Advanced CSP teaching materials, 2011: p. 1-106.
21. Zhu, G., *Development of an analytical optical method for linear Fresnel collectors*. Solar Energy, 2013. **94**: p. 240-252.
22. Sait, H.H., et al., *Fresnel-based modular solar fields for performance/cost optimization in solar thermal power plants: A comparison with parabolic trough collectors*. Applied Energy, 2015. **141**: p. 175-189.
23. Abbas, R. and J.M. Martínez-Val, *A comprehensive optical characterization of linear Fresnel collectors by means of an analytic study*. Applied Energy, 2017. **185**: p. 1136-1151.
24. Qiu, Y., et al., *Study on optical and thermal performance of a linear Fresnel solar reflector using molten salt as HTF with MCRT and FVM methods*. Applied Energy, 2015. **146**: p. 162-173.
25. Abbas, R., J. Muñoz, and J.M. Martínez-Val, *Steady-state thermal analysis of an innovative receiver for linear Fresnel reflectors*. Applied Energy, 2012. **92**: p. 503-515.
26. Yamamoto, T., et al., *Design and testing of the Organic Rankine Cycle*. Energy, 2001. **26**(3): p. 239-251.
27. IEA, *Global Energy Review 2021*. IEA, Paris, 2021.
28. Washom, B.J., *Vanguard I solar parabolic dish-Stirling engine module. Final report, May 28, 1982-September 30, 1984*. 1984, Advanco Corp., El Segundo, CA (USA).
29. Washom, B. *Parabolic dish Stirling module development and test results*. in *Proc., Intersoc. Energy Convers. Eng. Conf.:(United States)*. 1984. Advanco Corporation, Rancho Mirage, California.
30. IEA, *Concentrated Solar Power (CSP)*. IEA, Paris, 2021.
31. Romero, M., R. Buck, and J.E. Pacheco, *An update on solar central receiver systems, projects, and technologies*. J. Sol. Energy Eng., 2002. **124**(2): p. 98-108.
32. à Tour, C., *Conversion Thermodynamique de l'Energie Solaire (1982)*. Entropie, (103).
33. De Meo, E. and J. Galdo, *Renewable Energy Technology Characterizations TR-109496*. EPRI and DOE Topical Report, 1997. **270**: p. 270.
34. Grasse, W. and H. Hertlein, *Thermal solar power plants experience, Solar Power Plants, CJ Winter, RL Sizmann, and LL Vant-Hull, eds*. 1991.

35. Radosevich, L. and A. Skinrood, *The power production operation of Solar One, the 10 MWe solar thermal central receiver pilot plant*. 1989.
36. Pacheco, J.E. and R. Gilbert, *Overview of recent results of the solar two test and evaluations program*. 1999, Sandia National Labs., Albuquerque, NM (US).
37. Weinstein, L.A., et al., *Concentrating solar power*. Chemical reviews, 2015. **115**(23): p. 12797-12838.
38. Slocum, A.H., et al., *Concentrated solar power on demand*. Solar Energy, 2011. **85**(7): p. 1519-1529.
39. Mokhtar, G., B. Boussad, and S. Noureddine, *A linear Fresnel reflector as a solar system for heating water: Theoretical and experimental study*. Case Studies in Thermal Engineering, 2016. **8**: p. 176-186.
40. Muñoz, J., J.M. Martinez-Val, and A. Ramos, *Thermal regimes in solar-thermal linear collectors*. Solar Energy, 2011. **85**(5): p. 857-870.
41. Abbas, R., et al., *Solar radiation concentration features in Linear Fresnel Reflector arrays*. Energy Conversion and Management, 2012. **54**(1): p. 133-144.
42. Xu, G., et al., *Performance evaluation of a direct vapor generation supercritical ORC system driven by linear Fresnel reflector solar concentrator*. Applied Thermal Engineering, 2015. **80**: p. 196-204.
43. Gordon, J.M. and H. Ries, *Tailored edge-ray concentrators as ideal second stages for Fresnel reflectors*. Applied Optics, 1993. **32**(13): p. 2243-2251.
44. Negi, B.S., S.S. Mathur, and T.C. Kandpal, *Optical and thermal performance evaluation of a linear fresnel reflector solar concentrator*. Solar & Wind Technology, 1989. **6**(5): p. 589-593.
45. Montes, M.J., et al., *A comparative analysis of configurations of linear Fresnel collectors for concentrating solar power*. Energy, 2014. **73**: p. 192-203.
46. Mills, D.R. and G.L. Morrison, *Compact linear Fresnel reflector solar thermal powerplants*. Solar energy, 2000. **68**(3): p. 263-283.
47. Mills, D., *Advances in solar thermal electricity technology*. Solar energy, 2004. **76**(1-3): p. 19-31.
48. Pulido-Iparraguirre, D., et al., *Design, manufacturing and characterization of linear Fresnel reflector's facets*. Energies, 2019. **12**(14): p. 2795.
49. Kidger, M.J. *Fundamental optical design*. 2001. SPIE Bellingham.
50. Lin, M., et al., *Experimental and theoretical analysis on a linear Fresnel reflector solar collector prototype with V-shaped cavity receiver*. Applied Thermal Engineering, 2013. **51**(1): p. 963-972.
51. Barale, G., et al. *Optical design of a linear Fresnel collector for Sicily*. in *16th SolarPACES International Symposium Perpignan, France*. 2010.

52. He, Y.-L., et al., *Review of the solar flux distribution in concentrated solar power: non-uniform features, challenges, and solutions*. Applied Thermal Engineering, 2019. **149**: p. 448-474.
53. Balaji, S., K.S. Reddy, and T. Sundararajan, *Optical modelling and performance analysis of a solar LFR receiver system with parabolic and involute secondary reflectors*. Applied Energy, 2016. **179**: p. 1138-1151.
54. Beltagy, H., et al., *Theoretical and experimental performance analysis of a Fresnel type solar concentrator*. Renewable Energy, 2017. **101**: p. 782-793.
55. Negi, B., T. Kandpal, and S. Mathur, *Designs and performance characteristics of a linear Fresnel reflector solar concentrator with a flat vertical absorber*. Solar & wind technology, 1990. **7**(4): p. 379-392.
56. Karathanasis, S., *Linear Fresnel Reflector Systems Design Parameters*, in *Linear Fresnel Reflector Systems for Solar Radiation Concentration*. 2019, Springer. p. 97-136.
57. Negi, B.S., T.C. Kandpal, and S.S. Mathur, *Designs and performance characteristics of a linear fresnel reflector solar concentrator with a flat vertical absorber*. Solar & Wind Technology, 1990. **7**(4): p. 379-392.
58. Günther, M., et al., *Linear fresnel technology*. i Advanced CSP Teaching Materials, Enernena, 2006.
59. Zhu, Y., et al., *Design and thermal performances of a scalable linear Fresnel reflector solar system*. Energy Conversion and Management, 2017. **146**: p. 174-181.
60. Dersch, J. *Comparison of linear Fresnel and parabolic trough collector systems-system analysis to determine break even costs of linear Fresnel collectors*. in *15<sup>th</sup> International SolarPACES Symposium, 15.-18. September 2009, Berlin*. 2009.
61. Morin, G., et al., *Comparison of Linear Fresnel and Parabolic Trough Collector power plants*. Solar Energy, 2012. **86**(1): p. 1-12.
62. Häberle, A., et al. *The Solarmundo line focussing Fresnel collector. Optical and thermal performance and cost calculations*. in *Proceedings of the 2002 SolarPACES international symposium*. 2002.
63. Bernhard, R., et al. *Linear Fresnel Collector Demonstration on the PSA—Part I: Design, Construction and Quality Control*. in *14th International symposium on concentrated solar power and chemical energy technologies, SolarPACES*. 2008.
64. Brost, R. and G. Zhu, *Commercial development of an advanced, high-temperature, linear-Fresnel based concentrating solar power concept*. SkyFuel, Prepared Under DOE FOA No. DE-FC36-08GO18034, 2009.
65. Brost, R. and G. Zhu, *Design of a High-Temperature Molten Salt Linear Fresnel Collector*. US Department of Energy, Albuquerque, 2010.
66. Qiu, Y., et al., *Aiming strategy optimization for uniform flux distribution in the receiver of a linear Fresnel solar reflector using a multi-objective genetic algorithm*. Applied Energy, 2017. **205**: p. 1394-1407.

67. Conlon, W. *Superheated steam from CLFR solar steam*. in *17th SolarPACES International Symposium, Granada, Spain*. 2011.
68. Grena, R. and P. Tarquini, *Solar linear Fresnel collector using molten nitrates as heat transfer fluid*. *Energy*, 2011. **36**(2): p. 1048-1056.
69. Platzer, W., F. Dinter, and F. Cuevas, *Low-cost Linear Fresnel Collector*.
70. Hinterberger, H. and R. Winston, *Efficient light coupler for threshold Čerenkov counters*. *Review of Scientific Instruments*, 1966. **37**(8): p. 1094-1095.
71. Winston, R., J.C. Miñano, and P.G. Benitez, *Nonimaging optics*. 2005: Elsevier.
72. Baranov, V. and G. Melnikov, *Study of the illumination characteristics of hollow focons*. *Sov. J. Opt. Technol*, 1966. **33**(5): p. 408-411.
73. Winston, R. and H. Hinterberger, *Principles of cylindrical concentrators for solar energy*. *Solar Energy*, 1975. **17**(4): p. 255-258.
74. Rabl, A., *Optical and thermal properties of compound parabolic concentrators*. *Solar energy*, 1976. **18**(6): p. 497-511.
75. Rabl, A., *Active solar collectors and their applications*. 1985: Oxford University Press on Demand.
76. Bernhard, R., et al. *LINEAR FRESNEL COLLECTOR DEMONSTRATION ON THE PSA PART II—COMMISSIONING AND FIRST PERFORMNCE TESTS*. in *14th International Symposium on Concentrated Solar Power and Chemical Energy Technologies*. 2008.
77. Selig, M. and M. Mertins. *From saturated to superheated direct solar steam generation—technical challenges and economical benefits*. in *SolarPACES 2010 Conference*. 2010.
78. Bellos, E., C. Tzivanidis, and A. Papadopoulos, *Optical and thermal analysis of a linear Fresnel reflector operating with thermal oil, molten salt and liquid sodium*. *Applied Thermal Engineering*, 2018. **133**: p. 70-80.
79. Prasad, G.C., K. Reddy, and T. Sundararajan, *Optimization of solar linear Fresnel reflector system with secondary concentrator for uniform flux distribution over absorber tube*. *Solar Energy*, 2017. **150**: p. 1-12.
80. Abbas, R., et al., *Design of an innovative linear Fresnel collector by means of optical performance optimization: A comparison with parabolic trough collectors for different latitudes*. *Solar Energy*, 2017. **153**: p. 459-470.
81. Mathur, S., T. Kandpal, and B. Negi, *Optical design and concentration characteristics of linear Fresnel reflector solar concentrators—II. Mirror elements of equal width*. *Energy Conversion and Management*, 1991. **31**(3): p. 221-232.
82. Mathur, S., T. Kandpal, and B. Negi, *Optical design and concentration characteristics of linear Fresnel reflector solar concentrators—I. Mirror elements of varying width*. *Energy Conversion and Management*, 1991. **31**(3): p. 205-219.



83. Canavarro, D., J. Chaves, and M. Collares-Pereira, *Infinitesimal etendue and Simultaneous Multiple Surface (SMS) concentrators for fixed receiver troughs*. Solar Energy, 2013. **97**: p. 493-504.
84. Canavarro, D., J. Chaves, and M. Collares-Pereira, *Simultaneous Multiple Surface method for Linear Fresnel concentrators with tubular receiver*. Solar Energy, 2014. **110**: p. 105-116.
85. Zhu, G., *New adaptive method to optimize the secondary reflector of linear Fresnel collectors*. Solar Energy, 2017. **144**: p. 117-126.
86. Ahmadi, M.H., et al., *Solar power technology for electricity generation: A critical review*. Energy Science & Engineering, 2018. **6**(5): p. 340-361.
87. Kalogirou, S.A., *Solar energy engineering: processes and systems*. 2013: Academic Press.
88. Sorenson, B. and P. Breez, *Renewable Energy Focus Handbook*, 2009. Academic Press.
89. Chafie, M., et al., *Experimental investigation of parabolic trough collector system under Tunisian climate: Design, manufacturing and performance assessment*. Applied thermal engineering, 2016. **101**: p. 273-283.
90. Kalogirou, S.A., *Solar thermal collectors and applications*. Progress in Energy and Combustion Science, 2004. **30**(3): p. 231-295.
91. Mohammad, S.T., H.H. Al-Kayiem, and M.K. Assadi, *Developed mathematical model of solar thermal parabolic trough power plant at Universiti Teknologi Petronas*. J Eng Appl Sci, 2016. **11**(20): p. 12140-12145.
92. Geyer, M., et al. *EUROTROUGH-Parabolic trough collector developed for cost efficient solar power generation*. in *11th International symposium on concentrating solar power and chemical energy technologies*. 2002. Citeseer.
93. Liu, J., D. Lei, and Q. Li, *Vacuum lifetime and residual gas analysis of parabolic trough receiver*. Renewable energy, 2016. **86**: p. 949-954.
94. Zhang, H.L., et al., *Concentrated solar power plants: Review and design methodology*. Renewable and Sustainable Energy Reviews, 2013. **22**: p. 466-481.
95. Liberali, R. and A. Finat, *Concentrating Solar Power: from Research to Implementation*. European Communities, Luxembourg, 2007.
96. Padilla, R.V., et al., *Heat transfer analysis of parabolic trough solar receiver*. Applied Energy, 2011. **88**(12): p. 5097-5110.
97. Cheng, Z.D., Y.L. He, and F.Q. Cui, *Numerical study of heat transfer enhancement by unilateral longitudinal vortex generators inside parabolic trough solar receivers*. International Journal of Heat and Mass Transfer, 2012. **55**(21): p. 5631-5641.
98. Geyer, M. *Introducing Concentrated Solar Power on the International Markets: Worldwide Incentives, Policies and Benefits*. in *Proceedings of the 14 th Biennial Solar Power and Chemical Energy Systems (SolarPACES) Symposium, Las Vegas, NV*. 2008.

99. Barlev, D., R. Vidu, and P. Stroeve, *Innovation in concentrated solar power*. Solar Energy Materials and Solar Cells, 2011. **95**(10): p. 2703-2725.
100. White, M., S. Qiu, and R. Galbraith. *Phase change salt thermal energy storage for dish stirling solar power systems*. in *Energy Sustainability*. 2013. American Society of Mechanical Engineers.
101. Andraka, C.E., et al., *Metallic phase change material thermal storage for dish Stirling*. Energy Procedia, 2015. **69**: p. 726-736.
102. Shahbazfar, R., T. Fend, and M. Hamdan, *Advanced CSP Teaching Materials Chapter 7 Solar Dish Technology Authors*. Adv. CSP Teach. Mater., 2011: p. 1-63.
103. Kalogirou, S., *solar thermal collectors and applications progress in energy and combustion science, edition: London*. Washington DC, 2004.
104. Pitz-Paal, R. *Concentrating solar technologies: the key to renewable electricity and process heat for a wide range of applications*. in *Proceedings of the World Renewable Energy Congress VII on CD-ROM, Cologne, Germany*. 2002.
105. Sup, B.A., et al., *Effect of Rim Angle to the Flux Distribution Diameter in Solar Parabolic Dish Collector*. Energy Procedia, 2015. **68**: p. 45-52.
106. Malali, P.D., S.K. Chaturvedi, and T. Abdel-Salam, *Performance optimization of a regenerative Brayton heat engine coupled with a parabolic dish solar collector*. Energy Conversion and Management, 2017. **143**: p. 85-95.
107. Stine, W.B. and R.B. Diver, *A compendium of solar dish/Stirling technology*. 1994.
108. SES, *Stirling Energy Systems Inc., Solar Dish Stirling Systems Report*. 2007, NREL CSP Technology Workshop.
109. Laing, D.e.a., *Dish-Stirling-Systeme*“. In: *FVS Themen*. 2002. p. pp. 30-34.
110. Adkins, D., et al., *Heat pipe solar receiver development activities at Sandia National Laboratories*. 1999, Sandia National Labs., Albuquerque, NM (US); Sandia National Labs ....
111. Karimi, R., T.T. Gheinani, and V.M. Avargani, *A detailed mathematical model for thermal performance analysis of a cylindrical cavity receiver in a solar parabolic dish collector system*. Renewable energy, 2018. **125**: p. 768-782.
112. Kumar, N.S. and K. Reddy, *Comparison of receivers for solar dish collector system*. Energy Conversion and Management, 2008. **49**(4): p. 812-819.
113. Cherif, H., et al., *A receiver geometrical details effect on a solar parabolic dish collector performance*. Energy Reports, 2019. **5**: p. 882-897.
114. Clausing, A., *An analysis of convective losses from cavity solar central receivers*. Solar Energy, 1981. **27**(4): p. 295-300.
115. Li, H., et al., *Optical analysis and optimization of parabolic dish solar concentrator with a cavity receiver*. Solar energy, 2013. **92**: p. 288-297.

116. Reddy, K., G. Veershetty, and T.S. Vikram, *Effect of wind speed and direction on convective heat losses from solar parabolic dish modified cavity receiver*. Solar Energy, 2016. **131**: p. 183-198.
117. Harris, J.A. and T.G. Lenz, *Thermal performance of solar concentrator/cavity receiver systems*. Solar energy, 1985. **34**(2): p. 135-142.
118. Patel, S. and G. Reitenbach, *Dish Stirling Solar Plant Debuts*. Power, 2010. **154**(4): p. 12-12.
119. Kinoshita, G.S., *Shenandoah parabolic dish solar collector*. NASA STI/Recon Technical Report N, 1985. **85**: p. 28460.
120. Coventry, J. and C. Andraka, *Dish systems for CSP*. Solar Energy, 2017. **152**: p. 140-170.
121. Shagdar, E., et al., *Process analysis of solar steam reforming of methane for producing low-carbon hydrogen*. RSC Advances, 2020. **10**(21): p. 12582-12597.
122. Romero, M., et al., *Distributed power from solar tower systems: a MIUS approach*. Solar Energy, 1999. **67**(4-6): p. 249-264.
123. Chavez, J., G. Kolb, and W. Meinecke, *Second Generation Central Receiver Technologies—A Status Report*. Becker M., Klimas PC, Verlag CF Müller, Karlsruhe, Germany, 1993.
124. Cekirge, H., *A Comparison of Solar Power Systems (CSP): Solar Tower (ST) Systems versus Parabolic Trough (PT) Systems*. American Journal of Energy Engineering, 2015. **3**: p. 29.
125. Björkman, N., *Heliostat design*. 2014.
126. Vant-Hull, L.L., *Central tower concentrating solar power systems*, in *Concentrating solar power technology*. 2021, Elsevier. p. 267-310.
127. Pidaparthi, A., *Heliostat Cost Reduction for Power Tower Plants*. 2017.
128. Weinrebe, G., *Holistic Design and Optimization - Concept & Application*. 2014.
129. Jones, S.A. and K. Stone, *Analysis of solar two heliostat tracking error sources*. 1999, Sandia National Laboratories, Albuquerque, NM, and Livermore, CA.
130. García, L., M. Burisch, and M. Sanchez, *Spillage estimation in a heliostats field for solar field optimization*. Energy Procedia, 2015. **69**: p. 1269-1276.
131. Zhang, M., et al., *An efficient code to optimize the heliostat field and comparisons between the biomimetic spiral and staggered layout*. Renewable energy, 2016. **87**: p. 720-730.
132. Landman, W.A., *Optical performance of the reflective surface profile of a heliostat*. 2017, Stellenbosch: Stellenbosch University.
133. Bhattacharjee, R. and S. Bhattacharjee, *Performance of inclined heliostat solar field with solar geometrical factors*. Energy Sources, Part A: Recovery, Utilization, and Environmental Effects, 2020: p. 1-23.

134. Boudaoud, S., et al., *Thermal performance prediction and sensitivity analysis for future deployment of molten salt cavity receiver solar power plants in Algeria*. Energy Conversion and Management, 2015. **89**: p. 655-664.
135. Collado, F.J. and J. Guallar, *A review of optimized design layouts for solar power tower plants with campo code*. Renewable and Sustainable Energy Reviews, 2013. **20**: p. 142-154.
136. Riaz, M., *A theory of concentrators of solar energy on a central receiver for electric power generation*. 1976.
137. Jadhav, S. and V. Venkatraj. *Thermal losses in central receiver solar thermal power plant*. in *IOP Conference Series: Materials Science and Engineering*. 2018. IOP Publishing.
138. Servert, J., et al. *Sensitivity analysis of heliostat aiming strategies and receiver size on annual thermal production of a molten salt external receiver*. in *AIP Conference Proceedings*. 2017. AIP Publishing LLC.
139. Sánchez-González, A. and D. Santana, *Solar flux distribution on central receivers: A projection method from analytic function*. Renewable Energy, 2015. **74**: p. 576-587.
140. Ho, C.K. and J.E. Pacheco, *Levelized Cost of Coating (LCOC) for selective absorber materials*. Solar energy, 2014. **108**: p. 315-321.
141. Ho, C.K. and B.D. Iverson, *Review of high-temperature central receiver designs for concentrating solar power*. Renewable and Sustainable Energy Reviews, 2014. **29**: p. 835-846.
142. Segal, A. and M. Epstein, *The optics of the solar tower reflector*. Solar Energy, 2001. **69**: p. 229-241.
143. Slocum, A.H., et al., *Concentrated solar power on demand*. Solar Energy, 2011. **85**(7): p. 1519-1529.
144. Mokhtar, M., et al., *Performance of a 100 kWth concentrated solar beam-down optical experiment*. Journal of Solar Energy Engineering, 2014. **136**(4).
145. Battleson, K.W., *Solar power tower design guide: Solar thermal central receiver power systems. A source of electricity and/or process heat*. 1981, Sandia National Lab.(SNL-CA), Livermore, CA (United States).
146. Tian, Y. and C.Y. Zhao, *A review of solar collectors and thermal energy storage in solar thermal applications*. Applied Energy, 2013. **104**: p. 538-553.
147. Zhang, H., et al., *High-efficiency solar power towers using particle suspensions as heat carrier in the receiver and in the thermal energy storage*. Renewable Energy, 2017. **111**: p. 438-446.
148. Hoffschmidt, B., *Receivers for solar tower systems*. 2014.
149. Rodríguez-Sánchez, M.d.I.R., A. Sánchez-González, and D. Santana, *Feasibility study of a new concept of solar external receiver: Variable velocity receiver*. Applied Thermal Engineering, 2018. **128**: p. 335-344.
150. Salomé, A., et al., *Control of the flux distribution on a solar tower receiver using an optimized aiming point strategy: Application to THEMIS solar tower*. Solar Energy, 2013. **94**: p. 352-366.

151. Roldán, M., J. Fernández-Reche, and J. Ballestrín, *Computational fluid dynamics evaluation of the operating conditions for a volumetric receiver installed in a solar tower*. Energy, 2016. **94**: p. 844-856.
152. Hoffschmidt, B., et al., *Performance evaluation of the 200-kW th HiTRec-II open volumetric air receiver*. J. Sol. Energy Eng., 2003. **125**(1): p. 87-94.
153. Pabst, C., et al., *Experimental performance of an advanced metal volumetric air receiver for Solar Towers*. Renewable Energy, 2017. **106**: p. 91-98.
154. Roldán, M.I., J. Fernández-Reche, and J. Ballestrín, *Computational fluid dynamics evaluation of the operating conditions for a volumetric receiver installed in a solar tower*. Energy, 2016. **94**: p. 844-856.
155. Luo, Y., X. Du, and D. Wen, *Novel design of central dual-receiver for solar power tower*. Applied Thermal Engineering, 2015. **91**: p. 1071-1081.
156. Ho, C.K., et al. *Reduction of radiative heat losses for solar thermal receivers*. in *High and Low Concentrator Systems for Solar Energy Applications IX*. 2014. International Society for Optics and Photonics.
157. Behar, O., A. Khellaf, and K. Mohammedi, *A review of studies on central receiver solar thermal power plants*. Renewable and sustainable energy reviews, 2013. **23**: p. 12-39.
158. Kim, K., et al., *A study of solid particle flow characterization in solar particle receiver*. Solar Energy, 2009. **83**(10): p. 1784-1793.
159. Christian, J.M., et al., *CFD Simulation and Performance Analysis of Alternative Designs for High-Temperature Solid Particle Receivers*. 2011, Sandia National Lab.(SNL-NM), Albuquerque, NM (United States).
160. Price, H.W., D.D. Whitney, and H. Beebe, *SMUD Kokhala power tower study*. 1997, National Renewable Energy Laboratory, Golden, CO (United States).
161. Kribus, A., et al., *A solar-driven combined cycle power plant*. Solar energy, 1998. **62**(2): p. 121-129.
162. Buck, R., E. Lüpfert, and F. Tellez. *Receiver for solar-hybrid gas turbine and CC systems (REFOS)*. in *Solar Thermal 2000 International Conference*. 2000.
163. Vignarooban, K., et al., *Heat transfer fluids for concentrating solar power systems – A review*. Applied Energy, 2015. **146**: p. 383-396.
164. Pacio, J. and T. Wetzel, *Assessment of liquid metal technology status and research paths for their use as efficient heat transfer fluids in solar central receiver systems*. Solar Energy, 2013. **93**: p. 11-22.
165. Cordaro, J.G., N.C. Rubin, and R.W. Bradshaw, *Multicomponent molten salt mixtures based on nitrate/nitrite anions*. Journal of Solar Energy Engineering, Transactions of the ASME, 2011. **133**(1).
166. López-González, D., et al., *Characterization of different heat transfer fluids and degradation study by using a pilot plant device operating at real conditions*. Energy, 2013. **54**: p. 240-250.

167. Looser, R., M. Vivar, and V. Everett, *Spectral characterisation and long-term performance analysis of various commercial Heat Transfer Fluids (HTF) as Direct-Absorption Filters for CPV-T beam-splitting applications*. Applied energy, 2014. **113**: p. 1496-1511.
168. Peng, Q., et al., *High-temperature thermal stability of molten salt materials*. International Journal of Energy Research, 2008. **32**(12): p. 1164-1174.
169. Peng, Q., et al., *Design of new molten salt thermal energy storage material for solar thermal power plant*. Applied Energy, 2013. **112**: p. 682-689.
170. Goods, S.H. and R.W. Bradshaw, *Corrosion of Stainless Steels and Carbon Steel by Molten Mixtures of Commercial Nitrate Salts*. Journal of Materials Engineering and Performance, 2004. **13**(1): p. 78-87.
171. Gil, A., et al., *State of the art on high temperature thermal energy storage for power generation. Part 1—Concepts, materials and modellization*. Renewable and Sustainable Energy Reviews, 2010. **14**(1): p. 31-55.
172. Ouagued, M., A. Khellaf, and L. Loukarfi, *Estimation of the temperature, heat gain and heat loss by solar parabolic trough collector under Algerian climate using different thermal oils*. Energy Conversion and Management, 2013. **75**: p. 191-201.
173. Nkwetta, D.N., et al., *Experimental performance analysis and optimisation of medium temperature solar thermal collectors with silicon oil as a heat transfer fluid*. International Journal of Energy Research, 2013. **37**(6): p. 570-581.
174. Kasaeian, A., A.T. Eshghi, and M. Sameti, *A review on the applications of nanofluids in solar energy systems*. Renewable and Sustainable Energy Reviews, 2015. **43**: p. 584-598.
175. Dunn, R.I., P.J. Hearps, and M.N. Wright, *Molten-Salt Power Towers: Newly Commercial Concentrating Solar Storage*. Proceedings of the IEEE, 2012. **100**(2): p. 504-515.
176. Sohal, M.S., et al., *Conceptual design of forced convection molten salt heat transfer testing loop*. 2010, Idaho National Laboratory (United States). Funding organisation: DOE-NE ....
177. Kearney, D., et al., *Engineering aspects of a molten salt heat transfer fluid in a trough solar field*. Energy, 2004. **29**(5-6): p. 861-870.
178. Kearney, D., et al., *Assessment of a molten salt heat transfer fluid in a parabolic trough solar field*. J. Sol. Energy Eng., 2003. **125**(2): p. 170-176.
179. Bradshaw, R.W. and N.P. Siegel. *Molten nitrate salt development for thermal energy storage in parabolic trough solar power systems*. in *Energy Sustainability*. 2008.
180. Vignarooban, K., et al., *Heat transfer fluids for concentrating solar power systems—a review*. Applied Energy, 2015. **146**: p. 383-396.
181. Birnbaum, J., et al., *Steam temperature stability in a direct steam generation solar power plant*. Solar Energy, 2011. **85**(4): p. 660-668.
182. Modi, A. and F. Haglind, *Performance analysis of a Kalina cycle for a central receiver solar thermal power plant with direct steam generation*. Applied Thermal Engineering, 2014. **65**(1): p. 201-208.

183. Zarza, E., et al., *Direct steam generation in parabolic troughs: Final results and conclusions of the DISS project*. Energy, 2004. **29**(5-6): p. 635-644.
184. Zarza, E., et al., *INDITEP: The first pre-commercial DSG solar power plant*. Solar energy, 2006. **80**(10): p. 1270-1276.
185. Majumdar, A., *Advanced Research Projects Agency-Energy (ARPA-E) Annual Report for FY 2011*. 2011, USDOE Advanced Research Projects Agency-Energy (ARPA-E).
186. Feldhoff, J.F., et al., *Economic potential of solar thermal power plants with direct steam generation compared with HTF plants*. Journal of Solar Energy Engineering, 2010. **132**(4).
187. Hirsch, T., et al., *Advancements in the field of direct steam generation in linear solar concentrators—a review*. Heat Transfer Engineering, 2014. **35**(3): p. 258-271.
188. Pistocchini, L. and M. Motta, *Feasibility study of an innovative dry-cooling system with phase-change material storage for concentrated solar power multi-MW size power plant*. Journal of Solar Energy Engineering, Transactions of the ASME, 2011. **133**(3).
189. Liu, M., et al., *Impact of the heat transfer fluid in a flat plate phase change thermal storage unit for concentrated solar tower plants*. Solar Energy, 2014. **101**: p. 220-231.
190. Zunft, S., et al., *Jlich solar power tower-experimental evaluation of the storage subsystem and performance calculation*. Journal of Solar Energy Engineering, Transactions of the ASME, 2011. **133**(3).
191. Ávila-Marín, A.L., *Volumetric receivers in Solar Thermal Power Plants with Central Receiver System technology: A review*. Solar Energy, 2011. **85**(5): p. 891-910.
192. Muñoz-Antón, J., et al., *Performance study of solar power plants with CO<sub>2</sub> as working fluid. A promising design window*. Energy Conversion and Management, 2015. **92**: p. 36-46.
193. Cipollone, R., A. Cinocca, and A. Gualtieri, *Gases as working fluid in parabolic trough CSP plants*. Procedia computer science, 2013. **19**: p. 702-711.
194. Cau, G., D. Cocco, and V. Tola, *Performance and cost assessment of Integrated Solar Combined Cycle Systems (ISCCSs) using CO<sub>2</sub> as heat transfer fluid*. Solar Energy, 2012. **86**(10): p. 2975-2985.
195. Dostal, V., P. Hejzlar, and M.J. Driscoll, *The supercritical carbon dioxide power cycle: comparison to other advanced power cycles*. Nuclear technology, 2006. **154**(3): p. 283-301.
196. Padilla, R.V., et al., *Exergetic analysis of supercritical CO<sub>2</sub> Brayton cycles integrated with solar central receivers*. Applied Energy, 2015. **148**: p. 348-365.
197. Hirschier, I., P. Leumann, and A. Steinfeld, *Experimental and numerical analyses of a pressurized air receiver for solar-driven gas turbines*. 2012.
198. Bader, R., et al. *An air-based cavity-receiver for solar trough concentrators*. in *Energy Sustainability*. 2010.

199. Biencinto, M., et al., *Performance model and annual yield comparison of parabolic-trough solar thermal power plants with either nitrogen or synthetic oil as heat transfer fluid*. Energy conversion and management, 2014. **87**: p. 238-249.
200. Meier, G.H., *A review of advances in high-temperature corrosion*. Materials Science and Engineering: A, 1989. **120-121**: p. 1-11.
201. Klöwer, J., *High temperature Corrosion behaviour of iron aluminides and iron-aluminium-chromium alloys*. Materials and Corrosion, 1996. **47**(12): p. 685-694.
202. Chen, R.Y. and W.Y.D. Yeun, *Review of the High-Temperature Oxidation of Iron and Carbon Steels in Air or Oxygen*. Oxidation of Metals, 2003. **59**(5): p. 433-468.
203. Chen, R. and W. Yuen, *Oxide-scale structures formed on commercial hot-rolled steel strip and their formation mechanisms*. Oxidation of metals, 2001. **56**(1): p. 89-118.
204. Xu, X., et al. *Solar thermal closed-helium Brayton cycle with high temperature phase-change thermal storage*. in *Energy Sustainability*. 2010.
205. Massidda, L. and A. Varone, *A numerical analysis of a high temperature solar collecting tube, using helium as an heat transfer fluid*. 2007.
206. Ma, Z. and C.S. Turchi, *Advanced supercritical carbon dioxide power cycle configurations for use in concentrating solar power systems*. 2011, National Renewable Energy Lab.(NREL), Golden, CO (United States).
207. Boerema, N., et al., *Liquid sodium versus Hitec as a heat transfer fluid in solar thermal central receiver systems*. Solar Energy, 2012. **86**(9): p. 2293-2305.
208. Pacio, J., et al., *Thermodynamic evaluation of liquid metals as heat transfer fluids in concentrated solar power plants*. Applied thermal engineering, 2013. **60**(1-2): p. 295-302.
209. Pacio, J., et al., *Liquid metals as efficient coolants for high-intensity point-focus receivers: implications to the design and performance of next-generation CSP systems*. Energy Procedia, 2014. **49**: p. 647-655.
210. Frazer, D., et al., *Liquid metal as a heat transport fluid for thermal solar power applications*. Energy Procedia, 2014. **49**: p. 627-636.
211. Cabaleiro, D., et al., *Thermophysical properties of (diphenyl ether+biphenyl) mixtures for their use as heat transfer fluids*. The Journal of Chemical Thermodynamics, 2012. **50**: p. 80-88.
212. Tocci, L., et al., *Small scale Organic Rankine Cycle (ORC): A techno-economic review*. Energies, 2017. **10**(4): p. 413.
213. Lemmens, S., *Cost engineering techniques and their applicability for cost estimation of organic Rankine cycle systems*. Energies, 2016. **9**(7): p. 485.
214. Hung, T.-C., T. Shai, and S.K. Wang, *A review of organic Rankine cycles (ORCs) for the recovery of low-grade waste heat*. Energy, 1997. **22**(7): p. 661-667.
215. Alshammari, F., M. Usman, and A. Pesyridis, *Expanders for organic Rankine cycle technology*. Organic Rankine Cycle Technology for Heat Recovery, 2018. **41**.



216. Ibarra, M., et al., *Performance of a 5kWe Organic Rankine Cycle at part-load operation*. Applied Energy, 2014. **120**: p. 147-158.
217. Kang, S.H., *Design and preliminary tests of ORC (organic Rankine cycle) with two-stage radial turbine*. Energy, 2016. **96**: p. 142-154.
218. Pini, M., et al., *Preliminary design of a centrifugal turbine for organic rankine cycle applications*. Journal of Engineering for Gas turbines and power, 2013. **135**(4).
219. Colonna, P., et al., *Organic Rankine cycle power systems: from the concept to current technology, applications, and an outlook to the future*. Journal of Engineering for Gas Turbines and Power, 2015. **137**(10).
220. Colonna, P., et al., *Real-gas effects in organic Rankine cycle turbine nozzles*. Journal of Propulsion and Power, 2008. **24**(2): p. 282-294.
221. Rahbar, K., et al., *Review of organic Rankine cycle for small-scale applications*. Energy Conversion and Management, 2017. **134**: p. 135-155.
222. Hu, D., et al., *Off-design performance comparison of an organic Rankine cycle under different control strategies*. Applied Energy, 2015. **156**: p. 268-279.
223. Sauret, E. and Y. Gu, *Three-dimensional off-design numerical analysis of an organic Rankine cycle radial-inflow turbine*. Applied Energy, 2014. **135**: p. 202-211.
224. Vitale, S., et al. *Centrifugal Turbines for Mini-Orc Power Systems*. in *2nd International Seminar on Organic Rankine Cycle Power Systems*. 2013. NLD.
225. Pei, G., et al., *Construction and dynamic test of a small-scale organic rankine cycle*. Energy, 2011. **36**(5): p. 3215-3223.
226. Kang, S.H., *Design and experimental study of ORC (organic Rankine cycle) and radial turbine using R245fa working fluid*. Energy, 2012. **41**(1): p. 514-524.
227. Al Jubori, A., et al. *Development of Efficient Small Scale Axial Turbine for Solar Driven Organic Rankine Cycle*. in *ASME Turbo Expo 2016: Turbomachinery Technical Conference and Exposition*. 2016.
228. Da Lio, L., G. Manente, and A. Lazzaretto, *New efficiency charts for the optimum design of axial flow turbines for organic Rankine cycles*. Energy, 2014. **77**: p. 447-459.
229. Da Lio, L., G. Manente, and A. Lazzaretto, *Predicting the optimum design of single stage axial expanders in ORC systems: Is there a single efficiency map for different working fluids?* Applied Energy, 2016. **167**: p. 44-58.
230. Martins, G.L., S.L. Braga, and S.B. Ferreira, *Design optimization of partial admission axial turbine for ORC service*. Applied Thermal Engineering, 2016. **96**: p. 18-25.
231. Saitoh, T., N. Yamada, and S.-I. Wakashima, *Solar Rankine cycle system using scroll expander*. Journal of Environment and Engineering, 2007. **2**(4): p. 708-719.
232. Imran, M., et al., *Volumetric expanders for low grade heat and waste heat recovery applications*. Renewable and Sustainable Energy Reviews, 2016. **57**: p. 1090-1109.

233. Eyerer, S., et al., *Experimental study of an ORC (Organic Rankine Cycle) and analysis of R1233zd-E as a drop-in replacement for R245fa for low temperature heat utilization*. Energy, 2016. **103**: p. 660-671.
234. Chang, J.-C., et al., *Experimental study on low-temperature organic Rankine cycle utilizing scroll type expander*. Applied Energy, 2015. **155**: p. 150-159.
235. Smith, I. and N. Stosic. *Prospects for energy conversion efficiency improvements by the use of twin screw two-phase expanders*. in *2nd International Heat Power Cycles Conference, Paris, France*. 2001.
236. Clemente, S., et al., *Bottoming organic Rankine cycle for a small scale gas turbine: A comparison of different solutions*. Applied Energy, 2013. **106**: p. 355-364.
237. Ziviani, D., et al., *Characterizing the performance of a single-screw expander in a small-scale organic Rankine cycle for waste heat recovery*. Applied Energy, 2016. **181**: p. 155-170.
238. Quoilin, S., et al., *Techno-economic survey of Organic Rankine Cycle (ORC) systems*. Renewable and Sustainable Energy Reviews, 2013. **22**: p. 168-186.
239. Rayegan, R. and Y.X. Tao, *A procedure to select working fluids for Solar Organic Rankine Cycles (ORCs)*. Renewable Energy, 2011. **36**(2): p. 659-670.
240. Aljundi, I.H., *Effect of dry hydrocarbons and critical point temperature on the efficiencies of organic Rankine cycle*. Renewable Energy, 2011. **36**(4): p. 1196-1202.
241. Aghahosseini, S. and I. Dincer, *Comparative performance analysis of low-temperature Organic Rankine Cycle (ORC) using pure and zeotropic working fluids*. Applied Thermal Engineering, 2013. **54**(1): p. 35-42.
242. Chen, H., D.Y. Goswami, and E.K. Stefanakos, *A review of thermodynamic cycles and working fluids for the conversion of low-grade heat*. Renewable and sustainable energy reviews, 2010. **14**(9): p. 3059-3067.
243. Borsukiewicz-Gozdur, A., *Experimental investigation of R227ea applied as working fluid in the ORC power plant with hermetic turbogenerator*. Applied Thermal Engineering, 2013. **56**(1): p. 126-133.
244. Lee, Y.-R., C.-R. Kuo, and C.-C. Wang, *Transient response of a 50 kW organic Rankine cycle system*. Energy, 2012. **48**(1): p. 532-538.
245. Turboden. *Clean energy ahead Turboden A Pratt & Whitney Power Systems*. 13/06/2018]; Available from: [www.turboden.com](http://www.turboden.com).
246. Barber, R.E., *Current costs of solar powered organic Rankine cycle engines*. Solar Energy, 1978. **20**(1): p. 1-6.
247. Delgado-Torres, A.M. and L. García-Rodríguez, *Preliminary design of seawater and brackish water reverse osmosis desalination systems driven by low-temperature solar organic Rankine cycles (ORC)*. Energy Conversion and Management, 2010. **51**(12): p. 2913-2920.
248. De Ruyck, J., F. Delattin, and S. Bram, *Co-utilization of biomass and natural gas in combined cycles through primary steam reforming of the natural gas*. Energy, 2007. **32**(4): p. 371-377.

249. David G, M.F., *Small scale biomass power plant using organic Rankine cycle technology*. SAS Enertime, 2008.
250. Systems, A.P.W.P. *Clean energy ahead Turboden*. 2019; Available from: [www.turboden.com](http://www.turboden.com).
251. Schuster, A., et al., *Energetic and economic investigation of Organic Rankine Cycle applications*. Applied Thermal Engineering, 2009. **29**(8): p. 1809-1817.
252. Bidini, G., U. Desideri, and F. Di Maria, *A single flash integrated gas turbine-geothermal power plant with non condensable gas combustion*. Geothermics, 1999. **28**(1): p. 131-150.
253. Desideri, U. and G. Bidini, *Study of possible optimisation criteria for geothermal power plants*. Energy Conversion and Management, 1997. **38**(15-17): p. 1681-1691.
254. Heard, C., H. Fernández, and F. Holland, *Development in geothermal energy in Mexico—part twenty seven: The potential for geothermal organic rankine cycle power plants in Mexico*. Heat Recovery Systems and CHP, 1990. **10**(2): p. 79-86.
255. DiPippo, R., *Geothermal power plants: principles, applications, case studies and environmental impact*. 2012: Butterworth-Heinemann.
256. Schuster, A., et al., *Energetic and economic investigation of Organic Rankine Cycle applications*. Applied thermal engineering, 2009. **29**(8-9): p. 1809-1817.
257. Saleh, B., et al., *Working fluids for low-temperature organic Rankine cycles*. Energy, 2007. **32**(7): p. 1210-1221.
258. DiPippo, R., *Second Law assessment of binary plants generating power from low-temperature geothermal fluids*. Geothermics, 2004. **33**(5): p. 565-586.
259. Mohanty, B. and G. Paloso Jr, *Economic power generation from low-temperature geothermal resources using organic Rankine cycle combined with vapour absorption chiller*. Heat Recovery Systems and CHP, 1992. **12**(2): p. 143-158.
260. Chacartegui, R., et al., *Alternative ORC bottoming cycles FOR combined cycle power plants*. Applied Energy, 2009. **86**(10): p. 2162-2170.
261. Invernizzi, C., P. Iora, and P. Silva, *Bottoming micro-Rankine cycles for micro-gas turbines*. Applied Thermal Engineering, 2007. **27**(1): p. 100-110.
262. Najjar, Y.S. and A.M. Radhwan, *Cogeneration by combining gas turbine engine with organic Rankine cycle*. Heat Recovery Systems and CHP, 1988. **8**(3): p. 211-219.
263. Najjar, Y.S., *Efficient use of energy by utilizing gas turbine combined systems*. Applied Thermal Engineering, 2001. **21**(4): p. 407-438.
264. Gunther, M. and R. Shahbazfar, *Solar dish technology*. Advanced CSP teaching materials, 2011. **1**: p. 1-63.
265. Lovegrove, K. and W. Stein, *Concentrating solar power technology: principles, developments and applications*. 2012.

266. Sawin, J.L., et al., *Renewables 2017 global status report*. 2016.
267. Rinalder, L., et al., *Renewables in Cities 2021 Global Status Report*. REN21 Secretariat: Paris, France, 2021.
268. Electricity, S.T., *Technology Roadmap*. 2014.
269. IEA, *Renewables 2019*. 2019: Paris.
270. IEA, B., *Renewables 2020 Analysis and forecast to 2025*. 2020.
271. Boretti, A., S. Castelletto, and S. Al-Zubaidy, *Concentrating solar power tower technology: present status and outlook*. Nonlinear Engineering, 2019. **8**(1): p. 10-31.
272. Madaeni, S.H., R. Sioshansi, and P. Denholm, *Capacity value of concentrating solar power plants*. 2011, National Renewable Energy Lab.(NREL), Golden, CO (United States).
273. Sioshansi, R. and P. Denholm, *The value of concentrating solar power and thermal energy storage*. IEEE Transactions on Sustainable Energy, 2010. **1**(3): p. 173-183.
274. Davenport, T.L., T.A. Hough, and W.J. Cassarly. *Optimization for illumination systems: the next level of design*. in *Photon Management*. 2004. International Society for Optics and Photonics.
275. Cassarly, W.J. *Illumination merit functions*. in *Nonimaging Optics and Efficient Illumination Systems IV*. 2007. International Society for Optics and Photonics.
276. Fournier, F.R., W.J. Cassarly, and J.P. Rolland. *Optimization of single reflectors for extended sources*. in *Illumination Optics*. 2008. International Society for Optics and Photonics.
277. Singh, P.L., R.M. Sarviya, and J.L. Bhagoria, *Thermal performance of linear Fresnel reflecting solar concentrator with trapezoidal cavity absorbers*. Applied Energy, 2010. **87**(2): p. 541-550.
278. Davenport, T.L., T.A. Hough, and W.J. Cassarly. *Optimization for illumination systems: the next level of design*. in *Photon Management*. 2004. SPIE.
279. Mastellone, M.L., et al. *Performance comparison of different thermal fluids in concentrating solar plants*. in *ASTFE Digital Library*. 2020. Begel House Inc.
280. Fluent, A., *Ansys Fluent 12.0 Theory Guide*. ANSYS Inc., Canonsburg, PA, 2009.
281. Calow, P.P., *Encyclopedia of ecology and environmental management*. 2009: John Wiley & Sons.
282. Manual, U., *ANSYS FLUENT 12.0. Theory Guide*, 2009.
283. Abdalla, M. and S. Pannir, *Density of the Refrigerant Fluids of R365mfc and R152a: Measurement and Prediction*. 2016.
284. Forrest, E., et al., *Pool boiling performance of Novec TM 649 engineered fluid*. 2009.
285. Sharma, V., J.K. Nayak, and S.B. Kedare, *Effects of shading and blocking in linear Fresnel reflector field*. Solar Energy, 2015. **113**: p. 114-138.

- 286. Sharma, V., et al., *Effects of shading and blocking in compact linear fresnel reflector field*. Energy, 2016. **94**: p. 633-653.
- 287. Wakter, S. and F. Wikerman, *A novel shade analysis technique for solar photovoltaic systems*. 2014.
- 288. El Gharbi, N., et al., *A comparative study between parabolic trough collector and linear Fresnel reflector technologies*. Energy Procedia, 2011. **6**: p. 565-572.
- 289. Py, X., Y. Azoumah, and R. Olives, *Concentrated solar power: Current technologies, major innovative issues and applicability to West African countries*. Renewable and Sustainable Energy Reviews, 2013. **18**: p. 306-315.